Investigating the Influence of Substrate Stiffness and Cardiovascular Ageing: Structural, Functional and Metabolic Responses using Induced Pluripotent Stem Cell-Derived Cardiomyocytes

by

Leena Thakorbhai Patel

UNIVERSITY OF BIRMINGHAM

A thesis submitted to the University of Birmingham for the degree of Doctor of Philosophy

Institute of Cardiovascular Sciences
College of Medical and Dental Sciences
University of Birmingham
August 2024

Abstract

Background Cardiovascular ageing is characterised by fibrosis and increased stiffening of the extracellular matrix (ECM) due to excessive deposition of ECM proteins. The structural remodelling of the ECM can largely impact cardiomyocyte (CMs) behaviour and function. Induced pluripotent stem cell derived cardiomyocytes (iPSC-CMs) have been widely used in cardiac research to model cardiovascular diseases. Current experiments utilise tissue culture plastics, which are far stiffer than the natural environment of CMs, thus are not representative of physiological conditions.

Modelling cardiac ageing by recapitulating the stiffness of the healthy and fibrotic myocardium using biomaterials can provide insight into mechanisms and pathways altered by ageing, ultimately contributing to the development of novel therapeutic strategies. Furthermore, cardiac diseases that display accelerated ageing phenotypes, such as Alström Syndrome (AS), can also be studied to enhance our understanding of cardiac ageing disease mechanisms and pathways.

Aims: This work attempts to develop a representative model of the healthy and ageing myocardium, by mimicking stiffnesses using biomaterial hydrogels (Chapter 3). Characterise the effect of ECM stiffnesses on the structure of iPSC-CMs (Chapter 4). Characterise the effect of ECM stiffnesses on iPSC-CM metabolic function (Chapter 5). Assess whether AS is a model of accelerated ageing using Phenoage(Chapter 6). Investigate the cardiac role of *ALMS1* in AS using *ALMS1* knockout (KO) iPSC-CMs to assess changes in structure, senescence, metabolism and calcium (Ca^{2+}) handling dynamics (Chapter 7).

Methods: Polydimethylsiloxane (PDMS) hydrogels of 20kPa (healthy) and 130kPa (fibrotic) stiffnesses were developed. Ventricular iPSC-CMs were differentiated and plated onto PDMS hydrogels of stiffnesses and plastic/glass. Transcriptional, structural and functional profiles of iPSC-CMs on stiffnesses were investigated using methods such as Quantitative polymerase chain reaction (qPCR), Western blotting and Ca^{2+} optical mapping. Metabolic function of iPSC-CMs was

assessed using several techniques, including isotope labelled mass spectrometry.

Phenoage, a measure of biological ageing, was compared to chronological age for a cohort of patients with AS. Retrospective analysis of cardiovascular changes over time in AS patients using echocardiography were also assessed. *ALMS1* KO iPSC-CMs were assessed for molecular, functional and metabolic changes compared to wildtype iPSC-CMs.

Results: iPSC-CMs cultured on 20kPa PDMS mimicking the healthy myocardium exhibit greater structural alignment, expression of cardiac markers and altered Ca^{2+} handling dynamics, indicative of CM maturity. iPSC-CMs cultured on plastic substrates exhibit a preference to glycolytic metabolism, increased lactic acid production and signs of a disease profile compared to iPSC-CMs cultured on softer PDMS substrates.

Patients with AS displayed a higher Phenoage compared to their chronological age, indicating AS serves as a model of accelerated ageing. Furthermore, *ALMS1* KO iPSC-CMs displayed altered Ca^{2+} handling dynamics, changes in cellular bioenergetics and increased senescence, providing insight into the molecular changes occurring in AS.

Conclusions: The work supports the idea that ageing and stiffness of the ECM affects structure, function and metabolism of iPSC-CMs. The pathological metabolic phenotype of iPSC-CMs cultured on traditional cell culture plastics indicates that plastic may not serve as an effective control condition for experiments. iPSC-CM culture on softer substrates provides data of greater physiological relevance and is representative of a healthy myocardium, thus highlighting the importance of substrate stiffness and the impact the environment can have on iPSC-CM behaviour. This research demonstrates softer physiological substrates serve as an effective model for healthier and mature iPSC-CM cultures and should be used in research involving iPSC-CMs to accurately reflect cardiac environments. Novel findings also display AS as a disease model of accelerated ageing. The research further highlights the benefits of physiological model development and the use of iPSC-CMs to model cardiovascular diseases, allowing investigation into molecular mechanisms of diseases.

Declaration

I hereby declare that the work presented in the thesis titled 'Investigating the Influence of Substrate Stiffness and Cardiovascular Ageing: Structural, Functional and Metabolic Responses using Induced Pluripotent Stem Cell-Derived Cardiomyocytes' is my own work, unless stated otherwise. Parts of Chapter 1 have been adapted from my own work: **Patel, L**., Worch, J.C., Dove, A.P and Gehmlich, K. The Utilisation of Hydrogels for iPSC-Cardiomyocyte Research. *International Journal of Molecular Sciences*. 2023;24. Proteomics runs in Chapter 5 were performed by Dr Todd Mize (University of Birmingham). Chapter 6 is my own previously published work : **Patel, L**., Roy, A., Alvior, A.M.B., Yuan, M., Baig, S.,Bunting, K.V., Hodson, J., Gehmlich, K., Lord, J.M., Geberhiwot, T., Steeds, R.P. Phenoage and longitudinal changes on transthoracic echocardiography in Alström syndrome: a disease of accelerated ageing? *GeroScience*, 46, 1989–1999 (2024). Celluar Bioenergetics data analysis in Chapter 7 was conducted by Dr Jonathan Barlow (University of Birmingham). ImageJ fluorescence quantification script used in Chapter 7 was written by Dr Daniel Nieves (University of Birmingham). Chapter 7 has been submitted for publication and is currently under review: **Patel, L**., Roy, A., Barlow, J., O'Shea, C., Nieves, D., Azad, A.J., Hall, C., Davies, B., Rath, P., Pavlovic, D., Chikermane, A., Geberhiwot, T., Steeds, R.P., Gehmlich, K. Characterisation of infantile cardiomyopathy in Alström Syndrome using *ALMS1* Knockout induced pluripotent stem cell derived cardiomyocyte model. *Molecular Genetics and Metabolism.* 2024.

Acknowledgements

Firstly, I would like to express my gratitude and thanks to my supervisor, Professor Katja Gehmlich, for the support and guidance throughout, and for giving me the freedom to navigate and explore research. Thank you to Professor Daniel Tennant and Professor Andrew Dove for the mentorship and advice provided. A big thanks to Professor Rick Steeds, who provided me with new opportunities and support throughout the project. Thank you to the people who supported my learning; Dr Joshua Worch for helping me in chemistry, Dr Jonathan Barlow for the Seahorse expertise and Dr Bryan Marzullo for the mass spectrometry support. Thank you to my funders, MIBTP and BBSRC, who made this work possible.

A special thank you to Mum and Pri. None of this would have been possible without you both. Thank you for always believing in me and being the rocks I can always lean on.

Thank you to all of my friends I made during the years, and to the lovely Gehmlich group. Amar Azad- for the coffee chats, I appreciate your friendship. Max Cumberland- for the banter and laughs you brought into the lab everyday. Ashwin Roy- for being the older brother for me at work and always being supportive. Maya Noureddine- for your bubbly and positive personality. Sophie Broadway-Stringer- for all the liquid nitrogen trips! Danielle Lezama- for the deep TC chats, heartfelt moments, the kind words and our journey of sharing faith. Aleen Baber- for the friendship, the joke of the days, the matching bag and of course, the connection. Dylan Marques- for the sarcasm, the banter, the competitive climbing challenges and providing support for the breakdowns. Caitlin Hall- for being my fellow foodie. Sakaorna Jeyanathan- for starting this journey with me and being supportive. Ashleigh Renelt- For being such a legend and always helping me out with stores! I couldn't have done it without you guys.

To the best house, Louisa Brenninkmeijer, Joshua Roberts and Bethany Crow. Thank you for giving me hugs when there were tears, for the many moments of laughter and joy together, and for creating a loving home; I couldn't have asked for better friends. Emma Catterson and Orla Cassidy, thank you for all the fun walks, cat cuddles and adventures. My second brain, Kaosidi Nwankwo; your strength, prayers and positivity got me through this PhD. I am forever grateful and

thankful for your friendship. Mariyah Patel- for being a lifelong best friend.

And for the most unexpected surprise during the PhD, the final piece of my puzzle, Devan Dahya. Thank you for your constant optimism, your patience, your kindness and your belief in me. You've given me a level of peace and joy that I've never experienced, and I am beyond thankful for you.

Finally, thank you to God, for this journey of transformation, perseverance and growth, and for all the others adventures that are yet to come; I am eternally grateful.

Publications

Patel, L., Roy, A., Alvior, A.M.B., Yuan, M., Baig, S.,Bunting, K.V., Hodson, J., Gehmlich, K., Lord, J.M., Geberhiwot, T., Steeds, R.P. Phenoage and longitudinal changes on transthoracic echocardiography in Alström syndrome: a disease of accelerated ageing? *GeroScience*. 2024;46, 1989–1999. https://doi.org/10.1007/s11357-023-00959-3

Patel, L., Worch, J.C., Dove, A.P and Gehmlich, K. The Utilisation of Hydrogels for iPSC-Cardiomyocyte Research. *International Journal of Molecular Sciences*. 2023;24. https://doi.org/10.3390/ijms24129995

Patel, L., Roy, A., Barlow, J., O'Shea, C., Nieves, D., Azad, A.J., Hall, C., Davies, B., Rath, P., Pavlovic, D., Chikermane, A., Geberhiwot, T., Steeds, R.P., Gehmlich, K. Characterisation of infantile cardiomyopathy in Alström Syndrome using *ALMS1* Knockout induced pluripotent stem cell derived cardiomyocyte model. *Molecular Genetics and Metabolism* 2024. **Under review**.

Contents

Contents **vii**

1 Introduction **1**

1.1 Structure of the Heart 1

1.1.1 Cardiomyocytes 2

1.2 Cardiac Contraction 4

1.2.1 Excitation-contraction coupling 5

1.3 Calcium Ion channels 7

1.3.1 L-type voltage-gated Ca^{2+} channels (LTCC) 7

1.3.2 Ryanodine receptor (RYRs) 7

1.3.3 Sarcoplasmic Reticulum ATPase (SERCA) 8

1.3.4 Na^{+}/Ca^{2+} exchangers (NCX) channels 8

1.4 Mechanotransduction in CMs 9

1.4.1 Integrins and Costameres 9

1.4.2 YAP/TAZ signalling 11

1.5 Cardiac metabolism 12

1.5.1 Glucose metabolism 14

1.5.2 The Tricarboxylic Acid Cycle (TCA cycle) 15

1.5.3 Electron transport chain (ETC) and Oxidative phosphorylation 17
1.5.4 Lactate 17
1.5.5 Fatty acid oxidation 18
1.6 Cardiovascular ageing and disease 19
1.6.1 Cardiac Fibrosis 21
1.6.2 Ca^{2+} Ion channels in ageing and cardiac disease 22
1.6.3 Alström Syndrome 23
1.6.4 Metabolism in ageing and cardiac disease 25
1.7 Models of ageing and cardiac disease 26
1.7.1 Induced pluripotent stem cell models 27
1.7.2 Limitations of iPSCs 28
1.8 Physiological models of ECM stiffness 30
1.8.1 Hydrogels as models for ECM stiffness 31
1.9 Aims and Hypothesis 33
1.9.1 Developing hydrogel models of the stiffness of the myocardium and ECM 33
1.9.2 Characterisation of the effect of stiffness of the ECM on iPSC-CM function 34
1.9.3 Investigating the effect of stiffness of the ECM on iPSC-CM metabolism 34
1.9.4 Assessing Alström Syndrome as a model of accelerated ageing 34

1.9.5 Characterising the cardiovascular role of *ALMS1* in Alström Syndrome using iPSC-CMs 35

2 Materials and Methods 36

2.1 Materials 36

2.1.1 Antibodies 36

2.1.2 Quantitative polymerase chain reaction (qPCR) probes . . 38

2.2 Methods 39

2.2.1 iPSC cell culture 39

2.2.2 Quantitative Polymerase Chain Reaction (qPCR) 43

2.2.3 Western blotting 45

2.2.4 Immunofluorescence 46

2.2.5 Optical mapping 48

2.2.6 Contractility analysis using MuscleMotion 49

2.2.7 Isotope label Gas Chromatography-Mass Spectrometry (GC-MS) 51

2.2.8 Cellular Bioenergetics Seahorse Extracellular Flux 55

2.2.9 Proteomics 57

2.2.10 Senescence-Associated β-galactosidase assay 59

2.2.11 Statistical Analysis 60

3 Modelling ECM stiffness with biomaterial hydrogels 61

3.1 Introduction 61

3.2 Hypothesis and Aims 63

3.3 Methods 64

3.3.1 Polyethylene Glycol Hydrogel (PEG) synthesis 64
3.3.2 PEG hydrogel formation 66
3.3.3 Rheology 67
3.3.4 Young's modulus equations 68
3.3.5 PDMS hydrogel synthesis 68
3.4 Results 69
3.4.1 Structure of PEG thiol and alkyne precursors 69
3.4.2 Rheology and mechanical stiffness analysis 73
3.4.3 iPSC-CM viability on PEG hydrogels 76
3.4.4 Mechanical characterisation of PDMS hydrogels 79
3.4.5 Attachment of iPSC-CMs to PDMS substrates 80
3.5 Discussion 81
3.5.1 PEG hydrogels can mimic physiological stiffnesses of the ECM 82
3.5.2 PEG hydrogel incompatibility with iPSC-CM culture 82
3.5.3 Toxicity of PEG hydrogels 84
3.5.4 PDMS hydrogels for iPSC-CM culture 85
3.5.5 Limitations 86
3.5.6 Conclusions 87

4 Molecular and cellular characterisation of iPSC-CMs on physiological substrate stiffnesses 88

4.1 Introduction 88
4.2 Hypothesis and Aims 90

4.3 Results 91
4.3.1 Expression of Structural Cardiac Markers between days 20-30 of iPSC-CM differentiation 91
4.3.2 Expression of Cardiac Markers in day 25 iPSC-CMs on substrates 92
4.3.3 Cardiac markers of iPSC-CMs on substrate stiffnesses at protein level 94
4.3.4 Immunofluorescence of sarcomere organisation and alignment of iPSC-CMs on varying stiffnesses 95
4.3.5 Increased contractility of iPSC-CMs on softer substrates . . 97
4.3.6 Ion channel transcripts of iPSC-CMs on substrates 101
4.3.7 SERCA protein expression of iPSC-CMs on substrates . . 104
4.4 Discussion 105
4.4.1 Transcript expression of cardiac maturity markers 105
4.4.2 Substrate stiffness does not significantly alter contractility of iPSC-CMs 108
4.4.3 Stiffness of ECM alters Ca^{2+} handling dynamics of iPSC-CMs 109
4.5 Use of softer substrates for iPSC-CMs 112
4.6 Limitations 112
4.7 Conclusion 113

5 Metabolic characterisation of iPSC-cardiomyocytes on substrates 115

5.1 Introduction 115
5.2 Hypothesis and Aims 116

5.3 Results 117
5.3.1 Fatty acid treated iPSC-CMs 117
5.3.2 [U-^{13}C]-glucose Isotope labelled mass spectrometry 122
5.3.3 Oxygen consumption rate (OCR) and Extracellular acidification rate (ECAR) of iPSC-CMs on different substrates . . 128
5.3.4 Metabolic parameters from Cell Mito-Stress Seahorse assay 129
5.3.5 Proteomics analysis of iPSC-CMs on 20kPa PDMS, 130kPa PDMS and Plastic 131
5.3.6 Transcript expression of metabolic genes in iPSC-CMs . . . 138
5.3.7 Protein expression levels of metabolic genes with western blotting 143
5.4 Discussion 144
5.4.1 iPSC-CM profiles on 20kPa vs 130kPa PDMS substrates . 145
5.4.2 Stiffer substrates shift iPSC-CMs towards glycolytic metabolism146
5.4.3 Increased glycolytic metabolism characterisation using Seahorse assay 148
5.4.4 Energetics of CMs on substrates 150
5.4.5 iPSC-CMs on stiffer substrates display a cardiac disease profile using Proteomics 151
5.4.6 Substrate stiffness affects iPSC-CMs metabolic gene expression 154
5.4.7 PPARs in iPSC-CM metabolism 159
5.5 Conclusion 163

6 Phenoage and longitudinal changes on transthoracic echocardiography in Alström Syndrome: a disease of accelerated ageing? 164

6.1 Publication 164

6.2 Author Contributions 165

7 Characterisation of infantile cardiomyopathy in Alström Syndrome using *ALMS1* Knockout induced pluripotent stem cell derived cardiomyocyte model 178

7.1 Author contributions 180

7.2 Abstract 182

7.3 Keywords 183

7.4 Introduction 183

7.5 Materials and Methods 185

7.5.1 Generation of *ALMS1* knockout iPSC cells 185

7.5.2 Differentiation of ventricular induced pluripotent stem cell-derived cardiomyocytes 186

7.5.3 Immunofluorescence 186

7.5.4 Optical mapping 187

7.5.5 MuscleMotion contraction analysis 188

7.5.6 Senescence associated β-galactosidase staining 189

7.5.7 Real-time quantitative polymerase chain reaction (RT-qPCR) transcription levels 189

7.5.8 Cellular Bioenergetics 190

7.5.9 Statistical Analysis 192

7.6 Results 192
7.6.1 Validation of *ALMS1* KO in the cellular model 192
7.6.2 Contraction analysis 194
7.6.3 Altered Ca^{2+} handling in *ALMS1* KO cardiomyocytes 196
7.6.4 Changes in calcium handling genes in *ALMS1* KO cardiomyocytes 198
7.6.5 Real-time metabolic profiling of *ALMS1* KO cardiomyocytes 200
7.6.6 Cell Senescence 202
7.7 Discussion 206
7.7.1 Altered calcium dynamics and contractility in *ALMS1* KO iPSC-CMs 206
7.7.2 Increased metabolic capacity of *ALMS1* KO iPSC-CMs . . 208
7.7.3 Increased senescence in *ALMS1* KO iPSC-CMs 210
7.7.4 Limitations 211
7.8 Conclusions 211
7.9 Supplementary material 213
7.9.1 Generation of *ALMS1* KO iPSC cells 213
7.9.2 Human iPSC-CM differentiation protocol 214

8 Final Discussion 218

8.1 Summary of results 218
8.2 Chapter 3: Developing a hydrogel model of ECM stiffnesses 220
8.2.1 Limitations of Chapter 3 221
8.2.2 Chapter 3 Future work 221

8.3 Chapter 4: Molecular and cellular characterisation of the effect of ECM stiffness on iPSC-CM morphology and contractility 222
8.3.1 Limitations of Chapter 4 223
8.3.2 Chapter 4 Future work 223
8.4 Chapter 5: Investigating the effect of ECM stiffness on iPSC-CM metabolism 224
8.4.1 Limitations of Chapter 5 225
8.4.2 Chapter 5 Future work 226
8.5 Chapter 6: Assessing Alström Syndrome as a model of accelerated ageing and longitudinal cardiovascular changes 227
8.5.1 Limitations of Chapter 6 228
8.5.2 Chapter 6 Future work 228
8.6 Chapter 7: Understanding the cardiovascular role of ALMS1 in Alström Syndrome using iPSC-CMs 228
8.6.1 Limitations of Chapter 7 229
8.6.2 Chapter 7 Future work 230
8.7 General Limitations 230
8.8 Concluding remarks 231

Bibliography **233**

List of Figures

1.1 Diagram of heart structure with direction of blood flow 2

1.2 Schematic of the sarcomere 4

1.3 Schematic of cardiac conduction system 5

1.4 Schematic of excitation-contraction coupling in cardiomyocyte . . . 6

1.5 Schematic of the structure of the ECM with mechanotransducing integrins and costameres 11

1.6 YAP/TAZ signalling pathways with increased and decreased ECM stiffnesses 12

1.7 Cardiac metabolic pathways for ATP production 14

2.1 Differentiation protocol of iPSCs to iPSC-CMs 42

2.2 Schematic of Ca^{2+} optical mapping parameters 49

2.3 MuscleMotion contractility analysis outputs 51

2.4 Schematic of U-^{13}C-glucose carbon tracking into TCA cycle metabolites 53

2.5 Schematic of Seahorse XF Cell Mito-Stress Test parameters . . . 57

3.1 Fischer esterification reaction used for synthesis of alkyne or thiol functionalised PEG precursors 65

3.2 PEG hydrogel structure formed from combinations of 2-arm and 3-arm PEG precursors 66
3.3 Schematic of spin coating PDMS mixture of stiffness onto coverslip in a thin layer 69
3.4 Proton NMR of 3-arm thiol PEG precursor (1kg mol^{-1}) 70
3.5 Proton NMR of 3-arm alkyne PEG precursor (1kg mol^{-1}) 71
3.6 Proton NMR of 2-arm thiol PEG precursor (2kg mol^{-1}) 72
3.7 Proton NMR of 2-arm alkyne PEG precursor (2kg mol^{-1}) 73
3.8 Effect of varying ratios and combinations of PEG precursors on storage and loss moduli 74
3.9 Physical appearance of PEG hydrogels created with precursors in PBS 75
3.10 Rheometer characterisation of PEG hydrogel stability over 29 days in PBS 76
3.11 Day 30 iPSC-CMs cultured on 3AA, 2AT and 3AT PEG hydrogels . 77
3.12 Day 15 iPSC-CMs plated onto 3AA and 3AT hydrogels of varying alkyne to thiol groups and vice versa, coated with Geltrex 78
3.13 Rheology measurements of PDMS hydrogels 80
3.14 Monolayer of iPSC-CMs attached to PDMS hydrogel 81

4.1 Transcript expression of cardiac markers between days 20-30 of iPSC-CM differentiation 92
4.2 qPCR gene expression profiles of cardiac maturity markers in day 25 iPSC-CMs on 20kPa PDMS, 130kPa PDMS and plastic stiffnesses 93

4.3 Western blot protein expression and quantification of cardiac markers in day 25 iPSC-CMs on stiffnesses 94
4.4 Sarcomere organisation and alignment of iPSC-CMs on varying stiffnesses 96
4.5 Contractile parameters of iPSC-CMs on stiffnesses assessed by MuscleMotion software 98
4.6 Calcium transient durations of iPSC-CMs on 20kPa PDMS, 130kPa PDMS and plastic stiffnesses 100
4.7 Ca^{2+} optical mapping output parameters of iPSC-CMs on 20kPa PDMS, 130kPa PDMS and plastic stiffnesses 101
4.8 Transcript expression of Ion channels involved in Ca^{2+} handling in iPSC-CMs on 20kPa PDMS, 130kPa PDMS and plastic 103
4.9 Western blot protein expression and quantification of SERCA on stiffnesses 104

5.1 Confocal microscopy images of fatty acid droplets in iPSC-CMs . . 119
5.2 qPCR gene transcript levels of metabolic genes in fatty acid treated iPSC-CMs 121
5.3 Mass spectrometry iPSC-CM experiment plan 122
5.4 U-^{13}C-glucose labelling in pyruvate in iPSC-CMs on 20kPa PDMS, 130kPa PDMS and plastic using isotope labelled mass spectrometry 124
5.5 U-^{13}C-glucose labelling in lactate in iPSC-CMs on 20kPa PDMS, 130kPa PDMS and plastic using isotope labelled mass spectrometry 125

5.6 U-^{13}C-glucose labelling in citrate in iPSC-CMs on 20kPa PDMS, 130kPa PDMS and plastic using isotope labelled mass spectrometry 126

5.7 Total abundance of polar metabolites from iPSC-CMs on 20kPa PDMS, 130kPa PDMS and plastic using isotope labelled mass spectrometry 127

5.8 Oxygen consumption rate and extracellular acidification rate assessed by Cell Mito-Stress Test Seahorse assay of day 25 iPSC-CMs 129

5.9 Seahorse Cell Mito-Stress Test parameters of day 25 iPSC-CMs . 131

5.10 Volcano plot of proteomics data of iPSC-CMs on plastic compared to 130kPa PDMS at day 25 133

5.11 Proteomics genes of interest in iPSC-CMs on plastic compared to 20kPa PDMS at day 25 135

5.12 Volcano plot of proteomics results of iPSC-CMs on 20kPa PDMS compared to 130kPa PDMS at day 25 137

5.13 qPCR transcript expression profiles of metabolic genes in iPSC-CMs on 20kPa PDMS, 130kPa PDMS and plastic stiffnesses . . . 139

5.14 qPCR transcript expression profiles of PPAR genes in iPSC-CMs on 20kPa PDMS, 130kPa PDMS and plastic stiffnesses 141

5.15 qPCR transcript expression levels of pyruvate dehydrogenase complex genes in iPSC-CMs on 20kPa PDMS, 130kPa PDMS and plastic stiffnesses 142

5.16 Western blot protein expression and quantification of metabolic markers on stiffnesses 144

7.1 Supplementary; ALMS1 Immunostaining images of WT and *ALMS1* KO iPSC 193

7.2 Supplementary; qPCR of cardiac markers in WT and *ALMS1* KO iPSC-CMs between Days 20-30 of differentiation 194

7.3 Contractile parameters of WT and *ALMS1* KO iPSC-CMs assessed by MuscleMotion software 195

7.4 Calcium optical mapping of WT and *ALMS1* KO iPSC-CMs using ElectroMap software 197

7.5 qPCR of Ion channels involved in Ca^{2+} handling in WT and *ALMS1* KO iPSC-CMs 199

7.6 OCR and ECAR assessed by Cell Mito-Stress Test Seahorse assay of WT and ALMS1 KO iPSC-CMs on day 25 iPSC-CMs 201

7.7 Senescence associated-β-galactosidase staining in WT and *ALMS1* KO iPSC-CMs 203

7.8 Supplementary; Immunostaining of p16 in WT and ALMS1 KO iPSC-CMs 204

7.9 Supplementary; Immunostaining of p21 in WT and *ALMS1* KO iPSC-CMs 205

7.10 Supplementary; qPCR of *CDKN1A* and *CDKN2A* in WT and *ALMS1* KO iPSC-CMs between days 20-30 of differentiation 206

7.11 Supplementary; Sanger sequencing of ALMS1 F1/R2 PCR products from C23, C26 and C40 confirmed site specific deletion at the CRISPR target site 215

8.1 Summary of differences between 20kPa and 130kPa PDMS substrates 218

List of Tables

2.1 List of Primary antibodies 37

2.2 List of Secondary antibodies 37

2.3 List of Taqman quantitative polymerase chain reaction (qPCR) probes 38

2.4 List of SYBR green qPCR probes 39

3.1 Young's modulus stiffnesses of PEG hydrogels with varying PEG precursor ratios 75

5.1 Proteomics genes of interest in iPSC-CMs on plastic compared to 130kPa PDMS at day 25 134

5.2 Proteomics genes of interest in iPSC-CMs on plastic compared to 20kPa PDMS at day 25 136

5.3 Proteomics genes of interest in iPSC-CMs on 20kPa PDMS compared to 130kPa PDMS at day 25 138

7.1 Supplementary; Primary and secondary antibodies used for immunostaining 216

7.2 Supplementary; TaqMan and SYBR primers used for qPCR 217

Abbreviations

2D	two-dimensional
3D	three-dimensional
ATP	adenosine triphosphate
AS	Alström Syndrome
AVN	atrioventricular node
Ca^{2+}	calcium
CICR	calcium induced calcium release
CM	cardiomyocyte
CTD	calcium transient duration
CVD	cardiovascular disease
DCM	dilated cardiomyopathy
ECAR	extracellular acidification rate
ECM	extracellular matrix
ETC	electron transport chain

FA fatty acid

GC-MS gas chromatography-mass spectrometry

iPSC induced pluripotent stem cell

iPSC-CM induced pluripotent stem cell derived cardiomyocyte

KO knock-out

LTCC L-type calcium channel

MPC mitochondrial pyruvate carrier

NADH nicotinamide adenine dinucleotide hydrogen

NCX sodium calcium exchanger

NMR nuclear magnetic resonance

OA oleic acid

OCR oxygen consumption rate

PA palmitic acid

PBS phosphate buffer solution

PCR polymerase chain reaction

PDC pyruvate dehydrogenase complex

PDK pyruvate dehydrogenase kinases

PDMS polydimethylsiloxane

PEG polyethylene glycol

PPP pentose phosphate pathway

PPAR peroxisome proliferator-activated receptors

qPCR quantitative polymerase chain reaction

RGD arginine-glycyl-aspartic acid

ROS reactive oxygen species

RYR2 ryanodine receptor 2

SAN sinoatrial node

SERCA sarcoendoplasmic reticulum calcium ATPase

SR sarcoplasmic reticulum

TCA the tricarboxylic acid cycle

WT wild-type

Chapter 1

Introduction

1.1 Structure of the Heart

The heart is an essential organ that is responsible for pumping oxygenated blood around the body via vasculature. It consists of four chambers; the right atrium, right ventricle, left atrium and left ventricle (Figure 1.1). Deoxygenated blood from the body enters the right atrium, is pumped into the right ventricle and enters the lungs via pulmonary arteries, where blood undergoes oxygenation via a gas exchange system facilitated by the alveoli. Oxygenated blood then enters the left ventricle via the left atrium and is pumped through the aorta to the rest of the body. Contraction of the chambers of the heart, known as systole and relaxation of the heart chambers, known as diastole, facilitate the flow of blood through the heart. Tricuspid and mitral valves, situated between the atria and ventricles open during relaxation in response to pressure differences between the atria and ventricles, ensuring blood flow is unidirectional. During contraction, the aortic valve opens, allowing blood to flow into the aorta and into the rest of the body.

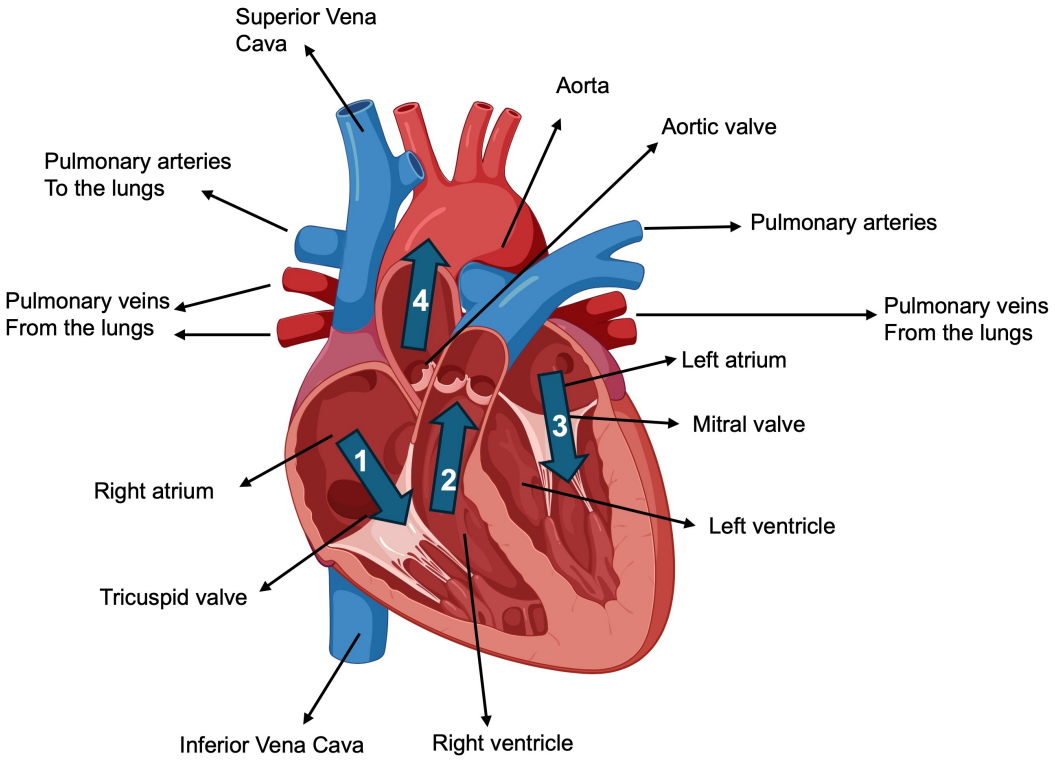

Figure 1.1: **Diagram of heart structure with direction of blood flow**
Deoxygenated blood from the body enters the heart via the Inferior and Superior vena cava into the right atrium. 1. Blood is pumped from the right atria into the right ventricle. 2. Blood flows to the lungs via the pulmonary arteries to undergo oxygenation and is carried back to the left atrium via pulmonary veins 3.Blood flows from the left atria into the left ventricles through the mitral valve 4.Oxygenated blood is pumped to rest of the body via the aorta. Adapted from Biorender.com

1.1.1 Cardiomyocytes

Heart muscle consists of several cell types, such as cardiomyocytes (CMs), cardiac fibroblasts, smooth muscle cells, immune cells and endothelial cells [1]. Although there are various cell types, cardiomyocytes (CMs) constitute 70-80% of the hearts volume, despite only accounting for 30-40% of total cell types in cardiac tissue [2]. In order to meet the high metabolic demands of the heart, CMs are abundant in mitochondria to enable adenosine triphosphate (ATP) synthesis [3]. CMs are individual rod-shaped muscle cells composed of myofibrils, acting as

contractile units of the heart [4]. The myofibrils consist of sarcomeres which enable coordinated contraction. The sarcolemma is the cell membrane surrounding the myofibrils.

The sarcomere is composed of repeating units of actin and myosin proteins, forming thin and thick filaments respectively which contribute to the striated appearance of the cell (Figure 1.2), also known as myofilaments [5]. The A-band, consisting of thick, thin and elastic filaments appears darker when viewed through a light microscope. The M-line refers to the centre of the sarcomere and serves as an anchor for thick filaments. The Z-line or Z-disc marks the border of the sarcomere, connecting the actin filaments and titin together with α-actinin. The I-band consists of only thin filaments, and is located next to the Z-disc.

As well as actin, thin filaments also consist of troponin and tropomyosin, which regulate contraction by blocking binding of myosin to actin. In a relaxed state, tropomyosin remains bound to troponin, preventing actin-myosin interaction. When calcium (Ca^{2+}) is released from the sarcoplasmic reticulum (SR) and in the presence of ATP, troponin undergoes conformational change, by exposing actin binding sites [6]. The globular myosin heads of thick filaments therefore attach to actin binding sites on thin filaments, pulling them towards the M-line, shortening the sarcomere, generating force and thus causing contraction [5].

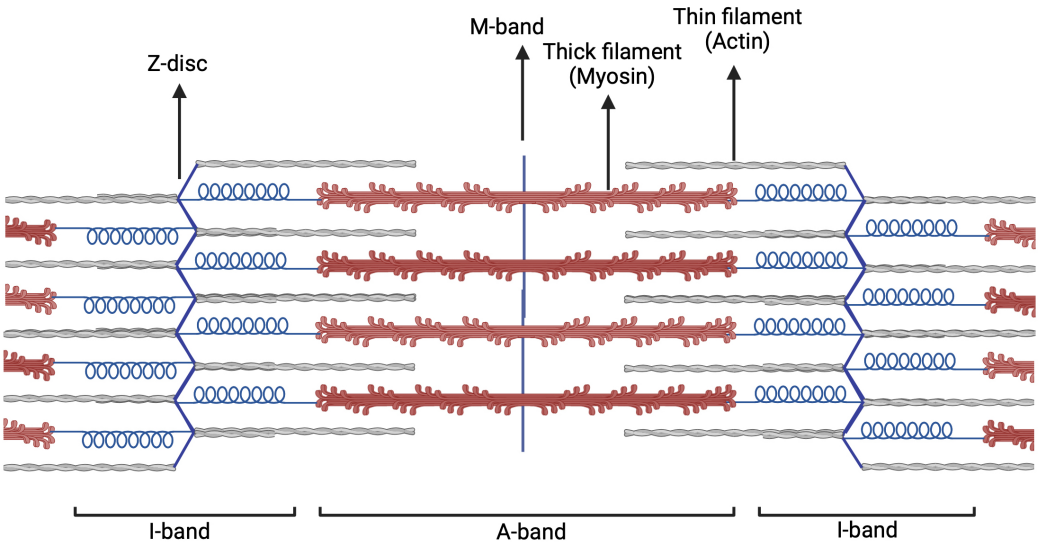

Figure 1.2: **Schematic of the sarcomere**
The sarcomere consists of thick and thin filaments, consisting of myosin and actin. Location of Z-disc, A-band and I-band indicated. Adapted from [7].

1.2 Cardiac Contraction

The contraction and relaxation of all four chambers of the heart is tightly regulated by an electrical conduction system (Figure 1.3). Contraction of the heart is initiated by signals at the sinoatrial node (SAN), located in the right atria. The SAN is composed of pacemaker cells, which spontaneously depolarise, inducing atrial contraction, causing blood to flow from the atria to ventricles [8]. The electrical signals are then propagated across the atria to the atrioventricular node (AVN), leading to contraction of the ventricles. Activation of the AVN leads to signal propagation through the Bundle of His, which carries the electrical signals across the left and right bundles to the Purkinje fibres, stimulating ventricular contraction to eject blood to the body.

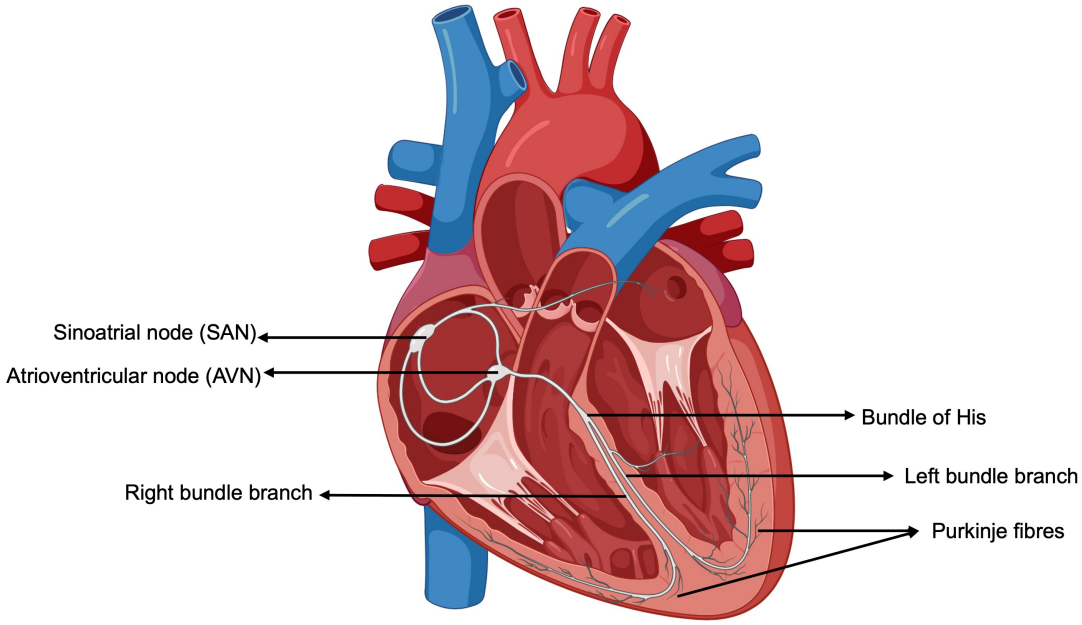

Figure 1.3: **Schematic of cardiac conduction system**
Electrical conduction pathway through the heart. Signal initiated from the sinoatrial node to the atrioventricular node. Signal propagates down the Bundle of His, through the left and right branch bundles and to the Purkinje fibres. Adapted from Biorender.com

1.2.1 Excitation-contraction coupling

The rapid transmission of action potentials between cells regulates cardiac contraction. Electrical conduction is mediated between cardiac muscle cells via gap junctions within intercalated discs, which propagate the electrical signal through transmission of charged ions, causing changes in membrane voltage [9].

Action potentials lead to contraction of CMs, known as excitation-contraction coupling [10] (Figure 1.4). Contractility is largely caused by changes in intracellular Ca^{2+}, acting as a key regulator in CM function. CM contraction is initially triggered by membrane depolarisation at transverse-tubules (t-tubules), resulting in activation of voltage-gated L-type calcium channels (LTCCs) in the cell membrane. Activation of LTCC causes Ca^{2+} influx into the cell, known as a Ca^{2+} spark,

but is not adequate to cause contraction [11]. Ca^{2+} influx causes opening of ryanodine receptor channels, specifically ryanodine receptor channel 2 (RYR2), causing Ca^{2+} release from the SR, a process known as calcium induced calcium release (CICR) [12], [13]. Ca^{2+} binds to troponin C, triggering CM contraction. Removal of cytosolic Ca^{2+} occurs via four main transporters; Ca^{2+} is pumped back into the SR via the sarcoplasmic reticulum calcium ATPase (SERCA2a), Ca^{2+} is moved out of the cell by Na^{+}/Ca^{2+} exchangers (NCX), sarcolemmal Ca^{2+} ATPase and the mitochondrial Ca^{2+} uniporter [14]. These transporters ultimately decrease Ca^{2+} concentrations, causing relaxation.

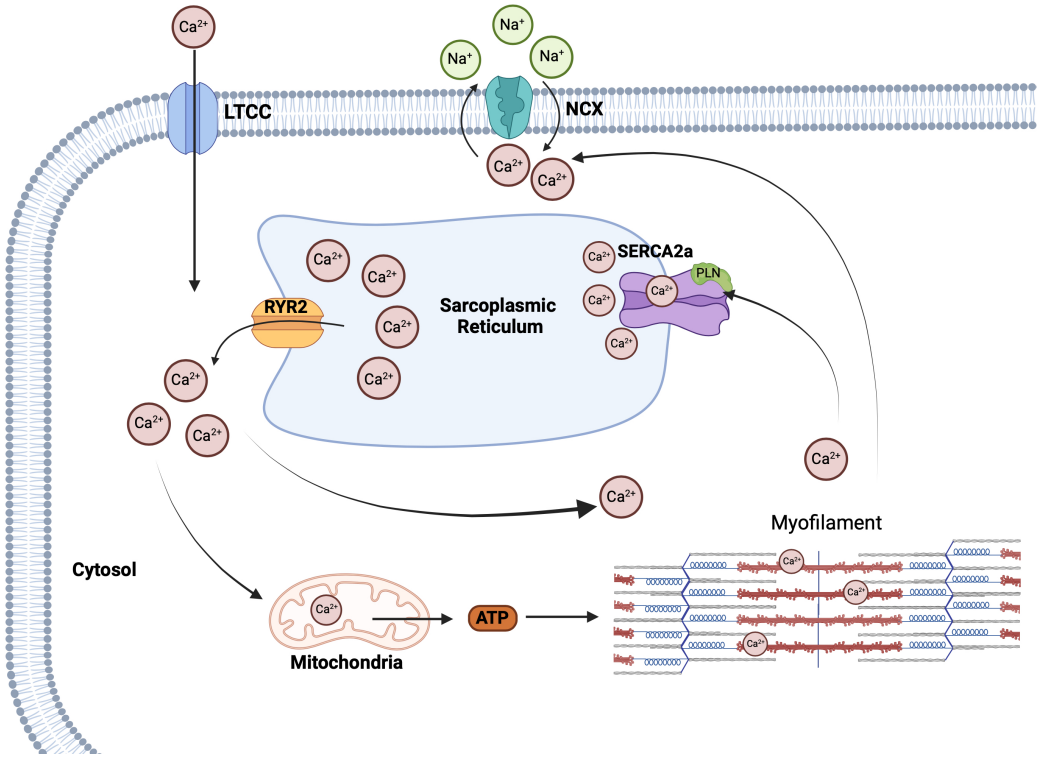

Figure 1.4: **Schematic of excitation-contraction coupling in cardiomyocyte** Ca^{2+} signalling in iPSC-CM. Entry of Ca^{2+} through L-type Ca^{2+} channel (LTCC) causes release of Ca^{2+} from the SR through ryanodine receptor 2 (RYR2), known as Ca^{2+} induced Ca^{2+} release (CICR). Ca^{2+} diffuses into the cytosol and is utilised by the mitochondria to stimulate ATP production and by myofilaments resulting in CM contraction. Ca^{2+} is then sequestered into the SR by SERCA2a. Remaining Ca^{2+} is removed from the cytosol out of the CM by Na^{+}/Ca^{2+} exchangers (NCX). Adapted from [15]

1.3 Calcium Ion channels

1.3.1 L-type voltage-gated Ca^{2+} channels (LTCC)

LTCC's are the major influx pathway of Ca^{2+} into a CM. They are long opening voltage-gated channels, with a pore forming $\alpha 1$ subunit, thus require a strong depolarisation to be activated [16]. Homeostasis of Ca^{2+} entry and exit into and out of the cell is regulated through LTCC's and NCX channels. There are multiple subunits of LTCC's in the heart, such as Cav1.3 (CACNA1D) and Cav1.4 (CACNA1F), with Cav1.2 (CACNA1C) being the predominant LTCC in CMs. LTCC's are highly expressed in both neonatal and adult CMs, as they play a key role in the initiation of CM contraction [17].

1.3.2 Ryanodine receptor (RYRs)

RYRs are members of Ca^{2+} release channels, with three main isoforms; RYR1 enriched in skeletal muscle, RYR2 predominantly in cardiac muscle and RYR3, found in the brain and skeletal muscle [18]. RYR2 is the predominant isoform in CMs, located on the SR and plays a key role in CICR when activated [19]. RYR2 is typically closed at low cytosolic Ca^{2+} levels, and when activated rapidly releases large amounts of Ca^{2+} from the SR into the cytosol, activating myofibril contraction [20]. The expression of RYR2 has been linked to the maturation of Ca^{2+} handling capacity in CMs, and has been shown to play a role in the homeostasis of the SR [19]. RYR2 can be regulated post-translationally, by oxidation and phosphorylation, thus impacting its function [21].

1.3.3 Sarcoplasmic Reticulum ATPase (SERCA)

Several subtypes of the SERCA family exist, with SERCA2a, encoded by the *ATP2A2* gene mainly expressed in CMs and skeletal muscle [22]. SERCA2a plays a key role in Ca^{2+} homeostasis, as it is used for reuptake of Ca^{2+} into the SR to relax CMs [23]. Phospholamban (PLN) is a known regulator of SERCA2a activity [24]. When PLN is phosphorylated at serine 16 amino acid site by protein kinase A, SERCA2a undergoes a conformational change into a Ca^{2+} binding state and is no longer inhibited by PLN [24]. PLN exists in a monomer pentamer equilibrium state, with a dynamic ability to shift between states [25]. PLN inhibits SERCA2a in its monomeric form [26].

1.3.4 Na^+/Ca^{2+} exchangers (NCX) channels

The major NCX channel expressed in CMs is NCX1, which plays a key role in maintaining heart function, as genetic ablation of NCX1 has been shown to alter electrical and contractile properties of the heart [27]. The Na^+/Ca^{2+} exchanger is another key regulator in Ca^{2+} homeostasis, as it acts as the major Ca^{2+} efflux mechanism of CMs, by catalysing the exchange of 3 Na^+ for 1 Ca^{2+} across the cell membrane [28]. NCX1 can operate in a bidirectional fashion, operating in 'forward mode' extruding Ca^{2+} from CMs in exchange for Na^+, or in 'reverse mode', extruding Na^+ in exchange for Ca^{2+} influx.

1.4 Mechanotransduction in CMs

The extracellular matrix (ECM) is a component of the cardiac environment that plays an essential role in cellular growth, signalling and function [29]. Fibroblasts, when activated into myofibroblasts are the primary cell type producing matrix proteins and contribute to the increased deposition of ECM proteins, whereas CMs can secrete ECM proteins such as matrix metalloproteinases under ischemic conditions, but are less responsible for ECM protein deposition [30]. Mechanical cues are converted into biochemical signals by connections in the cytoskeleton, therefore ECM remodelling can affect CM function, primarily through mechanotransduction [31]. Mechanosensing occurs at the cell surface, with plasma membrane receptors sensing and propagating cues to trigger signalling cascades, generating responses. Changes in the environment, such as response to injury are detected by mechanosensing, enabling cells to adapt and alter responses accordingly. Multiple signalling pathways are utilised for mechanotransduction in CMs.

1.4.1 Integrins and Costameres

Integrins are membrane bound receptors that transduce mechanical signals between CMs and the ECM environment, acting as critical mediators of cell-cell interactions and influencing contraction of CMs [32]. Binding of ECM ligands to integrins activates ‘outside in’ signalling, resulting in intracellular signalling cascades. However integrins can work in a bidirectional manner, therefore also have ‘inside out’ signalling, whereby events inside the cell can alter integrin-ECM bind-

ing [32].

Integrins in CMs are located in costameres, sites at which the Z-disc connect to the basement membrane [33]. Costameres play a key role in mechanotransduction in CMs, as they regulate the mechanical coupling of the ECM with sarcomeres in CMs, acting as specialised focal adhesion protein complexes, transmitting cytoskeletal contractile forces to CMs [34] (Figure 1.5). As integrins do not possess enzymatic activity, they transmit mechanical signals via adapter proteins, such as talin, α-actinin and vinculin [34]. They can also interact with ECM proteins, often via integrin recognition motifs, such as arginine-glycyl-aspartic acid (RGD) motifs. Integrins consist of α and β subunits, with $\alpha 1 \beta 1$, $\alpha 3 \beta 1$, $\alpha 5 \beta 1$ and $\alpha 7 \beta 1$ expressed in CMs, binding specifically to collagen, fibronectin and laminin [35]. Variations in the subunits can occur in response to age and pathological conditions. Mechanical forces detected by integrins, such as stiffness of the ECM, can be transmitted to the cell and costameres, causing stress remodelling, resulting in altered DNA replication and gene transcription [32]. Activation of integrins therefore initiates further downstream signalling cascades affecting cell morphology, proliferation, differentiation and survival [35].

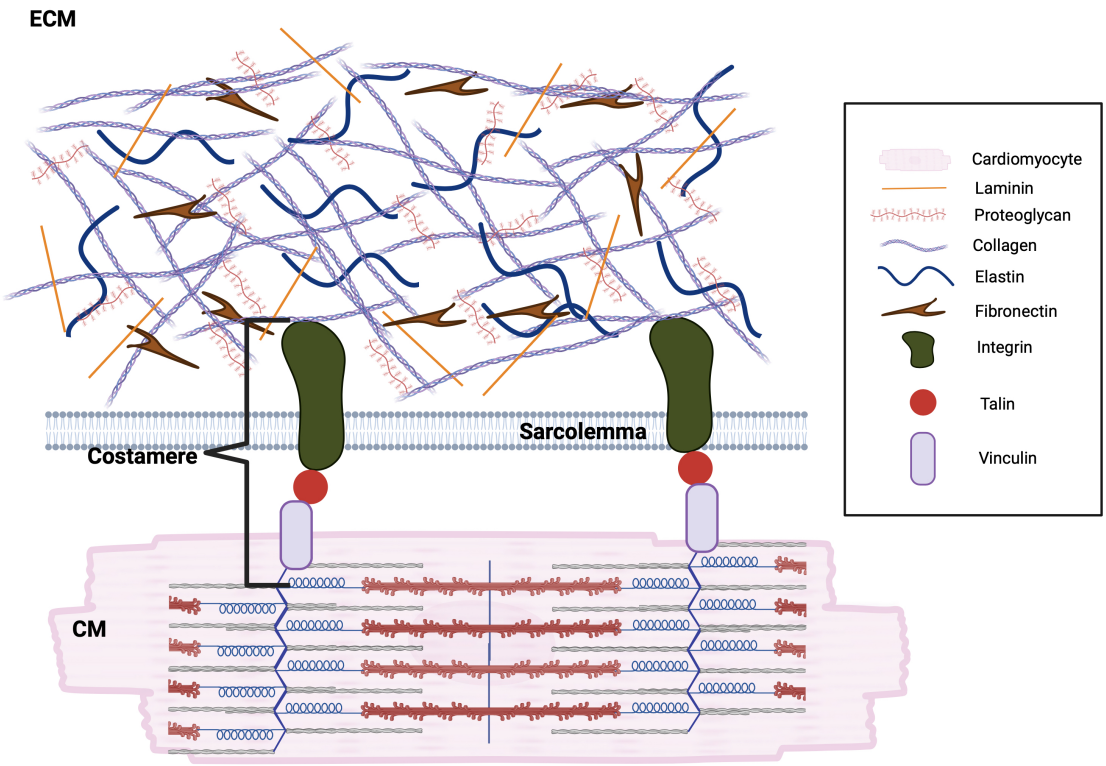

Figure 1.5: **Schematic of the structure of the ECM with mechanotransducing integrins and costameres**
Proteins forming the ECM, including proteoglycans, elastin, fibronectin and collagen. Mechanosensing of the ECM to cardiomyocytes relies on integrin signalling at costameres. Adapted from [34].

1.4.2 YAP/TAZ signalling

Hippo-yes associated protein (YAP) pathway has been identified as playing a key role in cardiac development and homeostasis by connections with mechanical cues, with aberrant activation of this pathway contributing to CVD such as myocardial hypertrophy and fibrosis [36]. YAP acts as a mediator of ECM and cell interaction, as activation of YAP and transcriptional activator with PDZ-binding motif (TAZ) signalling pathways leads to increased ECM production and consequently increased tissue stiffness [37]. Increased ECM stiffness has been proposed to promote cell spreading, causing actin cytoskeleton tension, resulting in

YAP/TAZ nuclear translocation [36] (Figure 1.6). The nuclear localisation of YAP can consequently alter gene expression. Signal transducers, such as GTPases RhoA and RAP2 have been identified as key players to relay stiffness signals to YAP/TAZ [36]. The effect of ECM stiffness on YAP/TAZ signalling remains incompletely understood.

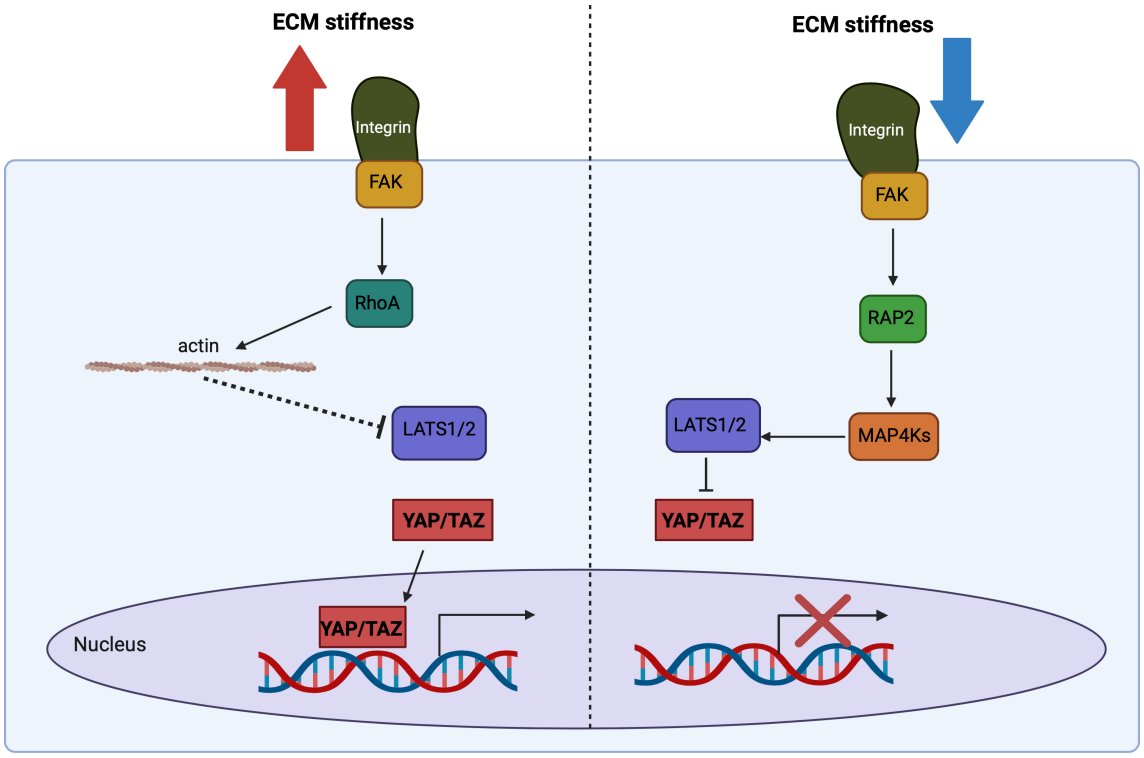

Figure 1.6: **YAP/TAZ signalling pathways with increased and decreased ECM stiffnesses**
Increased ECM stiffness (left side) activates RhoA (GTPase) which relays stiffness signals, resulting in actin stress fibre formation, and inhibition of LAT1/2, thus allowing YAP/TAZ nuclear localisation and alterated gene expression. Decreased ECM stiffness is relayed by RAP2, which causes LAT1/2 activation, thus inhibiting YAP/TAZ. Adapted from [36]

1.5 Cardiac metabolism

Cardiac metabolism refers to the processes by which the body produces ATP to provide energy to enable the heart to beat and effectively pump blood around

the body, maintaining cardiac pump function. The human heart is one of the most highly demanding metabolic organs, as it continuously has to produce 15-20 times its own weight of ATP in one day to sustain contractile function, maintain ionic homeostasis and metabolic processes [38].

To maintain this level of energy production, the heart is able to utilise several energy substrates (Figure 1.7), such as carbohydrates, lipids, amino acids and ketone bodies [39]. The hearts metabolic flexibility is essential to its adaptability, as the energy substrate utilised for ATP production largely depends on substrate availability and energy demand. Under physiological conditions, 60-70$\%$ of ATP produced arises from the oxidation of fatty acids, with the remaining 30-40$\%$ derived from other sources [40] [41]. As a result, over 95$\%$ of the ATP generated occurs via oxidative metabolism of substrates, and unsurprisingly the heart has a very high density of mitochondria to meet this demand, as this is where oxidative phosphorylation occurs [42].

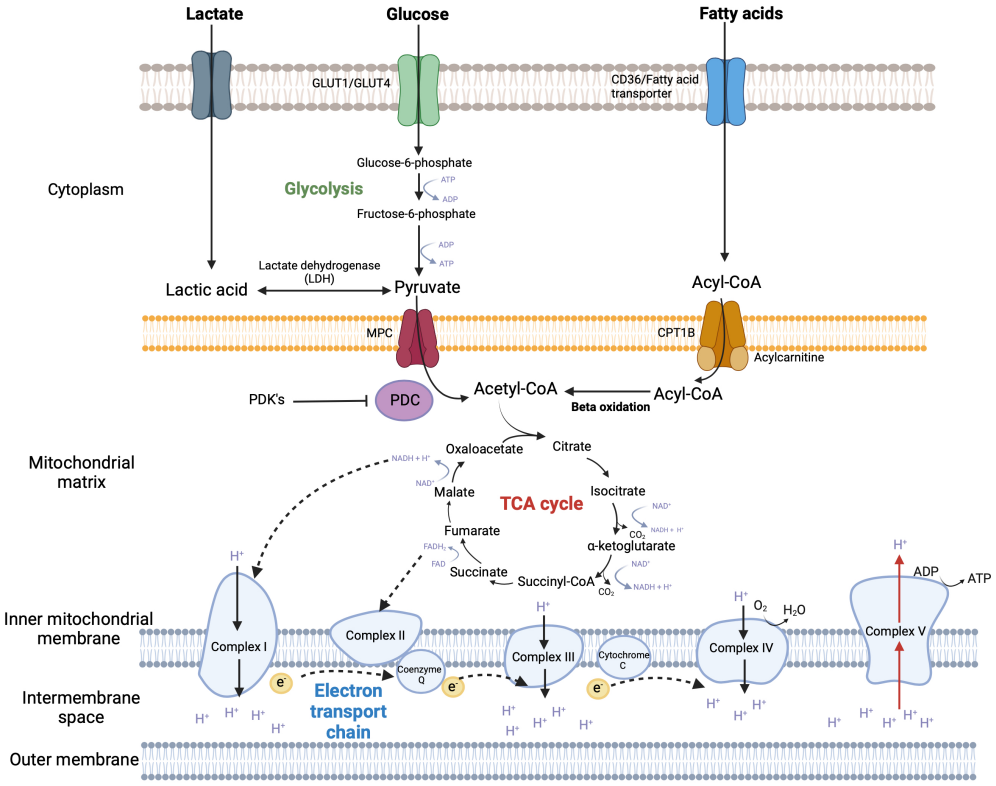

Figure 1.7: **Cardiac metabolic pathways for ATP production**
Metabolism of glucose, lactate and fatty acids. Glucose is broken down into pyruvate via Glycolysis. Pyruvate is consequently transported into the mitochondria using the mitochondrial pyruvate carrier, and is oxidised into acetyl-CoA by the pyruvate dehydrogenase complex (PDC). Acetyl-CoA enters the tricarboxylic acid cycle (TCA) where it forms reducing equivalents, NADH and $FADH_2$. These electrons are transported into the electron transport chain (ETC) where they are transferred along protein complexes to ATP synthase, where oxidative phosphorylation occurs, synthesising ATP. Adapted from [43]

1.5.1 Glucose metabolism

Despite the heart utilising fatty acids as its primary source of energy production, glucose is also a key source of energy metabolism in the heart [44]. Glucose is derived from glycogen stores or obtained from the bloodstream. Glucose metabolism begins with glucose uptake, which in CMs is mediated by glucose transporters (GLUT) at the cell surface, with GLUT1 expressed in foetal hearts and GLUT4 predominantly expressed in adult hearts [45] [46]. The breakdown of one glucose molecule produces two molecules of ATP, which are utilised to help

meet energetic demand and maintain contractile function [47].

Glycolysis refers to the breakdown of glucose into pyruvate (Figure 1.7), nicotinamide adenine dinucleotide hydrogen (NADH) and ATP via a series of biochemical reactions, which are tightly regulated by glycolytic enzymes such as hexokinase (HK), phosphofructokinase (PFKM) and pyruvate kinase [48]. HK conducts glucose phosphorylation, converting glucose to glucose-6-phosphate (G6P), thus acting as the first regulatory enzyme [49]. Two main isoforms of HK exist, HK1 expressed highly in newborn and foetal hearts, and HK2 expressed as the primary isoform in adult hearts [50][49]. G6P can be processed into several metabolic pathways; glycolysis, the pentose phosphate pathway (PPP) and the hexosamine biosynthetic pathway. In glycolysis, G6P is converted to fructose-6-phosphate catalysed by PFKM, and consequently is converted to fructose 1,6-biphosphate. This is further processed into glyceraldehyde-3-phosphate and converted into 1,3-diphosphoglycerate by GAPDH via oxidation and phosphorylation. Pyruvate kinase catalyses the irreversible conversion of phosphoenolpyruvate into the final product of glycolysis, pyruvate. Pyruvate acts as a substrate for further metabolic pathways.

1.5.2 The Tricarboxylic Acid Cycle (TCA cycle)

Pyruvate from glycolysis acts as a branch point for multiple metabolic pathways. The majority of pyruvate produced from glycolysis or lactate is transported from the cytoplasm into the mitochondria by the mitochondrial pyruvate carrier (MPC) [51]. Pyruvate is oxidised into acetyl-CoA by the pyruvate dehydrogenase com-

plex (PDC) and enters the tricarboxylic acid cycle (TCA). The PDC consists of three catalytic enzymes; pyruvate dehydrogenase (E1), dihydrolipoamide acetyltransferase (E2) and dihydrolipoamide dehydrogenase (E3) [52]. The enzyme complex catalyses the oxidative decarboxylation of pyruvate, also forming CO_2 and NADH. Pyruvate dehydrogenase kinases (PDK's) act as key enzymes regulating PDC function; PDK's inhibit PDC activity through phosphorylation, whereas dephosphorylation restores PDC activity [53]. PDK therefore decreases oxidation of pyruvate into acetyl-CoA, thus acting as a gatekeeper between glycolysis and the TCA cycle.

The TCA cycle acts as a centre of cell metabolism, as several substrates can enter at this stage (Figure 1.7). The cycle begins with combining acetyl-CoA with oxaloacetate, forming citrate. Citrate is converted into isocitrate; oxidative decarboxylation occurs, converting isocitrate into α-ketoglutarate [54]. α-ketoglutarate is converted into succinyl-CoA, releasing two molecules of CO_2 and generating two NADH molecules. Succinyl-CoA is converted into succinate, also producing a guanosine triphosphate (GTP) molecule. Succinate is then oxidised to generate fumarate; during this reaction, hydrogen atoms are transferred to FAD by succinate dehydrogenase, producing $FADH_2$. Fumarate gets converted into malate, and thereafter into oxaloacetate, continuing the TCA cycle. The reducing equivalents, NADH and $FADH_2$ are essential in this loop, as they are required to transfer electrons into the electron transport chain (ETC) [55].

1.5.3 Electron transport chain (ETC) and Oxidative phosphorylation

Oxidative phosphorylation occurs within the inner mitochondrial membrane and consists of the ETC (Figure 1.7), which are a series of protein complexes with the main role of pumping hydrogen ions from the mitochondrial matrix to the intermembrane space [56]. The series of complexes are composed of complex I (NADH dehydrogenase), complex II (Succinate dehydrogenase), complex III (cytochrome c reductase), complex IV (cytochrome c oxidase) and complex V (ATP synthase) [57], [58]. Complex I and II receive electrons from NADH and $FADH_2$ and are oxidised and transported to Complex III via Coenzyme Q, acting as an electron carrier [59]. The electrons are then transported to complex IV. The transfer and movement of electrons in the chain causes protons to be pumped into the intermembrane space, generating an electrochemical gradient, known as the mitochondrial membrane potential [60]. This consequently generates a proton motive force, whereby protons re-enter the mitochondrial matrix through ATP synthase, which couples the proton motive force to ATP production [61]. The mitochondria are well established as the 'powerhouse' of the cell, due to the vast amount of ATP synthesised from oxidative phosphorylation.

1.5.4 Lactate

Lactate is typically known as the by-product of glucose metabolism, with pyruvate being converted into lactic acid by lactate dehydrogenase [62] (Figure 1.7). This can occur during exercise, under anaerobic conditions when the demand for oxygen and ATP synthesis exceeds supply [63]. However, in the heart under normal

physiological conditions, lactate oxidation accounts for a large amount of cellular energy produced, particularly in CMs, acting as an important energy source [64]. Lactate is an important fuel source for the myocardium, with all of the lactate absorbed oxidized as fuel [65]. It has been shown as key regulator in cardiac homeostasis, playing roles in regulating cardiac electrophysiology, promoting angiogenesis and altering haemodynamics [66]. With ageing and CVD, there is a shift towards an upregulation of glycolysis, leading to an accumulation of lactate, which could result in lactic acidosis and organ dysfunction [67]. Lactate dehydrogenase (LDH) plays a key role in the regulation of lactic acid production, by catalysing the production of pyruvate, preventing accumulation of lactic acid [68].

1.5.5 Fatty acid oxidation

Fatty acids (FAs) are carboxylic acids that can be divided into groups based on the number of carbon atoms; short-chain FAs (up to 6 carbon atoms), medium-chain FAs (8-12 carbon atoms), long-chain FAs (14-18 carbon atoms) and very long-chain FAs (greater than 20 carbon atoms) [69].

FAs utilised in the heart are in the form of free FAs bound to albumin or are released from triacylglycerols [70]. The entry of exogenous FAs into CMs occurs via fatty acid transporters, such as fatty acid translocase (FAT/CD36) and fatty acid transport protein family [69]. The FAs are converted into fatty acyl-coenzyme A (Acyl-CoA) by acyl-CoA synthetase. Acyl-CoA is conjugated to carnitine via carnitine palmitoyl transferase-1 (CPT1) to produce long-chain acylcarnitine, allowing shutting into the mitochondrial matrix [71]. CPT1 exists in three main isoforms,

CPT1A, CPT1B and CPT1C, with CPT1B the predominant isoform expressed in CMs [72]. Once in the mitochondria, β-oxidation occurs, a catabolic process by which fatty acyl-CoA undergoes oxidation to produce acetyl-CoA, NADH and $FADH_2$.

1.6 Cardiovascular ageing and disease

Cardiovascular disease (CVD) is a leading cause of mortality worldwide, with heart and circulatory diseases responsible for approximately 27$\%$ of total deaths in the UK [73]. Several risk factors have been linked to CVD, such as smoking, hypertension, obesity and diabetes, with age as a major risk factor [74]. Ageing plays a large role in cardiac dysfunction, with an increased risk of CVD and heart failure in elderly adults [75]. Evidence has shown increased incidences of CVD with age, from 40$\%$ between ages of 40-59, to 75$\%$ between the ages of 60-79 and 86$\%$ in those aged above 80 years [76].

Ageing has been associated with a decline in physiological processes, particularly in CVD, leading to an increased prevalence of atherosclerosis, hypertension, stroke and myocardial infarction [77]. Pathological remodelling in the heart due to ageing and disease occurs as a protective response initially to maintain cardiac function, but can eventually lead to disrupted homeostasis and consequently heart failure [78].

The heart undergoes a series of changes at the molecular and cellular level with age, resulting in functional and anatomical transformation of the heart, such as hypertrophy, fibrosis, increased vascular stiffness and endothelial dysfunc-

tional [79]. Age-related stiffening, such as increased stiffness of the aorta occurs, due to decreased elastic fibres and increased collagen deposition [80]. Increased ECM deposition and fibrosis are key characteristics of aged hearts in human and animal models [81], [82], [83].

Apoptosis of CMs with age results in a decrease in total CM number, with remaining CMs undergoing hypertrophy to compensate for the loss in CM number, which can result in thickening of the ventricular wall [84]. The general increase in atrial and ventricular stiffening can also contribute to diastolic dysfunction, with slower contractions and altered relaxation [85], [86].

Ageing can also occur at a cellular level, with a series of molecular and cellular changes occurring over time, known as the 'hallmarks of ageing' [87]. These changes include genomic instability, loss of proteostasis, mitochondrial dysfunction, inflammation, cellular senescence and telomere shortening. Telomeres are the protective ends of chromosomes, with the function of preserving DNA stability [84]. Telomere shortening has been associated with ageing, as progressive shortening of telomere length with each division of the cell cycle contributes to decreased genomic stability and can lead to cell senescence or apoptosis [78]. Inflammation has also been linked with ageing and disease, with elevated levels of inflammatory cytokines and circulatory biomarkers, such as Interleukin-6, alongside a reduction in immune function [87]. Genomic instability is another key feature of ageing, as DNA damage such as mutations, chromosomal rearrangements, deletions and translocations can accumulate over time, as well as DNA repair mechanisms losing efficiency [87]. DNA damage can consequently alter

protein function, thus altering cellular mechanisms. Cellular senescence, known as the irreversible exit of cells from the cell cycle that do not undergo apoptosis are hypothesised to play a role in increasing the risk of age-associated diseases, although specific mechanisms of this process remain unknown [88]. The accumulation of senescent cells over time has been linked with ageing, as the senescent cells may retain function and contribute to mitochondrial dysfunction and inflammation through release of senescence associated secretory phenotypes (SASP) factors [89]. Ageing plays a key role in the development of cardiac disease, and understanding the impact of ageing on cardiac cells requires a model to allow investigation into altered mechanisms and pathways.

1.6.1 Cardiac Fibrosis

Cardiac ageing is further reflected in structural remodelling of the myocardium, with a hallmark feature of ventricular remodelling known as fibrosis [90]. Fibrosis is associated with the activation of cardiac fibroblasts into a myofibroblast phenotype, stimulated by acute or chronic injury [91]. Myofibroblasts are responsible for increased deposition of ECM proteins, ultimately leading to stiffening of the ECM [30]. The ECM is a complex network of fibrillar proteins, proteoglycans, glycoproteins and basement membrane, with fibrillar collagen the most abundant ECM protein [92]. The primary role of the ECM is to provide structural support for CMs, aiding force transmission and stiffness for the myocardial wall, thus maintaining cardiac homeostasis [93]. The maintenance of physiological stiffness of cardiac tissue ensures CM functionality, with studies suggesting embryonic CMs

had optimal contractility on matrices of physiological stiffness compared to stiffer matrices [94].

Extensive research has shown ageing is associated with increased deposition of collagen and ECM proteins, causing increased stiffness, impairing mechano-electrical coupling of CMs, thus leading to contractile dysfunction [95], [96]. The increased stiffness and rigidity of the ECM can consequently impact CM behaviour, altering phenotypes and structure [97]. ECM remodelling has been linked with biophysical changes contributing to the onset of disease; [98] have shown stiffness of post-infarct scar is 55kPa, approximately three-fold stiffer than the stiffness of healthy myocardium, 20kPa. Physiological stiffness of the ECM therefore acts as mechanical cue, affecting the development and mechanical properties of CMs, highlighting the importance of accounting for substrate stiffnesses in experiments.

1.6.2 Ca^{2+} Ion channels in ageing and cardiac disease

Expression of LTCC's have been proposed to alter with ageing, with reduced expression of LTCC subunits in aged CMs, potentially disrupting coupling with RYR2 and contributing to cardiac alternans [99],[100].

Studies have demonstrated no differences in expression levels of RYR2 between adult and aged CMs [101], [102]. However, increased oxidation of RYR2 with ageing can destabilise interaction domains and contribute to SR Ca^{2+} leak triggering Ca^{2+} waves [20],[103].

The impaired function and activity of SERCA2a is a hallmark of heart failure,

with research suggesting lower levels of SERCA2a activity contributing to cardiac dysfunction [104]. The reduction in SERCA activity reduces the rate of Ca^{2+} removal from the cytosol of the CM, therefore inhibiting myocardial relaxation [22].

There is also conflicting evidence for NCX activity and expression levels in the aged myocardium. An increase in the expression of NCX channels has been demonstrated in heart failure, contributing to prolongation of action potential durations and reactivation of LTCC's [105]. However, studies have also indicated a reduction in NCX channel protein expression in aged rat and mouse hearts [106]. In contrast, other studies have demonstrated aged ventricular CMs had increased NCX1 current activity compared to younger CM counterparts [107]. Changes in NCX channel expression and activity with ECM stiffness is largely unknown.

Research indicating changes in Ca^{2+} ion channel expression with ageing led to the question of whether these changes could be associated with the stiffening of the myocardium environment. The effect of substrate stiffness on Ca^{2+} channel expression has not been previously investigated, and could therefore contribute to understanding how altered Ca^{2+} signalling can contribute to cardiac contractility and arrhythmia.

1.6.3 Alström Syndrome

Alström Syndrome (AS) is an ultra-rare inherited disease, characterised by multi-organ dysfunction, such as retinal dystrophy, obesity, dyslipidaemia, renal dysfunction and CVD [108]. The prevalence of AS is 1:100,000 to 1:1,000,000. AS has been identified as a disease model of accelerated ageing, with patients dis-

playing a higher Phenoage, a measure of biological age using clinical parameters, compared to chronological age, as described in Chapter 6 [109]. The multi-organ dysfunction seen in AS is typical of changes progressing with age, further reinforcing the idea of AS a model of ageing.

Patients with AS present with infantile cardiomyopathy from onset of birth to 10 years [110]. Despite recovery in most patients, cardiac disease recurs in adulthood with high mortality and morbidity rates, drastically reducing the life expectancy [111]. Echocardiography and cardiac imaging have demonstrated restrictive and dilated cardiomyopathy, congestive heart failure and replacement fibrosis as adult phenotypes of AS [112]. The cardiac complications observed in AS are also accompanied by metabolic disturbances, such as severe insulin resistance and increased triglycerides, which further mimics metabolic disease states [110].

AS is caused by genetic variants in the *ALMS1* gene, with mutations prevalent in exons 8, 10 and 16 of the gene [113], [114]. The variants in *ALMS1* are predicted to result in a lack of protein translation due to the presence of stop codons and protein truncation, ultimately resulting in a reduction of ALMS1 function [110], [114],[115].

ALMS1 is a centrosome and cilia protein, playing key roles in cilia maintenance and cell cycle regulation [116], with mutations impairing ciliary function and altering trafficking of signalling proteins. Biallelic mutations in *ALMS1* can therefore contribute to mitogenic cardiomyopathy seen in AS patients, through impairment of cell cycle arrest in neonatal CMs [113]. Furthermore, ALMS1 has been

proposed to play a role in endosomal trafficking of glucose transporters, adipogenesis and adaptive thermogenesis [114]. Mutations in AS patients may therefore contribute to metabolic dysregulation, which could also impact cardiovascular function. However, the biological roles of *ALMS1* are unknown, particularly in a cardiac context, highlighting the importance of investigating the molecular mechanisms altered with ALMS1 deletion. Molecular characterisation of ALMS1 and how it can alter metabolic and senescent pathways is therefore required to provide insight into the link between ALMS1, accelerated ageing and cardiac diseases observed in AS.

1.6.4 Metabolism in ageing and cardiac disease

Under physiological conditions, the myocardium primarily uses fatty acids and oxidative phosphorylation as its main source of energy production [117]. However, with ageing, the availability of energy substrates shifts, with a switch towards increased glycolysis at the expense of lipid metabolism [118]. Ageing hearts have been shown to have a reduced capacity to oxidise fatty acids, with failing hearts portraying a 30-40$\%$ reduction in ATP synthesis [119]. The lack of efficient oxidative phosphorylation can be linked to mitochondrial dysfunction, a hallmark of ageing, with altered bioenergetics and increased reactive oxygen species (ROS) production [120]. In addition, activity of mitochondrial ETC complexes has also been found to decline in the heart with age [121],[122].

The shift to glycolysis reflects a switch back to foetal like metabolism [123], and often occurs in cardiac diseases linked with ageing, such as heart failure and

cardiac hypertrophy [124]. Ageing and metabolic remodelling has also been associated with changes at a molecular level, with increased expression of glycolytic proteins and a decline in expression of genes linked to fatty acid oxidation [125]. The dysregulation in contractile function often observed with ageing can also be linked to the lack of efficient ATP production through oxidative phosphorylation, leading to a loss of substrate flexibility and state of energy deficiency [119].

The main changes occurring in cardiac ageing are metabolic shift in substrate utilisation and remodelling of the myocardium, by increased deposition of ECM proteins. There is little evidence to portray whether there is a link between stiffening of the myocardium and the change in cardiac metabolism, highlighting the importance of investigating the potential link between the two.

1.7 Models of ageing and cardiac disease

The complex nature of CVD consequently requires models to replicate the complexity and allow investigation into disease mechanisms and therapies. However, the lack of availability of human samples, especially healthy human hearts highlight a need for other models. Animal models, commonly mice and rats have been used largely in cardiac research, as they are genetically similar to humans, allow investigation into *in vivo* parameters such as echocardiography and can accurately recapitulate ageing in humans [126]. Despite the advantages, the ethical and biological cost of animal research, as well as physiological differences [127] has led towards the use of alternative *in vitro* models. The use of primary cells from young or aged individuals suffer from limitations, as the lack of availability

of samples and finite nature of these cells due to Hayflick's limit of expansion capacity present barriers to research [128].

1.7.1 Induced pluripotent stem cell models

The discovery of 'Yamanaka factors', a set of transcription factors with the ability to reprogram cells by inducing pluripotency in somatic cells has transformed the field of cardiovascular research [129]. This key breakthrough provided the knowledge that stem cells could be reprogrammed and differentiated into specific cell types, by activation or inhibition of specific pathways. The production of induced pluripotent stem cells (iPSC) generated from mouse embryonic fibroblasts using Oct3/4, Sox2, Klf4 and c-Myc [130] was discovered, and also successful with human fibroblasts. The directed differentiation of iPSC into CMs was therefore established by manipulating Wnt signalling pathways [131]. Protocols typically involve pushing cells towards a mesoderm lineage, by using bone morphogenic protein 4 (BMP4) and Activin A. XAV939 and KY0211 act as Wnt/β-catenin pathway inhibitors, pushing cells towards cardiac lineage, thus promoting CM development.

iPSC technology has been used widely in cardiac research [132], [133]. Human iPSCs are advantageous over primary cells, as they can be produced continuously, acting as an unlimited source of cells with human physiology [128]. The ethical concerns around the use of embryonic stem cells is also overcome with iPSC's acting as 'artificial counterparts' [134]. Furthermore, genetic editing of induced pluripotent stem-cell derived cardiomyocytes (iPSC-CMs) using

CRISPR/Cas9 has enabled investigation into disease phenotypes, with the ability to introduce mutations and characterise underlying disease mechanisms [132].

The ability to manipulate the ageing process in iPSC's through various methods such as length of culture and use of ECM proteins allows investigation into the interactions between ageing and CM performance [128]. Additionally, iPSC-CMs can be combined with other cell types such as fibroblasts, which can more closely resemble the ECM and interactions occurring between cells [135]. iPSCs are also mechanosensing, and thus can respond to environmental changes, enabling the investigation of ECM stiffness on CM function. The creation of iPSC-CMs therefore allows investigation into molecular mechanisms and pathways altered in ageing and disease states.

1.7.2 Limitations of iPSCs

However, the use of iPSCs in cardiac research has also come with several challenges. As iPSC technology is a relatively new field, optimisation of differentiation protocols has to be conducted. A key drawback of iPSC-CMs is their structural and functional immaturity, often reflecting foetal human CMs than adult CMs [133]. iPSC-CMs have been shown to have poorly formed sarcomeres, absence of t-tubules and poor Ca^{2+} handling [136], [137], [138]. The purity of iPSC-CM cultures with non-CM cell types was previously a concern due to differentiation protocols. However, recent strategies of lactate selection, which include a glucose media starvation allowing only iPSC-CMs to survive on lactate provided up to 99$\%$ CM purity in differentiations [139].

The immature nature of iPSC-CMs therefore brings into question the comparability to adult CMs and applicability to ageing research. Several strategies have been employed to overcome these issues and produce adult CM phenotypes [140], [141].

Attempts to mature iPSC-CMs have been made through the development of three-dimensional (3D) models such as engineered heart tissue, by combining iPSC-CMs with other cardiac cell types, thus demonstrating improved Ca^{2+} handling, CM alignment and ability to propagate electrical signals [142], [143]. Several maturation methods for two-dimensional (2D) models of iPSC-CMs have also been developed. Research has shown iPSC-CMs cultured for longer periods of time can improve sarcomeric structure and Ca^{2+} handling properties of the cell [144]. Growth substrates iPSC-CMs are cultured on can alter maturation, with the use of micropatterned substrates improving structural alignment of iPSC-CMs, Ca^{2+} handling dynamics and induce expression of cardiac maturation markers [145], [146]. The use of fatty acids in growth culture media has also been shown to increase CM force, enhance mitochondrial function and metabolic maturation [147]. Electrical stimulation of iPSC-CMs demonstrated increased expression of cardiac troponin T and mature sarcomere structure [148], [149]. Rod-shaped morphology of CMs and increased sarcomere lengths were found on iPSC-CMs when cultured on Matrigel, indicating structural maturity of iPSC-CMs [150]. The use of coatings such as Geltrex or Matrigel, which are basement membrane matrices composed of ECM proteoglycans, also act as maturation methods as well as facilitating attachment of iPSC-CMs.

1.8 Physiological models of ECM stiffness

To investigate the effect of ECM stiffness on CM function, representative models of the physiological stiffness of the ECM are required. Current experiments conducted on cell culture plastics and glass hold stiffnesses of 1-70 GPa, which are far stiffer than the healthy myocardium, which has stiffnesses of 10-20kPa [151], [152]. The increased stiffness of these environments may be altering cell morphology through mechanotransduction, as literature has extensively shown that structure and function of cells are altered by stiffness, suggesting cells may not be displaying a 'healthy' phenotype [153],[97]. Investigation into molecular and structural changes in cells on different substrate stiffnesses compared to plastics are therefore required to understand how stiffness can impact cell behaviour.

As a result, several methods have been employed to mimic the native myocardium. *In vitro* 2D approaches include ECM protein coatings such as collagen, fibronectin and Geltrex for tissue culture, thus mimicking ECM environments [154]. However, a key limitation of ECM coatings is their batch-to-batch variability, which can lead to a lack of reproducibility [155]. The emergence of bioprinting has also enabled the development of 3D models, with bioinks composed of ECM components, allowing the formation of accurate cell and matrix distributions to assess molecular changes in cells [156], [154]. Despite the development of 3D models, the lack of 2D physiological models representative of the healthy and fibrotic ECM highlighted a gap in the field of cardiac research.

1.8.1 Hydrogels as models for ECM stiffness

The drive for 2D physiological models of the ECM therefore led to the use of substrates that could mimic different stiffnesses. Biomaterials have been utilised in tissue engineering techniques, due to the ability to interact with biological systems and act as scaffolds, thus maintaining mechanical cues and signalling [157], [158]. Biomaterial hydrogels have been used widely for medical applications such as wound repair and drug delivery [159], [160].

Natural and synthetic biomaterials have been used extensively for hydrogels. Hydrogels are 3D crosslinked networks with the ability to retain water, thus creating scaffolds with structural integrity [161]. Mechanical properties of hydrogels such as stiffness of the gel can be altered by varying the crosslinking density of polymer chains, with increased crosslinking leading to increased stiffness [162]. Properties of the biomaterial polymer, such as the molecular weight and chemical structure of the material can also influence the hydrophilicity and degradation of the hydrogel [163].

Natural biomaterials, such as collagen and hyaluronic acid have been used for hydrogel synthesis, due to the biocompatible nature, low toxicity and quick degradability [164]. Collagen has been used for hydrogel development due to its low cost, ease of availability and high biocompatibility, as no further ECM coatings are required on gels due to the presence of cell attachment motifs [165],[166]. Collagen hydrogels have been used in cell culture, with literature suggesting CM sarcomeric structures are aligned and maintained [167]. Hyaluronic acid is a natural glycosaminoglycan abundant in the ECM, making it an attractive biomaterial

for hydrogel synthesis [168]. Furthermore, collagen and other natural biomaterials can be blended with one another and other ECM proteins such as fibrin [169], expanding the capabilities and mechanical properties of natural hydrogels. However, natural biomaterials are limited due to the lack of ability to modify these materials, leading to natural biomaterial hydrogels only creating hydrogel stiffnesses of 1-200kPa [167], therefore unable to recapitulate stiffer ECMs which may be reflective of disease conditions. Rapid degradability of natural hydrogels further inhibits the use of these gels in long term cell culture experiments.

Alternatively, synthetic biomaterials have high stability, low degradability and flexibility to modify mechanical and chemical properties [170], [171]. Synthetic biomaterials such as Polyethylene glycol (PEG) and Polydimethylsiloxane (PDMS) have been used in the cardiac field widely, due to low cost, optical transparency of gels, ease of fabrication and delivery for bioactive molecules [172], [173]. The ability to modify chemical properties of synthetic polymers has enabled synthetic hydrogels to recapitulate a wide range of stiffnesses, such as PDMS hydrogels with stiffnesses from 12 kPa to 5.2 MPa [174]. Literature has shown PDMS and PEG hydrogels are compatible with cardiac fibroblasts and CMs [175], [176], highlighting further benefits of synthetic gels in cardiovascular research. A key limitation of synthetic materials is the lack of cell attachment due to hydrophobicity and absence of reactive functional groups, thus requiring further chemical functionalisation and addition of ECM coatings [177]. Chemical functionalisation can include addition of integrin binding peptides such as RGD to synthetic hydrogels, to promote cell attachment and adhesion, transforming hydrogels from bioinert to

bioactive gels [178].

The versatility, biocompatibility and flexibility to tailor chemical and structural properties of hydrogels enables them to be an effective physiological model in mimicking the myocardium and ECM compared to traditional cell culture plastics. The previous use of PEG and PDMS hydrogels in cardiac research indicated its compatability with iPSC-CMs and ability to recapitulate a range of stiffnesses made them ideal substrates for ECM models, allowing investigation into effect of the ECM environment on cardiac cell behaviour and structure. The ability to accurately reflect changes in myocardium stiffness that occur with ageing further enables our understanding of stiffness related mechanisms and disease pathways that could be targeted for therapeutics.

1.9 Aims and Hypothesis

The overall aim of this research was to investigate the effect of cardiac ageing on iPSC-CM morphology and function, by modelling physiological stiffnesses of the ECM.

1.9.1 Developing hydrogel models of the stiffness of the myocardium and ECM

Hypothesis: PEG/PDMS hydrogels can used to recapitulate the stiffness of a healthy myocardium (20kPa) and fibrotic myocardium (130kPa) and demonstrate biocompatibility with iPSC-CMs.

In order to test the hypothesis, Chapter 3 aimed to replicate the stiffness of healthy and fibrotic ECM, by developing hydrogels of healthy and diseased stiff-

nesses using biomaterials. PEG and PDMS were selected to replicate stiffnesses and compatibility with iPSC-CMs were assessed.

1.9.2 Characterisation of the effect of stiffness of the ECM on iPSC-CM function

Hypothesis: iPSC-CMs cultured on stiffer PDMS hydrogels (130kPa) display a disease phenotype.

ECM stiffness impacts cardiac function, with increased stiffness observed in ageing and heart failure. Chapter 4 therefore aimed to characterise the effect of ECM stiffnesses on iPSC-CM cellular and molecular mechanisms, specifically assessing changes in morphology, gene expression, contractility and Ca^{2+} handling dynamics.

1.9.3 Investigating the effect of stiffness of the ECM on iPSC-CM metabolism

Hypothesis: iPSC-CMs cultured on healthy ECM stiffness (20kPa) primarily utilise fatty acid metabolism, whereas iPSC-CMs cultured on stiffer ECM substrates (130kPa) switch to glycolysis as their primary energy substrate.

The shift in metabolism from fatty acid oxidation to glycolysis is a defining feature of cardiac ageing and heart failure. Chapter 5 aimed to investigate whether the shift in cardiac metabolism is linked to changes in ECM stiffness observed with ageing. Cellular bioenergetics, proteomics and isotope labelled mass spectrometry were used to assess metabolic function.

1.9.4 Assessing Alström Syndrome as a model of accelerated ageing

Hypothesis: AS patients demonstrate a higher Phenoage than chronological age.

Chapter 6 aimed to investigate whether AS could be considered as a model of accelerated ageing using Phenoage, a measure of biological age using nine blood marker parameters and chronological age. Cardiac ageing was also assessed using retrospective analysis of echocardiography.

1.9.5 Characterising the cardiovascular role of *ALMS1* in Alström Syndrome using iPSC-CMs

Hypothesis: *ALMS1* knockout (KO) iPSC-CMs demonstrate a disease phenotype with altered CM function.

Individuals with AS display infantile cardiomyopathy from a very early age, indicating accelerated ageing and cardiac dysfunction. Chapter 7 aimed to characterise the role of *ALMS1* in infantile cardiomyopathy, by characterising the effect of an *ALMS1* KO iPSC line, differentiating into iPSC-CM and assessing changes in contractility, Ca^{2+} handling, metabolism and senescence.

Chapter 2

Materials and Methods

2.1 Materials

All instruments and commercial kits used in experiments are stated throughout the methods.

2.1.1 Antibodies

Primary and secondary antibodies used for immunofluorescence (IF) and western blotting (WB) listed in Tables 2.1 and 2.2.

Table 2.1: **List of Primary antibodies**

Antigen	Host	Catalogue number	Company	Concentration
α-actinin	Rabbit	Ab68167	Abcam	1:5000 (WB)
α-actinin	Mouse	A7811	Sigma-Aldrich	1:500 (IF)
ALMS1	Rabbit	27231-1-AP	ProteinTech	1:1000(IF)
p16-INK4A	Rabbit	10883-1-AP	ProteinTech	1:200 (IF)
p21	Rabbit	10355-1-AP	ProteinTech	1:200 (IF)
PDK4	Rabbit	12949-1-AP	ProteinTech	1:1000 (WB)
PDH E1 alpha	Rabbit	18068-1-AP	ProteinTech	1:5000 (WB)
Phosphohistone 3 (PHH3)	Rabbit	11587110	Invitrogen	1:100 (IF)
PPARδ	Rabbit	PA1-823A	Invitrogen	1:750 (WB)
GAPDH	Rabbit	(14C10) 2118S	Cell Signalling Technology	1:5000 (WB)
GAPDH	Mouse	(D4C6R) 97166	Cell Signalling Technology	1:1000 (WB)
MLC2V	Rabbit	10906-1-AP	ProteinTech	1:1500 (WB)
SERCA/ATP2A2	Rabbit	D51B11	Cell Signalling Technology	1:750 (WB)

Concentrations of antibodies, manufacturer and catalogue numbers for primary antibodies stated. Abbreviations: IF- Immunofluorescence, WB-Western blotting

Table 2.2: **List of Secondary antibodies**

Secondary antibodies	Host	Catalog number	Company	Concentration
Alexa-Fluor 488 conjugated anti-Rabbit IgG	Goat	A-11034	Invitrogen	1:200 (IF)
Alexa-Fluor 488 conjugated anti-Mouse IgG	Goat	A11029	Invitrogen	1:200 (IF)
Alexa-Fluor 568 anti-Rabbit IgG	Goat	A-11011	Invitrogen	1:200 (IF)
Alexa-Fluor 568 anti-Mouse IgG	Goat	A11019	Invitrogen	1:200 (IF)
anti-Rabbit IgG IRDye 800CW	Goat	926-32211	LI-COR	1:5000 (WB)
anti-Mouse IgG IRDye 680RD	Goat	926-68070	LI-COR	1:5000 (WB)
DAPI (4', 6-Diaminido-2-Phenylindole, Dihydrochloride) Conjugated	N/A	D1306	ThermoFisher Scientific	1:400 (IF)
Phalloidin F-Actin (Conjugated)	N/A	A22284	ThermoFisher Scientific	1:500 (IF)
Amersham ECL-anti-Rabbit IgG HRP whole antibody	Donkey	NA934V	Cytiva	1:5000
Amersham ECL anti-Mouse IgG HRP whole antibody	Sheep	NXA931V	Cytiva	1:5000

Concentrations of antibodies, manufacturer and catalogue numbers for primary antibodies stated. Abbreviations: IF- Immunofluorescence, WB-Western blotting

2.1.2 Quantitative polymerase chain reaction (qPCR) probes

Genes of interest investigated using qPCR probes; TaqMan probes listed in Table 2.3 and SYBR green probes listed in Table 2.4.

Table 2.3: **List of Taqman quantitative polymerase chain reaction (qPCR) probes**

TaqMan probes	
Target gene	**Assay ID**
ACTN2 (FAM-MGB)	Hs05032285_s1
COL1A1 (FAM-MGB)	Hs00164004_m1
CD36 (FAM-MGB)	Hs00354519_m1
CDKN1A (FAM-MGB)	Hs00355782_m1
CDKN2A (FAM-MGB)	Hs00923894_m1
CPT1B (FAM-MGB)	Hs03046298_s1
GAPDH (VIC-MGB)	4626317E
HK2 (FAM-MGB)	Hs00606086_m1
LMNB1 (FAM-MGB)	Hs01059205_m1
PFKM (FAM-MGB)	Hs01075411_m1
PDK4 (FAM-MGB)	Hs01037712_m1
PLIN2 (FAM-MGB)	Hs00605340_m1
PLIN5 (FAM-MGB)	Hs00965990_m1
PPARGC1A (FAM-MGB)	Hs00173304_m1
PPARα (FAM-MGB)	Hs00947536_m1
PPARδ (FAM-MGB)	Hs04187066_g1
PPARγ (FAM-MGB)	Hs01115513_m1
MYH7 (FAM-MGB)	Hs01110632_m1
MYH6 (FAM-MGB)	Hs01101425_m1
MYL2 (FAM-MGB)	Hs00166405_m1
MYL7 (FAM-MGB)	Hs01085598_g1
NPPA (FAM-MGB)	Hs00383230_g1
NPPB (FAM-MGB)	Hs00173590_m1
TNNT2 (FAM-MGB)	Hs00943911_m1
TBP (VIC-MGB)	Hs00427620_m1

Taqman probes (Applied Biosystems) with gene of interest and assay ID numbers stated.

Table 2.4: **List of SYBR green qPCR probes**

SYBR primers	
Target gene	**Sequence (5'-3')**
ACTN2	F - GCT GAA GAA ATT GTT GAT GG R - ATA TCC TGA ATA GCA AAG CG
ATP2A2	F - AGA GTG GAA GGT GAT ACT TG R – GCA GAG TCA TTA CAA AGA GC
CACNA1C	F - GGA GAG TTT TCC AAA GAG AG R - TTT GAG ATC CTC TTC TAG CTG
CACNA1D	F - AAA ATG GGC ATC ATT CTT CC R - AGT TTC ATA ATA GCG GGT TC
CACNA1F	F - CAT TTT CAC CAT CCC AGA AG R - CTC ATC TAG GTA GGA AAG CC
CCND2	F - ACT TCA TTG AGC ACA TCT TG R - ACA TGG CAA ACT TAA AGT CG
DLAT	F - GGT TTT GAA GTA CAG GAA GAA G R -TAC AAT GAT ACA GAG TGG GG
DLD	F - AAG GTT GTT CAT GTC AAT GG R - AAG GAG TAA CTT CTG AAC CC
E2F1	F - CTG ATG AAT ATC TGT ACT ACG C R -CTT TGA TCA CCA TAA CCA TCT G
GAPDH	F - GAT TCC ACC CAT GGC AAA TTC R – GTC ATG AGT CCT TCC ACG ATA C
PDHA1	F - ATT CGA AGC TTA CAA CAT GG R - AGG ATA TCC CAT TCC ATC CAC
RYR2	F - CGT TGC GTA TCT TAG CTA TTC R - GGA CTT TCA AAG CAG TAG TAT C
SLC8A2	F - TAA GAA CAC GGT GGA TAA AC R - ATT GCC TCT AAA AAC TGC TC
SLC8A3	F - ATA GTA GAT GAG GAG GAA TAC G R- GTC ACA TCT GAT ATT CCA CG

SYBR green qPCR probes (Merck) with gene of interest and target sequences. All probes were human species.

2.2 Methods

2.2.1 iPSC cell culture

The KOLF2 human iPSC lines from a healthy individual was cultured and underwent differentiation into iPSC-CMs using a differentiation protocol. iPSC and iPSC-CMs were cultured in an incubator at 37℃, 5% CO_2, 20% O_2.

ALMS1 knockout (KO) iPSC lines were developed by University of Oxford, with CRISPR/Cas9 deletion of exons 10-13 of *ALMS1*, with a deletion size of 60kb.

CRISPR/Cas9 site specific guide RNA sequences were used with the following sequences; ALMS1-cr1 5'GGCTTGCATCCCATTCCCCGTGG'3' and ALMS1-cr2 5' TTGTGCCTAGCACCTGAGCTGGG'3'. Mutagenesis was conducted using the synthetic guide RNAs. Genotyping and Sanger sequencing were conducted to confirm deletion of the region. ALMS1 iPSC clone C23 were used for differentiation into iPSC-CMs.

All tissue culture plates, flasks and coverslips, with and without PDMS hydrogels were pre-coated with GelTrex (Life Technologies, cat no. A1413201) in DMEM with glucose and L-Glutamine, without pyruvate (ThermoFisher Scientific, cat no. 41965039-039) at a 1:200 ratio for 24 hours at 37℃ to facilitate attachment of iPSCs and iPSC-CMs.

KOLF2 iPSCs were maintained in mTeSR Plus media (StemCell Technologies, cat no. 100-0276), with medium changed every other day until cells had reached 90% confluency per well. Once confluent, cells were detached using 1X TrypLE Express Enzyme (Gibco, cat no. 12605-010) for 4 minutes at 37℃. After dissociation, cells were plated in 6 well plates (Corning) in mTeSR Plus media with 10μM Rho kinase Inhibitor (RI), Y-27632 (Selleck, cat no. S1049). Cells in mTeSR Plus containing RI were replaced with fresh mTeSR Plus media after 24 hours in culture. *ALMS1* KO iPSC cells were cultured in the same manner but maintained in mTeSR1 media (StemCell Technologies, cat no.85850).

2.2.1.1 Freezing iPSCs

iPSCs were detached using 1X TrypLE Express Enzyme for 4 minutes and re-suspended in 1ml of mFreSR (StemCell Technologies, cat no.05855). Cells in the solution were put into a cryovial at approximately 1x10^6 per vial. iPSC's were put into a Mr Frosty Freezing container (ThermoFisher Scientific) and stored at -80℃ overnight before storing into liquid nitrogen.

2.2.1.2 Thawing iPSCs

Frozen cells were thawed in a 37℃ water bath for a few minutes until a small amount of ice remained. Cells were then added to pre-warmed culture media and centrifuged at 220g for 3 minutes. The pellet of cells were resuspended in mTeSR Plus media containing 10 μM RI and plated in wells coated with Geltrex.

2.2.1.3 iPSC-CM differentiation protocol

iPSCs were differentiated within the lab using a published protocol [179], utilising growth factors and small molecules (Figure 2.1). iPSCs were plated 2-3 days before differentiation, with initiation of differentiation protocols when cells had reached 70-80% confluency. Pre-conditioning media was added to initiate day-1 of the differentiation protocol; StemPro-34 SFM (Gibco, cat no. 10639011) supplemented with 2mM L-Glutamine (ThermoFisher Scientific) in a ratio of 1:100, 1ng/ml Recombinant Human BMP4 Protein (R&D Systems, cat no.314-BP-010) and 1:100 dilution of GelTrex was added to the cells. The next day, media was changed to StemPro-34 media supplemented with 2mM L-Glutamine, 10ng/ml

BMP4 and 8ng/ml Activin A (Gibco, cat no. PHC9561) (Day 0). On day 2, media is replaced with RPMI 1640 (Gibco) with a B27 supplement without Insulin (Gibco, cat no. A18956-01) (RPMI-Ins), supplemented with 10μM KY0211 (R&D Systems, cat no. 4731/5) and 10μM XAV939 (R&D Systems, cat no. 3748/10) and added to the cells. A media change to RPMI 1640 with a B27 supplement containing Insulin (RPMI+Ins), (Gibco, cat no. 17504-044), 10μM KY0211 and 10μM XAV939 was added on day 4. On day 6, media was changed to RPMI+Ins. On day 8, media was changed to RPMI 1640 medium with no glucose (Gibco, cat no. 11879-020) to induce glucose starvation until day 10, purifying the CM population. Spontaneous contraction of iPSC-CMs occurred from day 8 onwards.

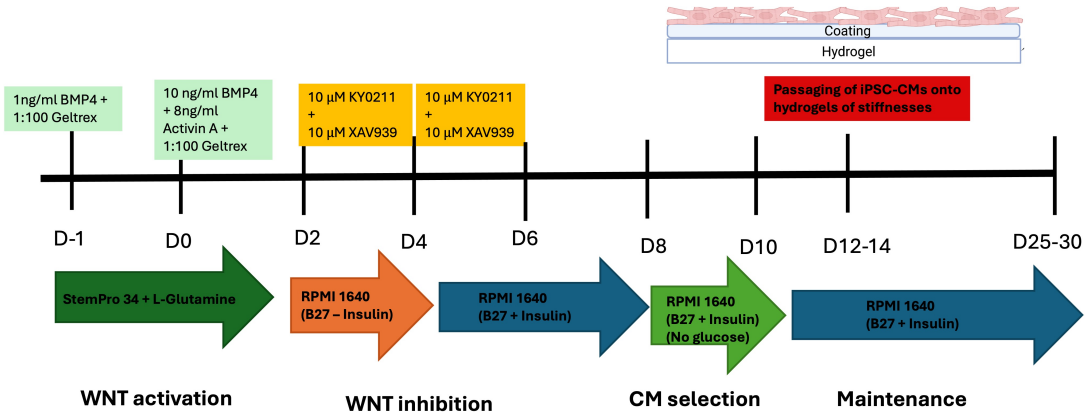

Figure 2.1: **Differentiation protocol of iPSCs to iPSC-CMs**
Schematic diagram of differentiation protocol for iPSC-CMs. The process begins with initiation of day -1 media when iPSCs are approximately 70-80% confluent. Mesoderm differentiation is initiated with BMP4 and Activin A. XAV939 and KY0211 inhibit Wnt signalling, promoting CM development. Selection of CMs occurs during glucose starvation between days 8-10 of differentiation. iPSC-CMs are split onto PDMS hydrogels on between days 12-14 of differentiation and remain on hydrogels until day of experiment. Created with Biorender.com

2.2.1.4 Passaging iPSC-CMs

Between days 12-14, iPSC-CMs were passaged onto PDMS hydrogels in plates or coverslips. 1ml TrypLE Express Enzyme was added per well of iPSC-CMs and

incubated for 8 minutes to facilitate detachment; after 4 minutes the plate was gently shaken. Plating media, consisting of RPMI+Ins, 10% Knockout Serum replacement (Gibco) and 2μM Thiazovivin was added to the TrypLE wells and cells were dissociated. CMs in solution were centrifuged for 3 minutes at 215g at room temperature. Plating media was removed, and the CM pellet was resuspended in plating media. The CMs were plated onto geltrex coated PDMS plates of varying stiffnesses at a density of approximately 1x10^6 cells per well. iPSC-CMs on PDMS gels were maintained in RPMI+Ins media and changed every other day until use in experiments. Between days 15-20, if iPSC-CMs portrayed signs of peeling off the PDMS gels, a second passage onto PDMS hydrogels was conducted from days 18-20.

2.2.2 Quantitative Polymerase Chain Reaction (qPCR)

Cells were harvested as pellets at day 25 of culture. TrypLE was used to dissociate cells, spun down at 215g for 3 minutes and collected in an Eppendorf tube. iPSC-CMs were resuspended in 1X phosphate buffered solution (PBS) and spun down at 13000g at 4℃ for 5 minutes, followed by aspiration of PBS. Pellets of cells were stored at -80℃ until use.

2.2.2.1 RNA extraction and cDNA conversion

RNA was extracted from iPSC-CM pellets using an RNEasy Mini Kit (Qiagen, cat no.74104) and QIAshredder homogenizers (Qiagen, cat no.79656), as per the Qiagen Mini protocol. Briefly, cell pellets were lysed using Buffer RLT and homog-

enized using the QIAshredder. 70% ethanol was added to the lysate, transferred into spin columns and centrifuged. Washes of RNA were conducted with Buffer RW1 and Buffer RPE. At the final stage of RNA extraction, RNA was collected in 50μl of Nuclease-free water (Promega). Concentration of RNA was measured using a NanoDrop 1000 Spectrophotometer (ThermoFisher Scientific), with samples measured twice and an average concentration calculated.

RNA from iPSC-CMs were converted to cDNA using Reverse transcriptase PCR, as per the High-Capacity cDNA Reverse Transcription Kit protocol (Applied Biosystems, cat no.4368814). Mastermixes contained RT buffer, dNTPs, RT primers, reverse transcriptase, nuclease-free water and 200ng RNA in a 20μl volume reaction. cDNA conversion was carried out using a MiniAmp Plus thermal cycler (Applied Biosystems), under the following conditions; 25℃ for 10 minutes, 37℃ for 120 minutes, 85℃ for 5 minutes, 4℃ hold. cDNA samples were stored in -80℃ until use.

2.2.2.2 Quantitative Real-Time Polymerase Chain Reaction (qRT-PCR)

qRT-PCR was conducted using TaqMan probes (Table 2.3) in combination with TaqMan Fast Advanced Master Mix 2X (Applied Biosystems, cat no.4444557) and KiCqStart SYBR primers (Merck, Sigma-Aldrich) (Table 2.4) in combination with PowerUP SYBR Green Master Mix (Applied Biosystems, cat no. A25742). qPCR assays were conducted on the QuantStudioTM 5 Real-Time PCR System (Applied Biosystems). Fold changes in gene transcript expression were calculated using the $\Delta\Delta$Ct method, with 2-Δ(ΔCt) using *GAPDH*, *ACTN2* or *TBP* as house-

keeping genes. TaqMan probes were used in duplex format; GAPDH probes were VIC dye labelled, whereas the gene of interest were FAM-dye labelled, allowing both probes to be combined in the same well.

2.2.3 Western blotting

Western blots were used to analyse changes in protein expression on the various stiffnesses.

2.2.3.1 Protein extraction

iPSC-CM pellets were collected at day 25 in the same manner as for qPCR. Pellets were resuspended in 50μl of 2X SDS buffer (consisting of 100mM Tris-HCL pH 6.8, 4% sodium dodecyl sulfate, 0.2% bromophenol blue, 200mM dithiothreitol and 20% glycerol) and denatured at 95℃ for 5 minutes. Protein samples then underwent sonication using a Fisherbrand^{TM} Q500 Sonicator with Probe (Fisher Scientific, cat no. 12893543) and were stored at -80℃ until use.

2.2.3.2 Gel electrophoresis and Western blot

Protein samples were ran on a 4-15% Polyacrylamide SDS-PAGE gels (BioRad, cat no.415-076) in a 1X Tris-Glycine-SDS buffer (National diagnostics, cat no. EC-870) and transferred to a nitrocellulose membrane using an iBlot 2 Gel Transfer machine (Invitrogen). Visualisation of total protein was carried out using Ponceau S solution (Sigma-Aldrich) for 30 seconds and washed off using deionised water. Blot membranes were then blocked using 5% skimmed milk in 0.1% Tween-20

(VWR, cat no. 9005-64-5) in tris buffer saline (TBST) for 1 hour, before primary antibodies were added in fresh TBST. Primary antibodies were diluted in 5% milk TBST and left overnight at 4℃ on a shaker. Membranes were washed 3 times with 0.1% TBST for approximately 15 minutes. Secondary antibodies were then added to 1% milk in 0.1% TBST for 1 hour at room temperature. Washes were conducted as described above, and membranes were imaged for protein bands using the Odyssey Fc Imaging Machine (LI-COR), using fluorescence at 700nm and 800nm. Protein quantification was carried out using ImageJ software. Primary and secondary antibodies used are listed in Tables 2.1 and 2.2.

2.2.4 Immunofluorescence

iPSC-CMs at the appropriate age were fixed with 4% Paraformaldehyde in 1X PBS for 15 minutes at room temperature. Cells were then washed in PBS for 5 minutes, with washes repeated 3 times and stored in PBS at 4℃ until staining was conducted.

Fixed cells were permeabilised with blocking buffer, consisting of 0.5% Triton-X-100 (Sigma, cat no. T8787) in 1X PBS, 5% Fetal Bovine Serum (FBS) (Gibco, cat no. A4766801) and 1% BSA (Sigma-Aldrich, cat no. A3311) for 1 hour at room temperature. Primary antibodies were diluted in blocking buffer and applied to cells overnight at 4℃. The following day, primary antibodies were washed off 3 times for 5 minutes each using blocking buffer. Secondary antibodies diluted in blocking buffer were added to cells for 1 hour at room temperature in the dark, followed by PBS washes as above. Cells on coverslips were mounted onto glass

microscopy slides using Hydromount mounting medium (National Diagnostics).

2.2.4.1 Confocal microscopy

Coverslips were imaged using confocal microscopy (Zeiss LSM780 and LSM880) using a C-Apochromat 63x/1.20 W Korr M27 objective oil immersion lense, a LD LCI Plan-Apochromat 25x/ 0.8 Imm Korr DIC M27 water lense or an alpha Plan-Apochromat 100x/1.46 Oil DIC M27 Elyra lense. Images were saved as 8-bit or 16-bit format on Zen Blue (v. 3.1) or Zen Black Software (v.3.0).

2.2.4.2 Image analysis

Confocal microscopy images were analysed using ImageJ software (v2.9.0). Quantification of p16 and p21 fluorescence in the nucleus and cytoplasm of cells was conducted using a script written in collaboration with Daniel Nieves. Briefly, DAPI and α-actinin masks were thresholded to create binary masks. DAPI masks were used to quantify nuclear expression of p16 and p21. Cytoplasmic expression was calculated by generating a new mask, by subtracting DAPI masks from α-actinin masks. Background fluorescence was corrected for, and the mean fluorescent intensity was then calculated from within the masked areas in original images.

2.2.4.3 Sarcomere length analysis

Confocal microscopy Images of α-actinin and Phalloidin staining were analysed for sarcomere lengths and Z-line lengths using a Z-line detection script described in [180] in MATLAB version (R2022b) 9.13.0.2049777.

2.2.5 Optical mapping

iPSC-CMs were plated into 35mm dishes at a density of 2x10^6 cells per dish to create a monolayer of cells. These cells were cultured in dishes and used for optical mapping between days 25-30. Cells were incubated at 37℃ with 5μM Fura-2 AM (Invitrogen™, F1221) in RPMI+Ins media for 20 minutes. Following this incubation, the Ca^{2+} dye was removed and cells were incubated with 2ml of prewarmed Tyrode's solution consisting of 129mM NaCl (VWR Chemicals, cat no.27810.295), 5.4mM KCl (Sigma, cat no. P9541), 10mM HEPES (Sigma, cat no. H3375), 48mM $MgCl_2$ solution (Honeywell, cat no. 63020), 1.8mM CaCl (Sigma, cat no.C8106) and 9.99mM D-Glucose (Sigma, cat no. G8270) dissolved in 96ml distilled water, pH 7.44-7.48. Fura-2 AM Ca^{2+} dye was excited at 380nm wavelength with fluorescent emission captured at 510/40nm. Ca^{2+} signals were recorded from dishes on a heating plate set to maintain 37℃ taken at 10X magnification. Spontaneous Ca^{2+} transients were imaged and recorded using an Evolve delta 512x512 EMCCD camera. The following settings were applied: exposure time 1.7ms, pixel size 8μm, 51x51 pixel resolution, binning settings 10, framerate set to 588 Hz and 40% gain using Winfluor software.

2.2.5.1 File conversion and data analysis

Raw files were extracted from Winfluor Fluorescence Image Capture and Analysis Programme (version 4.1.9) as TIF files and converted into MATLAB files using a conversion script. MATLAB files were then imported into ElectroMap software (version 1.0) from [181] for peak and midpoint analysis. Data were presented as

mean + SEM. Files were analysed at peak and midpoint transients. Outputs from optical mapping are displayed in Figure 2.2.

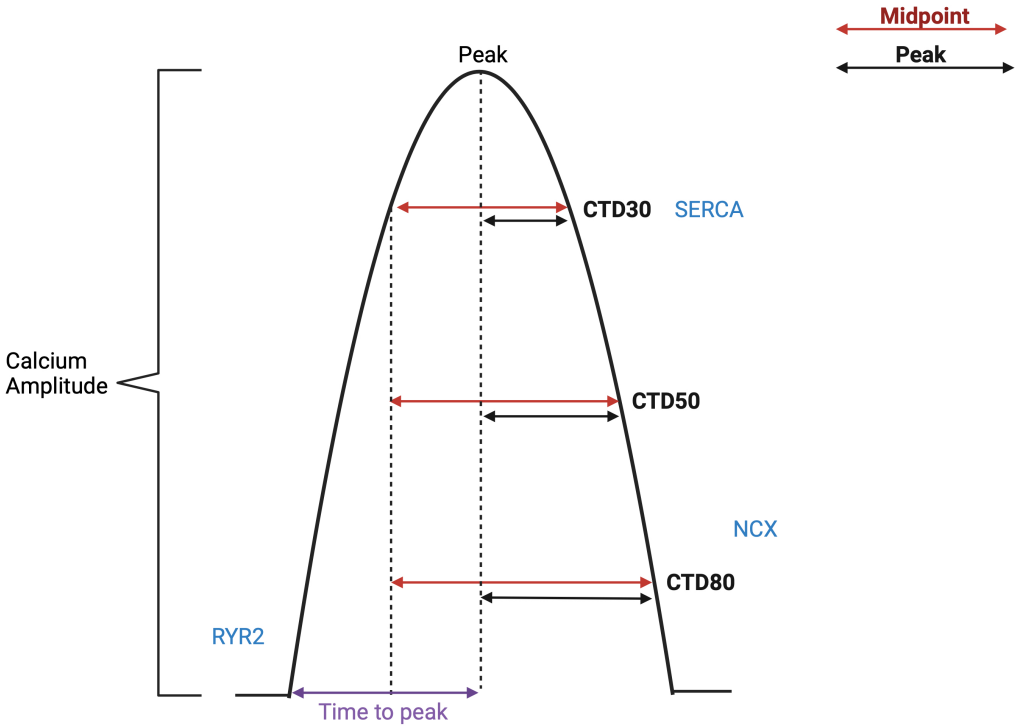

Figure 2.2: **Schematic of Ca^{2+} optical mapping parameters**
Diagram of Ca^{2+} transient with labelled optical mapping parameters for iPSC-CMs. Corresponding Ca^{2+} channels responsible for specific parts of the Ca^{2+} transient indicated. Calcium amplitude refers to amplitude of each calcium transient. CTD30, 50 and 80 refers to the reuptake of calcium at 30%, 50% and 80%. Peak measurements indicated by black arrows, Midpoint measurements indicated by red arrows. Abbreviations; CTD-calcium transient duration.

2.2.6 Contractility analysis using MuscleMotion

Spontaneous contraction of iPSC-CM monolayers, maintained in a 5% CO_2 incubator were recorded non-invasively in cell culture media using a GoPro H6 camera attached to a microscope using a 10X objective for a duration of 20-25 seconds at room temperature, with an oxygen concentration of 20.95%. 3 different areas per well were recorded, ensuring videos captured full monolayer contrac-

tion, with measurements made from multiple wells from one batch of iPSC-CMs, across several batches. The videos were converted to TIF sequence files at a 59.94 frame rate using Davinci Resolve software (v18.0.3). TIF files were converted into a stacked TIF file, which was processed using a MuscleMotion macro in FIJI/ImageJ software (v2.9.0), from [182]. MuscleMotion software calculated changes in pixel density in videos using masks of cell monolayers, calculating parameters relating to contractility. MuscleMotion outputs included contraction amplitude, time to peak, relaxation time and peak to peak time, as seen in Figure 2.3. MuscleMotion data was normalised to cells on plastic as the control condition to reduce variability of data. Average values per batch of iPSC-CMs were plotted, with values averaged across multiple wells and areas.

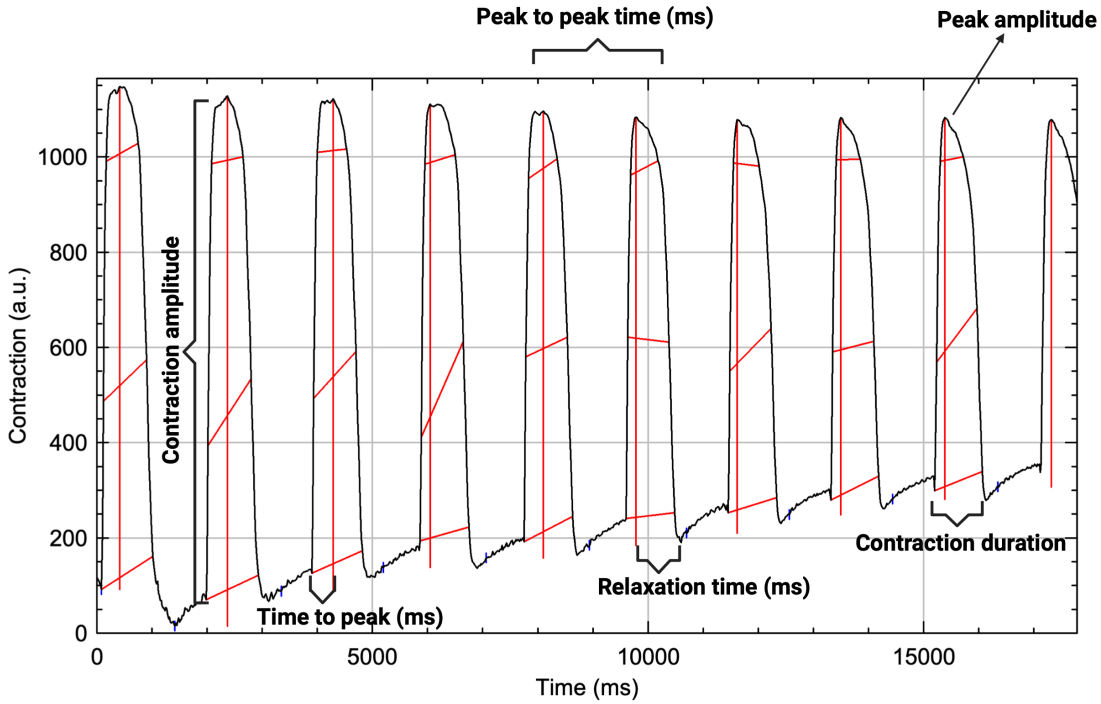

Figure 2.3: **MuscleMotion contractility analysis outputs**
Diagram of representative MuscleMotion outputs with contractility parameters indicated. Peak to peak time, referring to time taken between each peak of contraction of iPSC-CM. Peak amplitude refers to the peak contraction. Contraction amplitude refers to the 'force' of contraction. Time to peak refers to the time taken to reach peak of contraction. Relaxation time refers to the time taken for iPSC-CMs to relax from contraction. Contraction duration accounts for the time taken for iPSC-CM to contract and relax for a single contraction. Beat rate of iPSC-CMs can be calculated from these parameters.

2.2.7 Isotope label Gas Chromatography-Mass Spectrometry (GC-MS)

iPSC-CMs were differentiated and seeded onto PDMS hydrogels between days 12-15 at a density of 500,000 cells per well for Gas Chromatography Mass Spectrometry (GC-MS).

2.2.7.1 Conjugation of fatty acids to BSA

Palmitic acid (PA)(Sigma, cat no. P0500) and Oleic acid (OA) (Sigma, cat no. O1008) were dissolved in 70% ethanol at 70℃ to make 10mM stocks and frozen

at -20℃ until use. 10% BSA in RPMI+Ins (BSA media) solution was also made at 37℃. OA and PA stocks were heated to 70℃ and added at a 1:10 ratio to warmed BSA media, and left to warm in a 37℃ water bath for 1 hour. A further 1:10 dilution of the fatty acids in BSA media was added to RPMI+Ins media, filtered and added to the cells. Cells were treated with final concentrations of 50μM PA and 100μM OA in RPMI+Ins media for a period of 10 days, with media removed and replaced every other day.

2.2.7.2 Glucose Isotope labelling of iPSC-CM

SILAC RPMI 1640 Flex media, no glucose, no phenol red (Gibco, cat no. A2494201) was supplemented with L-Arginine (Sigma, 1.14mM), L-Lysine (Sigma, 0.2mM), L-Glutamine (Gibco, 2mM) and B27+Ins supplement (10X, Gibco). Isotope labelled D-Glucose ([U-$^{13}C_6$-glucose], (99%, Cambridge Isotope Laboratories, Item number: CLM-1396-PK) was added to the SILAC labelling media at 10mM. SILAC labelling media was also made up with unlabelled 10mM D-Glucose (Sigma, cat no. G8270) for control samples. Day 26 iPSC-CMs were incubated with SILAC labelling media with or without labelled glucose for 48 hours.

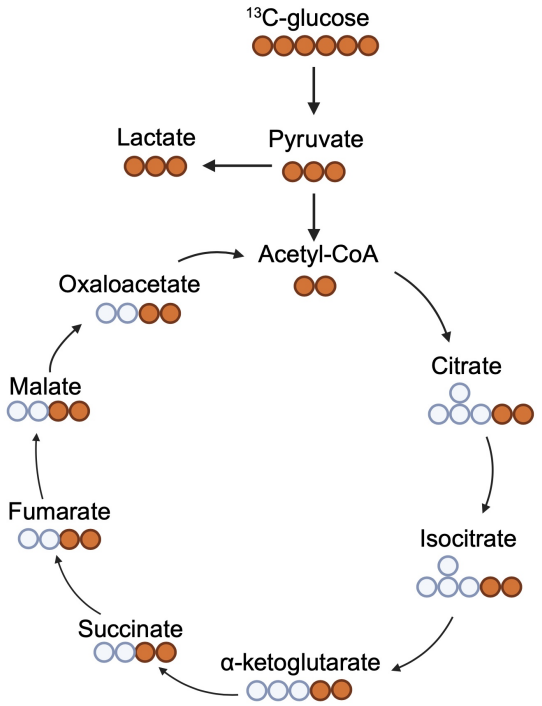

Figure 2.4: **Schematic of [U-^{13}C]-glucose carbon tracking into TCA cycle metabolites**
Schematic diagram of central carbon tracking; the percentage of labelled [U-^{13}C] glucose utilised in the formation of TCA cycle metabolites is tracked, indicating up or downregulation of specific pathways. Adapted from [183].

2.2.7.3 Polar Metabolite extraction of iPSC-CM

After isotope labelling, the cells were removed from incubation and metabolite extraction was conducted on ice. Cells were washed twice with 0.9% NaCl solution to remove excess media from samples. Pentanedioic d6 acid (D6) was used as the internal standard for samples. D6 was added at 1μg/ml concentration to GC-MS grade water. Cells were quenched with 500μl of ice cold HPLC grade methanol (Sigma, 34860). 200μl of GC-MS grade water containing D6 internal standard was added to the methanol on cells and scraped using a cell scraper. The scraped solutions were collected into eppendorf tubes and vortexed

for 15 seconds to ensure cell lysis. 500μl of HPLC grade chloroform (Sigma, cat no. 366927) was added to each tube and further vortexed for 10 seconds producing a cloudy mixture. Samples were centrifuged at 14,800g for 10 minutes at 4℃. 400μl of the upper phase solution containing the polar metabolites were transferred to a new Eppendorf tube. Samples were dried using a SpeedVac vacuum centrifuge (ThermoFisher, Savant^{TM} Integrated Vacuum concentrator) for 2-3 hours and stored at -80℃ until derivatisation.

2.2.7.4 Sample derivatisation

20μl of 2% methoxyamine hydrochloride and pyridine (Sigma-Aldrich) was added to the dried samples and placed on a shaker for 10 minutes at room temperature. Following shaking, samples were incubated at 60℃ for 1 hour on a heating block. 30μl of N-methyl-N[tert-butyldimethylsilyltrifluoroacetamide] (MTBSFA) with 1% tert-butyldimethyl-chlorosilane (TBDMSC) (Restek) were added to the samples, shaken for 10 minutes at room temperature and heated for 1 hour at 60℃ on a heating block. Samples were centrifuged for 15 minutes at 3000g and solution was transferred into GC-MS vials with glass inserts. Samples were run on an Agilent 7890B GC and 5977A MSD. 1 μl of sample was injected in splitless mode with helium carrier gas at a rate of 1 ml/min, sample inlet was 270℃. Initial oven temperature was held at 100℃ for 1 min before ramping to 160℃ at a rate of 10℃/min, followed by a ramp to 200℃ at a rate of 5℃/min, and a final ramp to 330℃ at a rate of 10℃/min with a 4 min hold. Transfer line was held at 270℃. Analytes were ionised via EI (70 eV) and source temperature of 230℃.

Compound detection was carried out in scan mode.

2.2.7.5 Analysis of samples

Analysis was conducted by the MTAC facility at University of Birmingham. All data processing was performed in MATLAB (2022a) using the METRAN script. Mass isotopomer distributions (MIDs) were corrected for natural isotope abundance. Each metabolite in all datasets were normalised to the internal standard D6-Glutaric acid (CDN Isotopes). Metabolite abundances and percentage of labelled isotopologues were calculated (Figure 2.4). Data were normalised to cell numbers from parallel dishes of the same differentiation from batches of iPSC-CMs cultured on PDMS substrates and plastics, treated under the same culturing and labelling conditions.

2.2.8 Cellular Bioenergetics Seahorse Extracellular Flux

96 well Seahorse Extracellular Flux (XF) microplates (Agilent Technologies) were split into thirds; one third was coated with 5μl of 20kPa PDMS hydrogel, another third coated with 5μl 130kPa PDMS hydrogel and the final third non-coated, kept as plastic. PDMS coated seahorse plates were washed 3 times with 1X PBS, followed by 70% ethanol for 1 hour and further washed in PBS 3 times before coating with Geltrex. iPSC-CMs were then seeded into the coated seahorse cell culture plates at a density of 20,000 cells per well. Wells A1, H1, A12 and H12 were kept empty and used as background correction wells. Seahorse XF Cell Mito Stress Test assay (Agilent, cat no. 103015-100) was conducted as stated in the

protocol, with the following alterations; the drug inhibitors (Figure 2.5) used were at final concentrations Oligomycin (2μg/ml), Bam15 (3μM), Rotenone/Antimycin A (2μM) and Monensin (20μM). 3 measurements, consisting of a 3 minute wait and 3 minute measure cycle was set after drug additions. After the seahorse assay was complete, cell plates were centrifuged at 1000rpm for 5 minutes to remove media and pellet iPSC-CMs. Cell pellets were lysed in RIPA buffer (10μl) and protein concentrations determined using a Pierce Rapid Gold BCA Protein Assay Kit (ThermoFisher Scientific, catalog number A53225). Protein concentrations were read using a SpectraMAX ABS plate reader (Molecular Devices, cat no. 736-0916) on Softmax Pro software (v 7.1.2).

2.2.8.1 Seahorse Analytics

Data from the Seahorse XF assay was analysed using Agilent Seahorse analytics (version 1.0.0-699). Following baseline correction and normalisation to protein concentration, several energetics parameters such as basal respiration, ATP-coupled respiration, maximal respiratory capacity, spare respiratory capacity, proton leak, non-mitochondrial respiration were obtained using oxygen consumption rates (OCR) (Figure 2.5). Extracellular acidification rates (ECAR) were used to indicate levels of lactic acid production.

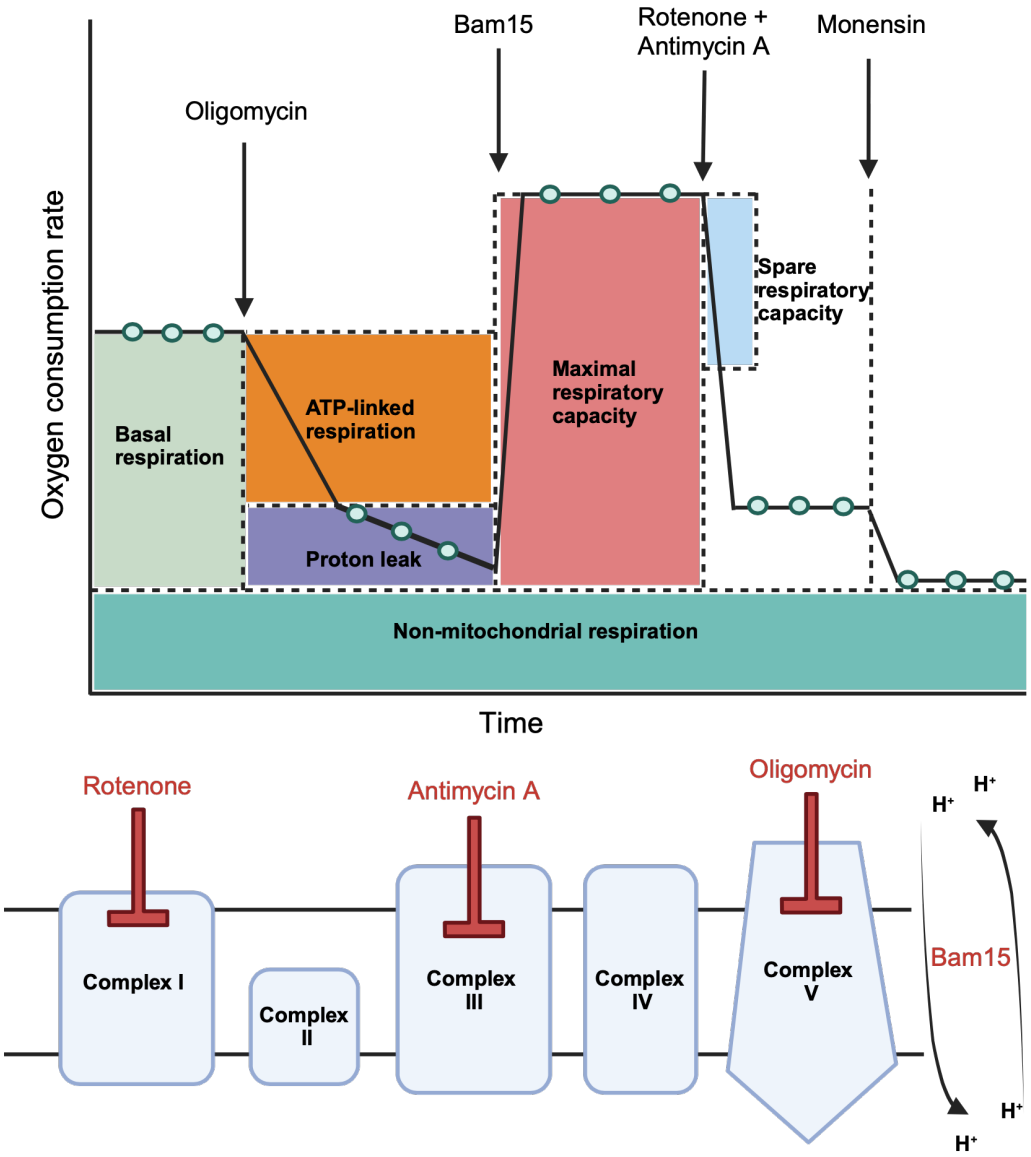

Figure 2.5: **Schematic of Seahorse XF Cell Mito-Stress Test parameters**
Diagram of representative trace of seahorse XF Cell Mito-Stress test assay with outputs indicated. Mitochondrial respiratory drug inhibitors of the ETC complexes, Oligomycin, Rotenone and Antimycin A labelled. Bam15 acts as a proton uncoupler, alllowing maxmimal respiration. Monensin acts by shutting down mitochondrial respiration. Adapted from [184].

2.2.9 Proteomics

Day 25 iPSC-CM cells grown on PDMS and plastic were pelleted and processed using the EasyPep Mini MS Sample Prep Kit (ThermoFisher Scientific, catalog

no A40006) as per stated in the protocol. Briefly, cells were lysed using 100μl of Lysis Solution and protein was quantified using the Pierce Rapid Gold BCA Protein Assay Kit as per stated in protocol (ThermoFisher Scientific, A53225). 40μg of protein from each sample was used for reduction and alkylation. Samples were digested overnight in a shaking incubator at 37℃ at 150rpm. Peptides were labelled with TMTpro^{TM} 16plex Mass Tag Labelling Reagent Set (ThermoFisher Scientific, cat no A44522) as per the EasyPep^{TM} MS Sample Prep kit protocol. Clean-up of peptides was conducted using clean up columns from the EasyPep^{TM} Mini MS Sample Prep Kit (ThermoFisher Scientific, cat no. A40006), until samples were in elution solution. The samples were taken to the Advanced Mass Spectrometry Facility at University of Birmingham, combined into one sample and underwent a ZipTip clean up (Merck Millipore, cat no. ZTC18S096). Mass spectrometry and quantative proteomics runs were conducted by Todd Mize.

2.2.9.1 Mass spectrometry for Proteomics

Samples were run on Precolumn Cartridges, Acclaim PepMap 100 C18, 5 μm 100 Å, 300 μm i.d. x 5 mm (Dionex) and separated in a Nano Series TM Standard Columns 75 μm i.d. x 15 cm, packed with C18 PepMap100, 3 μm, 100Å (Dionex). Gradients of 3.2% to 44% of Solvent B (0.1% formic acid in acetonitrile) were used for 30 minutes. Columns were then washed with 90% solvent B solution and further equilibrated with 3.2% solvent B. Peptides were eluted at 350 nL/min-1 via a Triversa Nanomate nanospray source (Advion Biosciences) into a QExactive HF Orbitrap mass spectrometer (ThermoFisher Scientific). Full FT-MS

scans (m/z 375-1600) and high energy collision dissociation MS/MS scans of the most abundant ions were conducted. Mass spectra were recorded at a resolution of 120,000 at m/z 200 and autonomic gain control of $3x10^6$. Precursor ions were fragmented in HCD MS/MS with a set resolution of 60,000 and a normalised collision energy of 32. The autonomic gain control target for HCD MS/MS was $1x10^5$. The precursor isolation window was set at 1.2 m/z and only multiply-charged precursor ions were selected for MS/MS. Spectra were obtained for 60 minutes.

2.2.9.2 Proteomics analysis and visualisation

The data was run in Proteome Discoverer (v2.5) against a Uniprot database to visualise proteins. Statistical quantification was conducted in Proteome Discoverer using an ANOVA, with protein volcano plots plotted in GraphPad Prism 9. A false discovery rate threshold was set at 0.05. A threshold of significance was set as $p < 0.05$, log2 fold change of significance set to 0.58, thus a log fold change of > 1.5. The precursor mass tolerance was set at 10 ppm and a MS/MS tolerance of 0.02 Da was set for processing and quantification.

2.2.10 Senescence-Associated β-galactosidase assay

iPSC-CMs were plated at a density of 500,000 cells per coverslip and cultured until day 30 of differentiation. Cell staining was conducted using Senescence β-Galactosidase (β-gal) Cell Staining kit (Cell Signalling Technology, cat no. 9860) as per protocol. Briefly, cells were fixed using a 1X Fixative solution for 15 minutes at room temperature. The coverslips were then rinsed twice using 1X PBS and

incubated overnight at 37℃ in a CO_2 free dry incubator with β-galactosidase staining solution. Following β-gal staining, cell nuclei were stained with DAPI in PBS for 15 minutes. Images were taken using an EVOS M500 Imaging system (Invitrogen, ThermoFisher Scientific), at 20X magnification.

2.2.11 Statistical Analysis

All statistical analysis was conducted using GraphPad Prism (version 9.5.1). To determine whether data had a gaussian distribution, Shapiro-Wilk normality tests were conducted. When comparing across multiple groups that were normally distributed, a one-way ANOVA with šidák post hoc test was applied. For non-parametric data compared between multiple groups, a Kruskal-Wallis test with Dunn's multiple comparisons test was conducted. A two-way ANOVA with multiple comparisons was conducted when comparing the effect of two or more parameters.

Data compared between 2 groups that were not normally distributed underwent a Mann-Whitney statistical test, whereas data normally distributed underwent an unpaired t-test with Welch's correction.

Statistical significance levels were considered as $p < 0.05$ (*), $p < 0.01$ (**), $p < 0.001$ (***), $p < 0.0001$ (****).

Chapter 3

Modelling ECM stiffness with biomaterial hydrogels

3.1 Introduction

The ECM acts as a cardiac microenvironment, serving as a structural scaffold for a vast network of interactions for cells, with the ability to transduce mechanical signals and alter cellular function [185]. The stiffness of the ECM can alter with cardiac ageing and disease, due to excess deposition of ECM proteins such as collagen, causing stiffening of the myocardium [186]. Healthy physiological tissue has stiffnesses of 10-25kPa, whereas diseased or fibrotic tissue has stiffnesses of $>$ 50kPa [187], [188], [170]. Tissue culture plastics and glass coverslips have stiffnesses of 1-70GPa [189], [190], thus are far stiffer than cardiac tissue and are not representative of physiological conditions. To investigate the effect of ageing and ECM stiffness, suitable models of physiological stiffnesses of the cardiac ECM are required. Several strategies have been developed to mimic the ECM, such as the use of decellularized ECM, electrospun nanofibers which utilise nanofibers made from ECM proteins to create fibrillar structures, and cardiac ECM patches consisting of multiple cell types [191], [192],[193].

Alternatively, hydrogels can be used as biological ECMs using biomaterials.

Biomaterials can be formed from both natural and synthetic components and play a key role in polymer biomaterial tissue engineering and model development by interacting with biological systems, such as providing mechanical cues [194]. Biomaterials have largely been used for hydrogels, which are a type of biomaterial that feature 3D crosslinked polymer networks which absorb and retain water [165]. The ability to retain water but maintain structural integrity make hydrogels ideal models for mimicking the ECM. A key advantage of synthetic hydrogels is the capacity to modify the mechanical properties of the hydrogel, such as elasticity and stiffness, by altering factors such as polymer composition and crosslinking density [195]. Varying the crosslinking density alters stiffnesses of hydrogels, with denser crosslinking resulting in stiffer gels. The ability to modify stiffnesses of hydrogels consequently led to their use as substrates for representing both healthy and fibrotic ECM.

A vast range of natural and synthetic hydrogels have been utilised to mimic the ECM. Natural hydrogels such as collagen, gelatin, polyacrylamide and PEG [164], [170] are often used due to their high biocompatibility and degradability [164]. However, natural hydrogels are less amenable to mechanical modification. On the other hand, synthetic hydrogels have high stability and can be easily chemically modified to change properties such as cell attachment [196].

PEG is a synthetic polymer that has been widely used in the biomedical field, such as tissue engineering, due to its high-water content and injectability [197]. It is commonly used for hydrogel synthesis due to its biocompatibility, hydrophilicity, versatility and its tunable mechanical properties [198]. The stiffness and elas-

ticity of PEG hydrogels can be altered through changing the molecular weight or concentration of PEG, thus changing the crosslinking density of the gel [199]. Furthermore, PEG hydrogels have been used in cardiac research, with previous research showing PEG hydrogels maintaining cardiac cell structures and contractility [176].

Other synthetic polymers include PDMS, which is a silicone-based polymer, widely used in biological research [173],[200]. PDMS has several advantageous properties ideal for hydrogel synthesis, such as low cost, transparency, elasticity, flexibility, stability and ease of fabrication [201],[173]. The stiffness of PDMS hydrogels can be easily altered by changing the ratio of curing agent and base agent, thus enabling PDMS hydrogels to possess a wide range of Young's moduli from 10 kPa- 2.5 MPa [202]. In addition, PDMS has been widely used in cardiovascular research for investigations into fibroblasts [175] and CMs [202], highlighting compatibility of PDMS hydrogels. Since both PEG and PDMS displayed desired characteristics for hydrogel synthesis, they were selected as base materials for developing representative ECM models.

3.2 Hypothesis and Aims

To mimic changes in stiffness of the ECM with ageing and disease, PEG and PDMS based hydrogels were used as tuneable substrates. The main objectives included identifying a suitable biomaterial for hydrogel synthesis, with the ability to model a healthy ECM stiffness (20kPa) and fibrotic ECM stiffness (130kPa). Furthermore, the hydrogels had to be biocompatible, showing successful iPSC-

CM attachment.

The hypothesis for this chapter was tested through the following aims:

1. Synthesise PEG hydrogel precursors possessing functional alkyne and thiol end groups
2. Produce PEG hydrogels of healthy ECM stiffnesses and determine compatibility with iPSC-CM culture
3. Produce PDMS hydrogels of healthy and fibrotic ECM stiffnesses
4. Assess compatibility of iPSC-CMs with PDMS hydrogels

3.3 Methods

3.3.1 Polyethylene Glycol Hydrogel (PEG) synthesis

3.3.1.1 2-Arm Thiol Functionalised PEG precursor (2.0 kg mol^{-1})

Esterification was carried out as previously published in [203] (Figure 3.1). 2-Arm $PEG_{2k}OH$ (20g, 10 mmol) (Sigma, cat no.84797) was combined with 3-Mercaptopropionic acid (4.23g, 40mmol) (Sigma, cat no.M5801) in a 500ml round bottom flask. To this, 150ml toluene (VWR Chemicals, cat no. 28676.322) and 5 drops of concentrated Sulfuric acid, H_2SO_4 (Fischer Scientific, UNI830) were added. The solution was heated to 125℃ to reflux under Dean-Stark conditions overnight. The reaction was cooled to room temperature and solvent was removed in vacuo. The crude product was dissolved in 250ml dichloromethane, CH_2Cl_2 (Fischer Scientific, cat no. UNI593) and washed with 50ml each of saturated sodium bicarbonate, $NaHCO_3$, NaCl and H_2O. The resultant product was

left overnight with magnesium sulfate $MgSO_4$ (Sigma, cat no.63136) and 0.2g activated charcoal (Sigma, 2422761). The mixture was filtered using Celite 545 Filter Agent (Sigma, cat no.68855-54-9). Dichloromethane was removed from the product by rotary evaporator, thus isolating the product, collected as a liquid (yield 7.1g).

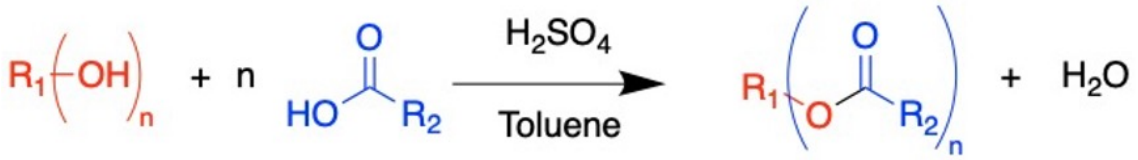

Figure 3.1: **Fischer esterification reaction used for synthesis of alkyne or thiol functionalised PEG precursors**
n= number of arms of PEG (2 or 3), R_1= PEG, R_2=CCH or CH_2CH_2SH

3.3.1.2 3-arm thiol functionalised PEG precursor (1.0 kg mol^{-1})

As per protocol above, an esterification reaction was carried out using glycerol ethoxylate (molar mass 1kg mol^{-1} , 10g, 10mmol) (Sigma, cat no.441864) and 3-Mercaptopropionic acid (6.37g, 60mmol) to collect the product as an oil (yield, 3g, 45%).

3.3.1.3 3-arm alkyne functionalised PEG precursor (1.0 kg mol^{-1})

As stated in the typical esterification, glycerol ethoxylate (molar mass 1kg mol^{-1} , 10g, 30mmol) was esterified with propiolic acid (14.25g, 180mmol) to collect the product as a yellow oil (yield 9.55g, 41%).

3.3.1.4 2-arm alkyne functionalised PEG precursor, (2.0 kg mol^{-1})

As stated in the typical esterification, 2-Arm $PEG_{2k}OH$ (20g, 10 mmol) was esterified with propiolic acid (2.79g, 40mmol) to collect the product as a white solid (yield 11.1g, 53%).

3.3.2 PEG hydrogel formation

1:1 ratios of alkyne group to thiol groups were used to synthesize all gels at 10% weight to solid content. A typical gel was produced by dissolving each PEG precursor in 200μl of PBS of pH 7.4. Varying ratios of 3-arm thiol, 2-arm thiol and 3-arm alkyne were used to develop hydrogels of balanced stoichiometry (Figure 3.2). The trio of precursors dissolved in 200μl of PBS were mixed together and vortexed, put into a small syringe and left at room temperature, with gelation taking 5-10 minutes, forming cylindrical hydrogels.

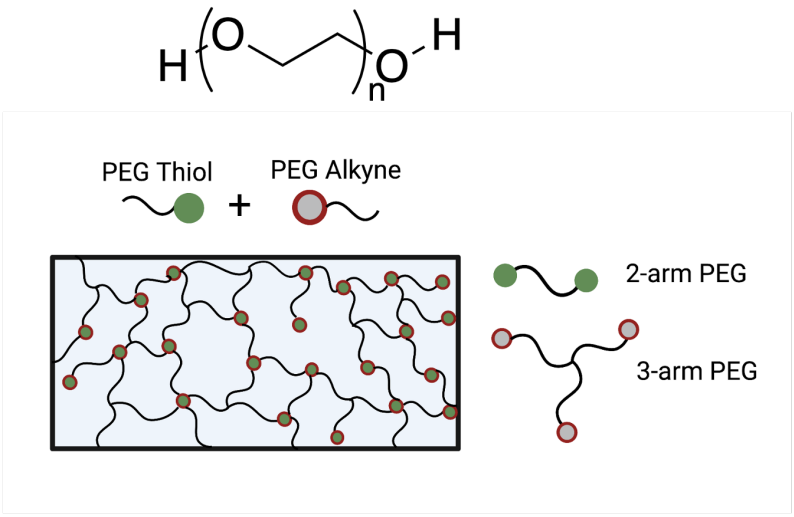

Figure 3.2: **PEG hydrogel structure formed from combinations of 2-arm and 3-arm PEG precursors**
Chemical structure of PEG, with visual representation of PEG hydrogel formed from 2-arm thiol precursor and 3-arm alkyne precursor, creating a hydrogel network. Adapted from [204].

3.3.2.1 Leaching techniques for hydrogel

Once synthesised, gels were washed with PBS several times to remove unreacted precursors not incorporated into the gel network. Gels were kept in PBS overnight at 37℃, before undergoing another PBS wash the following day. PBS washes were maintained for 2-3 days before cells were plated onto hydrogels. Gel washes with 70% ethanol and cell culture media over a series of three days were also tested. PEG hydrogels were coated with vitronectin or Geltrex to faciliate attachment of iPSC-CMs.

3.3.3 Rheology

Stiffnesses of hydrogels were measured using oscillatory shear rheology (Anton Parr MCR 302 rheometer) with a parallel plate setup, of diameter 8mm. Hydrogels of varying precursor combinations were created with PBS and placed onto the rheometer after gelation of at several time points. The plate was lowered until touching the hydrogel surface, with a normal force of zero. Amplitude sweeps were performed on the hydrogels, with 1Hz frequency and an applied strain ramped logarithmically from 0.01-1% to keep the measurements within the linear viscoelastic range. 20 points were recorded from each experiment, with amplitude sweeps carried out in triplicate on the same hydrogel. Storage moduli (G') and Loss moduli (G") were obtained from experiments. Average storage and loss modulus from the amplitude sweeps were used to calculate the Young's moduli.

3.3.4 Young's modulus equations

Young's moduli values were calculated using the following formulas:

E = 2G (1 + υ) and G = $\sqrt{(G'2 + G"2)}$

Where υ is Poisson's ratio (0.5 for hydrogels), E is Young's Modulus, G is shear modulus, G' is storage modulus and G" is loss modulus

3.3.5 PDMS hydrogel synthesis

PDMS substrate hydrogels were prepared using Sylgard 527 (Dow, cat no.1675167) and Sylgard 184 (Dow, cat no.63416-5S). PDMS stiffnesses of 20kPa and 130kPa were produced by adding different mass ratios of Sylgard 184: Sylgard 527, 1:10 and 1:5 respectively. Once mixed, the solution was pipetted into cell culture plates or spin coated onto glass coverslips using a vacuum assisted spin coater (SPIN-150i, Polos) at 1000 rpm for 40 seconds (Figure 3.3). The PDMS gels were then cured overnight at 65℃ before undergoing PBS washes, followed by 70% ethanol sterilisation for 1 hour at room temperature before further PBS washes to remove any remaining ethanol or unreacted precursors.

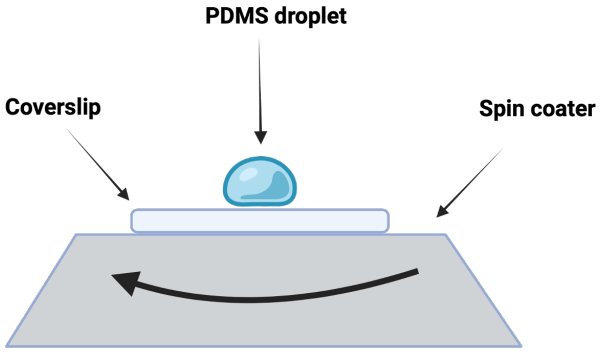

Figure 3.3: **Schematic of spin coating PDMS mixture of stiffness onto coverslip in a thin layer**
Spin coater used to spread PDMS as thin layers onto glass coverslips for Immunofluorescence experiments. Created with Biorender.com

3.4 Results

3.4.1 Structure of PEG thiol and alkyne precursors

^{1}H NMR spectroscopy was conducted following synthesis to determine molecular structure and assess purity of precursors. All ^{1}H NMR spectra portrayed a PEG backbone signal across all precursors at 3.6 ppm, as expected (Figures 3.4, 3.5, 3.6, 3.7, denoted as b). Thiol groups, also known as sulfhydryl groups, which appear as a triplet, were present in both thiol PEG precursors indicating successful functionalisation (Figures 3.4 and 3.6, point e). 3-arm thiol PEG precursor and 2-arm thiol PEG precursors featured methylene groups (Figures 3.4 and 3.6, peaks labelled c and d). Alkyne groups were present in alkyne precursors at approximately 3.0 ppm, highlighted by the peak labelled point d (Figures 3.5 and 3.7). Deuterated chloroform was used as a reference peak for all NMRs, identified at 7.26ppm.

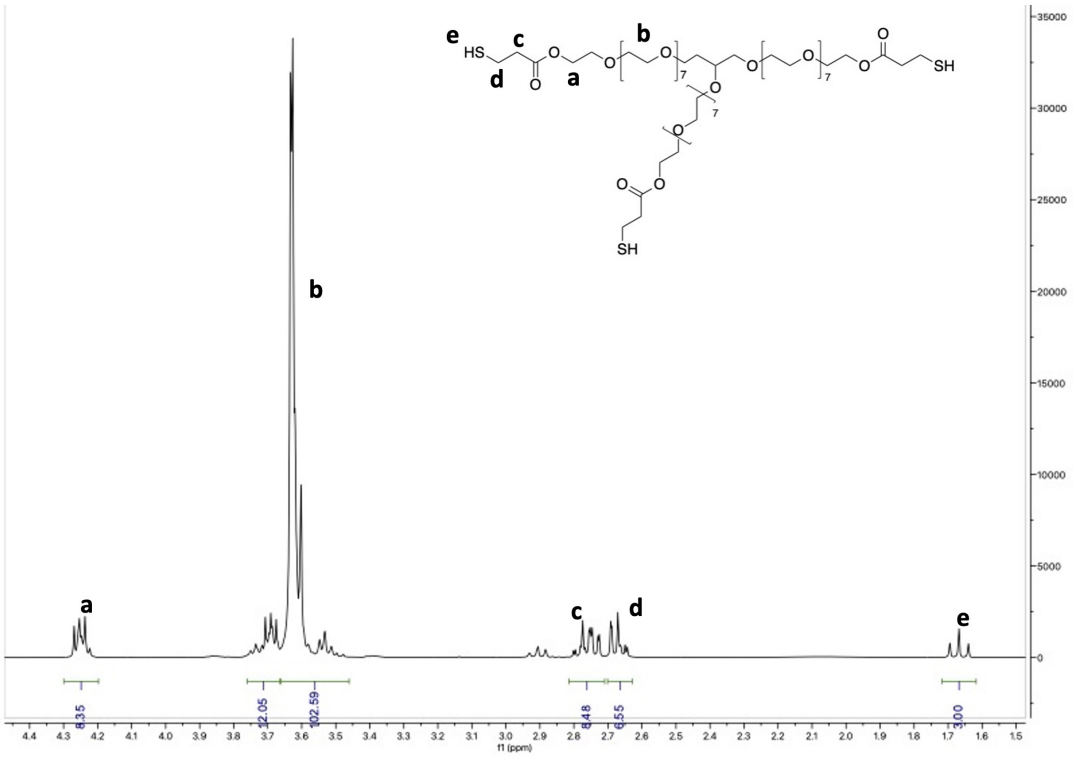

Figure 3.4: **Proton NMR of 3-arm thiol PEG precursor (1kg mol^{-1})**
^{1}H NMR ($CDCl_3$, 300MHz): (300 MHz, Chloroform-d) δ 4.30 – 4.20 (m, 8H), 3.76 – 3.66 (m, 12H), 3.66 – 3.46 (m, 103H), 2.81 – 2.71 (m, 8H), 2.70 – 2.63 (m, 7H), 1.67 (t, J = 8.2 Hz, 3H).

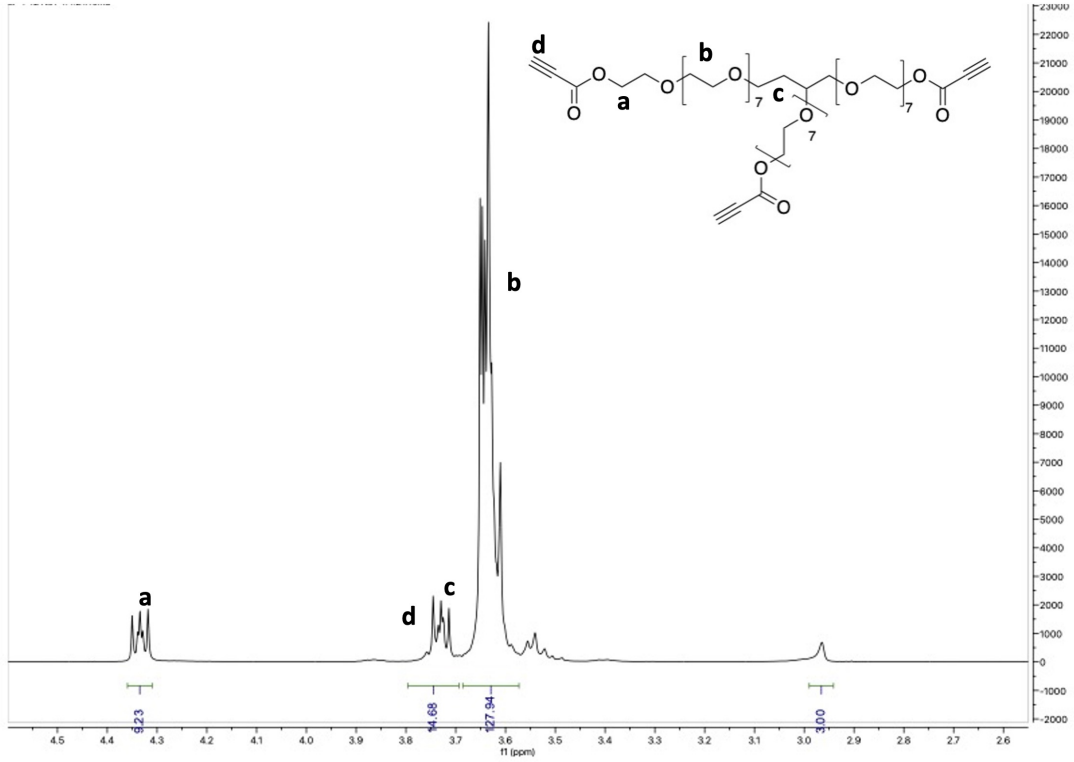

Figure 3.5: **Proton NMR of 3-arm alkyne PEG precursor (1kg mol^{-1})**
^{1}H NMR ($CDCl_3$, 300MHz): (300 MHz, Chloroform-d) δ 4.36 – 4.31 (m, 9H), 3.80 – 3.69 (m, 15H), 3.69 – 3.57 (m, 128H), 2.96 (s, 3H).

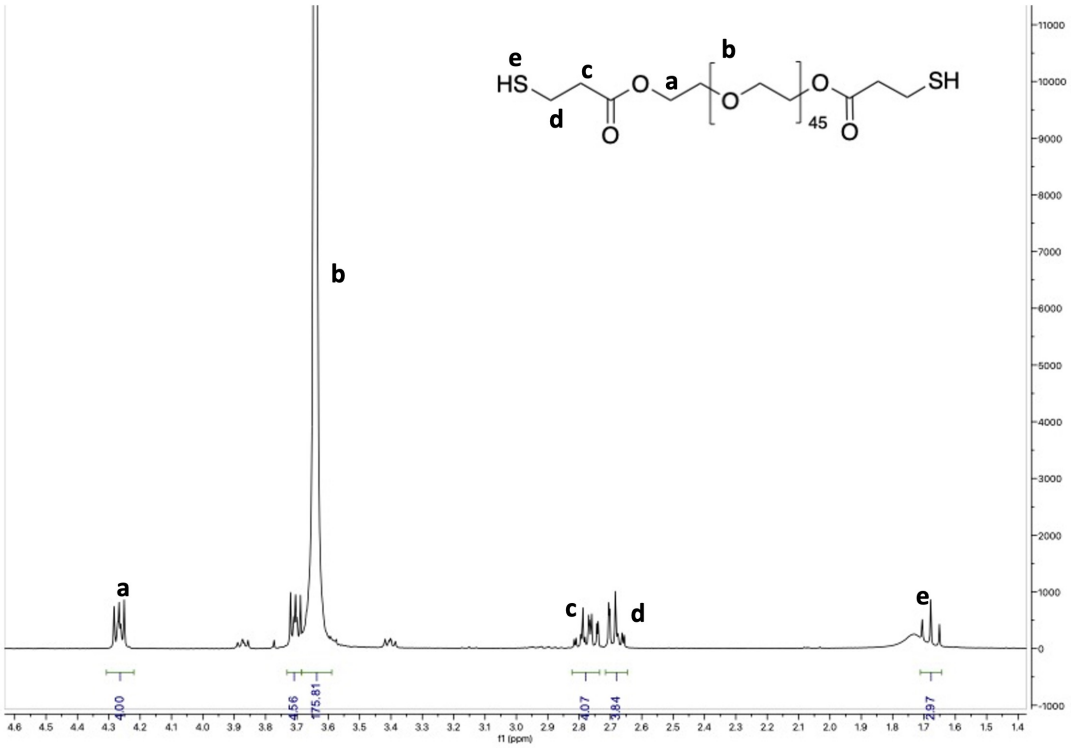

Figure 3.6: **Proton NMR of 2-arm thiol PEG precursor (2kg mol^{-1})**
^{1}H NMR(CDCl3, 300MHz): (300 MHz, Chloroform-d) δ 4.26 (dd, J = 14.7, 12.4 Hz, 4H), 3.73 – 3.69 (m, 5H), 3.64 (s, 176H), 2.82 – 2.73 (m, 4H), 2.72 – 2.65 (m, 4H), 1.68 (d, J = 16.3 Hz, 3H).

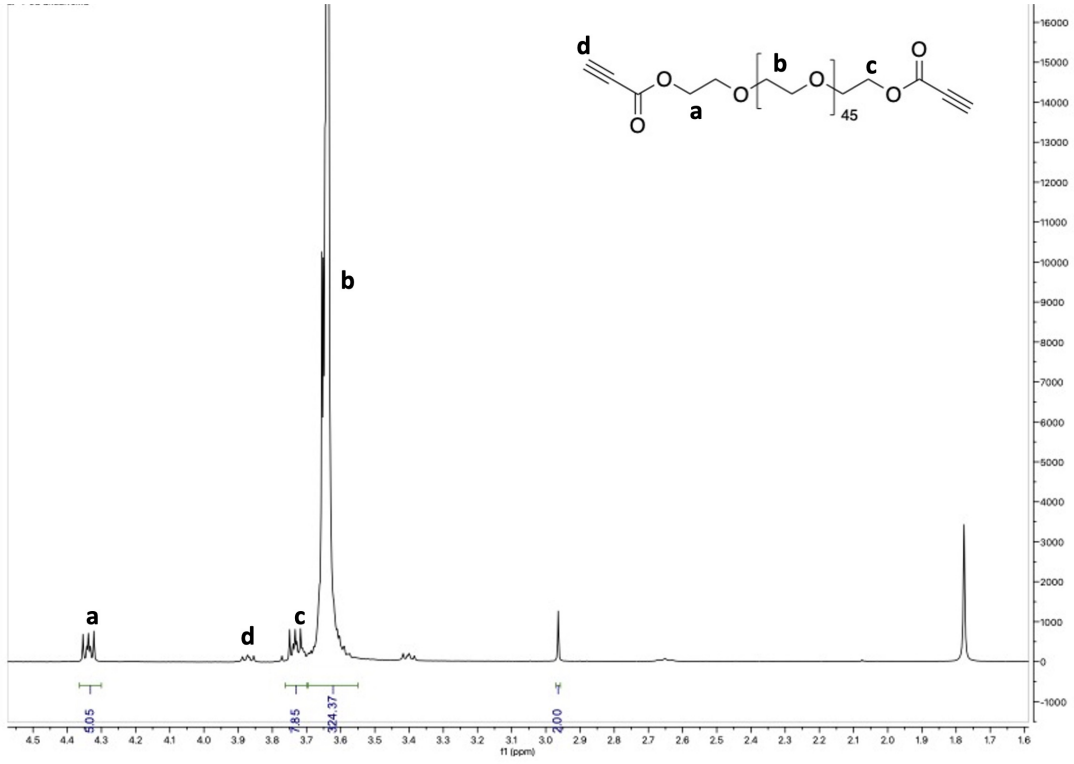

Figure 3.7: **Proton NMR of 2-arm alkyne PEG precursor (2kg mol^{-1})**
^{1}H NMR(CDCl3, 300MHz):(300 MHz, Chloroform-d) δ 4.36 – 4.30 (m, 5H), 3.76 – 3.70 (m, 8H), 3.64 (s, 324H), 2.96 (s, 2H).

3.4.2 Rheology and mechanical stiffness analysis

3.4.2.1 Young's modulus stiffness of PEG hydrogels

Rheological measurements (Figure 3.8) portrayed different ratios and combinations of 2-arm and 3-arm thiol and alkyne precursors altered the storage and loss moduli. To determine stiffness of hydrogels when PEG precursors were combined, a stiffness value known as Young's modulus was calculated using outputs from rheology. The young's modulus of PEG precursor combinations ranged from 7-58kPa (Table 3.1). A combination of 3-arm alkyne, 2-arm thiol and 3-arm thiol precursors in the ratio 1: 0.7 : 0.46 created hydrogels of approximately 20kPa, which represented the stiffness of a healthy myocardium. This combination of

precursors produced a transparent hydrogel (Figure 3.9) that was able to be created in a cell culture well format.

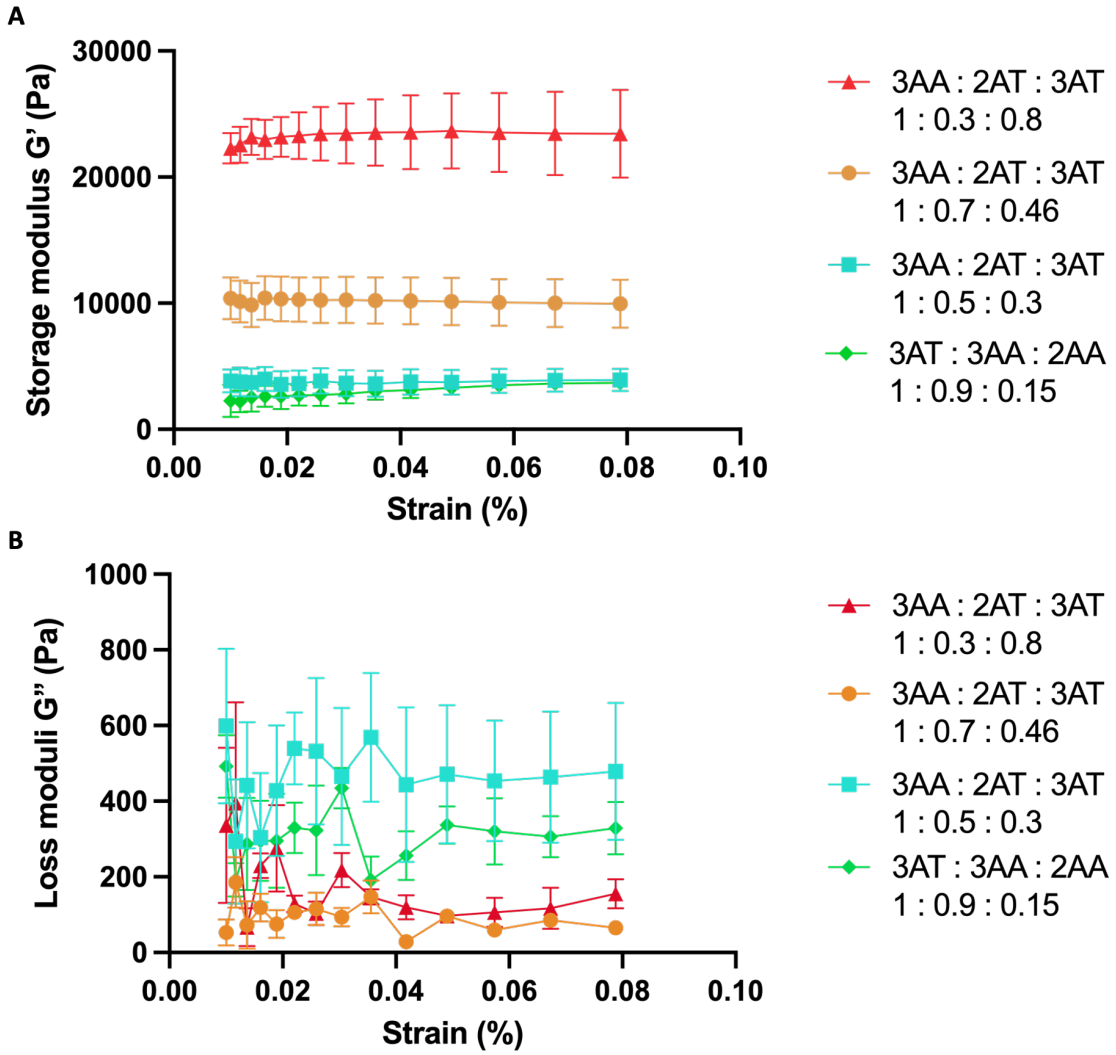

Figure 3.8: **Effect of varying ratios and combinations of PEG precursors on storage and loss moduli**
(A) Storage modulus curves obtained from rheometer, with 0.01-1% strain applied to the hydrogel (B) Loss modulus curves obtained from rheometer, with 0.01-1% strain applied to the hydrogel. Values plotted as mean ± SEM. 3AA- 3-arm alkyne, 2AT-2-arm thiol, 3AT- 3-arm thiol.

Table 3.1: **Young's modulus stiffnesses of PEG hydrogels with varying PEG precursor ratios**

PEG precursor combinations	Ratio of precursors	Young's modulus (kPa)
3AT + 3AA + 2AA	1 : 0.8 : 0.3	7.4
3AT + 3AA + 2AA	1 : 0.9 : 0.15	9.3
3AA + 2AT + 3AT	1 : 0.5 : 0.3	11.4
3AA + 3AT + 2AT	1 : 0.8 : 0.3	57.4
3AA + 2AT + 3AT	1 : 0.7 : 0.46	20.3

Combinations of precursors with corresponding ratios that were used. Young's modulus values of stiffness calculated using formulas using storage and loss moduli measurements from rheometry. 3AA-3-arm alkyne, 2AA-2-arm alkyne, 2AT- 2-arm thiol, 3AT-3-arm thiol.

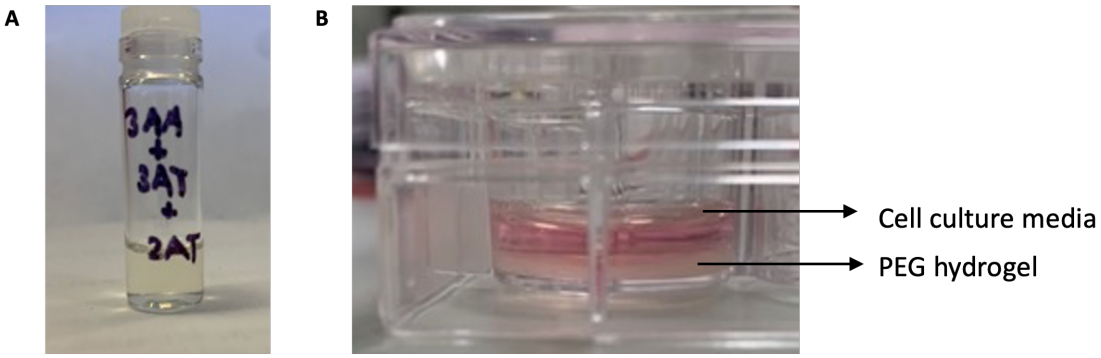

Figure 3.9: **Physical appearance of PEG hydrogels created with precursors in PBS** (A) Transparent hydrogel formed of combination of 3-arm alkyne precursor, 3-arm thiol precursor and 2-arm thiol precursor (B) Transparent PEG hydrogel formed in tissue culture plastic plate with cell culture medium

3.4.2.2 PEG Hydrogel stability

To determine whether mechanical stability of PEG hydrogels remained stable over time, 3-arm alkyne, 2-arm thiol and 3-arm thiol gels were tested using rheometry over a time course of 29 days in PBS in a 37℃ incubator. PEG hydrogels remained in the range of ideal stiffness (20-30kPa) throughout (Figure 3.10), suggesting PEG hydrogels were compatible with experiments involving extended cell

culture (25-30 days).

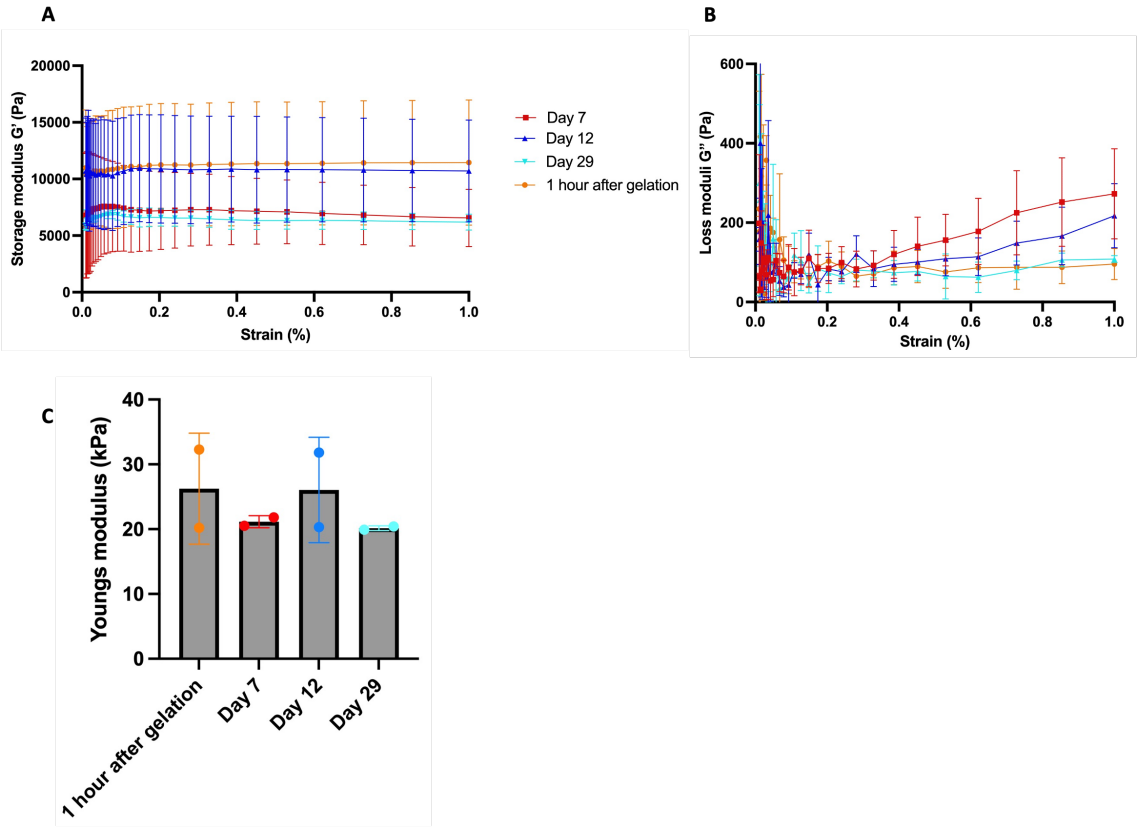

Figure 3.10: **Rheometer characterisation of PEG hydrogel stability over 29 days in PBS**
PEG hydrogel composed of 3-arm alkyne, 2-arm thiol and 3-arm thiol at ratios 1: 0.7 : 0.46. (A) Storage modulus curves obtained from rheometer, with 0.01-1% strain applied to the hydrogel. (B) Loss modulus curves obtained from rheometer, 0.01-1% strain applied to the hydrogel (C) Stiffness of hydrogels over time using Young's modulus values, calculated using storage and loss modulus measurements. 3AA-3-arm alkyne, 2AT- 2-arm thiol, 3AT- 3-arm thiol. n=2, values plotted as mean $\pm$ SD. Due to low n numbers, statistical analysis was not conducted.

3.4.3 iPSC-CM viability on PEG hydrogels

iPSC-CMs when plated onto Geltrex coated hydrogels consisting of 3AA, 2AT, 3AT portrayed some attachment, with cells attaching to the outer edges of the gel, although mostly portraying a rounded dead morphology in the centre of the gel (Figure 3.11). The majority of iPSC-CMs did not attach to the hydrogel. To further explore whether the ratio of thiol to alkyne precursors specifically altered cell

viability, a series of ratios were tested for cell attachment (Figure 3.12). The images portrayed no significant difference in cell attachment, with all combinations ultimately resulting in cell death.

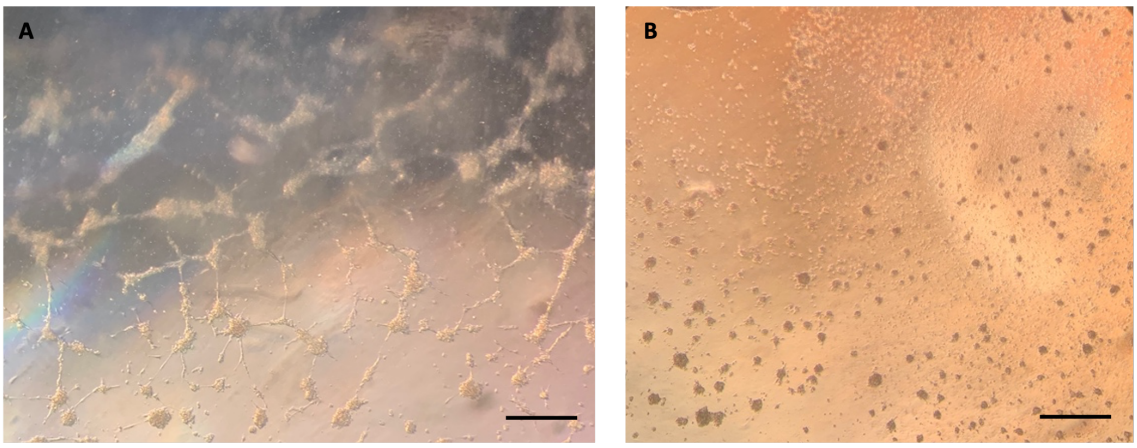

Figure 3.11: **Day 30 iPSC-CMs cultured on 3AA, 2AT and 3AT PEG hydrogels** PEG hydrogel composed of 3-arm alkyne, 2-arm thiol and 3-arm thiol. Day 30 iPSC-CMs split onto vitronectin coated PEG hydrogel. (A) iPSC-CMs on edge of well at 10X magnification (B) iPSC-CMs in middle of well at 4X magnification. Representative images of bright field view on a light microscope. Scale bar = 1 mm

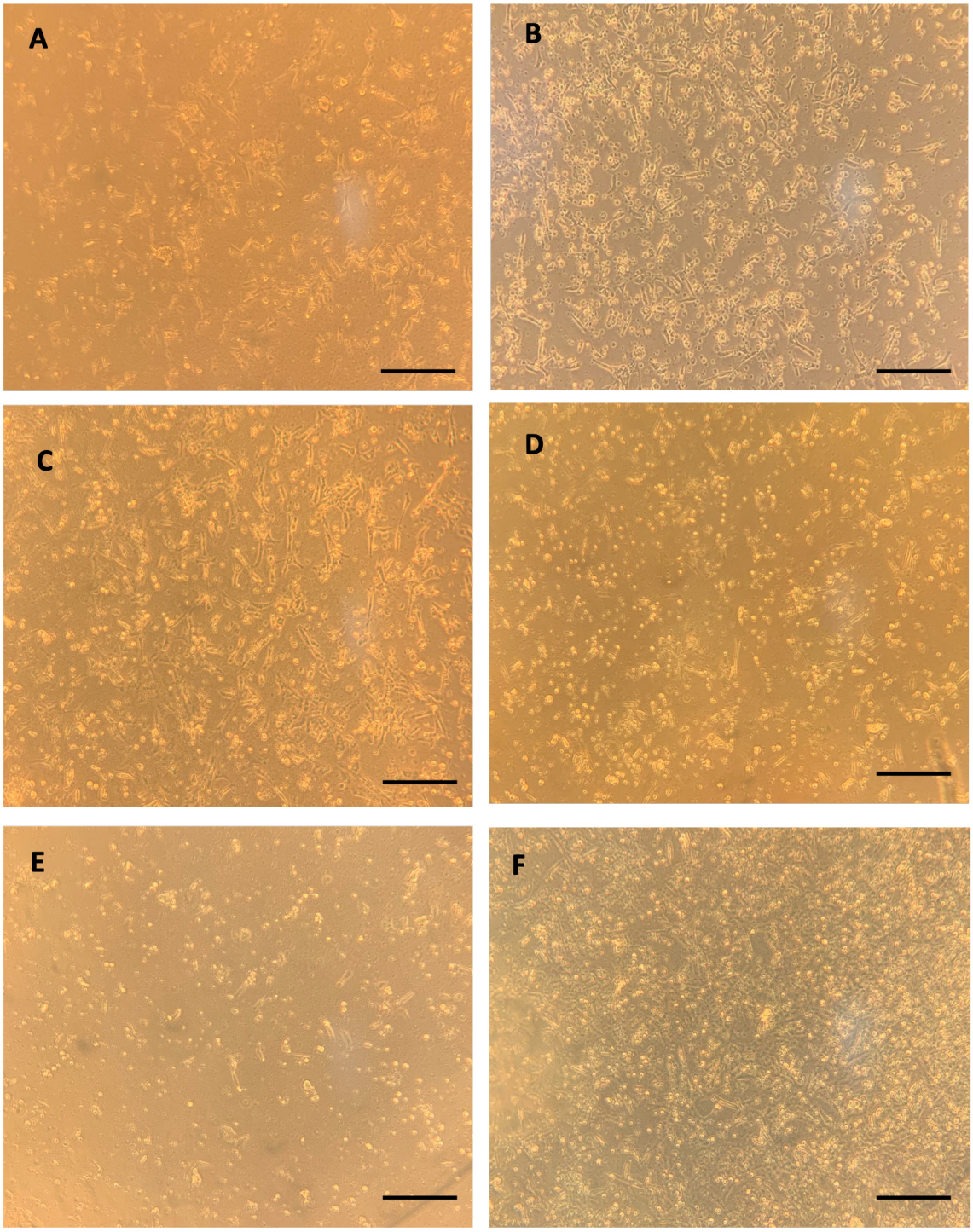

Figure 3.12: **Day 15 iPSC-CMs plated onto 3AA and 3AT hydrogels of varying alkyne to thiol groups and vice versa, coated with Geltrex**
(A) 0.8 (Alkyne) : 0.1 (Thiol) (B) 0.9 (Alkyne) : 1 (Thiol) (C) 0.9 (Thiol) : 1 (Alkyne) (D) 0.8 (Thiol) : 1 (Alkyne) (E) 1.05 (Thiol) : 1 (Alkyne) (F) 1.05 (Alkyne) : 1 (Thiol). Images representative of wells at 4X magnification on light microscope. Scale bar = 1 mm

3.4.4 Mechanical characterisation of PDMS hydrogels

PDMS hydrogels were synthesised using protocols described in the methods, and stiffness of PDMS hydrogels were assessed using rheology. Storage and loss modulus measurements were obtained using the rheometer (Figure 3.13 A and B) on hydrogels prepared to represent healthy and fibrotic stiffnesses, 20kPa and 130kPa respectively. The Young's modulus of PDMS hydrogels calculated using the storage and loss moduli (Figure 3.13C) portrayed 20kPa gels with stiffnesses of 25.88 $\pm$ 5.2 kPa and 130kPa gels of 115 $\pm$ 14.3 kPa, thus portraying PDMS as an ideal biomaterial to achieve the desired stiffnesses of both healthy and aged ECM.

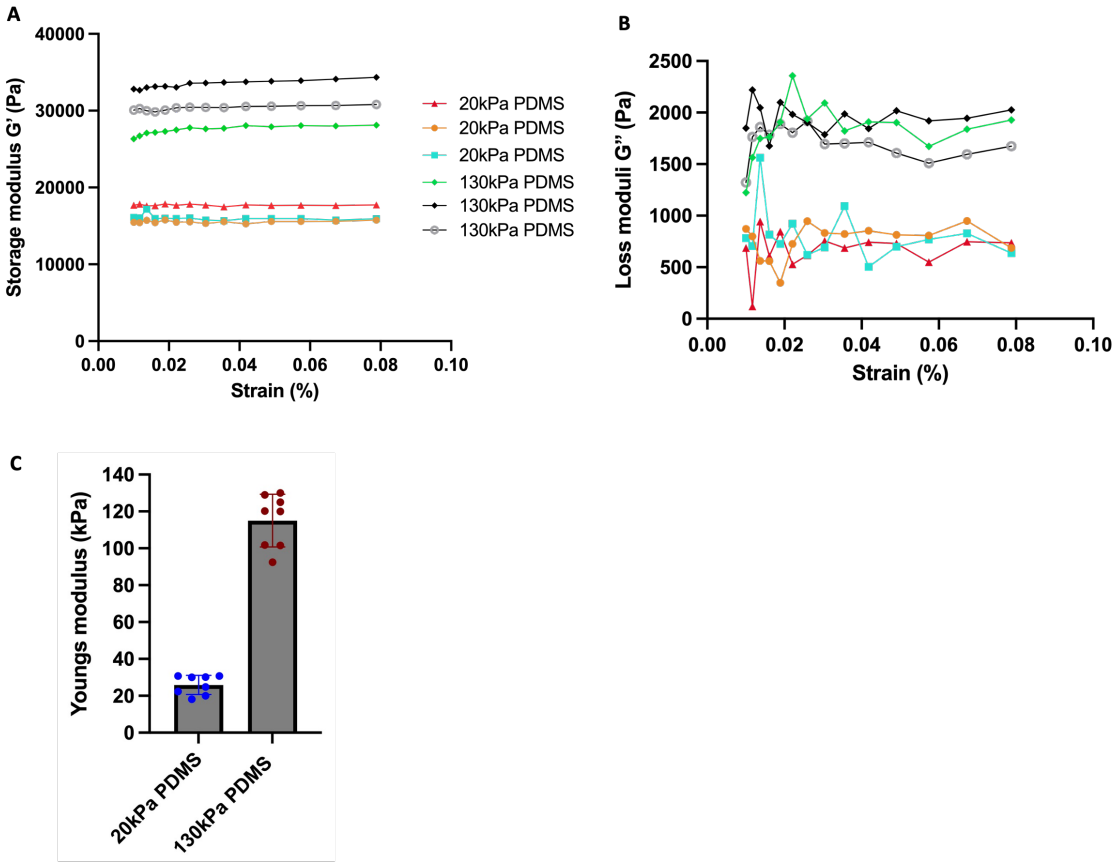

Figure 3.13: **Rheology measurements of PDMS hydrogels**
(A) Storage moduli of 20kPa and 130kPa PDMS hydrogels (B) Loss moduli of 20kPa and 130kPa PDMS hydrogels. (C) Young's modulus stiffness of PDMS hydrogels calculated from storage and loss moduli. Data displayed as mean ± SD, n=3 batches of PDMS hydrogels. Hydrogels of each stiffness were measured in duplicate.

3.4.5 Attachment of iPSC-CMs to PDMS substrates

iPSC-CM attachment on Geltrex coated PDMS hydrogels was successful, with iPSC-CMs forming spontaneously contracting monolayers (Figure 3.14). No cell toxicity or cell death was observed, indicating biocompatibility of PDMS hydrogels with iPSC-CMs.

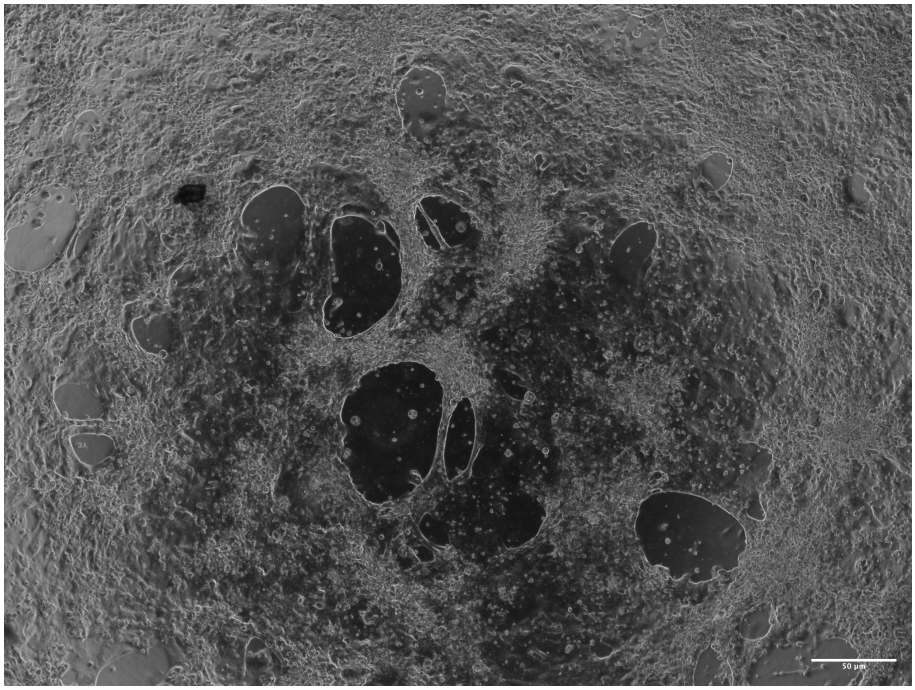

Figure 3.14: **Monolayer of iPSC-CMs attached to PDMS hydrogel**
Bright field microscopy image of iPSC-CM monolayer taken at 10X magnification, displaying attachment to Geltrex coated PDMS hydrogel with stiffness of 20kPa. Scale bar =50 μm

3.5 Discussion

This chapter aimed to develop biomaterial hydrogels of physiological stiffnesses, 20kPa and 130kPa, representative of healthy and fibrotic cardiac ECM that were compatible with iPSC-CM culture. PEG hydrogel synthesis and mechanical characterisation was conducted using rheology. A lack of iPSC-CM attachment and cell death occurred due to toxicity of PEG hydrogels. PDMS hydrogels were therefore synthesised and mechanical characterisation conducted. PDMS hydrogels were able to mimic healthy and fibrotic stiffnesses and were compatible with iPSC-CM culture, thus were used as models of ECM stiffness for subsequent experiments.

3.5.1 PEG hydrogels can mimic physiological stiffnesses of the ECM

Rheological measurements of PEG hydrogels portrayed combinations of 3AA, 3AT and 2AT created hydrogel stiffnesses of approximately 20-25kPa, which are representative of healthy myocardial stiffness [205], [170]. Previous literature has also shown this combination of precursors produces similar stiffnesses [203], further highlighting successful functionalisation of PEG precursors. The ability of PEG to recapitulate healthy myocardial stiffnesses was also consistent with literature, with studies showing PEG hydrogels of soft stiffnesses ranging from 1-15kPa in 2D and 3D contexts [176]. Altering the ratio of alkyne and thiol PEG precursors modified the architecture of the hydrogel network, by influencing the amount of end group reactivity and thus crosslinking density; with combinations of multi-arm precursors, denser network structures were formed [203].

3.5.2 PEG hydrogel incompatibility with iPSC-CM culture

Successful mechanical characterisation of the stiffness of PEG hydrogels led to investigating the compatibility with iPSC-CMs. iPSC-CM differentiation protocols required culture for a duration of 25-30 days, thus highlighting the need for long term cell culture compatibility.

3.5.2.1 Stability of PEG hydrogels over time

As PEG hydrogels were intended for use in cell culture, investigation into the stability of hydrogels in cell media and solutions were essential. PEG hydrogels in PBS portrayed a slight decline in Young's modulus stiffness between days

12-29, indicating potential dilution of network structures and increased spatial heterogeneity [206], leading to softer gels and decreased elastic stiffness. As hydrogels are 3D networks that absorb and retain water, swelling of hydrogels can often occur [161]. This swelling of hydrogels compromises the mechanical strength of the gel and impairs stability, thus leading to changes in stiffness. Despite the slight fluctuation in stiffness of PEG hydrogels in solution, the gel remained within the range of representative healthy ECM stiffness (20kPa-30kPa) and therefore showed potential for cell culture. The stability of PEG hydrogels was further portrayed by stable storage moduli values obtained during rheology amplitude sweeps, indicating the high elastic nature of the hydrogel, suggesting greater crosslinking density.

3.5.2.2 Varying hydrogel coatings did not alter attachment of iPSC-CMs onto PEG hydrogels

Despite hydrogels mimicking physiological stiffnesses, there were several issues with cell attachment to the surface of PEG hydrogels. Typically, PEG is a bioinert material with low protein adsorption and cell adhesion [207]. iPSC-CMs failed to attach to Geltrex coated PEG hydrogels. The lack of iPSC-CM attachment to Geltrex was primarily due to the visible separation and movement of the Geltrex layer from the hydrogel, leading to delamination of the layer when washed with PBS before cell plating.

As a result, other coatings commonly used to facilitate iPSC-CM attachment were explored. Poly-D-lysine has been previously used to facilitate attachment for

neuronal cultures due to its positive charge [208], therefore attracting the negative charge of cells. However, the lack of iPSC-CM attachment to poly-D-lysine coated PEG hydrogels further implied issues with cell attachment onto the surface of hydrogels.

PEG hydrogels often require functionalisation to enhance cell adhesion, through addition of bioactive peptides and functional groups, such as arginine-glycine-aspartic acid (RGD) peptides [198], [209]. Fibronectin and vitronectin are cell culture coatings that contain the integrin binding RGD domain, therefore are to commonly used to enhance cell attachment and adhesion [210]. The mechanism by which facilitated attachment to the ECM occurs involves recognition of the RGD sequence in ligands by integrins [211]. iPSC-CMs portrayed some attachment to vitronectin coated PEG hydrogels, which may be due to presence of the RGD domain.

3.5.3 Toxicity of PEG hydrogels

Despite successful initial attachment of iPSC-CMs on vitronectin coated hydrogels, after 1 day of plating, iPSC-CMs had died across all hydrogels, with cells displaying a rounded morphology. The successful attachment of iPSC-CMs indicated cytotoxicity of PEG hydrogels as a key issue, rather than issues with cell adhesion. This is contrary to literature, which has displayed compatibility of PEG hydrogels with CMs [212] [176].

Toxicity of hydrogels could be due to reactivity of excess free thiol groups, due to the lack of full end group conversion when mixed with alkyne precursors.

Thiol groups are subject to deprotonation and can form thiolates, which impact the balance of thiol to thiolate, thus influencing the redox state of cells [213]. In addition, thiol groups can react with biomolecules, altering biological function and resulting in cellular damage [214]. In addition, pH testing of PEG hydrogels kept in PBS revealed hydrogels had pHs between 6.5-6.86, indicating acidity of the hydrogels. Despite attempts at removal of excess acids with basic Amberlyst A21 beads using acid-base extraction, the acidity of PEG hydrogels could not be resolved. The proposed acid toxicity of the hydrogels may have been due to the production of propiolic acid. Propiolic acid was initially used for Fischer esterification reactions of PEG alkynes- washes with sodium bicarbonate and brine may not have successfully removed all acid, leaving some acid present in the precursors, therefore causing toxicity. Methods to remove excess acids from hydrogels typically include washes with distilled water and sodium bicarbonate, to convert acids into their water soluble states for removal [215].

3.5.4 PDMS hydrogels for iPSC-CM culture

PDMS hydrogels were therefore used as an alternative hydrogel to mimic ECM stiffness. Literature had portrayed PDMS hydrogels composed of Sylgard 184 and Sylgard 527 could produce hydrogels with a range of stiffnesses, from 12kPa-2.5MPa [174], highlighting its capability to mimic the ECM and model different conditions.

3.5.4.1 PDMS hydrogels can mimic physiological stiffnesses of the ECM

Rheological characterisation of PDMS hydrogels confirmed stiffnesses of 20kPa and 130kPa, thus showing alterations in the ratio of Sylgard 527:184 was successful for mimicking ECM stiffnesses. No issues with hydrogel swelling or degradation were encountered due to the synthetic nature of PDMS, with hydrogels remaining stable for months at a time, which had been extensively characterised in literature [216]. The stability of PDMS gels due to lack of degradation and modification of PDMS surfaces was advantageous for long term culture of iPSC-CMs.

3.5.4.2 PDMS hydrogel compatibility with iPSC-CMs

PDMS hydrogels coated with Geltrex portrayed successful iPSC-CM attachment, with no issues in hydrogel toxicity or cell death. Geltrex coating of PDMS hydrogels were required to facilitate iPSC-CM attachment, as a limitation of PDMS as a biomaterial was the hydrophobicity of its surface [177]. Geltrex coatings were used across all PDMS and plastic surfaces for iPSC-CM attachment, thus remained consistent across all experiments. The compatibility of PDMS with iPSC-CMs was consistent with literature, as PDMS has been shown to be successfully used with iPSC-CM cultures in 2D and 3D contexts [217], [218], further supporting the use of PDMS as a useful hydrogel biomaterial.

3.5.5 Limitations

A key requirement of PDMS hydrogels was to withstand long term culture of iPSC-CMs. In some cases, spontaneous contractility of iPSC-CMs on PDMS

hydrogels caused friction between the surfaces, which sometimes led to peeling of iPSC-CMs from the gels. To overcome these issues, iPSC-CM experiments were conducted from days 25-30, as iPSC-CMs portrayed cardiac maturity from these timepoints as shown in Chapter 4. Only iPSC-CMs which maintained a full monolayer of attachment to PDMS substrates were used, thus preventing the use of cells of lower quality to reduce variability.

3.5.6 Conclusions

PEG hydrogels were not compatible with iPSC-CM culture, as acid toxicity of the hydrogels led to cell death. Alternatively, PDMS provided a biocompatible, low cost and nondegradable hydrogel, able to mimic a range of ECM stiffnesses and facilitated iPSC-CM attachment. Despite some initial issues with iPSC-CM contractility causing peeling from PDMS hydrogels, iPSC-CMs formed functional beating monolayers on PDMS stiffnesses and maintained culture on hydrogels, thus were used for experiments in the following chapters.

Chapter 4

Molecular and cellular characterisation of iPSC-CMs on physiological substrate stiffnesses

4.1 Introduction

In the previous chapter, PDMS hydrogels were exhibited as ideal biomaterials to mimic physiological healthy and fibrotic ECM stiffnesses. It is well known that the myocardium and ECM environment can impact the structure and function of CMs, as CMs can sense mechanical cues [219]. As a result, intracellular signalling cascades such as YAP/TAZ signalling can cause alterations in cell behaviour, such as proliferation, contractility and gene expression [220]. Cardiac remodelling occurring with ageing and disease can change the composition and rigidity of the ECM, and thus can impact CM structure and function in several aspects.

Ageing and cardiac disease have been correlated with changes in the ECM and thus contractility of CMs, which can lead to arrhythmia and heart failure [221]. As CMs are the contractile units of the heart, regulation of contraction is important, highlighting the significance of investigating how stiffness of the ECM may impact contractility of CMs. Furthermore, regulation of Ca^{2+} signalling plays a key

role in the contraction of CMs [222], thus stiffness may further influence function of CMs through alterations in Ca^{2+} handling dynamics.

Cardiac research is often limited due to the availability of non-failing human hearts, which has led to the use of animal models such as mice, allowing investigations into *in vivo* parameters. However, issues surrounding animal use such as ethics, physiological relevance and costs can limit applications in cardiac research [223]. iPSCs have emerged in the field and advanced cardiac research, with key advantages including the reduction in the use of *in vivo* animal models, the capabilities to continuously generate cells and ability to model disease phenotypes with genomic editing [224]. iPSC-CMs are widely used for cardiac research, as they recapitulate primary human CM structural, electrophysiological and mechanical properties [225].

However, a key limitation of iPSC-CMs is the immature nature of the cells, with little resemblance to adult CM phenotypes [149]. Several strategies have been employed to increase maturity of iPSC-CMs, such as 3D engineered heart tissues and co-culture approaches with other cardiac cell types such as fibroblasts [226], [227], [179]. Further techniques include tuning substrate properties to increase physiological relevance, such as micropatterning of substrates, ECM-derived substrates and soft biomaterial hydrogels, all of which can promote maturation of iPSC-CMs [228], [149]. Despite the limitations, the variety of methods to mature iPSC-CMs enables them to be a useful model for assessing cardiac diseases.

Utilising PDMS hydrogels to mimic physiological stiffnesses of the ECM allows

investigations into molecular changes in iPSC-CMs influenced by stiffness, providing a greater insight into the molecular mechanisms of how structure, contractility and function of CMs change. The use of plastics and glass as stiff substrates act as a control condition, as iPSC-CMs are typically cultured on these substrates, thus reflect stiffnesses of an extreme cardiac disease condition. A comparison between iPSC-CM cultures on softer PDMS substrates and stiff substrates therefore may enhance or reveal changes in structural and moleuclar phenotypes based on stiffnesses.

4.2 Hypothesis and Aims

Age-related alterations in myocardium stiffness can alter CM behaviour, with changes in structure and contractility. The main objective of this chapter was to assess the effects of age-related stiffness of the myocardium on iPSC-CMs. Healthy and fibrotic ECM stiffnesses were modelled using PDMS hydrogels, onto which iPSC-CMs were cultured, and investigations into iPSC-CM structure, contractility and gene expression were conducted. iPSC-CMs on softer substrates were hypothesised to display greater cardiac maturity, greater contractility and Ca^{2+} handling.

The hypothesis for this chapter was tested through the following aims:

1. Assess how physiological soft and stiff substrates can impact iPSC-CM sarcomeric structure

2. Investigate how substrate stiffness can impact function of iPSC-CMs, through assessing contractility and Ca^{2+} handling dynamics

3. Investigate how stiffness can alter iPSC-CM cardiac maturity and Ca^{2+} channels at a transcript level

4.3 Results

4.3.1 Expression of Structural Cardiac Markers between days 20-30 of iPSC-CM differentiation

The transcript expression of cardiac structural markers was assessed in iPSC-CMs over a time course, specifically at days 20, 25 and 30 of differentiation (Figure 4.1) to observe any changes in maturity. Myosin heavy chain 7 (*MYH7*) and myosin light chain 2 (*MYL2*) encode for ventricular isoforms of myosin markers, whereas myosin heavy chain 6 (*MYH6*) and myosin light chain 7 (*MYL7*) encode for atrial isoforms markers. Significantly increased expression of ventricular markers were measured from days 20-30, with an increase of expression at day 25. *MYH6* expression significantly decreased from days 20-30, whereas *MYL7* expression remained constant over time. *MYH7*:*MYH6* ratios, indicating cardiac maturity, significantly increased in expression from days 20-30 (Figure 4.1). Similarly, a significant increase in *MYL2*:*MYL7* ratio was found between days 20-30. Cardiac troponin T, *TNNT2*, known as a structural marker of sarcomeric contraction was expressed at all timepoints, with a small but significant increase of expression at day 25 compared to day 20. As no significant differences in cardiac marker expression were found between days 25-30, day 25 iPSC-CMs were selected as the timepoint for subsequent experiments.

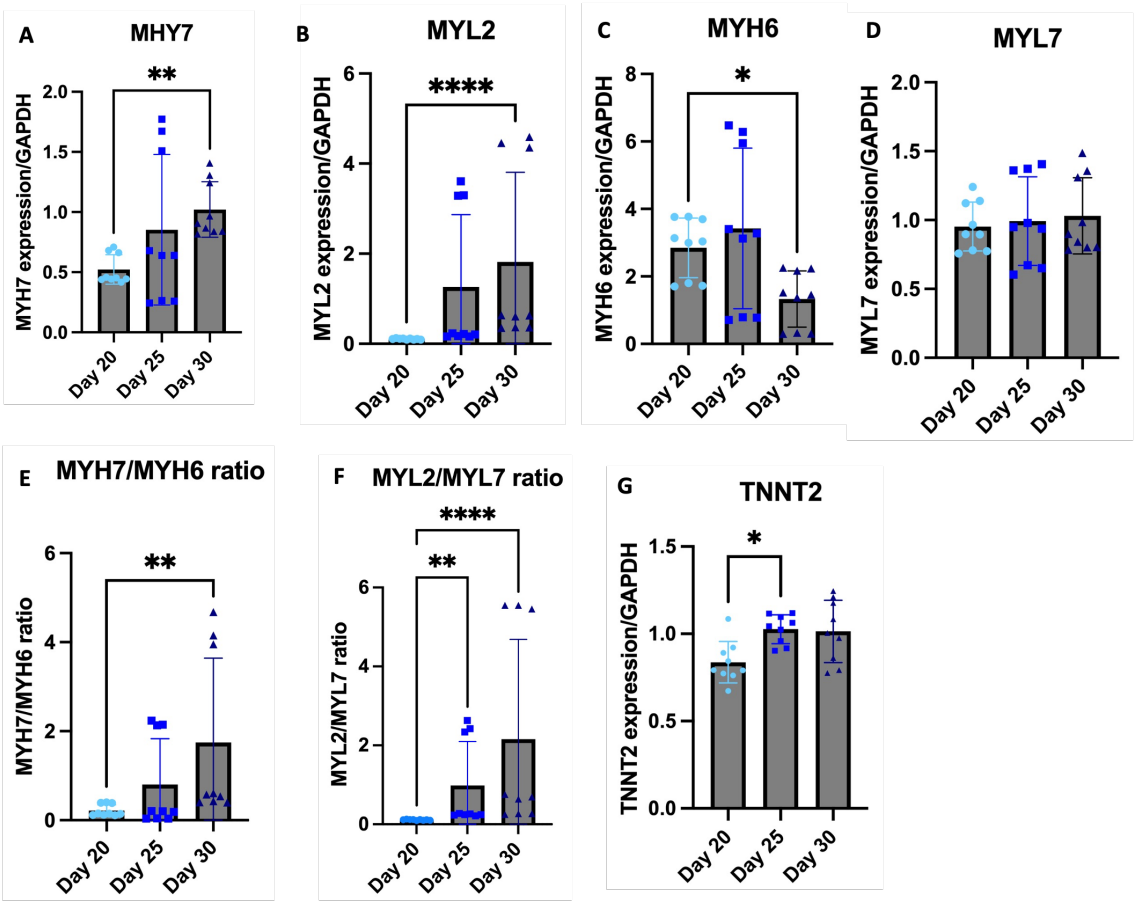

Figure 4.1: **Transcript expression of cardiac markers between days 20-30 of iPSC-CM differentiation**
Transcript expression of (A) MYH7 (B) MYL2 (C) MYH6 (D) MYL7 (E) MYH7/MYH6 ratio calculated by MYH7 divided by MYH6 values (F) MYL2/MYL7 ratio (G) TNNT2. Data normalised to GAPDH and made relative to day 30 conditions. Values are presented as mean $\pm$ SD. Each data point refers to 1 well of cells plated as 3 technical replicates per condition, across n=3 batches of iPSC-CM differentiations. Low sample numbers were conducted as this experiment was conducted as a preliminary study to confirm timepoints for use of iPSC-CMs. Statistical significance was assessed with a Kruskal-Wallis test as data was not normally distributed, with p values determined as <0.05 (*) < 0.01 (**), <0.0001 (****).

4.3.2 Expression of Cardiac Markers in day 25 iPSC-CMs on substrates

To investigate whether softer substrates induced maturation of iPSC-CMs, expression of cardiac maturation markers in iPSC-CMs were assessed on 20kPa PDMS, 130kPa PDMS and plastic. Although not significant, a trend towards increased expression of *MYH7*/*MYH6* ratios on 20kPa PDMS and 130kPa PDMS

compared to plastic surfaces were observed (Figure 4.2). *MYL2/MYL7* expression was significantly downregulated in iPSC-CMs on plastic compared to softer 20kPa PDMS. *TNNT2* was expressed in iPSC-CMs on all conditions, with significantly reduced expression in iPSC-CMs on 130kPa PDMS compared to plastic (Figure 4.2).

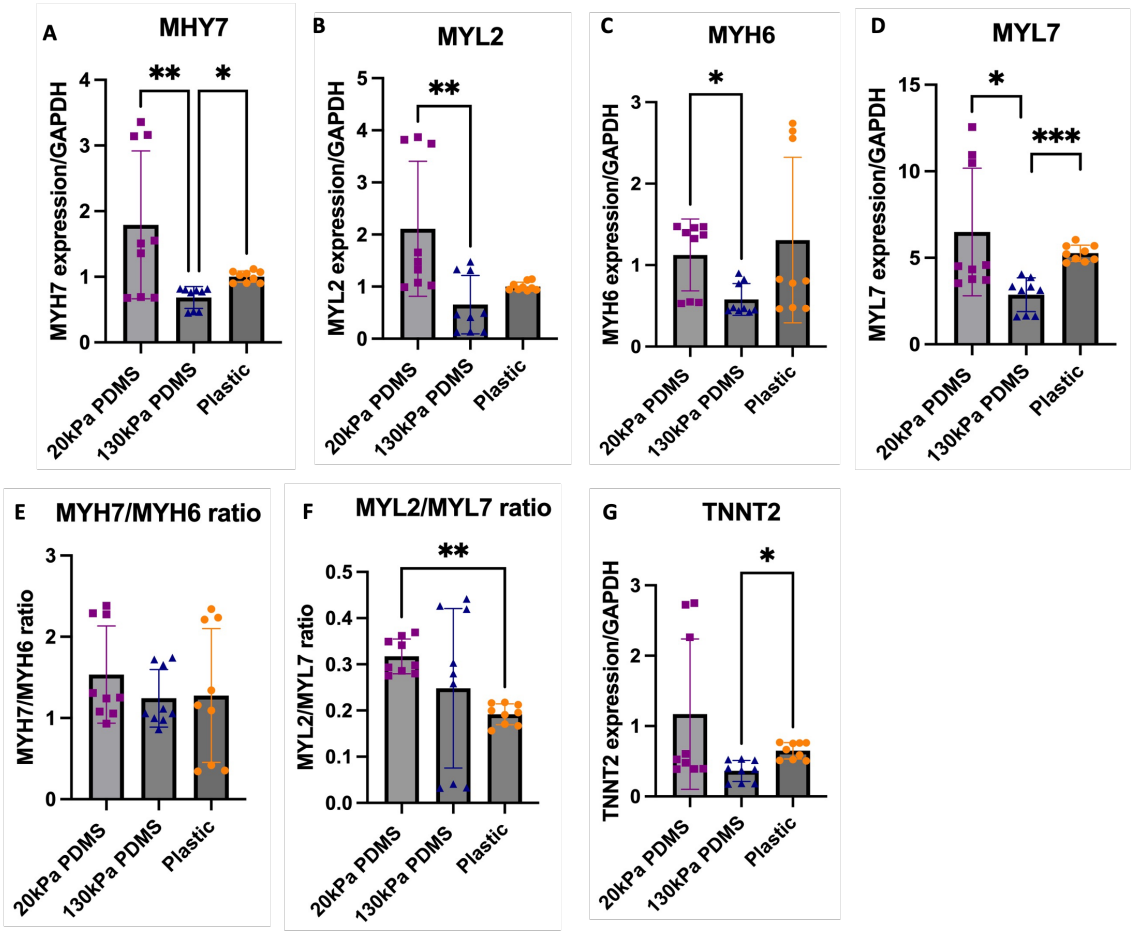

Figure 4.2: **qPCR gene expression profiles of cardiac maturity markers in day 25 iPSC-CMs on 20kPa PDMS, 130kPa PDMS and plastic stiffnesses**
(A) *MYH7* (B) *MYL2* (C)*MYH6* (D)*MYL7* (E) *MYH7/MYH6* ratio (F) *MYL2/MYL7* ratio (G) *TNNT2*. Data normalised to GAPDH and made relative to plastic. Values presented as mean $\pm$ SD. Each data point refers to 1 well of cells per condition, plated as 3 technical repeats, with a total of n=3 batches of iPSC-CM differentations. Statistical significance was assessed with a Kruskal-Wallis test as data was not normally distributed, with p values determined as <0.05 (*), < 0.01 (**), <0.001 (***).

4.3.3 Cardiac markers of iPSC-CMs on substrate stiffnesses at protein level

Confirmation of ventricular and cardiac marker expression of iPSC-CMs was further assessed using western blot (Figure 4.3). MLC-2v, encoding for *MYL2* ventricular isoform, typically expressed in ventricular myosin, displayed similar levels of expression across substrates with no significant differences. α-actinin (ACTN2), a sarcomeric protein was also expressed in iPSC-CMs across all conditions with no significant differences (Figure 4.3).

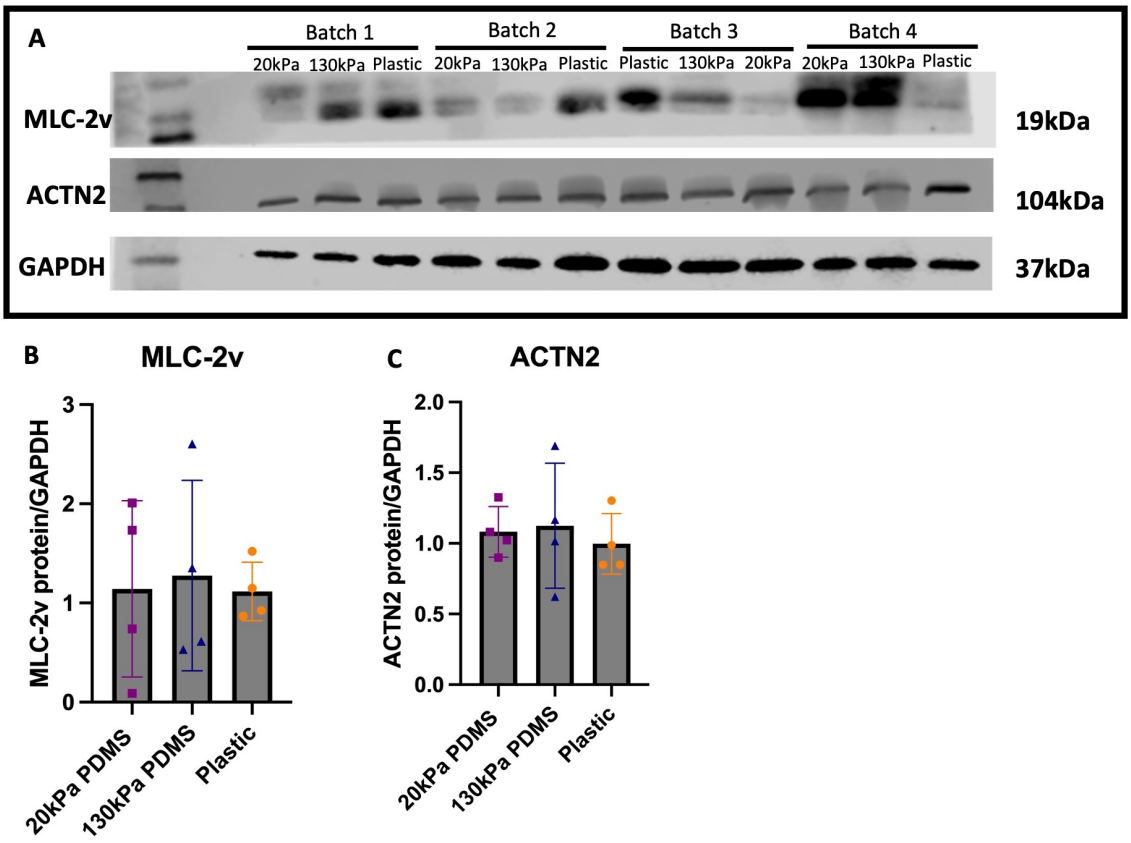

Figure 4.3: **Western blot protein expression and quantification of cardiac markers in day 25 iPSC-CMs on stiffnesses**
(A) Western blot of MLC-2v, ACTN2 and GAPDH protein expression from iPSC-CMs plated on 20kPa PDMS, 130kPa PDMS and plastic. (B) MLC-2v quantification of data normalised to GAPDH expression (C) α-actinin quantification of data normalised to GAPDH. Data presented as mean $\pm$ SD. Each data point refers to 1 well of cells per condition, across a total of n=4 batches of iPSC-CM differentations. Statistical significance was assessed with a Kruskal-Wallis test as data was not normally distributed.

4.3.4 Immunofluorescence of sarcomere organisation and alignment of iPSC-CMs on varying stiffnesses

To confirm whether substrate stiffness affected iPSC-CMs sarcomeric organisation, iPSC-CM structure was assessed using immunostaining and Z-line detection software. iPSC-CMs on softer substrates of 20kPa PDMS displayed significantly greater α-actinin arrangement and sarcomere alignment compared to 130kPa PDMS and glass, which showed disorganised sarcomere alignment (Figure 4.4 A&B). Average sarcomere lengths of 2.2μm were found in iPSC-CMs cultured on glass, which were significantly longer (7.7% increase) compared to shorter sarcomere lengths of 2.03μm on 130kPa PDMS (Figure 4.4 C). In addition, iPSC-CMs on 130kPa PDMS had significantly lower values for Z-line organisation compared to glass (Figure 4.4 E), a parameter referring to myofibrillar organisation.

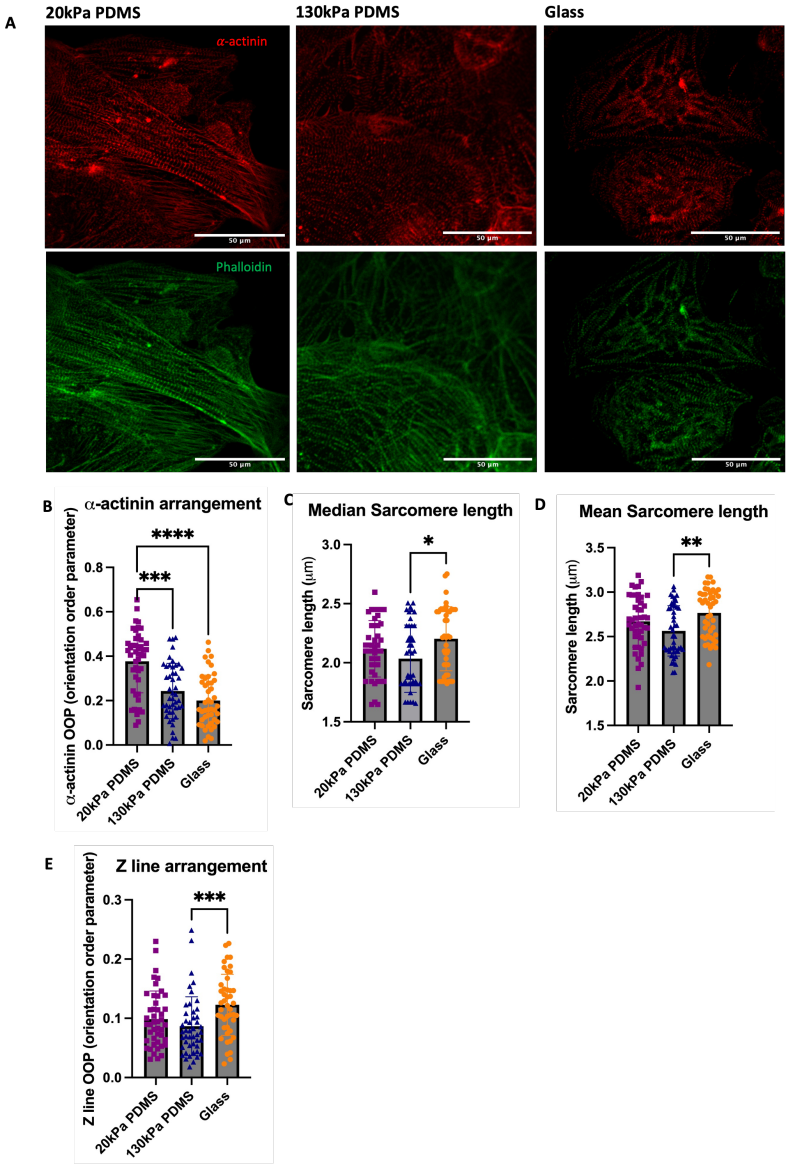

Figure 4.4: **Sarcomere organisation and alignment of iPSC-CMs on varying stiffnesses**
(A) Confocal microscopy images of α-actinin stain (red) and phalloidin stains (green) on day 25 iPSC-CMs cultured on 20kPa PDMS, 130kPa PDMS and glass coverslips. (B) α-actinin arrangement quantified from microscopy images, analysed using MatLAB z-line detection script. (C) Median sarcomere lengths quantified from microscopy images. (D) Mean sarcomere lengths calculated from images. (E) Z-line arrangement quantified from microscopy images. Data presented as mean $\pm$ SD. Each data point refers to 1 image taken from 1 well of cells across 5 technical replicates- 5 images were taken per well. 2 wells per condition per batch of iPSC-CM differentiations were taken. A total of n=4 batches of iPSC-CM differentiations were used to capture batch to batch variability. Scale bar equivalent to 50μm. Statistical significance was assessed with a Kruskal-Wallis test as data was not normally distributed, with p values determined as $<$0.05 (*), $<$0.01 (**),$<$0.001 (***), $<$0.0001(****).

4.3.5 Increased contractility of iPSC-CMs on softer substrates

To assess whether sarcomere organisation influenced the functional properties of cells, contractility of iPSC-CMs were assessed using MuscleMotion analysis. Videos of iPSC-CMs contracting on substrates were recorded using a GoPro camera. iPSC-CMs on 20kPa PDMS showed a trend towards greater contraction duration, contraction amplitude, peak to peak time and relaxation time compared to stiffer substrates (Figure 4.5), although not significant. Cells on plastic substrates demonstrated a trend towards decreased contractile parameters compared to iPSC-CMs cultured on softer substrates.

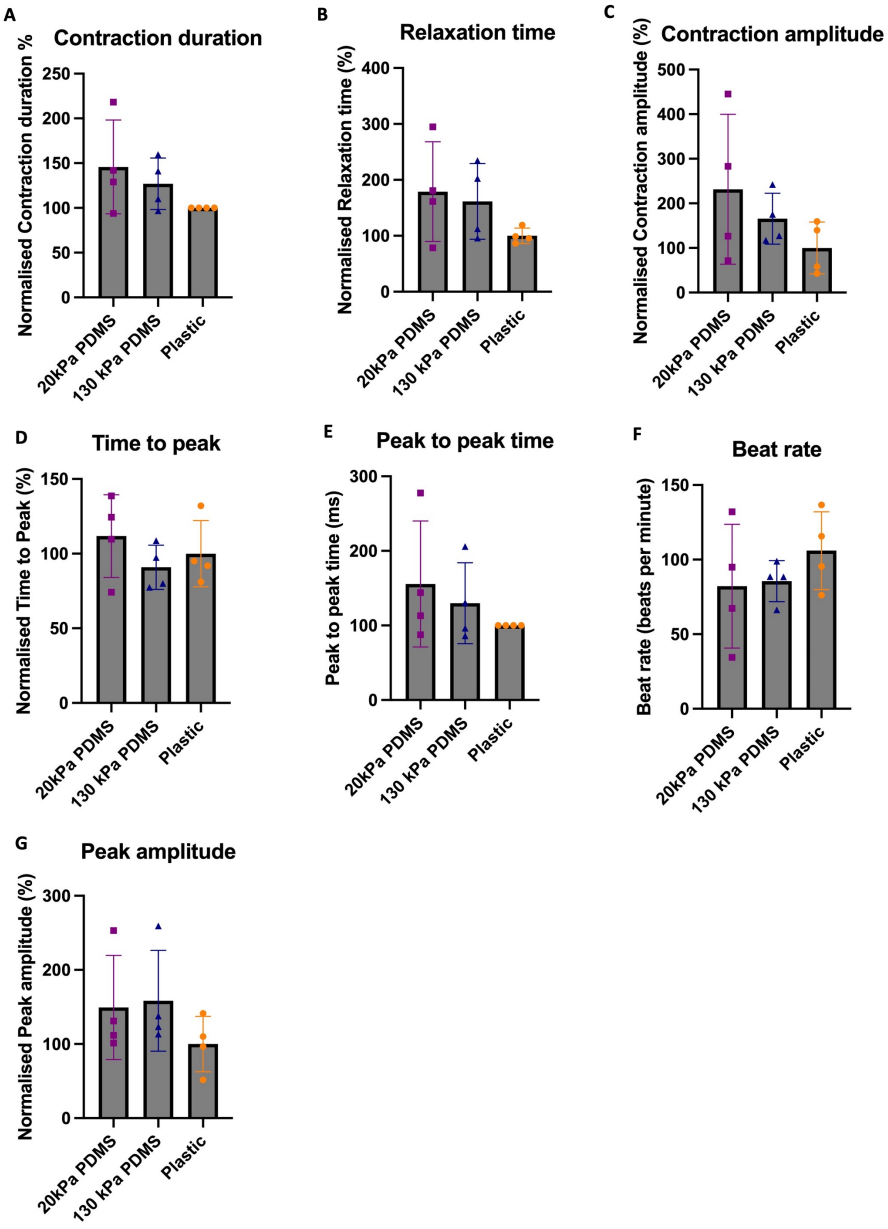

Figure 4.5: **Contractile parameters of iPSC-CMs on stiffnesses assessed by MuscleMotion software**
Contractility parameters analysed from GoPro videos of day 25 iPSC-CMs plated on 20kPa PDMS, 130kPa PDMS and plastic. (A) Contraction duration (B) Relaxation time (C) Contraction amplitude (D) Time to peak (E) Peak to peak time (F) Beat rate (G) Peak amplitude. Data presented as mean $\pm$ SD. 2-3 wells of cells per batch of iPSC-CMs were recorded, with 2-3 areas per well recorded and calculated as an average. This was conducted across a total of n=4 batches of iPSC-CM differentiations, with average values per batch shown with each data point. Data normalised to plastic conditions. Statistical significance was assessed with a Kruskal-Wallis test as data was not normally distributed. No significant differences were observed.

4.3.5.1 Ca^{2+} transients of iPSC-CMs on stiffnesses using Optical mapping

Ca^{2+} dynamics of cells were assessed using optical mapping; iPSC-CMs on substrates were incubated with a Fura-2 Ca^{2+} dye and analysed using ElectroMap software. iPSC-CMs on 20kPa PDMS showed significantly longer calcium transient durations (CTD's) at 30%, 50% and 80% reuptake compared to 130kPa PDMS (Figure 4.6). In addition, iPSC-CMs on 20kPa PDMS portrayed significantly greater Ca^{2+} amplitude than iPSC-CMs on 130kPa PDMS, suggesting greater Ca^{2+} cycling on soft substrates (Figure 4.7 A). iPSC-CMs on plastic substrates had significantly longer time to peak compared to cells on 130kPa PDMS (Figure 4.7 E) . No changes were identified in cycle length, beat rate and CTD30/80 ratio in iPSC-CMs across stiffness conditions.

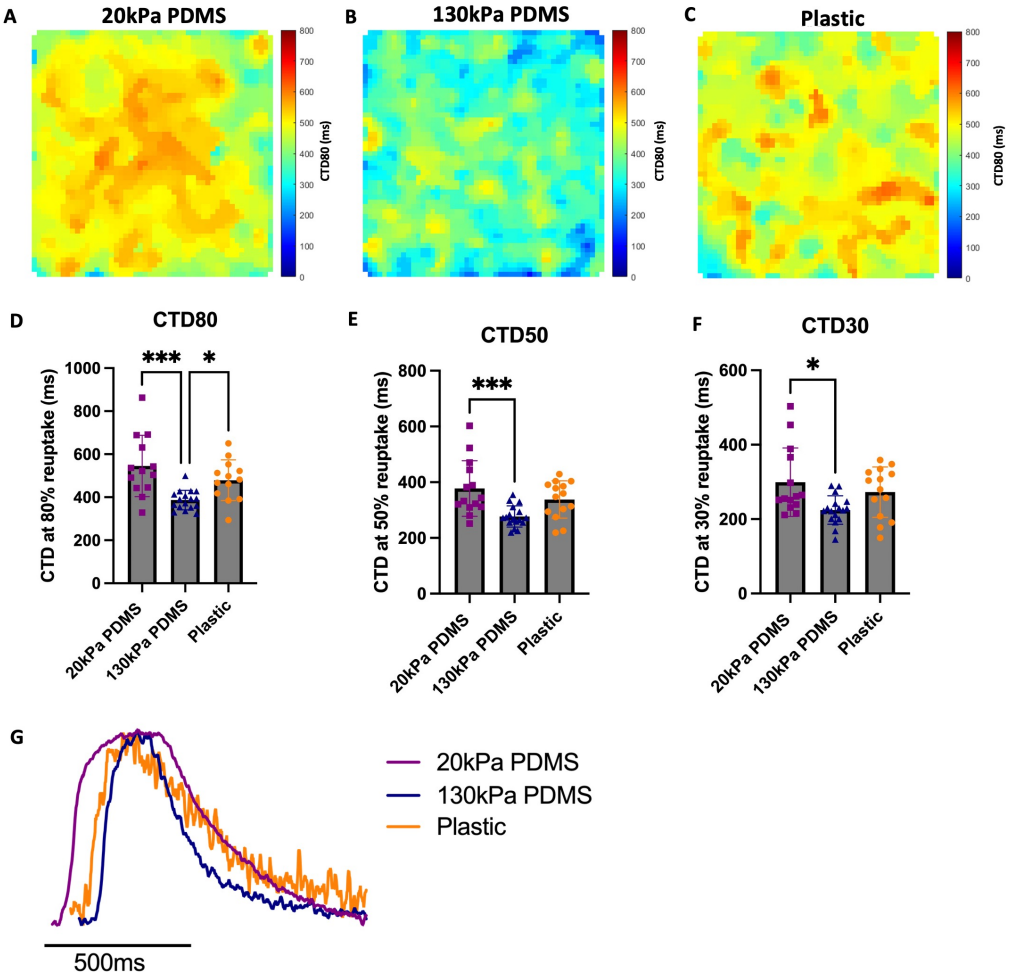

Figure 4.6: **Calcium transient durations of iPSC-CMs on 20kPa PDMS, 130kPa PDMS and plastic stiffnesses**
Ca^{2+} fluorescence heatmaps of day 25 iPSC-CMs on (A) 20kPa PDMS (B) 130kPa PDMS (C) Plastic (D) CTD's at 80% reuptake (E) 50% reuptake (F) 30% reuptake (G) Representative Ca^{2+} transient curves from iPSC-CMs on different stiffnesses. Data presented as mean $\pm$ SD. Each data point refers to data from 1 area of a dish recorded, with 1-3 different areas per dish of cells recorded per condition. 1-2 dishes of cells were used per condition to prevent variability between dishes. This was conducted across a total of n=6 batches of iPSC-CM differentiations to reduce any batch to batch variability. A Kruskal-Wallis test of significance was conducted on all parameters except CTD80 and CTD50, which were normally distributed and thus underwent statistical analysis using a one-way ANOVA test with Tukey's multiple comparisons post hoc test. Significance was determined as $p < 0.05$ (*), < 0.001 (***).

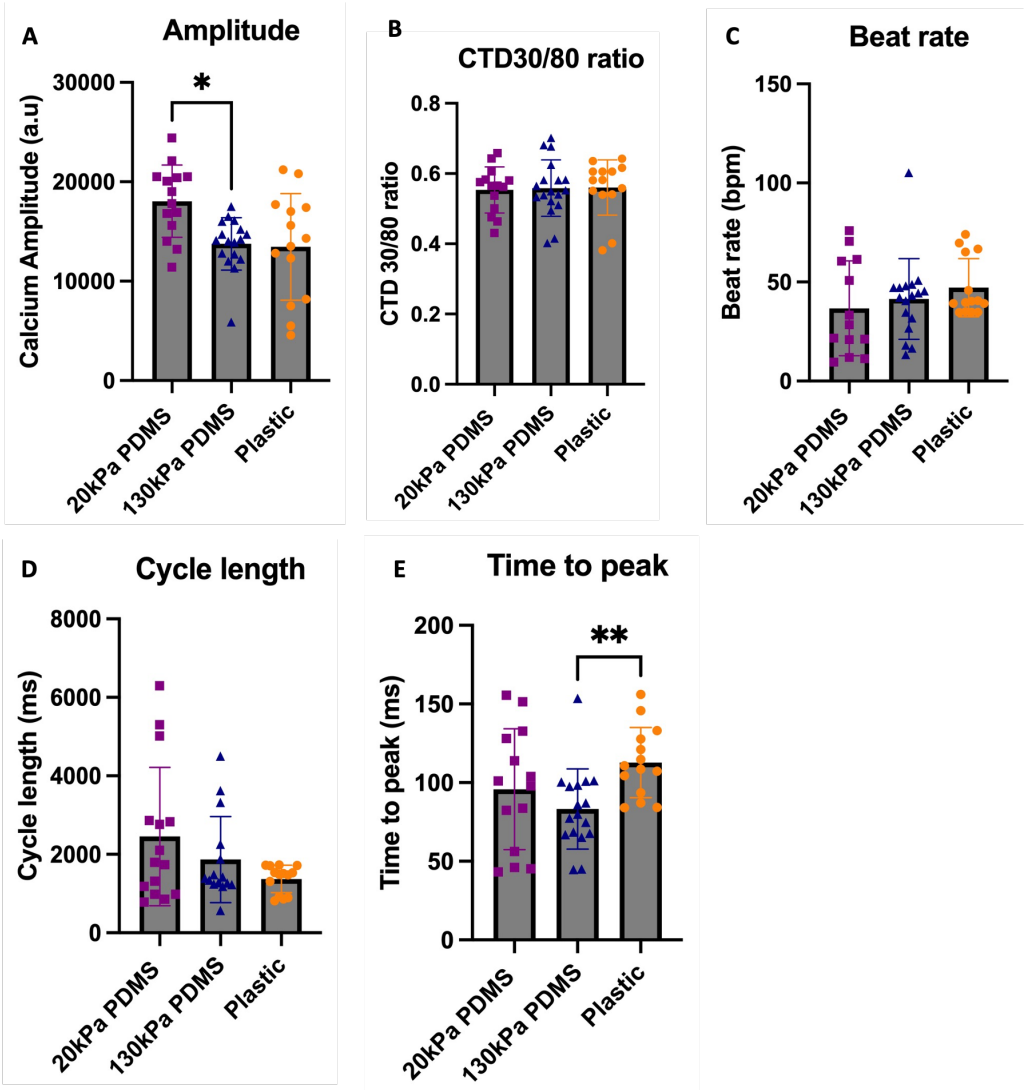

Figure 4.7: **Ca^{2+} optical mapping output parameters of iPSC-CMs on 20kPa PDMS, 130kPa PDMS and plastic stiffnesses**
Ca^{2+} optical mapping parameters on day 25 iPSC-CMs analysed using ElectroMap software. (A) Ca^{2+} amplitude (B) CTD30/80 ratio (C) Beat rate calculated using cycle lengths (D) Transient cycle length (E) Time taken to reach peak of Ca^{2+} transient. Data presented as mean $\pm$ SD. Each data point refers to data from 1 area of a dish recorded, with 1-3 different areas per dish of cells recorded per condition. 1-2 dishes of cells were used per condition to prevent variability between dishes. This was conducted across a total of n=6 batches of iPSC-CM differentiations to reduce any batch to batch variability. A Kruskal-Wallis test of significance was conducted on all parameters as data was not normally distributed. Significance was determined as p $<$0.05 (*), $<$0.01 (**).

4.3.6 Ion channel transcripts of iPSC-CMs on substrates

To further investigate changes in Ca^{2+}, the expression of ion channels linked to Ca^{2+} transport in iPSC-CMs was assessed using qPCR. Transcript levels of

ATP2A2, encoding for SERCA were not significantly different across conditions (Figure 4.8 A). A trend towards increased *RYR2* expression was identified on 20kPa PDMS compared to iPSC-CMs cultured on other substrates, although not significant (Figure 4.8 B). *PLN* expression, encoding for phospholamban, was significantly increased in iPSC-CMs on plastic compared to 130kPa PDMS (Figure 4.8C). Similarly, a trend towards increased *SLC8A1* expression on 20kPa PDMS compared to 130kPa PDMS and plastic was observed, although not significant (Figure 4.8 D). No significant differences were identified in transcript levels of *SLC8A2* and *SLC8A3* across substrates, encoding for sodium-calcium exchanger 2 and 3 respectively (Figure 4.8 E&F). L-type voltage gated calcium channels Cav1.2 (*CACNA1C*), Cav1.3 (*CACNA1D*) and 1.4 (*CACNA1F*) displayed a trend of slightly lower expression on plastic compared to 20kPa PDMS, although not significant (Figure 4.8 G-I).

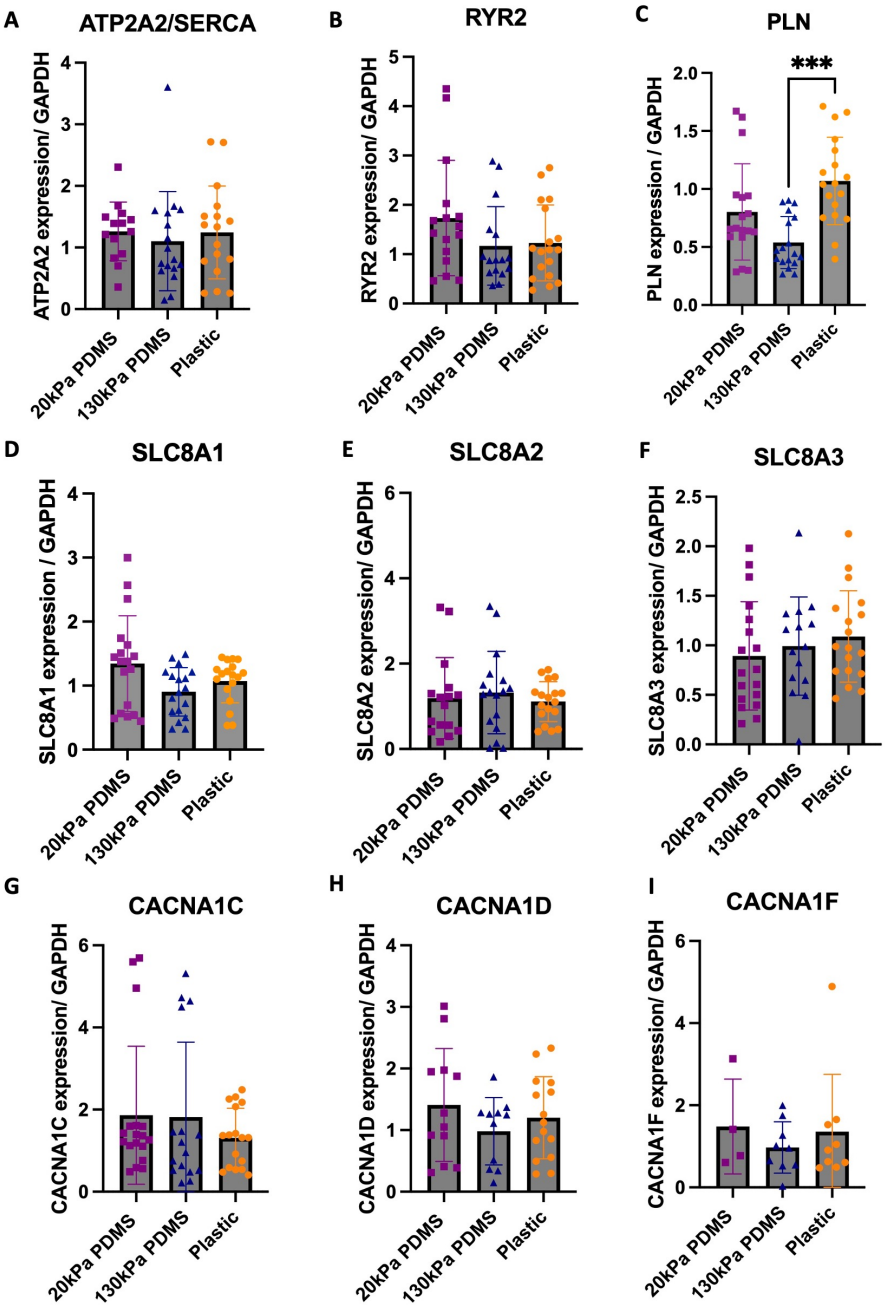

Figure 4.8: **Transcript expression of Ion channels involved in Ca^{2+} handling in iPSC-CMs on 20kPa PDMS, 130kPa PDMS and plastic**
Day 25 iPSC-CMs cultured on 20kPa PDMS, 130kPa PDMS and plastic stiffnesses. Ion channel gene expression of (A) *ATP2A2*/SERCA (B) *RYR2* (C) *PLN* (D) *SLC8A1* encoding for NCX1 (E) *SLC8A2* encoding for NCX2 (F) *SLC8A3* encoding for NCX3 (G) *CACNA1C*, encoding for Cav1.2 (H) *CACNA1D* encoding for Cav1.3 (I) *CACNA1F* encoding for Cav1.4. Data were normalised to GAPDH and plotted as mean $\pm$ SD. Each data point refers to 1 well of cells per condition plated as 3 technical replicates. This was conducted across a total of n=6 batches of iPSC-CM differentiations to capture batch to batch variability. Statistical significance was assessed with a Kruskal-Wallis test as data was not normally distributed. Significance was determined as $p < 0.001$ (***).

4.3.7 SERCA protein expression of iPSC-CMs on substrates

SERCA protein expression was further assessed using western blotting. Although no significant changes were identified, a trend towards decreased SERCA expression on plastic was found compared to both softer substrates of 20kPa and 130kPa PDMS (Figure 4.9).

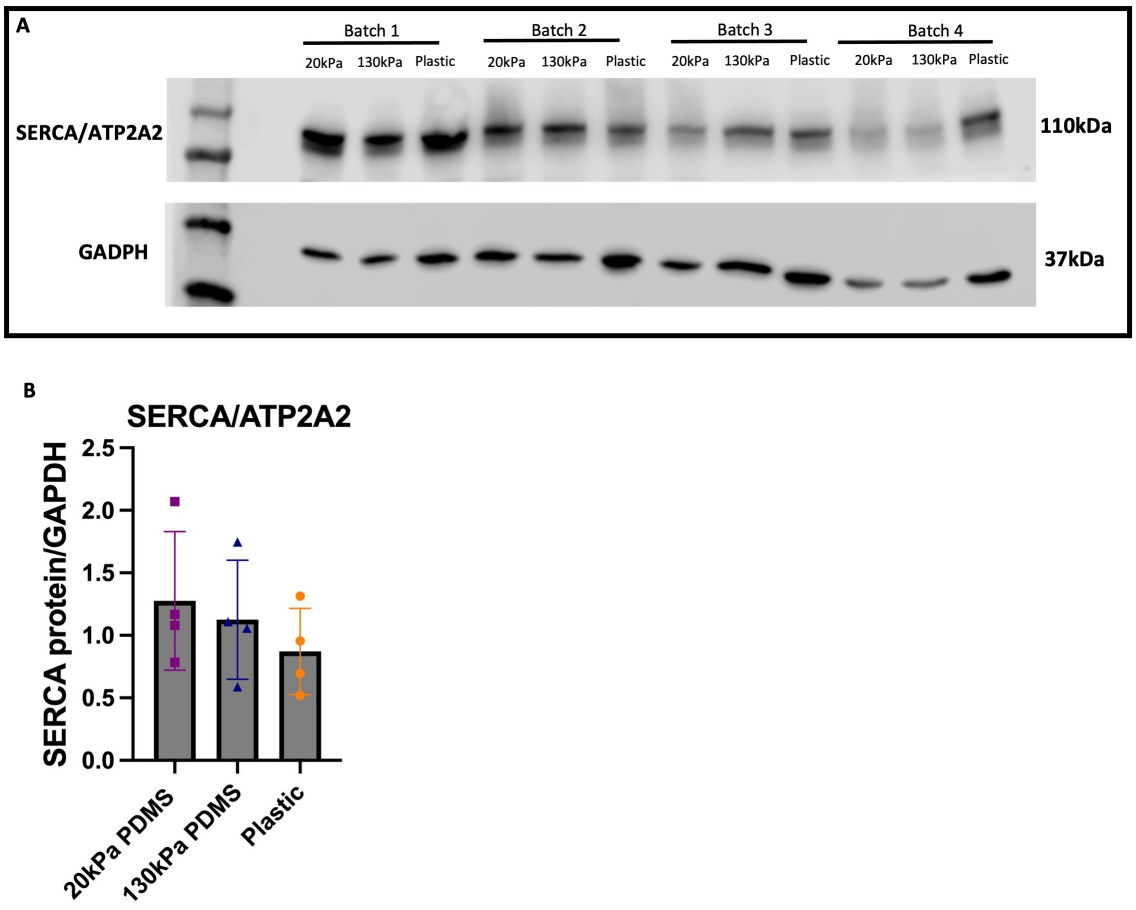

Figure 4.9: **Western blot protein expression and quantification of SERCA on stiffnesses**
(A) Western blot of SERCA and GAPDH protein expression from iPSC-CMs plated on 20kPa PDMS, 130kPa PDMS and plastic. (B) SERCA quantification of data normalised to GAPDH expression. Data presented as mean $\pm$ SD. Each data point refers to 1 well of cells per condition, across a total of n=4 batches of iPSC-CM differentiations. Statistical significance was assessed with a Kruskal-Wallis test as data was not normally distributed. No significant differences were observed.

4.4 Discussion

This chapter aimed to investigate whether the stiffness of the ECM altered sarcomeric structure and maturity of iPSC-CMs. Replicating physiological conditions of stiffness using PDMS rather than using cell culture plastics, which do not mimic healthy heart stiffnesses, may uncover disease phenotypes of iPSC-CMs, thus may not act as representative cells. iPSC-CMs on softer physiological substrates exhibited greater expression of cardiac maturity markers compared to stiffer substrates. Increased CTD's and Ca^{2+} amplitude of iPSC-CMs cultured on softer 20kPa substrates further indicates ECM stiffnesses can impact functional maturity. The alterations in maturity and structure of iPSC-CMs may consequently impact contractility of cells.

4.4.1 Transcript expression of cardiac maturity markers

To determine whether generated iPSC-CMs had undergone successful differentiation into ventricular CMs, transcript expression of cardiac maturity markers were investigated over time. The time point investigation also highlighted appropriate time points of cardiac maturity at which to use iPSC-CMs.

4.4.1.1 Cardiac transcript expression between days 20-30 of differentiation

Myofibrillar maturation in ventricular CMs is characterised by isoform switching of *MYH6* to *MYH7*, and *MYL7* to *MYL2*, reflecting the changes from foetal to adult human iPSC-CM phenotypes [229], [230]. The ventricular specificity of iPSC-CMs was therefore demonstrated by an increase in *MYH7* and *MYL2* transcript

expression between days 20-30, indicating successful differentiation. This further corresponded to the decrease in the atrial marker, *MYH6* between these time-points. The ratio of *MYH7/MYH6* and *MYL2/MYL7* acted as indicators of CM maturity, highlighting isoform switching. The significant upregulation of both ratios further highlighted an increase in iPSC-CM maturity and transition to adult CM phenotype between days 20-30 of differentiation. Consistent expression of cardiac troponin T confirmed the cardiac nature of the cells. As increased expression of cardiac maturity markers in iPSC-CMs occurred after day 20, iPSC-CMs from day 25-day 30 were primarily used for subsequent experiments.

4.4.1.2 iPSC-CMs exhibit cardiac maturity on PDMS stiffnesses

The cardiac maturity of iPSC-CMs on PDMS hydrogels of varying stiffnesses, representing healthy, fibrotic, and plastic/glass conditions was investigated at multiple levels. iPSC-CMs on softer 20kPa PDMS gels, representative of a healthy ECM displayed greater cardiac maturity, with increased transcript expression of *MYH7/MYH6* ratios, as well as *MYL2/MYL7* ratios compared to stiffer plastic conditions, confirming isoform switching to adult CM phenotypes [230]. Furthermore, increased *MYH7* and *MYL2* expression in iPSC-CMs on 20kPa PDMS compared to stiffer substrates further reinforces enhanced maturity and isoform switching on softer physiological substrates. This finding is consistent with literature showing physiological PDMS stiffnesses can induce maturation of iPSC-CM [231]. Additionally, cardiac marker ACTN2 and ventricular marker MLC-2v were expressed at protein level in iPSC-CMs on all substrates, confirming the cardiac model used

displayed adult ventricular CM markers [232].

4.4.1.3 Sarcomere organisation of iPSC-CMs differs with stiffness

iPSC-CM structure was significantly altered with substrate stiffness, with softer substrates inducing greater structural organisation and alignment of α-actinin in the sarcomeres. It is widely known that structural organisation of sarcomeres acts as a driver of cardiac maturation, with organised sarcomeres in CMs displaying stronger, coordinated contractions [229] [233]. The clear disorganisation and lack of α-actinin arrangement in iPSC-CMs on stiffer substrates corresponds with the lack of maturity observed at transcript level, further supporting the use of softer substrates as a maturation strategy for iPSC-CMs. This is consistent with other studies which have shown substrate stiffness can affect the structural enhancement of iPSC-CMs [234] [235]. The combined benefit of softer substrates for physiological relevance as well as iPSC-CM maturation is therefore of importance.

Sarcomere lengths also act as an indicator of maturity, with adult mature CMs typically having sarcomere lengths of approximately 2μm, whereas immature CMs had shorter sarcomeres of between 1.6μm and 1.8μm [236]. Consistent with the literature [235], iPSC-CMs on 20kPa PDMS substrates have longer sarcomere lengths of approximately 2.2μm compared to iPSC-CMs on 130kPa PDMS, suggesting stiffer substrates alter CM structural maturity. Interestingly, iPSC-CMs on glass in this instance exhibited sarcomere lengths typical of mature adult CMs; indicating the α-actinin organisation of these sarcomeres may

be disrupted on stiffnesses more so than the length of sarcomeres. The disorganisation of sarcomere and myofibrils on stiffer substrates has been previously demonstrated to decrease mechanical output of iPSC-CMs, thus is consistent with the trend of reduced force of contraction observed on stiff substrates [237].

4.4.2 Substrate stiffness does not significantly alter contractility of iPSC-CMs

As iPSC-CMs on softer substrates display increased maturity and sarcomere alignment, contractility of CMs was hypothesised to be affected as sarcomeres are the contractile units of CMs. Suprisingly, no significant differences in contractility were observed, although a trend towards increased contractility of iPSC-CMs were displayed on 20kPa PDMS compared to stiffer substrates. The lack of significant differences may be due to batch variability of iPSC-CMs, displayed by the large variation in the data.

Studies propose iPSC-CMs cultured on softer ECM substrates when compared to stiffer substrates such as glass, have increased contractility and greater synchronization [238]. Furthermore, studies have demonstrated stiffer substrates can decrease CTD's and amplitude [239], thus reducing contractility of CMs. The decreased contractility of iPSC-CMs on stiffer substrates has been linked to the immature nature of iPSC-CMs producing less efficient forces, as they lack the cellular machinery to adequately produce force [240]. ECM stiffness can also potentially impact contractility through changes in cytoskeletal organisation, as microtubules play a role in modulating CMs against external shear stress [241].

4.4.3 Stiffness of ECM alters Ca^{2+} handling dynamics of iPSC-CMs

Contractility of CMs is heavily regulated by intracellular Ca^{2+}, with alterations in Ca^{2+} signalling leading to cardiac dysfunction and arrhythmia [242]. In addition, CM development and maturity are strongly linked to Ca^{2+} handling dynamics [243]. Substrate stiffness and ECM environments can therefore largely impact functional properties of CMs via alterations in Ca^{2+}.

4.4.3.1 Softer substrates induce longer Ca^{2+} transient durations

Increased CTD's were identified at all points of reuptake on softer 20kPa substrates compared to 130kPa PDMS substrates, which is reflective of the increased maturity of iPSC-CMs. Increased maturity of iPSC-CMs on PDMS has been proposed to push cells towards mature excitation-contraction coupling, improved contractile mechanics, and electrophysiological maturation [225], [244]. Literature also supports the data, as longer action potentials and changes in Ca^{2+} kinetics were found in iPSC-CMs on physiological stiffnesses [245].

Potential mechanisms of increased maturation and consequent prolongation of Ca^{2+} transients may be linked to the improved organisation and alignment of RYR2 in iPSC-CMs on softer substrates; the distribution of RYR2 in iPSC-CMs on glass surfaces have been displayed as punctuate and immaturely distributed [246]. The trend towards increased *RYR2* transcript expression on 20kPa PDMS compared to stiffer substrates further indicates a link between alterations in RYR2 with ECM stiffness.

Decreased CTD's and Ca^{2+} amplitude on stiffer substrates may be due to the

increased stiffness of the surface inhibiting contraction of iPSC-CMs due to rigidity [247], leading to shorter contractions, whereas CMs on softer flexible surfaces were able to pull against the material, leading to higher transient durations and amplitude.

No changes in Ca^{2+} extrusion were identified in iPSC-CMs with stiffnesses, suggesting the changes identified in transients could be due to changes in entry of Ca^{2+} into the cell and SR. The lack of differences in beat rate in cells across substrates further supports the changes in Ca^{2+} dynamics were due to substrate stiffnesses rather than differences in contraction rate.

4.4.3.2 Substrate stiffnesses and Ca^{2+} channel expression of iPSC-CMs

The effect of substrate stiffness on SERCA2a expression was investigated, as SERCA2a relocalisation has been associated with changes in mechanotransduction [248]. Transcript expression of *ATP2A2* did not show any differences in iPSC-CMs across stiffnesses, whereas a trend of increased protein expression of SERCA was observed on 20kPa PDMS compared to stiffer substrates, although not significantly due to batch variability. The increase in SERCA expression may correlate with the enhanced Ca^{2+} amplitude and prolonged CTDs observed on softer substrates, as greater SERCA expression would enable greater Ca^{2+} uptake and removal from the cytosol into the SR, thus leading to more efficient excitation-contraction coupling [249].

PLN plays a key role in the regulation of Ca^{2+} handling, as it interacts with SERCA2a in its dephosphorylated state, inhibiting activity and reducing the rate of

Ca^{2+} uptake from the cytosol into the SR [250]. Significantly increased transcript expression of *PLN* in iPSC-CMs on plastic compared to softer substrates may be an attempt at cells compensating for the dysregulated contractile activity. The link between substrate stiffness and PLN expression is further supported by literature, indicating interactions occur between integrin linked kinases, SERCA2a and PLN in a DCM model [251]. However, the phosphorylation state of PLN would need to be investigated further to confirm how PLN is altering SERCA2a activity with substrate stiffness.

No significant differences were observed in Ca^{2+} LTCC expression in iPSC-CMs across conditions. Literature has shown substrate stiffness can cause structural remodelling and localisation of LTCC's to RYR2, leading to greater electrical coupling [246]. Alterations in the localisation of LTCC may therefore not lead to changes in levels of transcript expression. The lack of change in LTCC expression with stiffness is also reflected in literature, which found stiffness-related changes in Ca^{2+} currents of rat CMs were not due to changes in expression of the α subunit of LTCC [245].

ECM stiffnesses did not appear to largely alter transcript expression of NCX exchangers in iPSC-CMs, which may be consistent with the lack of changes observed in Ca^{2+} extrusion. In addition, iPSC-CMs in long term cultures have been shown to lack expression of ion channels compared to adult CMs, highlighting the potential immaturity of Ca^{2+} handling development [252], [253].

4.5 Use of softer substrates for iPSC-CMs

Overall, the data indicates softer substrates are effective for maturation of iPSC-CMs, with increased expression of cardiac maturation transcripts and increased structural sarcomeric organisation compared to culture on plastics. The improved structural organisation of CMs on softer substrates may also alter the contractility of CMs, demonstrated by the increased trend of greater contraction amplitude and contraction duration. Enhanced maturation of iPSC-CMs also altered Ca^{2+} dynamics in iPSC-CMs between 20kPa and 130kPa PDMS substrates and plastics, further demonstrating the effectiveness of softer substrates for analysing electrophysiological changes. Softer substrates are therefore an effective strategy for overcoming a key limitation of iPSC-CMs, their structural and electrophysiological immaturity. The enhanced maturity of iPSC-CMs cultured on softer substrates can consequently influence iPSC-CM function, thus providing data of a more representative and physiological nature.

4.6 Limitations

Batch to batch variability of iPSC-CMs can be observed in the data shown, with variation often seen within the same batch between wells. This was overcome by using multiple batches of iPSC-CMs for experiments. Contractility data obtained using MuscleMotion also suffers from several limitations. Videos of contractility were taken in a room with no control over temperature, therefore interrupting sounds or vibrations such as doors opening and closing may have impacted the quality of recordings. The lack of a controlled environment whilst recording there-

fore may have affected the beat rate of iPSC-CMs. Furthermore, the time taken to collect contractility recordings of individual wells within a plate led to iPSC-CMs being out of temperature controlled incubators for extended periods of time, therefore visibly altering contractility. To mitigate this, recordings of individual wells within a plate were taken one at a time, and the plate was returned to the incubator after each well to stabilise contractility of iPSC-CMs before being removed from the incubator for the next recording.

Additionally, substrate anisotropy, referring to the directionality and topography of substrates, such as microgrooves and ridges [254] were not investigated in these experiments. The anisotropy of scaffolds iPSC-CMs are cultured on have been shown to alter several properties of iPSC-CMs, as they can elongate and align according to the direction of the anisotropic feature [255]. Sarcomere length, cardiac marker expression and contractility of iPSC-CMs can be altered with anisotropy [256]. The isotropic nature of PDMS substrates therefore may also have influenced the molecular characterisation of iPSC-CMs.

4.7 Conclusion

This chapter has demonstrated substrate stiffnesses representative of changes in the ECM can impact iPSC-CM structure and function of cells. iPSC-CMs on softer ECM stiffnesses similar to physiological healthy adult myocardium express higher levels of cardiac transcript maturity markers, improved sarcomeric alignment and thus CM structure. Consequently, softer substrates lead to increased CTD's and altered Ca^{2+} dynamics, further highlighting the beneficial effect of

softer substrates for iPSC-CM functional maturity. iPSC-CMs on stiffer substrates of 130kPa PDMS exhibited dysregulation in iPSC-CM structure and Ca^{2+} handling dynamics, relative to 20kPa PDMS, thus diplaying phenotypes similiar to that of CMs in disease conditions. Glass/plastic stiffnesses were also sufficient in displaying diseased states of iPSC-CMs, indicating substrates mimicking physiological stiffnesses can improve the performance of iPSC-CMs, further highlighting the importance of ECM environments on iPSC-CM function.

Chapter 5

Metabolic characterisation of iPSC-cardiomyocytes on substrates

5.1 Introduction

As outlined in Chapter 4, ECM stiffnesses can influence maturation state of iPSC-CMs, with alterations in sarcomere organisation, Ca^{2+} dynamics and contractility. There are significant amounts of literature showing physiological stiffnesses can induce maturation of iPSC-CMs [246], [237]. Consequently, structural changes and maturation of iPSC-CMs can alter the metabolic function of mitochondria and cells, which are particularly important for CM contractility and maintaining high energetic demand [257]. Under normoxic conditions, a healthy adult heart obtains 95% of its ATP production from oxidative phosphorylation, with the remaining 5% coming from glycolysis and the TCA cycle [40]. Impaired bioenergetics can have a detrimental impact on cardiac function and ATP production, often leading to contractile dysfunction, followed by cardiomyopathies and heart failure [258].

During cardiac development, there is a significant switch in substrate utilisation; foetal hearts show a greater preference for utilisation of glucose, lactate and

pyruvate, whereas adult hearts rely on fatty acids as their primary source of fuel for oxidative phosphorylation [259]. In the diseased or aged heart, there is a reduction in myocardial lipid metabolism and relative increase in anaerobic glycolysis, known as the Randle cycle [260]. These changes are reflected in CMs; mature CMs primarily use fatty acids as their source of energy and rely on transport of fatty acids into the cell, such as long chain fatty acids via CD36 [261]. The balance between fatty acid uptake and oxidation is tightly regulated. In aged hearts, imbalances can often occur, due to decreased fatty acid oxidation with an accumulation of free fatty acids, subsequently leading to increased ROS production and lipotoxicity [262].

The shift in metabolic substrate with ageing and disease in hearts is well established, but it is unknown whether the shift in metabolism is associated with stiffening of the ECM, which occurs through fibrosis and ECM deposition. As CMs play a significant role in cardiac metabolism, modelling physiological conditions of the ECM and investigating changes in iPSC-CMs on these substrates can help elucidate molecular mechanisms through which stiffness may alter metabolic regulation.

5.2 Hypothesis and Aims

The main objective of this chapter was to investigate whether the shift in metabolic substrate utilisation that occurs with ageing and cardiac disease correlates with changes in the stiffness of the ECM, modelled by iPSC-CMs cultured on PDMS hydrogels of 20kPa PDMS, 130kPa PDMS and plastic (1-25GPa).

Stiffer substrates of 130kPa PDMS and plastic, representing ageing and disease were hypothesised to shift metabolism of iPSC-CMs towards a glycolytic foetal phenotype, whereas softer substrates of 20kPa PDMS, representing healthy physiological ECM were hypothesised to show preferences towards lipid metabolism. Metabolism of iPSC-CMs on different substrate stiffnesses were therefore assessed by several aspects.

The hypothesis for this chapter were tested through the following aims:

1. To determine whether substrate stiffness can alter metabolic source of iPSC-CMs with fatty acid treatment using [U-^{13}C]-glucose labelled mass spectrometry.

2. To determine whether the ECM stiffness alters cellular functional metabolism using Seahorse cellular energetics assays.

3. To assess how culture of iPSC-CM on healthy and fibrotic substrate stiffnesses can impact metabolic protein levels using proteomics.

4. To perform molecular characterisation of metabolic changes in iPSC-CMs by assessing whether substrate stiffness affects transcript and protein levels of key metabolic genes.

5.3 Results

5.3.1 Fatty acid treated iPSC-CMs

In order to investigate the metabolic preference of iPSC-CMs, iPSC-CMs were supplemented with OA and PA to provide the cells with options for metabolic sub-

strates, specifically for mass spectrometry experiments. Fatty acid supplementation was not used for all experiments, to ensure the effect of substrate stiffness was the primary variable influencing results.

5.3.1.1 Confirmation of uptake of fatty acids in iPSC-CMs

To determine the uptake of oleic acid (OA) and palmitic acid (PA) by iPSC-CMs, confocal microscopy was conducted using BODIPY C_{16} dye, both with and without L-carnitine supplementation. L-carnitine is typically used for transporting long chain fatty acids across the inner mitochondrial membrane [71]. iPSC-CMs treated with a combination of 100 μm (OA) and 50 μm PA, both with and without additional 200 μm L-carnitine had increased lipid droplets (Figure 5.1 A&B). Cells with no fatty acid treatment had no lipid droplets (Figure 5.1C).

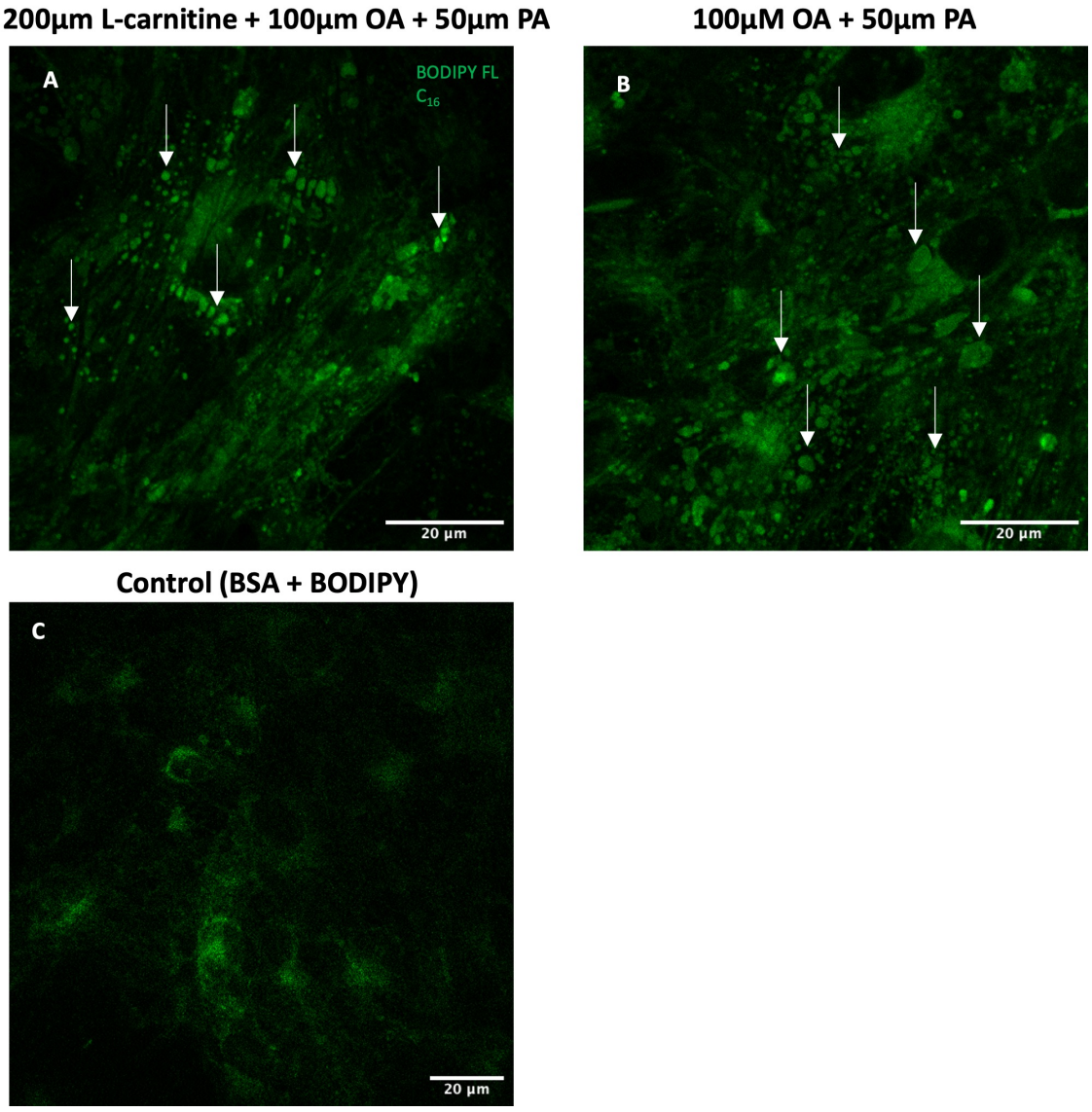

Figure 5.1: **Confocal microscopy images of fatty acid droplets in iPSC-CMs**
(A) Representative confocal images of iPSC-CMs treated with 200 μm L-carnitine, 100 μm OA and 50 μm PA. Cells stained with a BODIPY FL C_{16} dye (green). Fatty acids were conjugated with BSA (B) Images of iPSC-CMs treated with 100 μm OA, 50 μm PA and BODIPY FL C_{16} dye (green).(C) Images of iPSC-CMs with no fatty acid treatment, treatment with BSA conjugated with BODIPY FL C_{16} dye (green) as control. Lipid droplets indicated by white arrows. Images taken at 100x magnification, 5-6 images taken per well, n=1 batch, 1-2 wells per condition.

5.3.1.2 Transcript expression of metabolic gene targets with fatty acid supplementation

To investigate whether fatty acid related gene transcript levels were affected by fatty acid supplementation, qPCR was conducted on mRNA extracted from iPSC-CMs cultured in control conditions or a combination of 100 μm OA and 50 μm PA treatment, with and without additional 200 μm L-carnitine (Figure 5.2). No significant changes were seen in perilipin 2 (*PLIN2*) or perilipin 5 (*PLIN5*) expression, which are responsible for encoding proteins that integrate into the outer surface of lipid droplets. A significant increase in carnitine palmitoyltransferase 1B (*CTP1B*) transcript expression was observed in cells treated with L-carnitine, OA and PA compared to those without L-carnitine ($p < 0.05$). Significant increases in *CD36* transcript expression, a fatty acid transporter gene identified in OA + PA treated iPSC-CMs compared to untreated ($p< 0.05$). Pyruvate dehydrogenase kinase 4 (*PDK4*), involved in pyruvate dehydrogenase complex (PDC) regulation, had significantly increased expression in OA +PA treated cells compared to controls ($p < 0.05$). No significant changes were observed in PPAR isoforms across conditions.

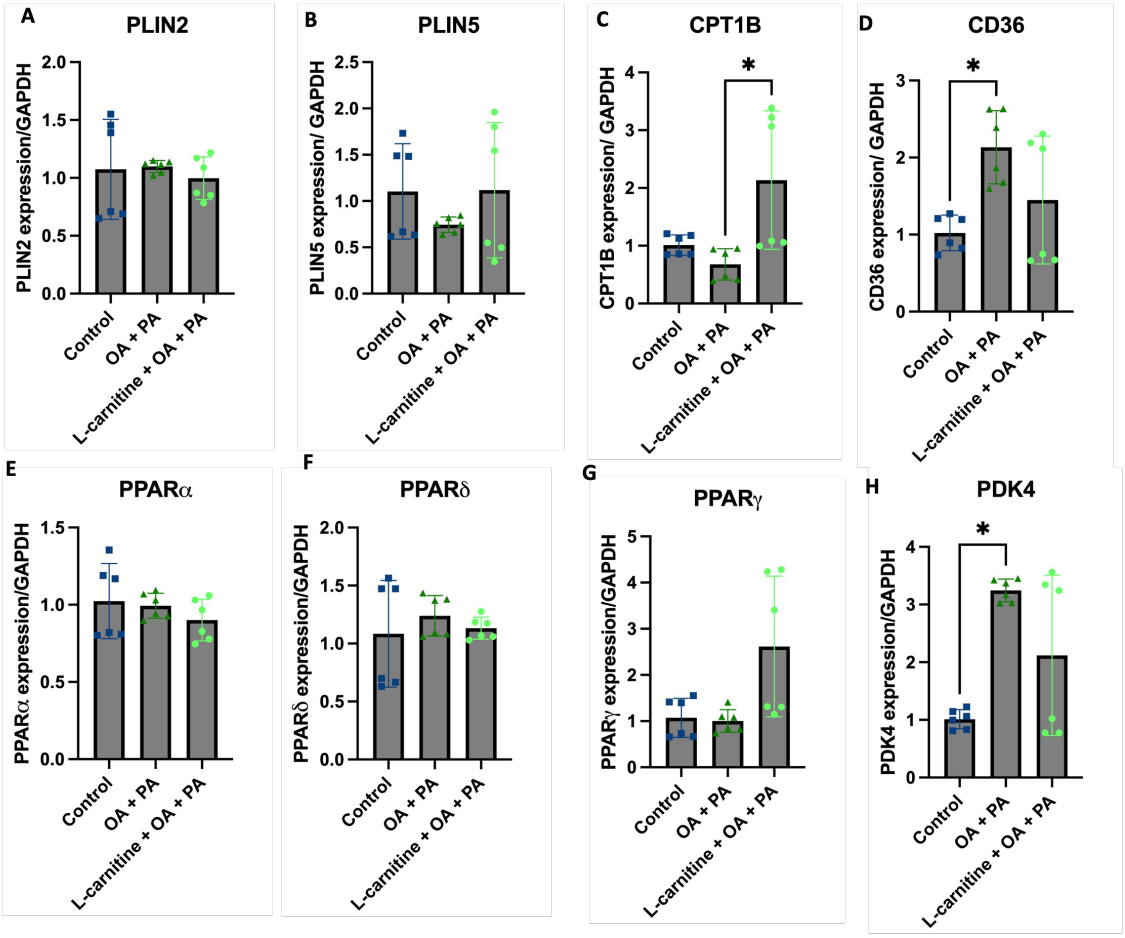

Figure 5.2: **qPCR gene transcript levels of metabolic genes in fatty acid treated iPSC-CMs**
iPSC-CMs treated with 100μm OA, 50μm PA and 200μm L-carnitine (A) PLIN2 transcript levels. (B) PLIN5 transcript levels (C) CPT1B transcript levels. (D) CD36 transcript levels. (E) PPARα transcript levels. (F) PPARδ transcript levels. (G) PPARγ transcript levels. (H) PDK4 transcript levels. Data presented as mean $\pm$ SD. Each data point refers to 1 well of cells plated from 1 technical repeat, with a total of n=2 batches of differentiated iPSC-CMs. Low sample numbers were conducted as this was a preliminary test to observe changes with FA supplementation. Statistical significance was assessed with a Kruskal-Wallis test as data was not normally distributed, with p values determined as <0.05 (*).

5.3.2 [U-^{13}C]-glucose Isotope labelled mass spectrometry

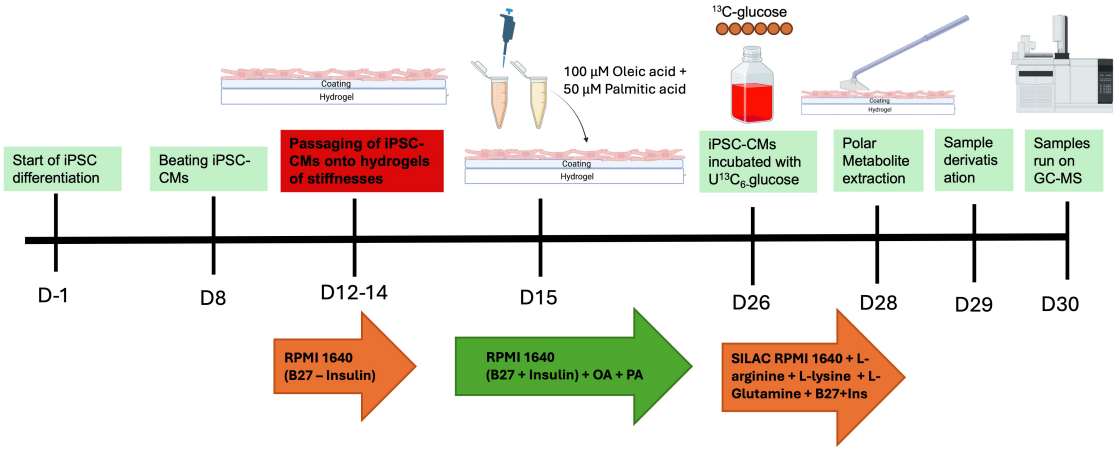

Figure 5.3: **Mass spectrometry iPSC-CM experiment plan**
Experiment plan and treatment of iPSC-CMs with fatty acids. iPSC's were differentiated into iPSC-CMs and split onto hydrogels of different stiffnesses. Day 15 iPSC-CMs were supplemented with 100μm OA and 50μm PA for a period of 10 days. Isotope labelled glucose was incubated with iPSC-CMs for 48 hours before undergoing metabolite extraction and sample derivatisation, and ran on a GC-MS.

Stable isotope-enriched nutrients were incubated with iPSC-CMs and their incorporation into cellular metabolite was used to examine the metabolism of iPSC-CMs on different substrates. iPSC-CMs were supplemented with 50μm PA and 100μm OA. [U-^{13}C]-glucose was added to iPSC-CMs on different substrates and tracked through central carbon metabolism. The percentage of [U-^{13}C]-glucose converted into pyruvate (M+3) was significantly higher in iPSC-CMs on plastic compared to 20kPa PDMS (71$\%$ compared to 64$\%$) (Figure 5.4). Similar trends were seen in the amount of [U-^{13}C]-glucose converted into lactate (M+3); the percentage of labelled glucose was significantly higher in iPSC-CMs on plastic compared to 20kPa PDMS ($p<0.01$) and 130kPa PDMS ($p<0.05$) (Figure 5.5). M0, referring to unlabelled carbons from glucose forming pyruvate, was significantly higher in 20kPa PDMS than plastic. Significant changes in the amount of unlabelled glucose forming lactate was also significantly increased on 20kPa

PDMS and 130kPa PDMS compared to plastic.

To investigate whether the entry of [U-^{13}C]-glucose was altered in TCA cycle, metabolites in the TCA cycle were assessed. The percentage of [U-^{13}C]-glucose in acetyl-coA converted into citrate (M+2 isotopologue) showed no significant differences in iPSC-CMs across substrates (Figure 5.6). Significant differences in the proportion of glucose incorporation into citrate (M+4 and M+5 isotopologues) may reflect the increased entry of carbons through carboxylation of pyruvate alongside through acetyl-coA. The same patterns of glucose labelling were observed in a different fragment observed for citrate (Citrate591).

Total abundance of metabolites in iPSC-CMs across substrates were also assessed (Figure 5.7). Despite no significant changes in the total amount of metabolites, a trend towards increased amounts of pyruvate, lactate and citrate were observed in iPSC-CMs cultured on plastic compared to softer PDMS substrates.

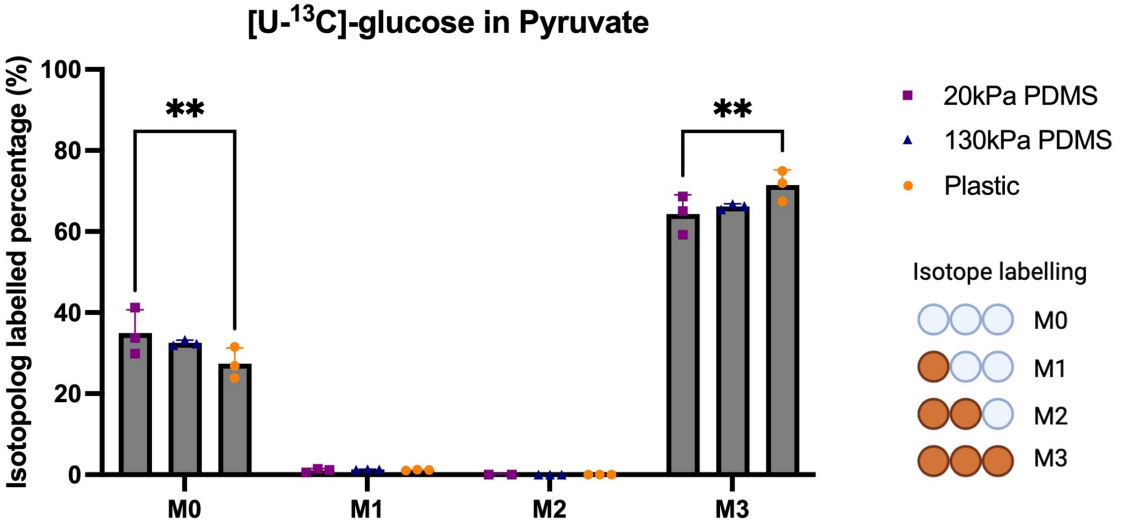

Figure 5.4: **[U-^{13}C]-glucose labelling in pyruvate in iPSC-CMs on 20kPa PDMS, 130kPa PDMS and plastic using isotope labelled mass spectrometry**
Percentage of labelled [U-^{13}C]-glucose in pyruvate from metabolites extracted from day 27 iPSC-CMs cultured on 20kPa PDMS, 130kPa PDMS and plastic. M0 refers to pyruvate with 0 carbons coming from the supplemented labelled glucose, M1 refers to pyruvate with 1 carbon coming from labelled glucose, M2 refers to pyruvate with 2 carbons coming from labelled glucose and M3 refers to all 3 carbons in pyruvate coming from labelled glucose through glycolysis, as shown in the key. Data presented as mean $\pm$ SD. Each data point refers to 1 well from 1 batch of iPSC-CMs, with a total of n=3 batches of differentiations per condition. Data normalised to cell number from plates differentiated in parallel under same conditions. Statistical significance was assessed with a 2way ANOVA test as data was normally distributed, with p values determined as < 0.01 (**).

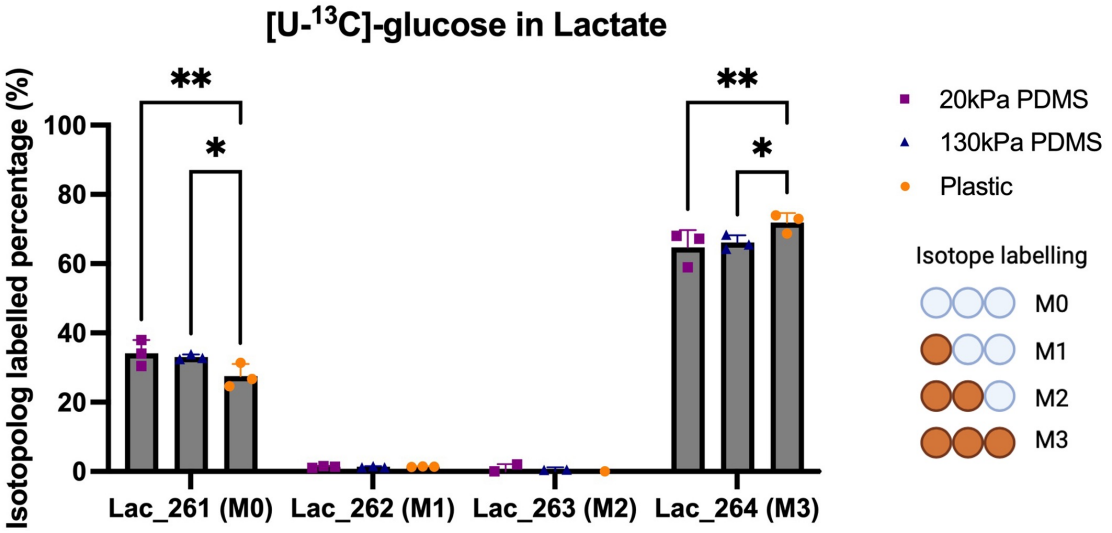

Figure 5.5: **[U-^{13}C]-glucose labelling in lactate in iPSC-CMs on 20kPa PDMS, 130kPa PDMS and plastic using isotope labelled mass spectrometry**
Percentage of labelled [U-^{13}C]-glucose incorporated into lactate from metabolites extracted from day 27 iPSC-CMs cultured on 20kPa PDMS, 130kPa PDMS and plastic. M0 refers to lactate with 0 carbons coming from the supplemented labelled glucose, M1 refers to lactate with 1 carbon coming from labelled glucose, M2 refers to lactate with 2 carbons coming from labelled glucose and M3 refers to all 3 carbons in lactate coming from labelled glucose through glycolysis, as shown in the key. Data presented as mean $\pm$ SD. Each data point refers to 1 well from 1 batch of iPSC-CMs, with a total of n=3 batches of differentiations per condition. Data normalised to cell number from plates differentiated in parallel under same conditions. Statistical significance was assessed with a 2way ANOVA test as data was normally distributed, with p values determined as < 0.05 (*), < 0.01 (**).

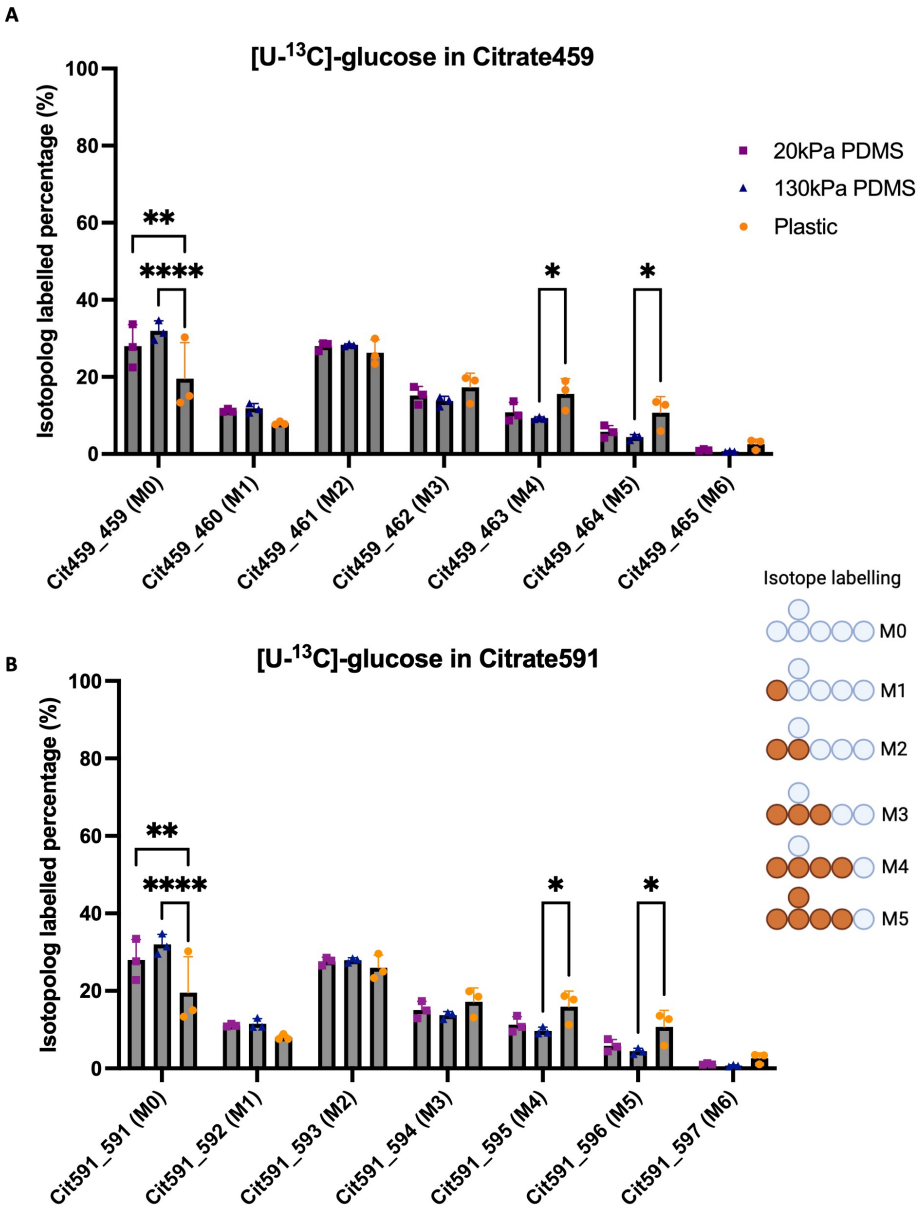

Figure 5.6: **[U-^{13}C]-glucose labelling in citrate in iPSC-CMs on 20kPa PDMS, 130kPa PDMS and plastic using isotope labelled mass spectrometry**
Percentage of labelled [U-^{13}C]-glucose in (A) Citrate459 and (B) Citrate591 from metabolites extracted from day 27 iPSC-CMs cultured on 20kPa PDMS, 130kPa PDMS and plastic. M0 refers to citrate with 0 carbons coming from the supplemented labelled glucose, M1 refers to citrate with 1 carbon coming from labelled glucose. After 1 turn of the TCA cycle, 2 labelled carbons from acetyl-CoA derived from labelled glucose would be incorporated into citrate, known as M2. M3 refers to 3 carbons in citrate coming from labelled glucose, as shown in the key. The presence of M4 and M5 labelled carbons in citrate indicate citrate was formed from acetyl-CoA derived from labelled glucose. Data presented as mean $\pm$ SD. Each data point refers to 1 well from 1 batch of iPSC-CMs, with a total of n=3 batches of differentiations per condition. Statistical significance was assessed with a 2way ANOVA test as data was normally distributed, with p values determined as < 0.01 (**).

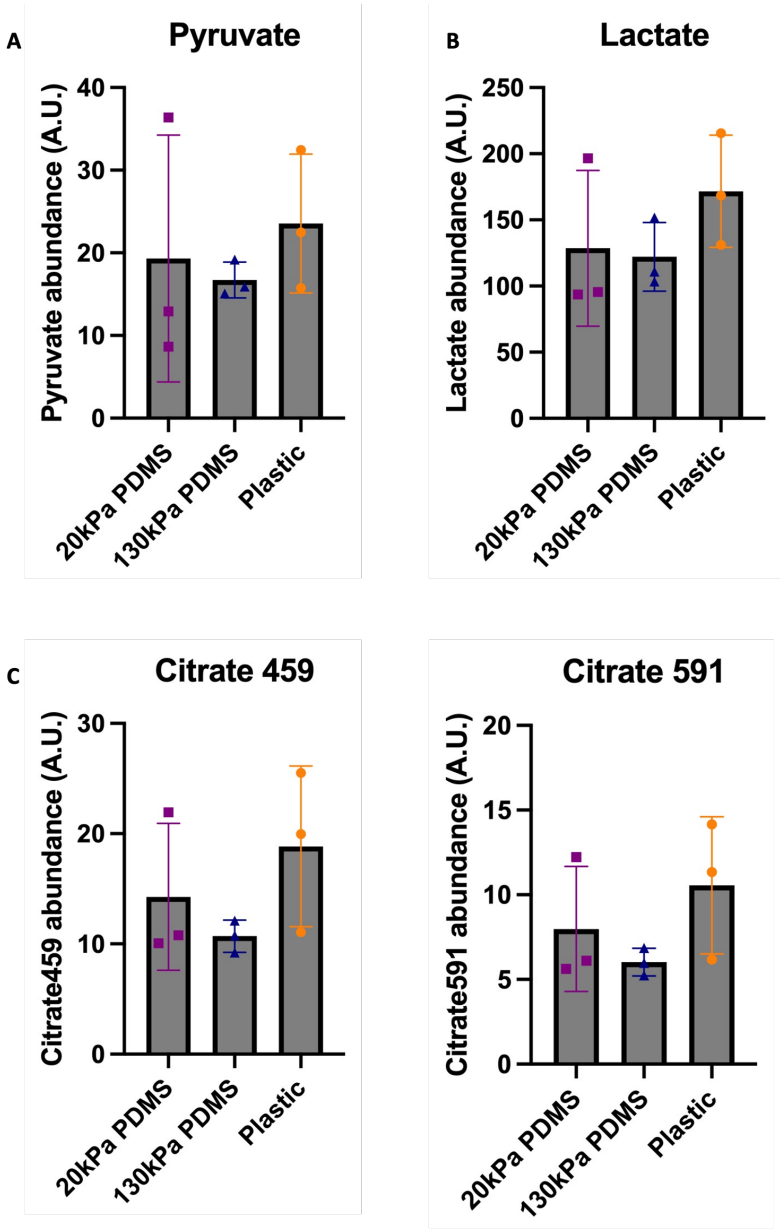

Figure 5.7: **Total abundance of polar metabolites from iPSC-CMs on 20kPa PDMS, 130kPa PDMS and plastic using isotope labelled mass spectrometry**
Day 27 iPSC-CMs cultured on 20kPa PDMS, 130kPa PDMS and plastic. (A) Pyruvate abundance (B) Lactate abundance (C) Citrate 459 abundance (D) Citrate 591 abundance. Data presented as mean $\pm$ SD. Each data point refers to 1 well from 1 batch of iPSC-CMs, with a total of n=3 batches of differentiations per condition. Data normalised to cell number from plates differentiated in parallel under same conditions. Statistical significance was assessed with a one way ANOVA test as data was normally distributed. No significant differences were observed.

5.3.3 Oxygen consumption rate (OCR) and Extracellular acidification rate (ECAR) of iPSC-CMs on different substrates

Seahorse Cell Mito-Stress test assays were conducted on day 25 iPSC-CMs plated on 20kPa PDMS, 130kPa PDMS and plastic to investigate mitochondrial respiration in cells. OCR refers to the amount of oxygen consumed by the cells as measured through changes in concentration of dissolved oxygen and free protons observed in the extracellular media. OCR of iPSC-CMs on different substrates were not significantly different, although a slight increased trend of OCR was identified on both PDMS substrates compared to plastic (Figure 5.8 A & B).

ECAR refers to changes in the pH of the media, which is mainly due to lactic acid production as a result of glycolysis. iPSC-CMs on plastic have a significantly higher ECAR compared to both 20kPa ($p < 0.001$) and 130kPa PDMS substrates ($p < 0.0001$), suggesting higher lactate production on stiff substrates (Figure 5.8 C & D).

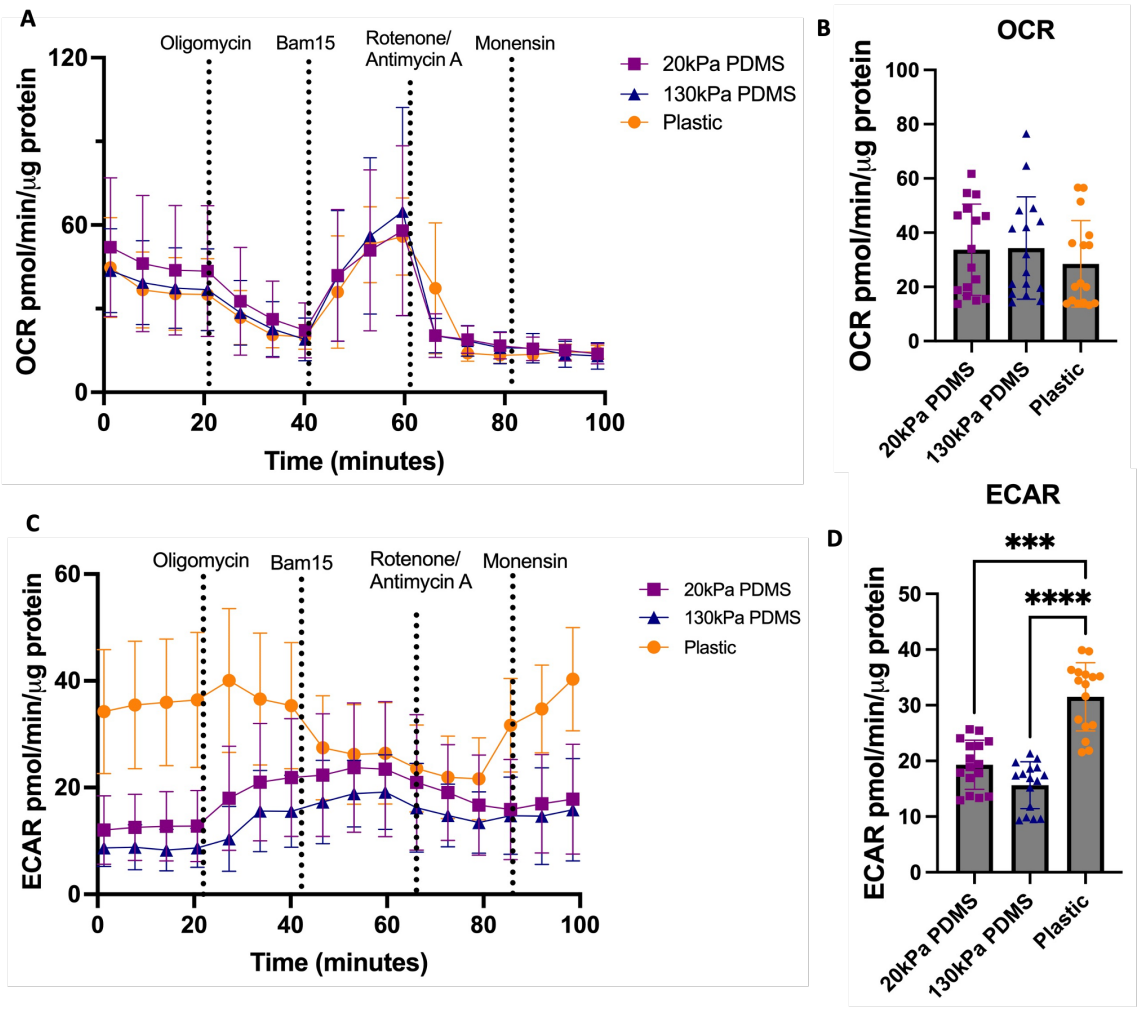

Figure 5.8: **Oxygen consumption rate and extracellular acidification rate assessed by Cell Mito-Stress Test Seahorse assay of day 25 iPSC-CMs**
(A) Oxygen consumption rate (OCR) of iPSC-CMs plated on 20kPa PDMS, 130kPa PDMS and plastic conditions using Seahorse assay. OCR measurements taken at basal levels and after drug additions. (B) Quantification of OCR on 20kPa, 130kPa PDMS and plastic conditions. (C) Extracellular acidification rate (ECAR) of iPSC-CMs plated on 20kPa PDMS, 130kPa PDMS and plastic conditions using Seahorse assay. ECAR measurements taken at basal levels and after drug additions. (D) Quantification of ECAR on 20kPa, 130kPa PDMS and plastic conditions. Data normalised to protein levels of cells. Values are presented as mean $\pm$ SD. Each data point refers to 16 well of cells per condition per batch, conducted using an n=2 batches of iPSC-CMs differentiations. Statistical significance was assessed with a Kruskal-Wallis test as data was not normally distributed, with p values determined as < 0.001 (***), <0.0001 (****).

5.3.4 Metabolic parameters from Cell Mito-Stress Seahorse assay

Several parameters were obtained from the metabolic assay. Basal respiration refers to the oxygen consumption used to meet the cellular ATP demand (Fig-

ure 5.9). An increased trend of basal respiration was observed in iPSC-CMs on 20kPa PDMS compared to 130kPa PDMS and plastic (Figure 5.9 A). ATP-linked respiration, a measure of respiration directly linked to ATP production, showed a similar trend, with increased ATP-linked respiration on 20kPa PDMS compared to other substrates (Figure 5.9 B). Maximal respiration refers to OCR observed after uncoupling of the proton gradient from the ETC activity using the ionophore, Bam15 thus allowing maximal respiratory capacity. No significant differences were observed in maximal respiration across conditions (Figure 5.9 C). Proton leak refers to the remaining portion of basal respiration not linked to ATP production. Proton leak was significantly increased on iPSC-CMs on plastic ($p < 0.05$) compared to 20kPa PDMS (Figure 5.9 D). Spare respiratory capacity refers to the capability of a cell to respond to energetic demand, often an indicator of cell fitness. No significant differences were observed in spare respiratory capacity in iPSC-CMs on different substrates. Non-mitochondrial respiration refers to the OCR after the addition of rotenone/antimycin A, which shuts down mitochondrial respiration. No significant differences were found in non-mitochondrial respiration across substrates (Figure 5.9 F).

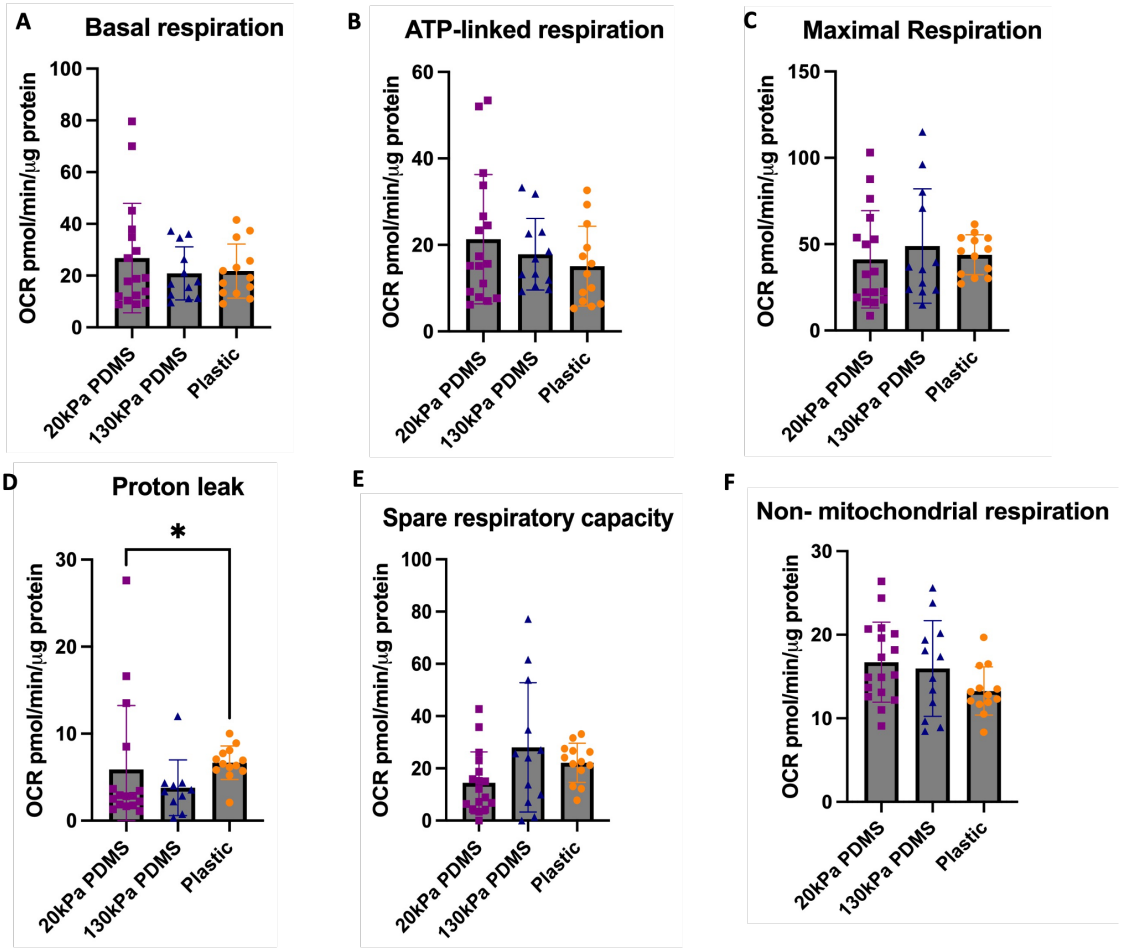

Figure 5.9: **Seahorse Cell Mito-Stress Test parameters of day 25 iPSC-CMs** (A) Basal respiration of iPSC-CMs plated on 20kPa PDMS, 130kPa PDMS and Plastic conditions. (B) ATP-linked respiration measurements (C) Maximal respiration (D) Proton leak (E) Spare respiratory capacity (F) Non-mitochondrial respiration. Data normalised to total protein quantity of cells. Values are presented as mean $\pm$ SD. Each data point refers to 7-10 wells of cells per condition per batch, conducted using an n=2 batches of iPSC-CMs differentiations. Statistical significance was assessed with a Kruskal-Wallis test as data was not normally distributed, with p values determined as < 0.05 (*).

5.3.5 Proteomics analysis of iPSC-CMs on 20kPa PDMS, 130kPa PDMS and Plastic

Proteomics was conducted using liquid chromatography mass spectrometry (LC-MS) to identify differentially expressed proteins in iPSC-CMs cultured on 20kPa PDMS, 130kPa PDMS and plastic substrates. 858 proteins were identified in total before proteins were identified as differentially expressed when the fold change

threshold was set to $>$1.5, with few proteins reaching both the fold change criteria and statistical significance adjusted p value threshold ($<$0.05).

5.3.5.1 Plastic vs 130kPa PDMS

Comparison between iPSC-CMs on plastic and 130kPa PDMS highlighted 6 proteins of interest, with 1 protein displaying differential expression at both fold change and statistical thresholds (Figure 5.10). Serine protease *(HTRA1)* was identified as significantly downregulated in iPSC-CMs on plastic, with an adjusted p value of 0.004 and log fold change of -0.75 (Table 5.1).

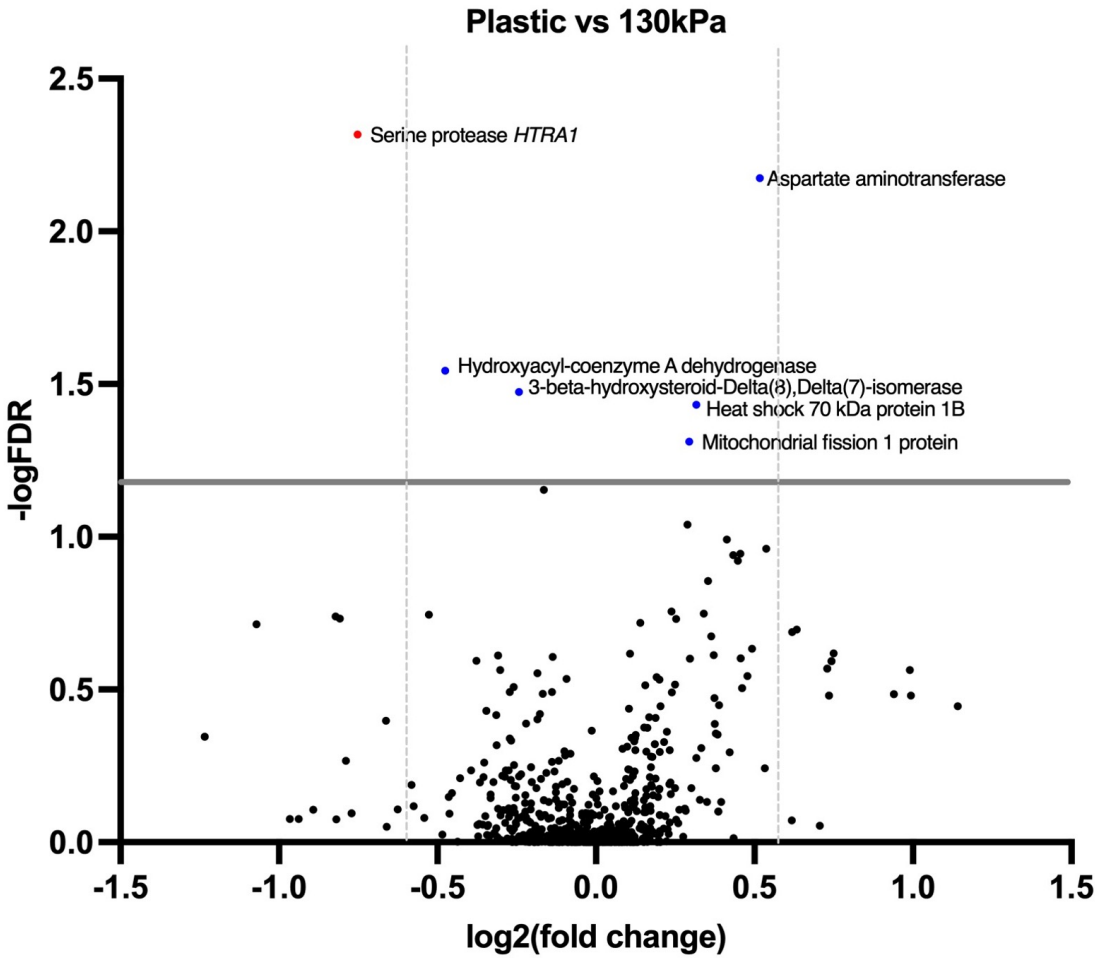

Figure 5.10: **Volcano plot of proteomics data of iPSC-CMs on plastic compared to 130kPa PDMS at day 25**
On the x axis, 0 indicates no change in protein expression, dots to the right show up-regulation of proteins, whereas dots to the left indicate downregulation of proteins. The solid grey line at 1.3 FDR refers to a significance threshold, adjusted p value of 0.05. The dashed grey line refers to log fold change threshold values of $>$ 1.5x control. Blue dots refer to proteins that have a p value of $<$ 0.05, but do not have a fold change of greater than 1.5x. Red dots refer to proteins that are significantly differentially expressed compared to control ($p < 0.05$) and greater than 1.5x fold change. Data was obtained from 1 well of cells per condition across N=4 batches of iPSC-CM differentiations.

Table 5.1: **Proteomics genes of interest in iPSC-CMs on plastic compared to 130kPa PDMS at day 25**

Description	Gene name	Fold change	Adj p value
Serine protease	HTRA1	-0.75	0.004
Aspartate aminotransferase	GOT1	0.52	0.006
Heat shock 70kDa protein 1B	HSPA1B	0.32	0.036
Hydroxyacyl-coenzyme A dehydrogenase	HADH	-0.48	0.028
3-beta-hydroxysteroid Δ8,Δ7 isomerase	EBP	-0.24	0.033
Mitochondrial fission 1 protein	FIS1	0.29	0.048

Gene descriptions and names of proteins with fold change values and adjusted p value. Proteins listed were significant according to p value but may not have reached significance according to log fold change. Statistical significance was determined as p value <0.05, and log fold change of $<$ or $>$ 0.53 (equivalent to 1.5x fold change).

5.3.5.2 Plastic vs 20kPa PDMS

Comparisons between iPSC-CMs on plastic and 20kPa PDMS identified 4 proteins of interest, all of which were significantly different according to adjusted p values (<0.05) but did not meet the criteria for log fold change. Of these, 2 proteins were involved in the ETC, acting as NADH dehydrogenase proteins which play a role as part of complex I of the ETC (Table 5.2).

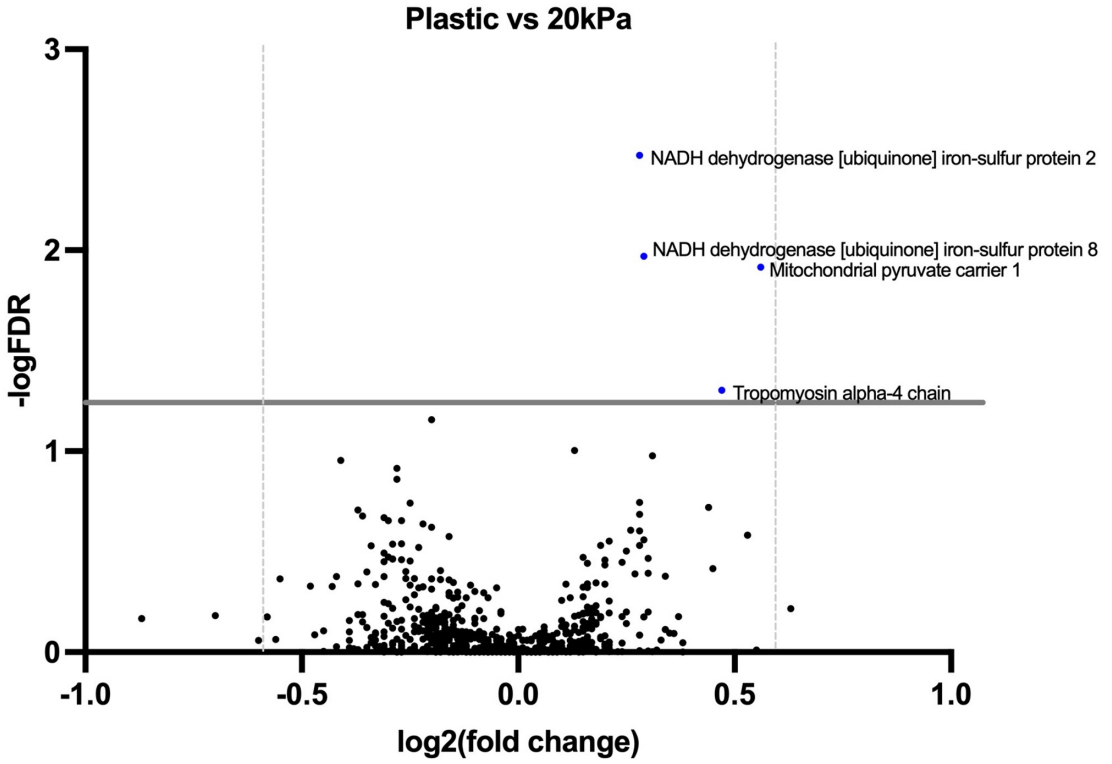

Figure 5.11: **Proteomics genes of interest in iPSC-CMs on plastic compared to 20kPa PDMS at day 25**
0 indicates no change in protein expression, dots to the right show upregulation of proteins, whereas dots to the left indicates downregulation of proteins. The solid grey line at 1.3 FDR refers to a significance threshold, p value of 0.05. The dashed grey line refers to log fold change threshold values of $>$ 1.5x control. Blue dots refer to proteins that have an adjusted p value of $<$ 0.05, but do not have a fold change of greater than 1.5x. Red dots refer to proteins that are significantly different to control ($p < 0.05$) and greater than 1.5x fold change. Data was obtained from 1 well of cells per condition across N=4 batches of iPSC-CM differentiations.

Table 5.2: **Proteomics genes of interest in iPSC-CMs on plastic compared to 20kPa PDMS at day 25**

Description	Gene name	Fold change	Adj p value
NADH dehydrogenase ubiquinone iron-sulfur protein 2	NDUFS2	0.28	0.003
NADH dehydrogenase ubiquinone iron-sulfur protein 8	NDUFS8	0.29	0.010
Mitochondrial pyruvate carrier 1	MPC1	0.56	0.012
Tropomyosin α-chain 4	TPM4	0.47	0.049

Gene descriptions and names of proteins with fold change values and adjusted p value. Proteins listed were significant according to p value but may not have reached significance according to log fold change. Statistical significance was determined as p value $<$0.05, and log fold change of $<$ or $>$ 0.53 (equivalent to 1.5x fold change).

5.3.5.3 20kPa vs 130kPa PDMS

Comparisons between both PDMS substrates highlighted 6 proteins of interest, 1 of which was differentially downregulated on 20kPa PDMS; Hydroxyacyl-coenzyme A dehydrogenase (HADH) (p$<=$ 0.007 and -0.67 fold change). The other 5 proteins reached significance in adjusted p values, but did not meet significant fold change criteria (Table 5.3).

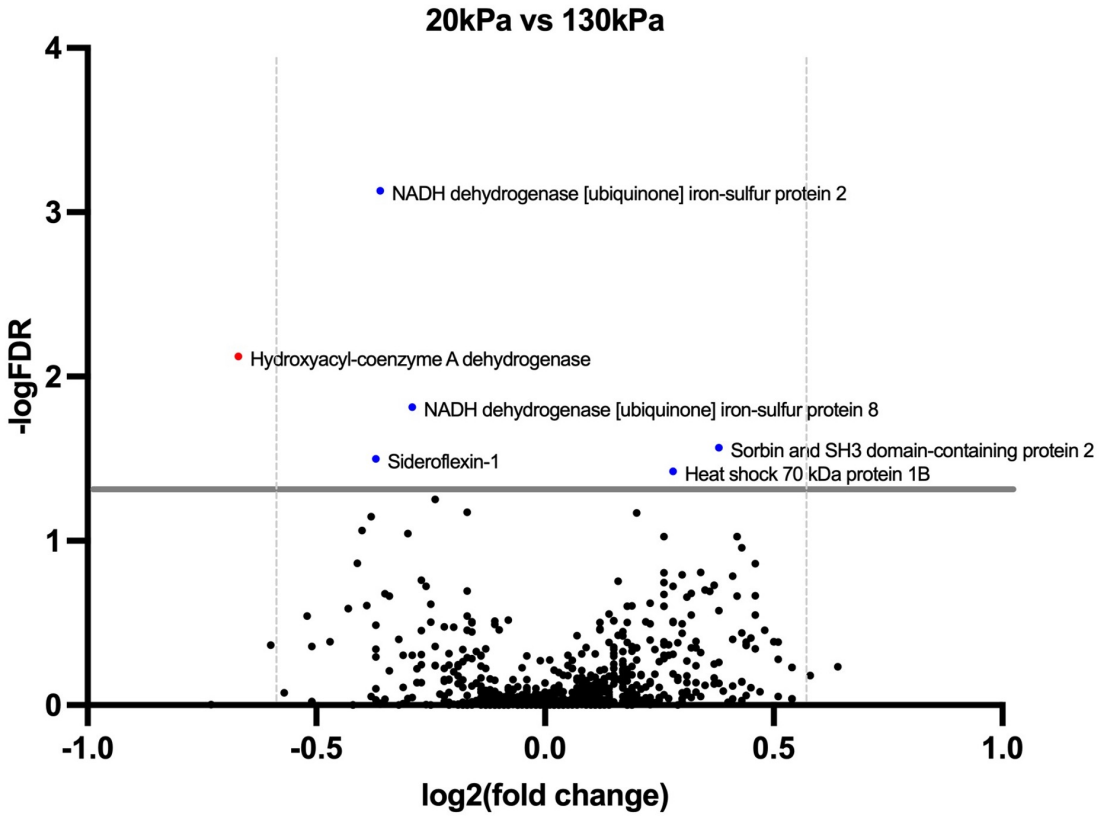

Figure 5.12: **Volcano plot of proteomics results of iPSC-CMs on 20kPa PDMS compared to 130kPa PDMS at day 25**
0 indicates no change in protein expression, dots to the right show upregulation of proteins, whereas dots to the left indicate downregulation of proteins. The solid grey line at 1.3 FDR refers to a significance threshold, p value of 0.05. The dashed grey line refers to log fold change threshold values of $>$ 1.5x control. Blue dots refer to proteins that have an adjusted p value of $<$ 0.05, but do not have a fold change of greater than 1.5x. Red dots refer to proteins that are significantly different to iPSC-CMs cultured on plastic (p $<$ 0.05) and greater than 1.5x fold change. Data was obtained from 1 well of cells per condition across N=4 batches of iPSC-CM differentiations.

Table 5.3: **Proteomics genes of interest in iPSC-CMs on 20kPa PDMS compared to 130kPa PDMS at day 25**

Description	Gene name	Fold change	Adj p value
Hydroxyacyl-coenzyme A dehydrogenase	HADH	-0.67	0.007
NADH dehydrogenase ubiquinone iron-sulfur protein 2	NDUFS2	-0.36	0.0007
Sideroflexin-1	SFXN1	-0.37	0.031
Sorbin and SH3 domain-containing 2	SORBS2	0.38	0.027
Heat shock 70kDa protein 1B	HSPA1B	0.28	0.037
NADH dehydrogenase ubiquinone iron-sulfur protein 8	NDUFS8	-0.29	0.015

Gene descriptions and names of proteins with fold change values and adjusted p value. Proteins listed were significant according to p value but may not have reached significance according to log fold change. Statistical significance was determined as adjusted p value <0.05, and log fold change of $<$ or $>$ 0.53 (equivalent to 1.5x fold change).

5.3.6 Transcript expression of metabolic genes in iPSC-CMs

The expression of key metabolic genes involved in glycolysis, *HK2*, hexokinase 2 and *PFKM*, 6-phosphofructokinase were assessed using qPCR (Fig 5.13). No significant changes in *HK2* or *PFKM* were seen in iPSC-CMs on PDMS substrates (Fig 5.13 D & E). Genes involved in fatty acid oxidation were also investigated. Transcript levels of *CD36*, a fatty acid transporter had no significant changes across conditions (Fig 5.13 A). *CPT1B*, carnitine palmitoyltransferase

1B, responsible for the oxidation of long chain fatty acid β-oxidation pathway showed no significant differences across conditions (Fig 5.13 B). *PDK4*, pyruvate dehydrogenase 4, responsible for inhibiting the pyruvate dehydrogenase complex and enhancing fatty acid oxidation displayed an increased trend of expression in cells on 20kPa PDMS compared to plastic (Fig 5.13 C).

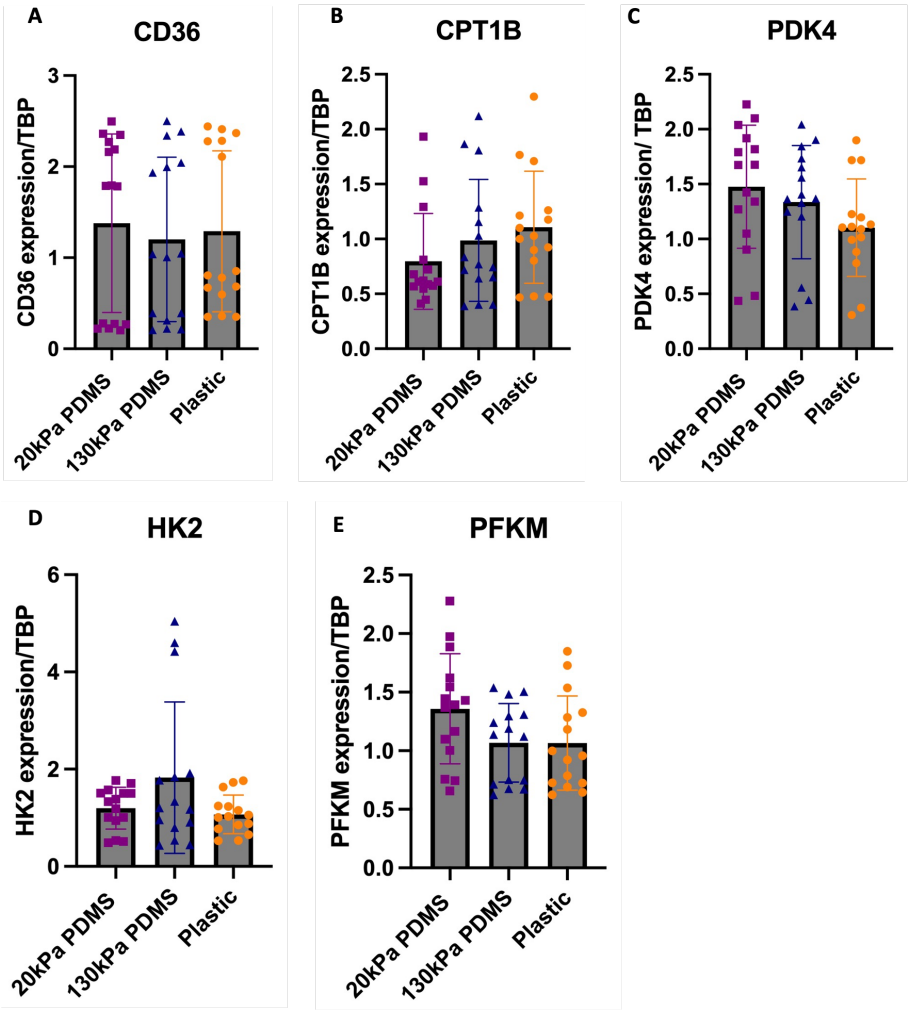

Figure 5.13: **qPCR transcript expression profiles of metabolic genes in iPSC-CMs on 20kPa PDMS, 130kPa PDMS and plastic stiffnesses**
(A) *CD36* transcript levels of day 25 iPSC-CMs plated on 20kPa PDMS, 130kPa PDMS and plastic conditions. (B) *CPT1B* transcript levels (C) *PDK4* transcript levels (D) *HK2* transcript levels (E) *PFKM* transcript levels. Data has been normalised to *TBP* and made relative to plastic. Values are presented as mean $\pm$ SD. Each data point refers to 1 well of cells plated as 3 technical replicates, with a total of n=5 batches of differentiated iPSC-CMs. Statistical significance was assessed with a Kruskal-Wallis test as data was not normally distributed.

5.3.6.1 Transcript expression levels of metabolic transcriptional regulators in iPSC-CMs

Peroxisome proliferator-activated receptors (PPARs) function as transcription factors and regulate expression of genes involved in lipid and glucose metabolism. No significant differences in PPARα or PPARγ expression levels were found in iPSC-CMs on different substrates (Figure 5.14 A & C). A significant increase in PPARδ expression was observed in iPSC-CMs on 20kPa PDMS compared to plastic ($p < 0.01$) (Figure 5.14 B). *PPARGC1A*, PPARγ Coactivator 1 alpha regulates the activity of PPARγ, showed no significant differences in expression across conditions (Figure 5.14 D).

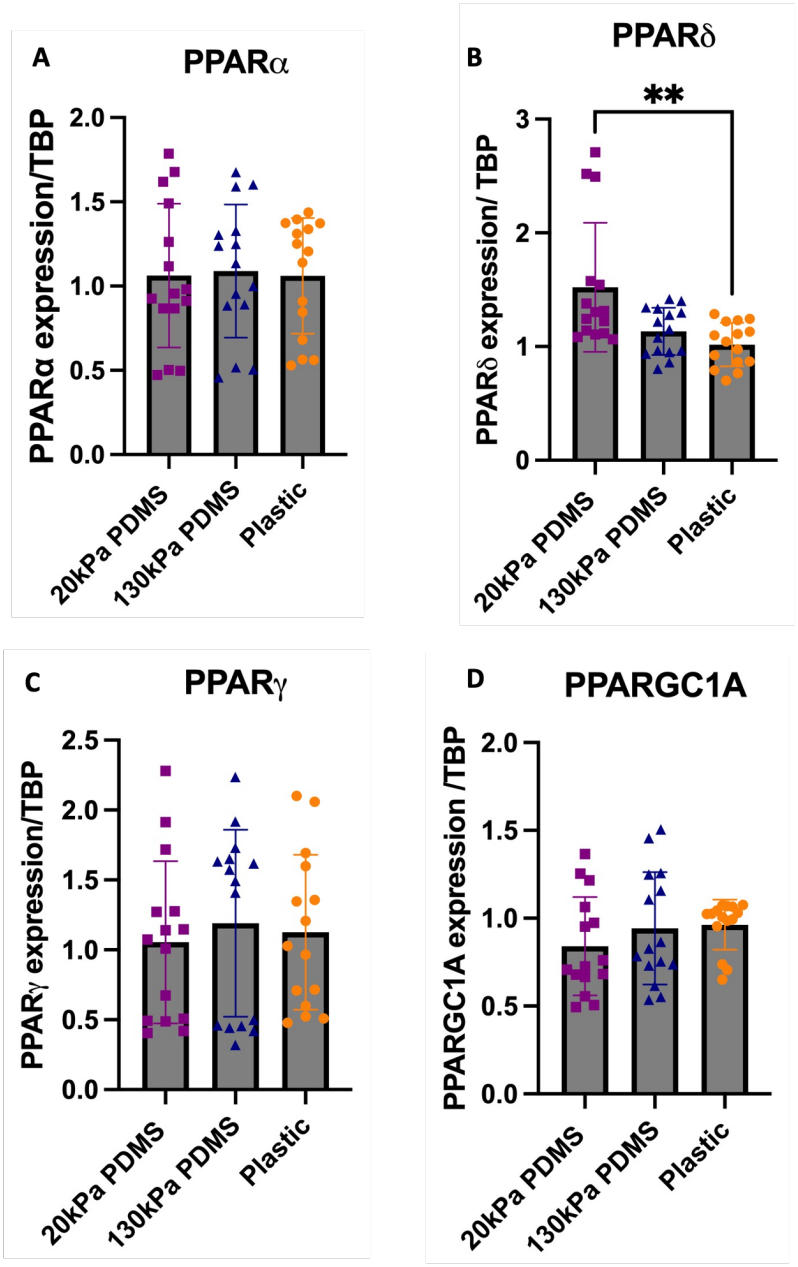

Figure 5.14: **qPCR transcript expression profiles of PPAR genes in iPSC-CMs on 20kPa PDMS, 130kPa PDMS and plastic stiffnesses**
(A) PPARα transcript levels of day 25 iPSC-CMs plated on 20kPa PDMS, 130kPa PDMS and Plastic conditions. (B) PPARδ transcript levels (C) PPARγ transcript levels (D) *PPARGC1A* transcript levels. Data has been normalised to TBP and made relative to plastic. Values are presented as mean $\pm$ SD. Each data point refers to 1 well of cells plated as 3 technical replicates, with a total of n=5 batches of differentiated iPSC-CMs. Statistical significance was assessed with a Kruskal-Wallis test as data was not normally distributed, with p values determined as < 0.01 (**).

5.3.6.2 Transcript expression levels of pyruvate dehydrogenase complex genes in iPSC-CMs on substrates

The pyruvate dehydrogenase complex consists of 3 enzymes, pyruvate dehydrogenase E1, (*PDHA1*), Dihydrolipoyl transacetylase E2 (*DLAT*) and Dihydrolipoyl dehydrogenase (*DLD*). No significant differences in *PDHA1* or *DLD* transcript levels were found across iPSC-CMs on substrates (Figure 5.15 A & C). A significant increase in transcript levels of DLAT ($p < 0.01$) was identified in iPSC-CMs on plastic compared to 130kPa PDMS (Figure 5.15 B).

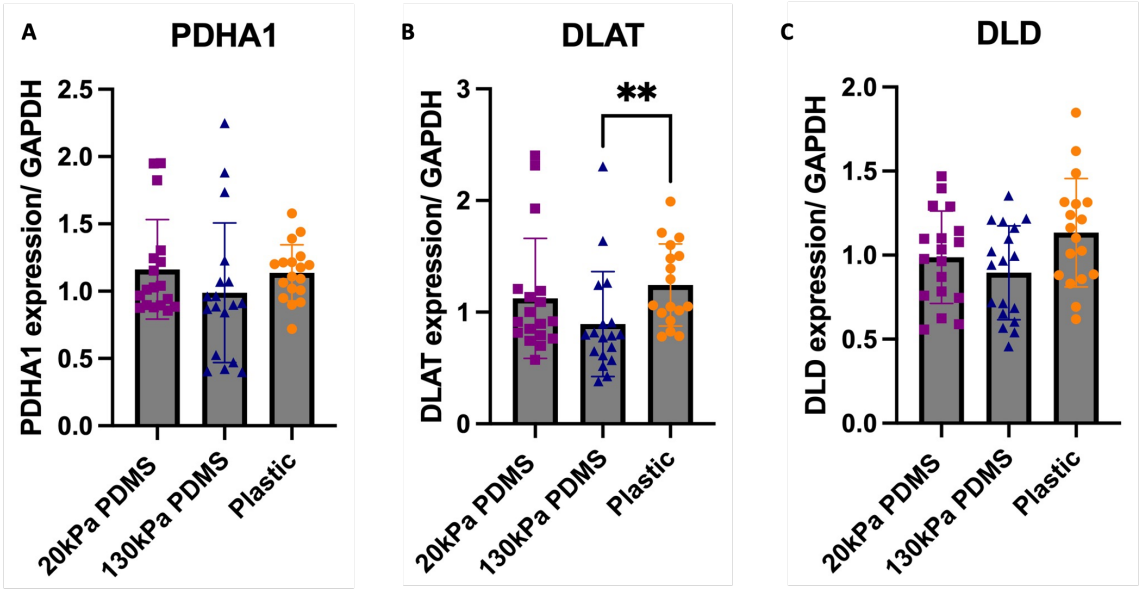

Figure 5.15: **qPCR transcript expression levels of pyruvate dehydrogenase complex genes in iPSC-CMs on 20kPa PDMS, 130kPa PDMS and plastic stiffnesses** (A) *PDHA1*, pyruvate dehydrogenase E1 alpha subunit component transcript levels of day 25 iPSC-CMs plated on 20kPa PDMS, 130kPa PDMS and Plastic conditions. (B) *DLAT*, dihydrolipoyl transacetylase, known as the E2 component of PDH transcript levels (C) *DLD*, dihydrolipoamide dehydrogenase known as the E3 component transcript levels. Data has been normalised to GAPDH and made relative to plastic. Values are presented as mean $\pm$ SD. Each data point refers to 1 well of cells plated as 3 technical replicates, with a total of n=5 batches of differentiated iPSC-CMs. Statistical significance was assessed with a Kruskal-Wallis test as data was not normally distributed, with p values determined as < 0.01 (**).

5.3.7 Protein expression levels of metabolic genes with western blotting

Western blotting of proteins was conducted to further validate changes in expression of metabolic genes (Figure 5.16). Consistent with the transcript levels, PPARδ exhibited an increased trend of expression on 20kPa PDMS compared to other substrates (Figure 5.16 A & B). PDK4 displayed the same trend as seen at transcript level on a protein level, with increased expression on 20kPa PDMS compared to 130kPa PDMS and plastic (Figure 5.16 C). Despite trends towards increased expression on 20kPa PDMS, changes in PDHA1 on substrates were not significant (Figure 5.16 D).

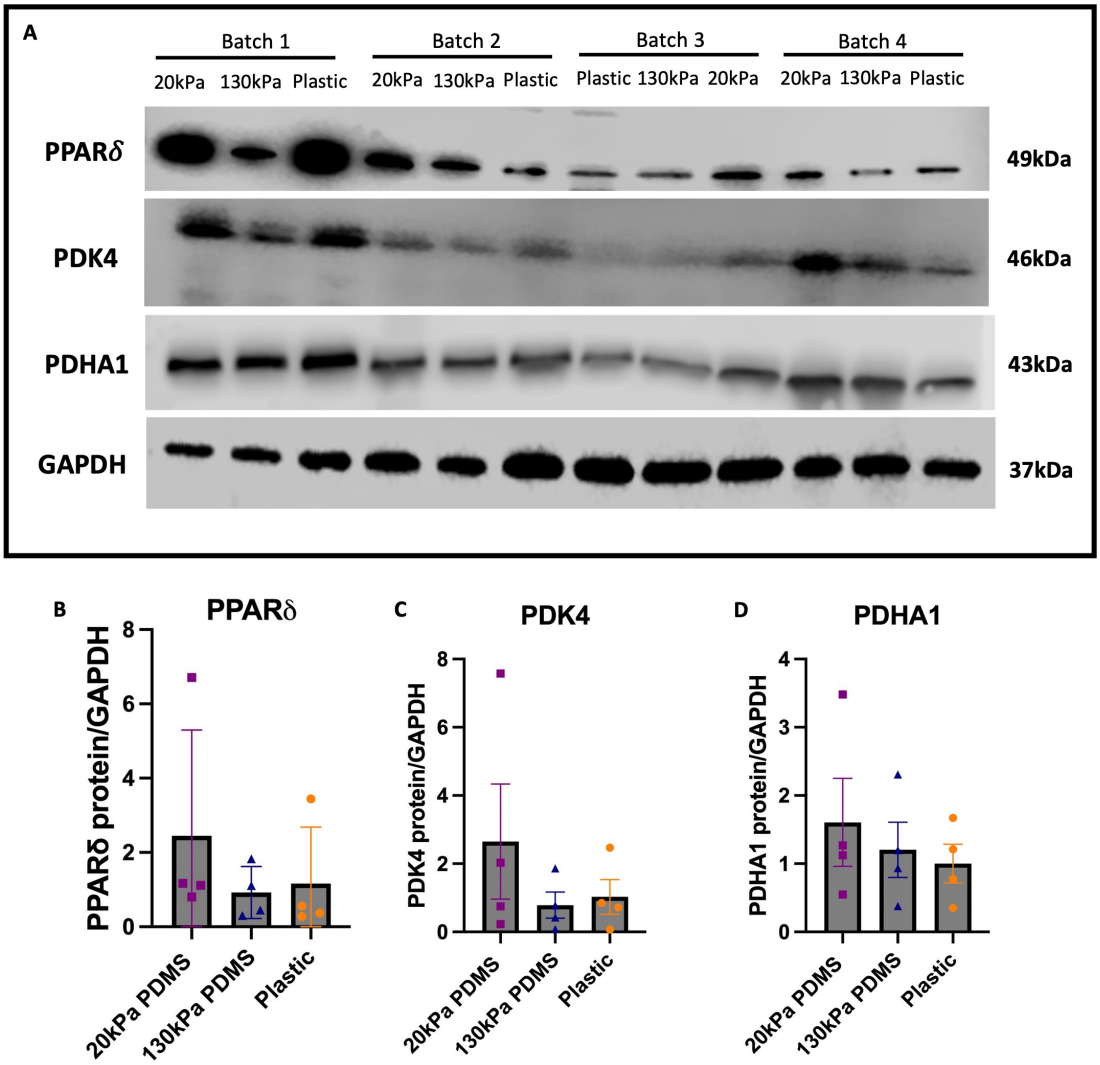

Figure 5.16: **Western blot protein expression and quantification of metabolic markers on stiffnesses**
(A) Western blot of PPARδ, PDK4, PDHA1 and GAPDH protein expression from day 25 iPSC-CMs plated on 20kPa PDMS, 130kPa PDMS and plastic. (B) PPARδ quantification of data normalised to GAPDH expression (C) PDK4 quantification of data normalised to GAPDH. (D) PDHA1 quantification of data normalised to GAPDH. Data presented as mean $\pm$ SD. Each data point refers to 1 well of cells per condition, across a total of n=4 batches of iPSC-CM differentiations. Statistical significance was assessed with a Kruskal-Wallis test as data was not normally distributed.

5.4 Discussion

This chapter aimed to characterise and reflect on the metabolic remodelling associated with ageing and the stiffness of the ECM on iPSC-CMs. To further understand whether the switch between fatty acid oxidation and glycolysis were linked

to substrate stiffness, iPSC-CMs were cultured on 20kPa and 130kPa stiffnesses, and a range of experiments were conducted to determine the metabolic state of cells. iPSC-CMs on plastic substrates exhibited greater glycolytic metabolism and anaerobic respiration, with upregulated lactate and pyruvate production both at an intracellular and extracellular level. Consequently, substrate stiffnesses appear to significantly alter energetics of iPSC-CMs, highlighting how ECM stiffness can contribute to heart failure and cardiac disease.

5.4.1 iPSC-CM profiles on 20kPa vs 130kPa PDMS substrates

iPSC-CMs cultured on 20kPa PDMS, representative of a healthy myocardium demonstrated a healthier metabolic phenotype, with trends towards less lactic acid production, slightly increased PPARδ expression at transcript and protein level and trends of increased protein expression of genes such as PDK4 and PDHA1 compared to iPSC-CMs cultured on stiffer 130kPa PDMS. These changes may reflect the upregulation of genes involved in oxidative phosphorylation, and the preference of using fatty acids as a primary source of energy production for healthy CMs, therefore downregulating genes involved in glycolytic metabolism. Although not significant, a trend towards slightly decreased basal respiration and decreased ATP-linked respiration could further reflect the stressed disease state of iPSC-CMs cultured on the stiffer 130kPa PDMS, demonstrating how stiffer substrates can impact bioenergetics of iPSC-CMs. Despite some observed trends, the metabolic profile of iPSC-CMs cultured on 130kPa did not always reflect the expected disease state across all experiments, indicating that 130kPa PDMS

may not be a sufficient stiffness to induce large metabolic changes. Substrates with stiffnesses closer to plastic (GPa) may show greater metabolic differences in iPSC-CMs.

5.4.2 Stiffer substrates shift iPSC-CMs towards glycolytic metabolism

In cardiac disease conditions associated with fibrosis, increased ECM deposition leads to stiffening of the myocardium, with the heart reverting back to foetal-like metabolism, primarily using glycolysis as the primary source of energy production [263]. The potential link between changes in stiffness of the ECM and subsequent change in metabolic source were unexplored. The upregulation of glycolytic activity in iPSC-CMs on stiffer substrates therefore mimics disease conditions, suggesting ECM stiffness may be linked to the switch in metabolism between healthy and diseased hearts.

Cells have the ability to sense changes in the ECM and environment through integrin receptors and change downstream signalling pathways such as cell proliferation and survival. As metabolism provides energy for cell proliferation, the stiffness of matrices can directly influence cell metabolism. This phenomenon has been shown in cancer cells, where increased stiffness upregulates anaerobic glycolysis in order to meet metabolic demands [264]. The switch in iPSC-CMs to glycolysis on stiffer ECMs can also be linked to the disrupted organisation of actomyosin cytoskeletal networks [265], which are also reflected in the disorganisation of sarcomere structures of iPSC-CMs shown in Chapter 4.

5.4.2.1 Glycolytic preference of iPSC-CMs determined by mass spectrometry

iPSC-CMs cultured on stiffer substrates also demonstrated a shift towards glycolytic metabolism when assessed through intracellular metabolites. Significantly higher levels of [U^{13}C]-glucose utilised for pyruvate and lactate production were identified in iPSC-CMs on plastics compared to softer substrates, indicating greater levels of glycolysis, consistent with Seahorse data. Literature has shown iPSC-CMs cultured in high glucose media labelled with [U^{13}C]-glucose have high lactate production and a high fraction of labelled glucose in lactate [266]. This is consistent with data shown as despite the supplementation of media with OA and PA, iPSC-CMs still demonstrated a preference for glycolysis on stiffer substrates. Additionally, total metabolite levels of lactate and pyruvate on plastic compared to PDMS substrates were higher, suggesting not only alterations in glucose utilisation, but also changes in metabolite usage with substrate stiffness. To further characterise changes associated between stiffness and lactate production, the activity and expression of lactate dehydrogenase could also be investigated.

5.4.2.2 Glycogen storage

A high level of unlabelled glucose was utilised in pyruvate and lactate production across substrate stiffnesses, indicating iPSC-CMs may be utilising glycogen stores. Glycogen can serve as a source for high energy demands, with similar contributions of glycogen metabolism in failing hearts and healthy hearts [124]. Although iPSC-CMs have the ability to store glycogen, mature iPSC-CMs gener-

ally have a lower capacity of glycogen storage [267], thus highlighting a general metabolic immaturity of iPSC-CMs. However increased glycogen levels may still be responsible for the high level of unlabelled glucose present in pyruvate, as high lactate levels can cause increased glycogen synthesis [268]. The high lactic acid production observed in iPSC-CMs from the Seahorse data may contribute to increased glycogen stores in iPSC-CMs and thus unlabelled glucose.

5.4.3 Increased glycolytic metabolism characterisation using Seahorse assay

A key characterisation of the effect of substrate stiffness on iPSC-CMs was the significant shift in metabolic sources to meet energetic demands. In ageing and failing hearts, a compensatory response to a lack of mitochondrial oxidation and energy deficit is an upregulation of glycolysis [40]. The significantly higher ECAR level identified in iPSC-CMs cultured on plastic compared to both softer PDMS substrates suggests higher lactic acid production, portraying higher glycolytic activity. Increased lactic acid production is typically reflective of the anaerobic activity upregulated in ageing and ischemic hearts [269], [270]. Previous research has demonstrated no differences in ECAR and glycolytic flux between iPSC-CMs six weeks of age compared to twelve weeks of age [271], further reinforcing that the shift towards glycolysis on stiffer substrates was primarily due to stiffness of the ECM, rather than age of iPSC-CMs.

Stiffness of the ECM has been proposed to regulate glycolytic activity of CMs through several pathways and mechanisms. Potential mechanisms of substrate stiffnesses regulating glycolysis involve rho/ROCK actin pathway [272], alterations

in phosphofructokinase [265] or translocation of the GLUT4 transporter [272]. In addition, increased ECM stiffness has been shown to activate YAP/TAZ signalling, which promotes glycolysis in CMs and regulates glycolysis through several mechanisms [273]. It is possible that these pathways could be altered in iPSC-CMs on substrates, thus shifting metabolic activity. Further investigation into the potential alterations in downstream signalling pathways is required.

In addition to glycolytic changes, iPSC-CMs on softer PDMS substrates showed a slightly higher OCR than on plastic, suggesting that stiffness can affect oxidative phosphorylation levels. The slight decline of OCR in iPSC-CMs on plastic reflects features of cardiac disease, with reduction in activity of the ETC and maximal respiration [274]. Furthermore, ATP production from oxidative phosphorylation accounts for 36-38 ATP molecules per glucose oxidised, compared to 2 ATP per glucose for glycolysis alone. Despite findings showing a small increase in ATP-linked respiration on 20kPa PDMS compared to 130kPa PDMS and plastic, this small change may more significantly impact ATP production and therefore may have a greater physiological impact in CMs. iPSC-CMs on stiffer substrates recapitulate metabolic age as literature has shown ATP-linked respiration decreases with ageing, due to impaired activity of ETC complexes, particularly complex III, IV and V [275].

Maturation state of iPSC-CMs can also impact OCR. Studies have demonstrated mature iPSC-CMs have a capacity to switch to glucose utilisation when fatty acid oxidation is compromised [229]. As Chapter 4 has demonstrated, iPSC-CMs cultured on soft substrates undergo structural and functional maturation.

The lack of maturation on stiffer substrates may therefore limit the number and size of mitochondria [257], thus limiting the oxygen consumption of cells, shifting them towards utilising glucose as a primary source of energy production. Future studies could determine the amount of mitochondria present in iPSC-CMs cultured on stiffnesses, such as measurement of mitochondrial DNA to identify whether switches in metabolism were linked to mitochondrial changes. Overall, changes in OCR and ECAR from these experiments clearly display an increased state of glycolysis and lactic acid production in iPSC-CMs on stiffer substrates, correlating well with metabolic ageing and cardiac disease states.

5.4.4 Energetics of CMs on substrates

The ageing phenotype of iPSC-CMs on stiff substrates is further reflected by Seahorse data. Proton leak refers to the migration of protons to the matrix independent of ATP synthase, thus uncoupling substrate oxidation and ATP production [276]. The significantly increased proton leak levels in iPSC-CMs cultured on plastic compared to 20kPa PDMS also supports the concept of cardiac disease phenotypes on stiff substrates. Increased proton leak has been observed in aged mouse mitochondria, with increased proton leak in aged cardiomyocytes occurring through the ANT1 protein [277]. In addition, increased proton leak has been identified in cases when the heart is under oxidative stress, such as ischemic reperfusion injury, thus suggesting proton leak is linked with increased ROS production and decreased viability of CMs [278], [279]. The data demonstrates a strong metabolic characterisation of a glycolytic, aged disease phenotype of CMs

on stiff substrates, indicating signs of mitochondrial damage and a metabolic substrate switch.

5.4.5 iPSC-CMs on stiffer substrates display a cardiac disease profile using Proteomics

TMT-labelled proteomics was conducted to further investigate proteins from iPSC-CMs that may be differentially regulated due to ECM stiffness. Changes in iPSC-CM maturity, structure and switch of metabolic source could influence downstream pathways, thus altering protein expression and function.

5.4.5.1 Increased ECM stiffness induces cardiovascular disease protein expression

Proteomics data indicated signs of a cardiac disease profile of iPSC-CMs cultured on the stiffest substrate, plastic. Aspartate aminotransferase plays a key role in the maintenance of the NAD^+/NADH ratio, which are essential cofactors for glycolysis, the TCA cycle and fatty acid oxidation, thus are key for maintaining cell function and viability [280]. Significantly increased levels of aspartate aminotransferase in iPSC-CMs on plastic compared to 130kPa PDMS may be reflective of the greater metabolic dysregulation on stiff plastics, thus iPSC-CMs are upregulating aspartate aminotransferase to compensate for the stressed metabolic state. Further evidence for iPSC-CMs cultured on stiff substrates showing a cardiac disease profile is highlighted by upregulation of FIS1, which has been identified in cases of murine cardiomyocytes under hypoxic conditions or ischemic reperfu-

sion [281]. FIS1, responsible for regulating mitochondrial fission, has also been shown to lead to mitochondrial fragmentation and disruption of the myocardial network through cell apoptosis [282]. Upregulation of both of these proteins suggests iPSC-CMs on stiffer substrates may be more stressed and therefore begin to indicate signs of cardiac dysfunction.

The switch from fatty acid oxidation to glycolysis in heart failure and ageing is also represented at protein level in iPSC-CMs. HADH is an enzyme that catalyses the third step of β-oxidation, and thus regulates fatty acid utilisation [283]. The downregulation of HADH in iPSC-CMs on plastic compared to 130kPa PDMS indicates a reduction in the utilisation of fatty acids and breakdown through β-oxidation. MPC1, coding for mitochondrial pyruvate carrier 1 acts as a transporter for pyruvate into the mitochondria [284]. An upregulation of MPC1 in iPSC-CMs on plastic compared to 20kPa PDMS may correspond to the anaplerotic metabolism of pyruvate to oxaloacetate, which supports further TCA cycle activity and therefore contribution to the maintenance of mitochondrial membrane potential [284], [285]. The alternative utilisation of pyruvate, other than for oxidative phosphorylation, may reflect the stressed state of iPSC-CMs on stiffer substrates.

Serine protease (HTRA1), an ECM protein involved in collagen 1 secretion and degradation, was significantly downregulated in iPSC-CMs cultured on plastic compared to 130kPa PDMS. Downregulation of serine protease was also identified in iPSC-CMs cultured on plastic compared to 20kPa PDMS, but did not meet the significance threshold. Increased HTRA1 expression has been identified in patients with DCM and is strongly correlated with fibrosis [286]. The downregula-

tion of HTRA1 may be due to the secretion of HTRA1 out of CMs into the media, as an attempt to regulate the fibrotic phenotype on iPSC-CMs on plastic. Despite the lack of significantly differentially expressed proteins, the identified proteins may reflect the subtle changes that stiffness of the myocardium can have on iPSC-CM proteins, with stiffness potentially altering proteins involved in metabolic stress and cardiac disease.

5.4.5.2 Protein characterisation between soft and fibrotic substrates

Stiffnesses in the GPa range displayed changes in protein profiles of iPSC-CMs. To investigate whether physiological and fibrotic ECM stiffnesses altered protein expression, differences between PDMS substrates were assessed.

HADH, a protein involved in the oxidation of fatty acids [283], was differentially downregulated on 20kPa PDMS compared to 130kPa PDMS, contradicting previous evidence of increased fatty acid utilisation on softer substrates. However, the lack of changes in oxidative phosphorylation across substrate stiffnesses in Seahorse and mass spectrometry data indicated that there may not be significant differences in the amount of β-oxidation occurring. In addition, HADH is a component of the mitochondrial trifunctional protein (MTP) with several α and β subunits [157]; downregulation of one component may not alter the overall function of MTP and thus may not alter β-oxidation. Furthermore, as iPSC-CMs in this experiment were not supplemented with fatty acids, the iPSC-CMs did not require the machinery for fatty acid oxidation, which may lead to downregulation of proteins.

iPSC-CM maturity on softer substrates was further highlighted with proteomics data. SORBS2 has been identified as playing a role in cell adhesion, and typically localises with actin organisation [287]. The data indicated a potential increase in SORBS2 on softer 20kPa PDMS compared to 130kPa PDMS. Knockout of CM specific SORBS2 in mice has led to DCM phenotypes with defective microtubule polymerization [288]. Differentially expressed SORBS2 on 130kPa PDMS in combination with the structural disorganisation and changes in contractility of iPSC-CMs on stiffer substrates shown in Chapter 4 indicate 130kPa PDMS may be reflective of a cardiac disease phenotype, both on a molecular and structural level.

5.4.6 Substrate stiffness affects iPSC-CMs metabolic gene expression

Functional data showed alterations in iPSC-CMs metabolism with ECM stiffness. To elucidate whether these changes were recapitulated at transcript level, gene expression levels of key metabolic targets were assessed.

5.4.6.1 Fatty acid transporter gene upregulation on stiff substrates and lipotoxicity

CMs typically have tight regulation between lipid uptake and oxidation to prevent accumulation of excess lipids [70]. Ageing has been linked to lipid toxicity, due to reduced oxidation of fatty acids, thus leading to the accumulation of free fatty acids, often present in cardiac hypertrophy [289], [290]. The balance of β-oxidation and fatty acid uptake was assessed in iPSC-CMs on substrates, to

investigate whether stiffer substrates, which mimic an aged myocardium display altered fatty acid transporter expression.

CPT1B catalyses the carnitine conjugation of long chain fatty acids to facilitate the uptake into the mitochondria for β-oxidation in CMs [291], [292], [293]. Consistent with its role for mitochondrial transportation of fatty acids, CPT1B transcript expression significantly increased in iPSC-CMs treated with OA and PA. A trend of increased CTP1B expression was identified in iPSC-CMs on stiffer substrates compared to softer, although not significantly, which may be due to iPSC-CM batch variability. Previous studies in failing human hearts found that despite other fatty acid oxidation genes being downregulated, CPT1B expression is not suppressed [294]. Furthermore, aged rat hearts show increased CPT1B expression and high triglyceride levels compared to younger hearts [295]. This indicates increased expression of fatty acid transporters may be increased in aged cells, without an increase in β-oxidation, leading to cardiac lipotoxicity. Increased CPT1B transcript expression on stiffer substrates may therefore reflect and contribute to the increased accumulation of lipids seen in aged CMs, thus fitting a disease phenotype. This is supported by literature, where studies identified increased levels of lipid transporters in the elderly myocardium [296], [297].

CD36 plays a significant role in lipid myocardial metabolism, by regulating the uptake of long chain fatty acids in CMs [191]. Similarly to CTP1B expression, when iPSC-CMS were treated with OA and PA, CD36 expression significantly increased, highlighting the role of CD36 in the uptake of long chain fatty acids. Previous studies have shown increased expression of CD36 in aged mouse my-

ocardium; expression may increase to accommodate the accumulation of long chain fatty acids over time, linked to lipid cytotoxicity and myocardial contractile dysfunction [297], [118]. ECM stiffness has also directly been linked to translocation of CD36 to the cell membrane, by activating AMP-activated protein kinase and increasing fatty acid ingestion [272]. Surprisingly, no changes were detected in CD36 transcript expression across substrate stiffnesses. This may be due to the translocation of CD36, which therefore may not alter transcript expression. Furthermore, other factors such as insulin levels and contraction can influence the translocation of CD36 to the sarcolemma [298], which may also alter transcriptional expression. In order to investigate whether stiffness alters fatty acid transporters, further experiments looking at protein expression using western blotting and immunofluorescence to observe localisation could be conducted to further elucidate changes.

5.4.6.2 ECM stiffnesses and upregulation of glycolytic genes

Consistent with previous data shown in this chapter, upregulation of genes involved in glycolysis were detected in iPSC-CMs on stiffer substrates. HK2, which is the predominant hexokinase isoform in the adult heart, catalyses the first step of glucose metabolism, phosphorylating glucose into glucose-6-phosphate (G6P). This can be utilised via catabolic pathways such as glycolysis, or anabolic pathways such as glycogen storage or PPP [299]. A trend of increased expression of HK2 in iPSC-CMs on 130kPa PDMS was identified compared to softer substrates, correlating with the shift to glycolysis in cardiac ageing. Literature supports this,

as increased activity and levels of HK2 were found in hypertrophied hearts, supposedly through increased ROS [300]. However, similar levels of HK2 transcript expression were identified between 20kPa PDMS and plastic stiffnesses, which may highlight the metabolic flexibility of iPSC-CMs to utilise glucose and switch between substrates to meet energetic demand [301].

The metabolic maturity of iPSC-CMs on softer substrates is further reflected at gene level. Phosphofructo-1-kinase muscle type (PFKM) is the enzyme responsible for the regulation of glycolysis, by converting fructose-6-phosphate to fructose-1,6 bisphosphate [302]. As a result, PFKM catalyses the rate limiting step of glycolysis, and thus increases in mature iPSC-CMs in long term cultures [271]. The increased trend of PFKM expression in iPSC-CMs on 20kPa PDMS compared to plastic may reflect the maturity of iPSC-CMs on softer substrates, although no significant differences were found. This is coherent with literature suggesting PFKM downregulation inhibits oxidative phosphorylation and cell apoptosis in a H9c2 CM cell line [303], further supporting the healthier phenotype of iPSC-CMs on softer physiological substrates.

5.4.6.3 Substrate stiffness affects pyruvate decarboxylation

The conversion of pyruvate to acetyl-CoA, known as pyruvate decarboxylation, is an important metabolic step involving key proteins such as PDKs and PDH [275]. PDK4 regulates the switch between glycolysis and glucose oxidation, controlling the flux of pyruvate into the TCA cycle by regulating PDC [304]. Studies have shown lower levels of PDK4 with ageing; three times lower expression of PDK4

was identified in aged mice CMs compared to young mice [305]. The decreased expression of PDK4 in iPSC-CMs on stiffer substrates, both at a gene and protein level, correlate with the increased amount of lactate previously shown in this chapter. This suggests the pyruvate produced from increased glycolytic activity in ageing and cardiac disease could be directly converted to lactate, rather than being oxidised to acetyl-CoA. PDK4 levels can also correlate with maturity of iPSC-CMs, as literature has shown PDK4 expression increases in long term culture of iPSC-CMs, as well as in 3D engineered heart tissue models [306],[271]. The increased PDK4 expression therefore also demonstrates how soft substrates can not only induce maturation of iPSC-CMs structurally, but also metabolically. Additionally, the effect of substrate stiffness on expression of other PDKs could also be explored, in order to confirm whether similar changes are observed.

PDKs also interact with PDH and regulate activity, by phosphorylating PDHA1, a gene encoding for pyruvate dehydrogenase E1 alpha subunit component, part of the PDC [275]. The PDC is a rate-limiting step for glucose oxidation, catalysing the breakdown of pyruvate into acetyl CoA and thus acting as a mediator between glycolysis and the TCA cycle [307]. Studies have shown increased PDH activity and expression of PDH subunits in failing hearts, in combination with decreased PDK4 expression, suggesting a greater reliance on glucose oxidation [308], [309]. However, iPSC-CMs on substrates did not show any significant differences in PDHA1 expression at transcript or protein level.

Interestingly, other subunits of PDC were altered by substrate stiffnesses. DLAT, known as dihydrolipoyl transacetylase or E2, was significantly upregulated

in iPSC-CMs on plastic compared to 130kPa PDMS. The E2 component of PDC has been proposed to be a binding site for other enzymes and consequently can alter the overall rate of the complex [310]. The significant upregulation of this component indicates stiffness may upregulate PDC transcription, influencing PDH protein expression and potentially alter downstream mechanisms, which could alter the conversion of pyruvate into acetyl-CoA. This would be consistent with an ageing and disease phenotype, by reducing the required acetyl-CoA for oxidative phosphorylation. E3, known as dihydrolipoyl dehydrogenase (DLD), displayed similar levels of transcript expression across substrates. The alterations in DLAT expression with stiffness could be further explored by analysing protein level. However, to truly investigate the effect of stiffnesses on activation or inhibition of PDC, the phosphorylation state of PDC subunits should be explored further, as this is the key mechanism of regulation by PDKs. Overall, changes in substrate stiffnesses induces slight trends in metabolic gene expression of iPSC-CMs.

5.4.7 PPARs in iPSC-CM metabolism

The effect of ECM stiffness on PPAR regulation and downstream metabolic pathways are largely undescribed. Much of our understanding of the roles of the PPAR isoforms, PPARα, PPARδ and PPARγ is in metabolic regulation, as they play roles in insulin sensitivity, glucose homeostasis and oxidation of fatty acids and cardiac disease [311]. As PPARs influence metabolic changes in a cardiac context, and metabolic changes were shown to be affected by ECM stiffness,

PPARs were investigated.

5.4.7.1 Substrate stiffness does not affect PPARα or PPARγ expression in iPSC-CMs

Contrary to literature, PPARα expression did not change in response to OA and PA treatment. PPARα is typically the cardiac isoform of interest in iPSC-CMs, and is responsible for the regulation of lipid metabolism by activating genes involved in fatty acid uptake, β-oxidation and ATP production [312]. Extensive evidence suggests that PPARα decreases with ageing and in cardiac diseases such as in hypertrophied hearts and CMs, reducing the capacity for fatty acid oxidation and ultimately resulting in increased rates of glucose utilisation [313], [311]. Despite other changes in PPAR receptor expression, the data showed no changes in PPARα transcript expression in iPSC-CMs across substrate stiffnesses. This may be due to the lack of fatty acids in cell culture media, therefore iPSC-CMs do not require PPARα to regulate lipids. This is further supported by the lack of fatty acid droplets shown in the BODIPY staining with no fatty acid supplementation.

In addition, the lack of PPARα changes may be due to significant alterations of PPARδ expression with stiffness, as PPARδ can activate PPARα targets and has overlapping downstream metabolic pathways, potentially leading to little changes in PPARα [314]. PPARδ can create an autoregulatory loop by inducing the expression of PGC-1α, which, despite being an activator of PPARα, can also further increase the expression of PPARδ [315].

Substrates stiffness did not alter changes in transcript expression of PPARγ

in iPSC-CMs. PPARγ regulates expression of genes involved in fatty acid uptake and storage, whilst also regulating glucose homeostasis and insulin sensitivity [316]. Despite the protective effects of PPARγ in other cell types, increased PPARγ expression in mouse CMs has led to DCM from lipotoxicity and increased triglyceride storage [317]. The lack of changes in *PPARGC1A* transcript expression, a coactivator of PPARγ, further reinforce the lack of relationship between substrate stiffness and PPARγ. In addition, PGC1A is responsible for regulation of mitochondrial quality and function [318], thus suggesting mitochondria may be functioning within the capacity required by iPSC-CMs, causing transcript levels to remain unchanged.

5.4.7.2 Role of PPARδ in iPSC-CMs maturity and metabolic shift on substrate stiffnesses

A key finding of interest was the significantly increased transcript expression of PPARδ in iPSC-CMs cultured on 20kPa PDMS compared to plastic. Ligand-mediated activation of PPARδ has been shown to switch energy production to fatty acid oxidation by increasing fatty acid uptake and catabolism [319]. Previous studies have shown increased expression of PPARδ in iPSC-CMs supplemented with fatty acids [266], [320]. Increased expression and activation of PPARδ has been linked to iPSC-CM maturation, with increased myofibrillar alignment, greater contractility, electrophysiological maturity and enhanced metabolic modifications to switch to fatty acid oxidation rather than glycolysis [321]. The significantly increased expression of PPARδ on 20kPa PDMS is therefore consistent with the

literature, reflecting the overall increased maturation state of iPSC-CMs on softer substrates.

Furthermore, PPARδ KO mice had myocardial lipid accumulation, dysregulated sarcomeric CM structure, reduced fatty acid oxidation gene expression and cardiac hypertrophy in mice [322]. This reinforces the role of PPARδ in iPSC-CMs maintaining fatty acid oxidation and cardiac function on softer substrates. A trend towards increased protein expression levels of PPARδ corroborates the link between softer substrates and upregulation of genes involved in fatty acid oxidation. Literature has also shown PPARδ activation in iPSC-CMs increases expression of genes linked to fatty acid oxidation, such as PDK4 and CD36 [321]. The increased trend of PDK4 at protein and gene expression level on 20kPa PDMS is therefore also consistent with the changes in PPARδ and literature.

The decline in PPARδ expression with increased stiffness and ageing may be linked to the production of ROS, which has been heavily associated with ageing [316], [296]. PPARδ has been shown to regulate the expression of antioxidants, copper/zinc superoxide dismutase (SOD1) and manganese superoxide dismutase (SOD2), supporting the antioxidant role of PPARδ [323]. Substrate stiffness may link to the mitochondrial theory of ageing, with disrupted redox regulation, increased ROS production and mitochondrial damage occurring with age, consequently altering metabolism [324].

In summary, the data exhibits evidence of altered PPARδ expression in iPSC-CMs with ECM stiffness. Increased stiffness is potentially linked to downregulation of genes involved in oxidative phosphorylation and the immaturity of iPSC-

CMs.

5.5 Conclusion

To conclude, ECM stiffness can directly impact the metabolic function of iPSC-CMs. Stiffer substrates induce a switch to increased glycolytic metabolism and increased lactic acid production, reflective of a cardiac disease and ageing phenotype. Furthermore, substrate stiffness can influence the expression of metabolic genes, with novel evidence of increased PPARδ expression on softer substrates, indicating a shift towards metabolic maturity. Substrate stiffness can also impact protein levels of metabolic genes. In addition, 20kPa and 130kPa PDMS can serve as accurate models for healthy and fibrotic stiffnesses of the ECM, with both stiffnesses demonstrating changes in metabolism of iPSC-CMs. Further characterisation of metabolic genes of interest identified from the chapter at protein expression level and post translational modifications linked to activity, such as phosphorylation status in iPSC-CMs on substrate stiffnesses would be informative. Localisation of key metabolic proteins where relevant and investigation into the activity of these key metabolic enzymes can help confirm metabolic mechanisms and pathways that are altered.

Chapter 6

Phenoage and longitudinal changes on transthoracic echocardiography in Alström Syndrome: a disease of accelerated ageing?

6.1 Publication

This research was originally published as a research article in *Geroscience*, 2024.

Patel, L., Roy, A., Alvior, A.M.B.,Yuan, M., Baig, S., Bunting, K.V., Hodson, J., Gehmlich, K., Lord, J.M., Geberhiwot, T., Steeds, R.P. Phenoage and longitudinal changes on transthoracic echocardiography in Alström syndrome: a disease of accelerated ageing?

6.2 Author Contributions

Author contributions are listed below.

Leena Patel Roles: Conceptualization, Data Curation, Formal Analysis, Investigation, Methodology, Project Administration, Resources, Software, Supervision, Validation, Visualization, Writing – Review & Editing

Ashwin Roy Roles: Conceptualization, Data Curation, Formal Analysis, Methodology, Project Administration, Resources, Writing – Original Draft Preparation, Writing – Review & Editing

Amor Mia B Alvor Roles: Resources, Data Curation, Methodology, Writing – Review & Editing

Mengshi Yuan Roles: Resources, Data Curation, Methodology, Writing – Review & Editing

Shanat Baig Roles: Resources, Data Curation, Methodology, Writing – Review & Editing

Karina Bunting Roles: Resources, Data Curation, Methodology, Writing – Review & Editing

James Hodson Roles: Methodology, Data Curation, Formal Analysis, Software, Visualization, Writing – Review & Editing

Katja Gehmlich Roles: Conceptualization, Funding acquisition, Project Administration, Supervision, Writing – Review & Editing

Janet M Lord Roles: Conceptualization, Resources, Project Administration, Supervision, Writing – Review & Editing

Tarekegn Geberhiwot Roles: Conceptualization, Resources, Project Admin-

istration, Supervision, Writing – Review & Editing

Richard P Steeds Roles: Conceptualization, Funding acquisition, Project Administration, Supervision, Writing – Review & Editing

GeroScience (2024) 46:1989–1999
https://doi.org/10.1007/s11357-023-00959-3

ORIGINAL ARTICLE

Phenoage and longitudinal changes on transthoracic echocardiography in Alström syndrome: a disease of accelerated ageing?

Leena Patel · Ashwin Roy · Amor Mia B Alvior · Mengshi Yuan · Shanat Baig · Karina V. Bunting · James Hodson · Katja Gehmlich · Janet M Lord · Tarekegn Geberhiwot · Richard P. Steeds

Received: 6 September 2023 / Accepted: 21 September 2023 / Published online: 2 October 2023

Abstract Alström syndrome (AS) is an ultra-rare disorder characterised by early-onset multi-organ dysfunction, such as insulin resistance, obesity, dyslipidaemia, and renal and cardiovascular disease. The objective is to explore whether AS is a disease of accelerated ageing and whether changes over time on echocardiography could reflect accelerated cardiac ageing. Cross-sectional measurement of Phenoage and retrospective analysis of serial echocardiography were performed between March 2012 and November 2022. The setting is a single national tertiary service jointly run by health service and patient charity. Forty-five adult patients aged over 16 years were included, 64% were male and 67% of White ethnicity. The median Phenoage was 48 years (interquartile range [IQR]: 35–72) in the 34 patients for whom this was calculable, which was significantly higher than the median chronological age of 29 years (IQR: 22–39, $p<0.001$). Phenoage was higher than chronological age in 85% ($N=29$) of patients, with a median difference of +18 years (IQR: +4, +34). On echocardiography, significant decreases were observed over time in left ventricular (LV) size at end-diastole (average of 0.046 cm per year, $p<0.001$) and end-systole (1.1% per year, $p=0.025$), with significant increase in posterior wall thickness at end-diastole (0.009 cm

Supplementary Information The online version contains supplementary material available at https://doi.org/10.1007/s11357-023-00959-3.

L. Patel · A. Roy · K. V. Bunting · K. Gehmlich · R. P. Steeds
Institute of Cardiovascular Sciences, University of Birmingham, Birmingham, UK

A. Roy (✉) · A. M. B. Alvior · M. Yuan · S. Baig · K. V. Bunting · R. P. Steeds
Department of Cardiology, University Hospital Birmingham NHS Foundation Trust, Birmingham, Birmingham, UK
e-mail: a.roy@bham.ac.uk

J. Hodson
Research Development and Innovation, University Hospitals Birmingham NHS Foundation Trust, Birmingham, Birmingham, UK

K. Gehmlich
Division of Cardiovascular Medicine, Radcliffe Department of Medicine and British Heart Foundation Centre of Research Excellence Oxford, University of Oxford, Oxford, UK

J. M. Lord
MRC-Versus Arthritis Centre for Musculoskeletal Ageing Research, Institute of Inflammation and Ageing, University of Birmingham, Birmingham, UK

T. Geberhiwot
Department of Endocrinology, University Hospital Birmingham NHS Foundation Trust, Birmingham, Birmingham, UK

T. Geberhiwot
Institute of Metabolism and System Research, University of Birmingham, Birmingham, UK

per year, p=0.008). LV systolic function measured by global longitudinal strain reduced (0.34 percentage points per year, p=0.020) and E/e'lat increased (2.5% per year, p=0.019). Most AS patients display a higher Phenoage compared to chronological age. Cardiac changes in AS patients were also reflective of accelerated ageing, with a reduction in LV size and increased wall thickening. AS may be a paradigm disease for premature ageing.

Keywords Ageing · Echocardiography · Phenoage · Cardiovascular · Rare diseases

Introduction

Alström syndrome (AS) is a rare autosomal recessive ciliopathy characterised by childhood retinal dystrophy, neuronal hearing loss and obesity [1]. The phenotype has since been extended to incorporate extreme insulin resistance, type 2 diabetes, dyslipidaemia, accelerated non-alcoholic fatty liver disease and premature renal and cardiovascular disease [2]. The syndrome is caused by loss of function genetic variants in *ALMS1*, a 23-exon gene located on chromosome 2p13 [3]. Infantile cardiomyopathy is the earliest and one of the most frequent manifestations of the syndrome, although the majority survive with apparent complete cardiovascular recovery [4]. However, in a significant proportion, cardiovascular disease either recurs or manifests for the first time in adulthood, with high rates of morbidity and mortality. Both the quality and length of life are reduced in adults with AS, and few survive beyond 50 years [5].

In adult AS subjects, autopsy data demonstrate replacement myocardial fibrosis in non-coronary artery patterns, and diffuse interstitial fibrosis has been detected on cardiovascular magnetic resonance (CMR) by elevation in T1 relaxation and increased extracellular volume [6]. Cardiac fibrosis provokes pathological changes culminating in chamber dilatation, cardiomyocyte hypertrophy and cellular hypertrophy, leading to reduced compliance and accelerated progression to heart failure. Previous studies of AS using echocardiography were limited to a case series that included patients with advanced disease with impaired ejection fraction (EF) [7] and a cross-sectional study of a younger cohort with impaired global longitudinal strain (GLS) [8]. Whilst AS is rare, it offers a model of accelerated cardiomyopathy that reflects disease processes that are common in the ageing population. Given the lack of genotype-phenotype correlation in AS, it is feasible that these fibrotic changes may reflect the long-term impact of obesity, insulin resistance and metabolic syndrome.

Phenoage is a reliable measure of biological ageing calculated using chronological age and nine blood markers representing the functional state of organs [9]. Albumin and alkaline phosphatase (ALP) represent the liver, creatinine the kidney, glucose the pancreas, c-reactive protein (CRP), lymphocyte immune cell percentage and white blood cell count (WCC) represent immune ageing, mean cell volume (MCV) and red cell distribution width (RDW) represent bone marrow age. Phenoage is a reliable predictor for a variety of ageing outcomes, including all-cause mortality, cancer, health span, and physical functioning, but does not incorporate cardiac ageing.

Therefore, the aims of this study were [1] to explore the possibility that AS is a paradigm for accelerated ageing and [2] to explore cardiovascular changes over time in AS.

Methods

Ethics

This study was limited to secondary use of information previously collected during normal care (without an intention to use it for research at the time of collection) and is therefore excluded from ethical review according to the UK Health Research Authority decision tool and was registered at our centre as an audit (CARMS-18179).

Study design

This was an observational, retrospective review of adults (aged over 16 years) with genetically proven AS attending the National Centre for Alström Syndrome at the Queen Elizabeth Hospital Birmingham, UK. Patients attend the centre approximately annually for follow-up assessments, which include blood sampling and transthoracic echocardiography (TTE). All such assessments occurring between March 2012 and November 2022 (the date of data extraction) were identified, and demographic, clinical, biochemical, and cardiovascular data collected were extracted from patient records.

Data were also collected on comorbidities. History of cardiomyopathy was defined as a history of infantile cardiomyopathy [10], presence of myocardial fibrosis identified by late gadolinium enhancement in a non-ischaemic pattern on CMR, and restrictive cardiomyopathy. Ischaemic heart disease was defined as previous myocardial infarction or history of coronary revascularization. Diabetes included a history of both type 1 and 2, regardless of treatment. Renal impairment was defined an estimated glomerular filtration rate (eGFR) <90 mL/min/1.73 m^2.

Phenoage

Phenoage was calculated using chronological age and the above nine clinical blood test parameters. Eight of the nine blood markers were included in the routine panel of blood tests performed at every follow-up assessment. However, CRP only became part of this panel in the final year of the study period. As such, Phenoage was only calculated for the most recent assessment for each patient, and those without a CRP were excluded from analyses of Phenoage.

The cohort was divided into groups based on the difference between their chronological and Phenoage at the final scan. Patients where this difference was within ±10 years were classified as having "concordant" Phenoage, with those with a difference of >10 years classified as "discrepant" Phenoage [9].

Transthoracic echocardiography

Resting transthoracic echocardiography (TTE; ie33 and EPIC, Phillips) was performed by an accredited sonographer (AMA) according to the British Society of Echocardiography minimum dataset [11]. Diastolic function was graded by an experienced cardiologist specialising in echocardiography (RPS) according to current guidelines. Linear internal measurements were obtained from 2D images in the parasternal long axis measured immediately below mitral valve leaflet tips. 2D volumetric measurements were also recorded. There was a focus on parameters considered to be age dependent; a full list of these parameters, along with definitions of the abbreviations used, is reported in Supplementary Table 1.

Statistical methods

Initially, chronological age and Phenoage at the final scan were compared using Wilcoxon's Signed Ranks test. This relationship was further assessed using a linear regression model, with the resulting gradient compared to a value of 1, to assess whether Phenoage was increasing at a different rate to chronological age. The Phenoage discrepancy at the final scan was calculated for each patient as Phenoage *minus* chronological age. Patient characteristics, blood markers and TTE parameters were compared between patients with concordant and discrepant Phenoage, using Mann-Whitney *U* tests for continuous variables and Fisher's exact tests for nominal variables.

Trends over time in blood markers and TTE parameters were then assessed for the whole cohort, as well as by Phenoage discrepancy. Analyses of these factors needed to account for the non-independence of repeated measures on the same patient, which was achieved using two different approaches. The first used generalised estimating equations (GEEs) to adjust for the correlations between repeated measures on the same patient. The second used an "individual regressions" approach, which produced a separate regression model for each patient to estimate the rate of change over time; the gradients of which were extracted and used for analysis. These two approaches applied different weightings to repeated measures on the same patient, with the GEE approach giving greater influence to patients with greater numbers of scans, whilst the individual regressions approach weighted all patients equally. Further details about the two approaches are detailed in the Supplementary Material. Gradients from the models are reported as units per year, % per year, or percentage points (pps) per year, as applicable, along with 95% confidence intervals (95% CIs). Continuous variables are summarised as mean ± standard deviation where approximately normally distributed or as median (interquartile range (IQR)) otherwise; correlation coefficients are reported as Spearman's rank correlation coefficients (rho). All analyses were performed using IBM SPSS 24 (IBM Corp. Armonk, NY), with $p<0.05$ deemed to be indicative of statistical significance throughout.

Results

Cohort characteristics

Of the $N=49$ AS patients treated at the centre, $N=4$ opted for continued follow-up at their local centre after their initial assessment and so were excluded

from analysis. The remaining *N*=45 patients were followed up for a median of 6.0 years (IQR: 3.2–9.5), during which they attended a total of 257 follow-up assessments (median: 6 per patient, IQR: 2–8, maximum: 12). The final scan was within one year of data collection in *N*=30 patients; of the remainder, *N*=6 died and *N*=9 were due their next assessment. Patients had median ages of 21 years (IQR: 19–33) and 29 years (IQR: 23–39) at the first and final scan, respectively. Further details of the cohort are reported in Table 1.

Phenoage

Analyses of Phenoage only included data from the blood tests taken at each patient's final scan. This resulted in *N*=11 patients being excluded due to lack of CRP values at the time of final scan. Of these, *N*=10 had their final scan prior to CRP being routinely recorded, and *N*=1 did not undergo at blood test at their final scan. The remaining *N*=34 patients had a median Phenoage of 48 years (IQR: 35–72) at their final scan, which was significantly higher than the median

Table 1 Cohort characteristics

	Whole cohort (*N*=45)	By Phenoage at final scan (*N*=34)		
		Concordant (N=11)	*Discrepant (N=23)*	*p* value
Demographics				
Chronological age (years)				
First scan	21 (19–33)	19 (18–24)	21 (18–39)	0.329
Final scan	29 (23–39)	27 (21–54)	30 (22–41)	0.348
Gender (% male)	29 (64%)	6 (55%)	15 (65%)	0.709
Ethnicity (% White)	30 (67%)	7 (64%)	17 (74%)	0.692
SBP (at first scan)	130 ± 17	130 ± 21	130 ± 16	0.713
DBP (at first scan)	82 ± 10	83 ± 11	82 ± 10	0.754
Comorbidities*				
Cardiomyopathy	23 (51%)	5 (45%)	11 (48%)	1.000
Ischaemic heart disease	7 (16%)	1 (9%)	2 (9%)	1.000
Hypertension	32 (71%)	6 (55%)	17 (74%)	0.434
Hyperlipidaemia	33 (73%)	6 (55%)	17 (74%)	0.434
Diabetes	37 (82%)	8 (73%)	21 (91%)	0.300
Renal impairment	17 (38%)	0 (0%)	13 (57%)	**0.002**
Physiological markers at final scan**				
Heart rate (bpm)	85 ± 13	80 ± 14	89 ± 9	0.071
Albumin (g/L)	42 ± 4	43 ± 3	40 ± 3	**0.023**
ALP (U/L)	86 (72–108)	71 (56–75)	94 (82–136)	**<0.001**
Creatinine (μmol/L)	97 (78–144)	78 (69–85)	116 (87–148)	**0.002**
Glucose (mmol/L)	6.9 (5.1–12.4)	4.8 (4.0–6.7)	9.9 (5.9–15.9)	**0.002**
HbA1c	53 (39–71)	38 (36–42)	60 (49–77)	**0.002**
CRP (mg/L)	4 (2–16)	2 (1–15)	6 (3–17)	0.133
Lymphocyte (%)	26.9 ± 8.5	28.9 ± 6.3	23.7 ± 8.6	**0.038**
WCC (10^9/L)	8.7 ± 2.2	9.0 ± 2.7	9.0 ± 2.2	0.854
MCV (Fl)	86.8 ± 6.1	87.5 ± 4.3	87.2 ± 6.4	0.568
RDW (%)	15 (13–16)	14 (13–14)	15 (13–18)	**0.043**

Continuous variables are reported as mean ± standard deviation, or as median (interquartile range), with *p* values from Mann-Whitney *U* tests. Nominal variables are reported as *N* (%), with *p* values from Fisher's exact tests. Bold *p* values are significant at $p<0.05$

*As diagnosed either at baseline or at any point during follow-up

**Data for the whole cohort were only available for *N*=44 for the blood markers, with the exception of CRP, which was only available in *N*=34

chronological age of 29 years (IQR: 22–39, $p<0.001$). Phenoage was higher than chronological age in 85% ($N=29$) of patients, with a median difference of +18 years (IQR: +4, +34), and the largest difference being in a patient with a Phenoage vs. chronological age of 96 vs. 22 years. The association between chronological and Phenoage was assessed using a linear regression approach, visualised in Fig. 1. The gradient of the resulting model, representing the estimated increase in Phenoage per one year of chronological age, was 1.24 (95% CI: 0.54–1.94), which did not differ significantly from a value of 1 ($p=0.448$).

The cohort was divided into subgroups with concordant Phenoage ($N=11$; differences ranging from −8 to +8 years) and discrepant Phenoage ($N=23$; differences ranging from +11 to +74 years, all of whom had a Phenoage greater than chronological age). Comparisons between these two groups found no significant differences in baseline demographics (Table 1). Analysis of comorbidities identified a significant difference in the rates of renal impairment, with a rate of 0% in those with concordant Phenoage, compared to 57% in the discrepant group, with analysis of blood markers at the final scan similarly finding significantly higher creatinine levels in those with discrepant Phenoage (median: 116 vs. 78 µmol/L). Those with discrepant Phenoages also had significantly higher ALP, glucose, HbA1c and RDW levels, as well as significantly lower albumin and lymphocyte counts. Analysis of TTE parameters at the final scan found only LVEDvol 2D to differ significantly between subgroups ($p=0.035$, Supplementary Table 2).

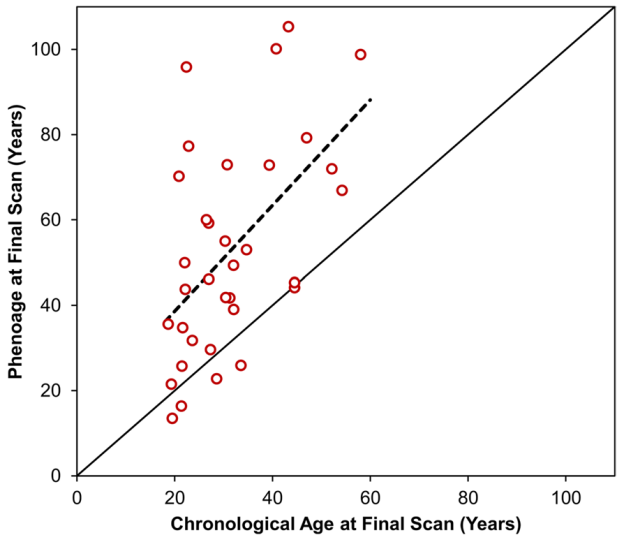

Fig. 1 Association between chronological and Phenoage at the final scan. The plot only includes those patients where the Phenoage was calculable at the final scan ($N=34$). The solid line is plotted at $y=x$, and the broken line is from a linear regression model

Trends in blood markers and TTE parameters for the whole cohort

For the cohort of $N=45$ patients, GEE analysis identified significant progression in three blood markers (Table 2), with albumin declining by an average of 0.44 g/L per calendar year, lymphocytes declining by 0.52 pp per year, and creatinine increasing by 2.6% per year. Of the TTE parameters considered, significant decreases were observed in LVEDd and LVESd, with significant increases in LVPWd and LVESvol 2D (Table 2). Analysis using the individual regressions approach in the $N=32$ with data for more than two scans returned similar results, additionally identifying significant increases over time in ALP (2.2% per year), glucose (5.9% per year), GLS total (0.34 pp per year,) and E/e'lat (2.5% per year).

Trends in blood markers and TTE parameters by Phenoage discrepancy

Both statistical approaches found significant differences in two TTE parameters by Phenoage discrepancy (Table 3). The first was MV A max, which the GEE approach found to be increasing by 1.07 cm/s per year in those with concordant Phenoage, compared to a reduction of 0.28 cm/s per year in those with discrepant Phenoage ($p=0.023$, Supplementary Fig. 1a/b). The individual regressions approach returned similar results, with a negative correlation between the degree of Phenoage discrepancy and MV A max gradient (rho: −0.495, $p=0.016$, Fig. 2a). The second parameter was E/A, for which the GEE analysis identified trends of −2.5% vs. +0.4% per year for concordant vs. discrepant Phenoage ($p=0.020$, Supplementary Fig. 1c/d), with the individual regressions approach finding a significant positive correlation between the degree of Phenoage discrepancy and E/A gradient (rho: 0.451, p=0.031, Fig. 2b).

The GEE approach additionally identified a significant difference in the gradients for EF, which was increasing by 0.97 pp per year in those with concordant Phenoage, but decreasing by 0.29 pp per year in those where this was discrepant ($p=0.025$, Supplementary Fig. 1e/f).

Table 2 Trends in blood markers and TTE parameters for the whole cohort

Parameter	GEE approach				Individual regressions approach		
	No. Pts.	*No. Scn.*	*Gradient per year (95% CI)*	*p value*	*No. Pts.*	*Gradient per year (95% CI)*	*p value*
Albumin (g/L)	45	251	−0.44 (−0.62, −0.26)	**<0.001**	32	−0.78 (−1.03, −0.53)	**<0.001**
ALP*	45	251	0.7% (−0.8%, 2.1%)	0.387	32	2.2% (0.3%, 4.1%)	**0.027**
Creatinine*	45	251	2.6% (0.4%, 4.7%)	**0.019**	32	3.2% (0.5%, 6.0%)	**0.020**
Glucose*	45	251	0.8% (−1.7%, 3.3%)	0.545	32	5.9% (0.5%, 11.5%)	**0.034**
WCC (10^9/L)	45	251	−0.03 (−0.11, 0.06)	0.518	32	−0.16 (−0.34, 0.02)	0.075
Lymphocyte (pp**)	45	251	−0.52 (−0.82, −0.22)	**<0.001**	32	−0.60 (−1.08, −0.12)	**0.017**
MCV (Fl)	45	251	0.07 (−0.21, 0.35)	0.642	32	0.03 (−0.29, 0.35)	0.863
RDW (pp**)	45	251	0.04 (−0.05, 0.13)	0.412	32	0.13 (−0.04, 0.30)	0.130
Heart rate (bpm)	45	256	0.35 (−0.25, 0.95)	0.251	32	0.78 (−0.39, 1.96)	0.184
LVIVSd (cm)	45	245	−0.006 (−0.012, 0.001)	0.090	32	−0.004 (−0.012, 0.003)	0.272
LVEDd (cm)	45	248	−0.046 (−0.071, −0.021)	**<0.001**	32	−0.042 (−0.064, −0.020)	**0.001**
LVPWd (cm)	45	245	0.009 (0.002, 0.015)	**0.008**	32	0.016 (0.007, 0.025)	**0.002**
LVESd*	45	231	−1.1% (−2.0%, −0.1%)	**0.025**	32	−1.0% (−1.8%, −0.1%)	**0.031**
EF (pp**)	45	222	−0.03 (−0.56, 0.50)	0.921	32	−0.37 (−0.97, 0.23)	0.215
LVEDvol 2D (ml)	41	133	0.51 (−1.09, 2.10)	0.534	28	0.14 (−1.81, 2.10)	0.880
LVESvol 2D*	41	133	2.8% (0.1%, 5.7%)	**0.042**	28	3.8% (0.3%, 7.4%)	**0.032**
LVEF 2D (pp**)	41	133	−0.44 (−1.13, 0.24)	0.207	28	−1.23 (−2.52, 0.06)	0.061
GLS 4C (pp**)	42	157	0.01 (−0.17, 0.19)	0.913	30	0.09 (−0.20, 0.37)	0.541
GLS total (pp**)	42	156	0.17 (−0.05, 0.39)	0.136	30	0.34 (0.06, 0.63)	**0.020**
LAV*	44	245	0.5% (−1.3%, 2.3%)	0.585	32	1.9% (−0.2%, 4.1%)	0.080
MV E max (cm/s)	45	250	−0.14 (−0.73, 0.44)	0.635	32	0.49 (−0.48, 1.45)	0.310
MV A max (cm/s)	44	242	0.01 (−0.60, 0.62)	0.971	31	−0.03 (−0.74, 0.69)	0.941
MV DT (ms)	43	222	−0.81 (−2.34, 0.72)	0.298	30	0.10 (−5.67, 5.87)	0.973
E/A*	44	241	−0.9% (−2.1%, 0.4%)	0.175	31	0.2% (−1.7%, 2.1%)	0.810
E/E'lat*	45	245	1.4% (−0.1%, 2.8%)	0.064	32	2.5% (0.4%, 4.7%)	**0.019**
E/E'sep	45	235	0.09 (−0.09, 0.26)	0.321	32	0.21 (−0.05, 0.48)	0.113
TDI RV s (cm/s)	43	155	0.07 (−0.10, 0.25)	0.416	31	−0.04 (−0.27, 0.19)	0.712
AV Vmax (cm/s)	45	219	−0.26 (−1.28, 0.76)	0.616	32	0.55 (−0.66, 1.76)	0.362
LVOT Vmax (cm/s)	45	219	−0.08 (−0.83, 0.66)	0.827	32	−0.64 (−1.29, 0.01)	0.054

Analyses were performed using two different approaches. The generalised estimating equation (GEE) approach used GEE models with the timing of the scan test, relative to the first scan, as a covariate, and the stated parameter as the dependent variable. The individual regressions approach first produced separate regression models for each patient with >2 scans (N=32) and then took the mean of the resulting gradients, using a one-sample t-test, to compare this to a value of zero. Further details of the methodologies used are reported in the Supplementary Material. For both approaches, gradients represent the rate of change per year in each parameter. Bold p values are significant at $p<0.05$

*Parameter was log-transformed prior to analysis to improve model fit; the resulting coefficient was then anti-logged and converted into a percentage change per year

**Gradients are reported in percentage points (pps) per year (e.g. a value of 1 would represent an increase from 55 to 56% in one year)

No. Pts. number of pts, *No. Scn.* number of scans

However, the individual regressions analysis found no significant association between the degree of Phenoage discrepancy and the EF gradient, with the effect being in the opposite direction (rho: 0.183, p=0.391).

The individual regressions approach also identified significant positive correlations between the degree of Phenoage discrepancy and gradients in both ALP (p=0.015, Fig. 2c) and creatinine

Table 3 Trends in blood markers and TTE parameters by Phenoage discrepancy at the final scan

Parameter	Generalised estimating equation approach					Individual regressions approach		
	No. Pts.	*No. Scn.*	*Gradient: concordant subgroup*	*Gradient: discrepant subgroup*	*Interaction p value*	*No. Pts.*	*Spearman's rho*	*p value*
Albumin (g/L)	34	194	−0.46 (−0.84, −0.07)	−0.40 (−0.61, −0.18)	0.792	24	−0.330	0.115
ALP*	34	194	−1.7% (−4.3%, 1.0%)	1.5% (−0.2%, 3.3%)	0.051	24	0.492	**0.015**
Creatinine*	34	194	0.7% (−1.6%, 3.1%)	2.9% (−0.3%, 6.3%)	0.283	24	0.424	**0.039**
Glucose*	34	194	−0.1% (−3.7%, 3.6%)	1.1% (−2.3%, 4.5%)	0.638	24	0.392	0.058
WCC (10^9/L)	34	194	0.00 (−0.10, 0.10)	0.02 (−0.11, 0.14)	0.843	24	−0.345	0.098
Lymphocyte (pp**)	34	194	−0.57 (−1.09, −0.05)	−0.54 (−0.91, −0.17)	0.925	24	−0.109	0.613
MCV (Fl)	34	194	−0.23 (−0.56, 0.10)	0.15 (−0.26, 0.56)	0.163	24	0.102	0.636
RDW (pp**)	34	194	−0.02 (−0.09, 0.05)	0.03 (−0.09, 0.16)	0.506	24	0.101	0.639
Heart rate (bpm)	34	194	1.05 (−0.09, 2.19)	0.37 (−0.32, 1.05)	0.314	24	−0.128	0.552
LVIVSd (cm)	34	186	−0.004 (−0.017, 0.009)	−0.007 (−0.016, 0.001)	0.670	24	−0.289	0.171
LVEDd (cm)	34	188	−0.053 (−0.103, −0.002)	−0.025 (−0.054, 0.003)	0.357	24	−0.034	0.875
LVPWd (cm)	34	186	0.008 (−0.006, 0.022)	0.008 (−0.001, 0.017)	0.998	24	−0.350	0.094
LVESd*	34	179	−1.7% (−3.3%, −0.2%)	−0.5% (−1.7%, 0.7%)	0.224	24	0.075	0.728
EF (pp**)	34	172	0.97 (0.12, 1.83)	−0.29 (−0.99, 0.41)	**0.025**	24	0.183	0.391
LVEDvol 2D (mL)	32	102	1.40 (−1.99, 4.78)	0.99 (−1.10, 3.08)	0.842	23	0.123	0.578
LVESvol 2D*	32	102	7.6% (0.1%, 15.7%)	3.0% (−0.7%, 6.9%)	0.294	23	0.021	0.925
LVEF 2D (pp**)	32	102	0.00 (−1.10, 1.10)	−0.57 (−1.43, 0.29)	0.423	23	0.118	0.593
GLS 4C (pp**)	32	124	−0.20 (−0.48, 0.07)	0.06 (−0.14, 0.27)	0.548	24	−0.227	0.286
GLS total (pp**)	32	123	0.01 (−0.26, 0.28)	0.20 (−0.11, 0.51)	0.357	24	−0.284	0.178
LAV*	33	187	−2.5% (−6.1%, 1.2%)	1.1% (−1.1%, 3.4%)	0.099	24	−0.346	0.098
MV E max (cm/s)	34	190	−0.52 (−1.66, 0.63)	0.07 (−0.61, 0.76)	0.387	24	0.070	0.744
MV A max (cm/s)	33	184	1.07 (0.23, 1.91)	−0.28 (−1.09, 0.53)	**0.023**	23	−0.495	**0.016**
MV DT (ms)	32	172	−0.99 (−3.24, 1.26)	−0.74 (−3.02, 1.54)	0.879	23	0.301	0.162
E/A*	33	184	−2.5% (−4.3%, −0.6%)	0.4% (−1.1%, 1.9%)	**0.020**	23	0.451	**0.031**
E/E'lat*	34	186	1.4% (−1.5%, 4.4%)	1.1% (−0.4%, 2.6%)	0.857	24	−0.127	0.554
E/E'sep	34	177	0.02 (−0.27, 0.31)	0.12 (−0.13, 0.37)	0.617	24	−0.047	0.828
TDI RV s (cm/s)	32	117	0.04 (−0.12, 0.19)	0.12 (−0.17, 0.42)	0.623	23	−0.350	0.101
AV Vmax (cm/s)	34	166	−0.63 (−1.83, 0.57)	−0.22 (−1.77, 1.32)	0.684	24	0.076	0.725
LVOT Vmax (cm/s)	34	166	1.02 (0.29, 1.74)	−0.27 (−1.41, 0.87)	0.063	24	−0.193	0.366

For the generalised estimating equation (GEE) approach, only *N*=34 patients for whom Phenoage was calculable at the final scan were included. GEE models were produced with the stated parameter as the dependent variable and the timing of the scan/blood test, subgroup (discrepant vs. concordant Phenoage) and an interaction term as covariates. The "gradients" represent the rate of change per year in each parameter and are reported with the 95% confidence interval; the "interaction" is the *p* value for the interaction term in the model, representing a comparison between the gradients in the two subgroups. The individual regressions approach first produced separate regression models for each patient with >2 scans for whom Phenoage was calculable at the final scan (*N*=24). The correlations between the resulting gradients and the Phenoage discrepancy (Phenoage minus chronological age) were then assessed using Spearman's rho. Further details of the methodologies used are reported in the Supplementary Material. Bold *p* values are significant at $p<0.05$

*Parameter was log-transformed prior to analysis to improve model fit; the resulting gradient was then anti-logged and converted into a percentage change per year

**Gradients are reported in percentage points (pps) per year (e.g. a value of 1 would represent an increase from 55 to 56% in one year)

No. Pts. number of pts, *No. Scn.* number of scans

(p=0.039, Fig. 2d), implying that these markers saw more pronounced increases over time in those with more discrepant Phenoage; similar trends were observed in the GEE analyses.

Discussion

In this longitudinal study of the largest cohort of AS patients published, we identified accelerated ageing

as a defining feature, with most adults displaying an advanced Phenoage compared with chronological age. In the cohort, 85% of patients with Phenoage data exhibited a higher Phenoage than chronological age, consistent with the reduced life expectancy observed in AS.

There was no evidence to suggest that Phenoage increased at a faster rate than chronological age in this

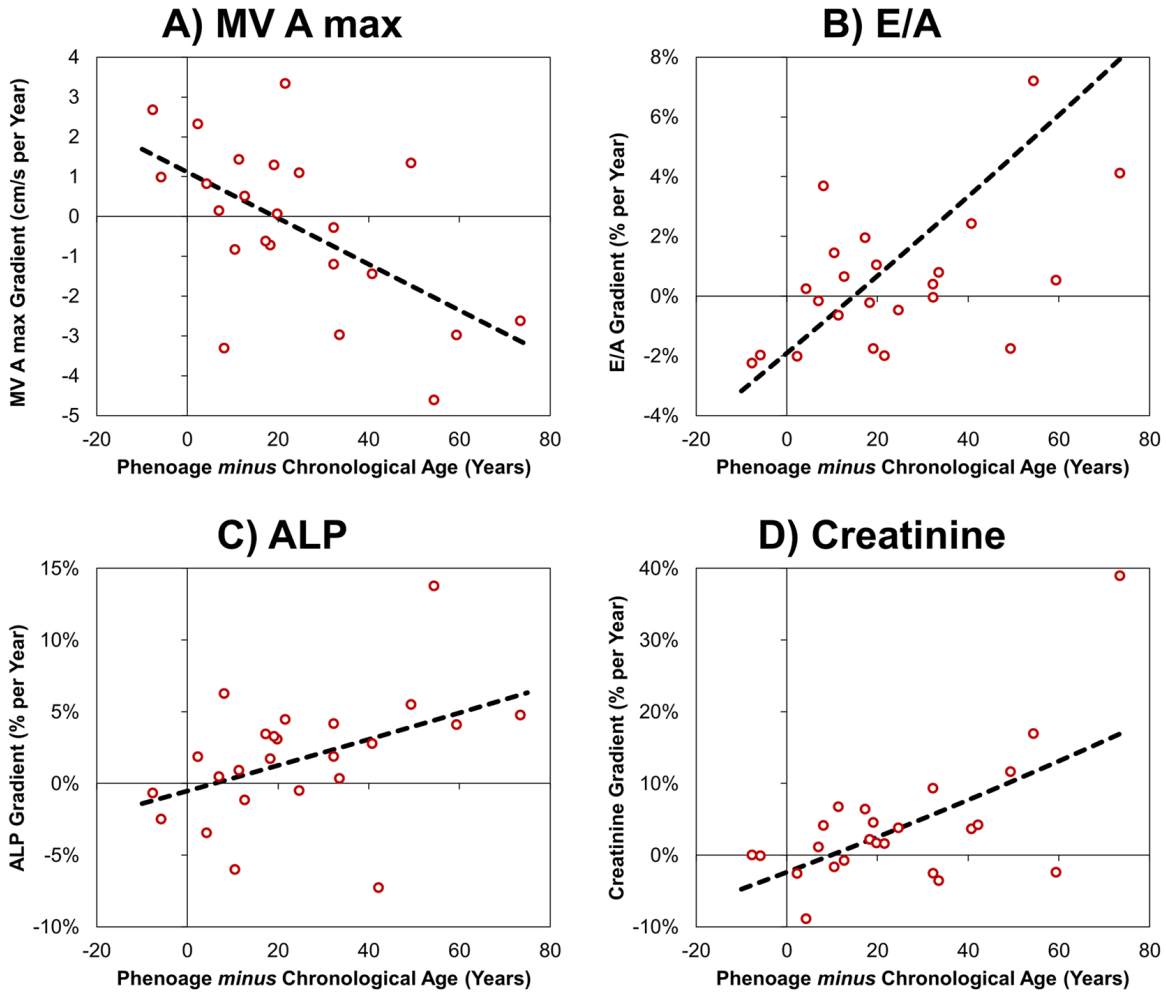

Fig. 2 Associations between the magnitude of Phenoage discrepancy and trends in blood markers/TTE parameters. Points represent individual patients, with gradients calculated as per the individual regressions approach (see Table 3) and the magnitude of the Phenoage discrepancy calculated at the final scan. Broken lines are from linear regression models

indicating impaired structural and functional status of organs at an earlier age than expected. This raises the possibility that AS is a paradigm disease for accelerated ageing, with potential to act as a model for multi-organ dysfunction that occurs with obesity, insulin resistance, type 2 diabetes, and dyslipidaemia. The dysregulation and impairment of underlying biological processes may therefore act as a mechanism of premature ageing, cohort; instead, the discrepancy appeared to be present at referral to the service and to persist thereafter.

Of patients displaying accelerated ageing, significant changes were detected in blood markers relating to renal and liver dysregulation. Serum creatinine was significantly increased and positively correlated with Phenoage discrepancy, indicating reduced creatinine clearance and glomerular filtration rates (GFR)

representing renal injury [12, 13]. Reduced GFR and elevated serum creatinine represent a decline in renal function, which decreases with age [14]. Trends of elevated ALP and Phenoage discrepancy indicate hepatic involvement contributing an accelerated ageing. AS patients display chronic kidney disease, hepatic fibrosis and renal impairment from early ages, which progress linearly with age [15, 16]. Renal impairment may be linked to *ALMS1* playing a role in sodium reabsorption, affecting renal sodium transporters, further impacting endocytosis and impairing renal function [17, 18].

In addition, elevated Hba1c levels were identified in the discrepant Phenoage group, consistent with the phenomenon of impaired glucose tolerance seen in AS [19]. *ALMS1* mutations can alter glucose homeostasis, by reducing glucose transporter expression (GLUT4) and relocalisation in cells, leading to aberrant glucose transport, altering insulin trafficking [20, 21]. Reduced insulin sensitivity is seen in the elderly population, supporting the concept of accelerated metabolic ageing in AS [22].

Low serum albumin may also reflect ageing and associations have been demonstrated between reduced serum albumin and elevated mortality in elderly cohorts [23]. Low albumin further served as a prognostic marker for other impairments such as inflammation and malabsorption. Albumin misfolding and structural modifications with age may impair its homeostatic functions, contributing to an inflammatory state [24]. This is supported by a reduced lymphocyte count, portraying a compromised immune system in those with discrepant Phenoages [25]. The collective changes in serum parameters are congruous with the multi-organ involvement in AS.

LV dimensions including LVEDd and LVESd decreased significantly over time, denoting reduced LV size. This is consistent with published longitudinal studies demonstrating marked reduction in LVEDd with physiological ageing [26]. Increased LVPWd is consistent with a thicker LV wall, seen in physiological ageing [27]. LV wall thickening may be due to cardiomyocyte hypertrophy, rather than increased cardiomyocyte number, as reduced cardiomyocyte number is associated with ageing [28]. Hypertension which elevates LV end-diastolic pressure can lead to cardiomyocyte thickening as a compensatory mechanism to preserve cardiac output [29].

Dividing the cohort into concordant and discrepant Phenoage, a significant positive correlation in E/A ratio with the degree of Phenoage discrepancy suggests increased LV pressure, impacting diastolic function, often impaired with age [30]. Diastolic dysfunction may occur in AS due to increased LV stiffening from fibrosis [31] related to excess collagen deposition, impairing relaxation [32]. Changes in contractility could be linked to the primary role of *ALMS1* in cell cycle regulation and extracellular matrix production [33]. AS patients with mutant *ALMS1* may consequently display altered cellular proliferation, leading to cardiomyocyte senescence and thus altering diastolic function [34]. This is further reflected by a reduction in MV A max in the discrepant Phenoage cohort, supporting LV stiffening and diastolic dysfunction. Variations in these parameters are expected to alter with age, supporting the concept of premature cardiovascular ageing in AS. Whilst ageing can be reflected with cardiac parameters, they do not impact Phenoage.

Strengths and limitations

This study has several strengths, chief amongst which are the large sample size for a rare disease and long follow-up time with a median of six years. Data were also available from regular assessments for blood markers and TTE parameters, allowing for a range of factors to be analysed. These two statistical approaches used generally gave consistent results, providing additional validation to these findings.

However, there were also some limitations that need to be considered when interpreting the findings. Primarily, CRP was not routinely tested during the study period; therefore, it was only possible to calculate Phenoage at patients' final follow-up assessments. This resulted in a quarter of patients being excluded from Phenoage analysis and also precluded analyses of longitudinal trends in Phenoage. Additionally, Phenoage was assessed at the end of the study period and compared to previous follow-up. Consequently, the findings of the analysis cannot be interpreted as indicating the ability for Phenoage discrepancy to predict future trends in blood markers or TTE parameters.

In addition, there was a large variation in the numbers of scans per patient due to different dates patients were initially referred to the service, with most patients having a follow-up assessment within one year of the end of the study. During the COVID-19 pandemic, numbers

were reduced as patients had either died or been lost to follow-up before the end of the study period. As such, the truncation of follow-up in these patients may have introduced some degree of selection bias. Whilst the two statistical approaches generally returned consistent results, there were some inconsistencies, specifically when assessing trends in EF by Phenoage. Consequently, it is not possible to reliably draw conclusions where the two approaches had inconsistent findings.

Conclusion

AS is a disease model of accelerated ageing, with most patients displaying an increased biological Phenoage compared to chronological age. A wide discrepancy in Phenoage was present from entry into the clinical service, suggesting that multi-organ dysfunction and an altered ageing trajectory occur at an early age, with the difference then stabilising with age. Accelerated cardiac ageing in AS was also found on longitudinal assessment using TTE, with progressive LV reduction in size, increase in LV wall thickness and reduction in mitral early filling with increase in atrial filling. Despite recapitulating cardiac re-modelling in AS, cardiac parameters have less impact on Phenoage discrepancy. The findings open up new possibilities for treatment via the use of repurposed drugs able to slow or reverse the rate of biological ageing [35].

Declarations

Competing interests The authors declare no competing interests.

References

1. Alstrom CH, Hallgren B, Nilsson LB, Asander H. Retinal degeneration combined with obesity, diabetes mellitus and neurogenous deafness: a specific syndrome (not hitherto described) distinct from the Laurence-Moon-Bardet-Biedl syndrome: a clinical, endocrinological and genetic examination based on a large pedigree. Acta Psychiatr Neurol Scand Suppl. 1959;129:1–35.
2. Marshall JD, Beck S, Maffei P, Naggert JK. Alström syndrome. Eur J Hum Genet. 2007;15:1193–202.
3. Hearn T, Renforth GL, Spalluto C, et al. Mutation of ALMS1, a large gene with a tandem repeat encoding 47 amino acids, causes Alström syndrome. Nat Genet. 2002;31:79–83.
4. Bond J, Flintoff K, Higgins J, et al. The importance of seeking ALMS1 mutations in infants with dilated cardiomyopathy. J Med Genet. 2005;42:e10.
5. Marshall JD, Bronson RT, Collin GB, et al. New Alström syndrome phenotypes based on the evaluation of 182 cases. Arch Intern Med. 2005;165:675–83.
6. Baig S, Dowd R, Edwards NC, et al. Prospective cardiovascular magnetic resonance imaging in adults with Alström syndrome: silent progression of diffuse interstitial fibrosis. Orphanet J Rare Dis. 2020;15:139.
7. Makaryus AN, Zubrow ME, Marshall JD, Gillam LD, Mangion JR. Cardiac manifestations of Alström syndrome: echocardiographic findings. J Am Soc Echocardiogr. 2007;20:1359–63.
8. Brofferio A, Sachdev V, Hannoush H, et al. Characteristics of cardiomyopathy in Alström syndrome: prospective single-center data on 38 patients. Mol Genet Metab. 2017;121:336–43.
9. Levine ME, Lu AT, Quach A, et al. An epigenetic biomarker of aging for lifespan and healthspan. Aging (Albany NY). 2018;10:573–91.
10. Shenje LT, Andersen P, Halushka MK, et al. Mutations in Alstrom protein impair terminal differentiation of cardiomyocytes. Nat Commun. 2014;5:3416.
11. Robinson S, Rana B, Oxborough D, et al. A practical guideline for performing a comprehensive transthoracic echocardiogram in adults: the British Society of Echocardiography minimum dataset. Echo Res Pract. 2020;7:G59–93.
12. Kashani K, Rosner MH, Ostermann M. Creatinine: from physiology to clinical application. Eur J Intern Med. 2020;72:9–14.
13. Mercado MG, Smith DK, Guard EL. Acute kidney injury: diagnosis and management. Am Fam Physician. 2019;100:687–94.
14. Kanasaki K, Kitada M, Koya D. Pathophysiology of the aging kidney and therapeutic interventions. Hypertens Res. 2012;35:1121–8.
15. Baig S, Paisey R, Dawson C, et al. Defining renal phenotype in Alström syndrome. Nephrol Dial Transplant. 2020;35:994–1001.
16. Tahani N, Maffei P, Dollfus H, et al. Consensus clinical management guidelines for Alström syndrome. Orphanet J Rare Dis. 2020;15:253.
17. Jaykumar AB, Caceres PS, King-Medina KN, et al. Role of Alström syndrome 1 in the regulation of blood pressure and renal function. JCI Insight. 2018;3

18. Li G, Vega R, Nelms K, et al. A role for Alström syndrome protein, alms1, in kidney ciliogenesis and cellular quiescence. PLoS Genet. 2007;3:e8.
19. Dassie F, Favaretto F, Bettini S, et al. Alström syndrome: an ultra-rare monogenic disorder as a model for insulin resistance, type 2 diabetes mellitus and obesity. Endocrine. 2021;71:618–25.
20. Favaretto F, Milan G, Collin GB, et al. GLUT4 defects in adipose tissue are early signs of metabolic alterations in Alms1GT/GT, a mouse model for obesity and insulin resistance. PLoS One. 2014;9:e109540.
21. Hearn T. ALMS1 and Alstrom syndrome: a recessive form of metabolic, neurosensory and cardiac deficits. J Mol Med (Berl). 2019;97:1–17.
22. Kalyani RR, Egan JM. Diabetes and altered glucose metabolism with aging. Endocrinol Metab Clin North Am. 2013;42:333–47.
23. Lai KY, Wu TH, Liu CS, et al. Body mass index and albumin levels are prognostic factors for long-term survival in elders with limited performance status. Aging (Albany NY). 2020;12:1104–13.
24. Tsao FHC, Meyer KC. Human serum albumin misfolding in aging and disease. Int J Mol Sci. 2022;23
25. Valiathan R, Ashman M, Asthana D. Effects of ageing on the immune system: infants to elderly. Scand J Immunol. 2016;83:255–66.
26. Peverill RE. Changes in left ventricular size, geometry, pump function and left heart pressures during healthy aging. Rev Cardiovasc Med. 2021;22:717–29.
27. Agrawal T, Nagueh S. Changes in cardiac structure and function with ageing. J Cardiovasc Aging. 2022;2:13
28. Singam NSV, Fine C, Fleg JL. Cardiac changes associated with vascular aging. Clin Cardiol. 2020;43:92–8.
29. Saheera S, Krishnamurthy P. Cardiovascular changes associated with hypertensive heart disease and aging. Cell Transplant. 2020;29:963689720920830.
30. Pyszko J, Václavík J, Václavík T, et al. Effects of age on left ventricular diastolic function. Cor et Vasa; 2018.
31. Brofferio A, Sachdev V, Hannoush H, et al. Characteristics of cardiomyopathy in Alstrom syndrome: prospective single-center data on 38 patients. Mol Genet Metab. 2017;121:336–43.
32. Cheng S, Fernandes VR, Bluemke DA, McClelland RL, Kronmal RA, Lima JA. Age-related left ventricular remodeling and associated risk for cardiovascular outcomes: the Multi-Ethnic Study of Atherosclerosis. Circ Cardiovasc Imaging. 2009;2:191–8.
33. Marshall JD, Maffei P, Collin GB, Naggert JK. Alström syndrome: genetics and clinical overview. Curr Genomics. 2011;12:225–35.
34. Li H, Hastings MH, Rhee J, Trager LE, Roh JD, Rosenzweig A. Targeting age-related pathways in heart failure. Circ Res. 2020;126:533–51.
35. Fahy GM, Brooke RT, Watson JP, et al. Reversal of epigenetic aging and immunosenescent trends in humans. Aging Cell. 2019;18:e13028.

Chapter 7

Characterisation of infantile cardiomyopathy in Alström Syndrome using *ALMS1* Knockout induced pluripotent stem cell derived cardiomyocyte model

The following has been submitted to *Molecular Genetics and Metabolism*, as a research article. Cellular bioenergetics analysis was conducted by Dr Jonathan Barlow (University of Birmingham). ImageJ fluorescence quantification script was written by Dr Daniel Nieves(University of Birmingham).

Patel, L[1]., Roy, A[1,2]., Barlow, J[3]., O'Shea, C[1]., Nieves, D[4]., Azad, A.J[1,5]., Hall, C[1]., Davies, B[6,7]., Rath, P[7]., Pavlovic, D[1]., Chikermane, A[11]., Geberhiwot, T[8,9]., Steeds, R.P[1,2]., Gehmlich, K[1,10]. Characterisation of infantile cardiomyopathy in Alström Syndrome using *ALMS1* Knockout induced pluripotent stem cell derived cardiomyocyte model.

[1] Institute of Cardiovascular Sciences, University of Birmingham, Birmingham, UK

[2] Department of Cardiology, Queen Elizabeth Hospital, University Hospital Birmingham NHS Foundation Trust, Birmingham, Birmingham, UK

[3] Cellular Health and Metabolism Facility, School of Sport, Exercise and Rehabilitation, University of Birmingham, Birmingham, UK

[4] Institute of Immunology and Immunotherapy, University of Birmingham, UK

[5] Center of Biological Design, Berlin Institute of Health at Charité, Universitätsmedizin Berlin, Berlin, Germany

[6]Genetic Modification Service, The Francis Crick Institute, London, UK

[7] Wellcome Centre for Human Genetics, University of Oxford, Oxford, UK

[8] Department of Inherited Metabolic Diseases, University Hospital Birmingham NHS Foundation Trust, Birmingham, Birmingham, UK

[9]Institute of Metabolism and System Research, University of Birmingham, Birmingham, UK

[10]Division of Cardiovascular Medicine, Radcliffe Department of Medicine and British Heart Foundation Centre of Research Excellence Oxford, University of

Oxford, Oxford, UK

[11]Paediatric Cardiology, Birmingham Children's Hospital, University Hospital Birmingham NHS Foundation Trust, Birmingham, Birmingham, UK

7.1 Author contributions

Leena Patel Roles: Conceptualization, Data Curation, Formal Analysis, Investigation, Methodology, Project Administration, Resources, Software, Supervision, Validation, Visualization, Writing -Original Draft Preparation, Writing– Review & Editing

Ashwin Roy Roles: Conceptualization, Methodology, Supervision, Resources, Writing – Review & Editing

Jonathan Barlow Roles: Methodology, Formal Analysis, Data Curation, Resources, Visualization, Writing – Review & Editing

Christopher O'Shea Roles: Software, Methodology, Resources, Data Curatiom, Writing – Review & Editing

Daniel Nieves Roles: Software, Methodology, Data Curatiom, Writing – Review & Editing

Amar Azad Roles: Conceptualization, Methodology, Supervision, Writing – Review & Editing

Caitlin Hall Roles: Methodology

Ben Davies Roles: Resources, Methodology, Writing – Review & Editing

Phalguni Rath Roles: Resources, Methodology, Writing – Review & Editing

Davor Pavlovic Roles: Writing – Review & Editing

Ashish Chikermane Roles: Writing – Review & Editing

Tarek Geberhiwot Roles: Conceptualization, Supervision

Richard Steeds Roles: Conceptualization, Supervision, Writing – Review & Editing, Funding acquisition

Katja Gehmlich Roles: Conceptualization, Supervision, Writing – Review & Editing, Funding acquisition

7.2 Abstract

Alström syndrome (AS) is an inherited rare ciliopathy characterised by multi-organ dysfunction and premature cardiovascular disease. This may manifest as an infantile-onset dilated cardiomyopathy with significant associated mortality. An adult-onset restrictive cardiomyopathy may also feature later in life. Loss of function mutations in *ALMS1* have been identified in AS patients, leading to a lack of ALMS1 protein. The biological role of *ALMS1* is unknown, particularly in a cardiovascular context. To understand the role of *ALMS1* in infantile cardiomyopathy, the reduction of ALMS1 protein seen in AS patients was modelled using human induced pluripotent stem cell-derived cardiomyocytes (iPSC-CMs), in which *ALMS1* was knocked out. MuscleMotion analysis and calcium (Ca^{2+}) optical mapping experiments suggest that *ALMS1* knockout (KO) cells have increased contractility, with altered Ca^{2+} extrusion and impaired Ca^{2+} handling dynamics compared to wildtype (WT) counterparts. Seahorse metabolic assays showed *ALMS1* KO iPSC-CMs had increased glycolytic and mitochondrial respiration rates, with *ALMS1* KO cells portraying increased energetic demand and respiratory capacity than WT counterparts. Using senescence associated β-galactosidase (SA-β-gal) staining assay, we identified increased senescence of *ALMS1* KO iPSC-CMs. Overall, this study provides insights into the molecular mechanisms in AS, particularly the role of *ALMS1* in infantile cardiomyopathy in AS, using iPSC-CMs as a 'disease in a dish' model to provide insights into multiple aspects of this complex disease.

7.3 Keywords

Alström syndrome, iPSC, cardiomyopathy, characterisation, ALMS1.

7.4 Introduction

Alström syndrome (AS) is an ultra-rare genetic disease characterised by childhood onset retinal dystrophy and obesity [108]. Patients also develop auditory manifestations, renal dysfunction, insulin resistance, dyslipidaemia and premature cardiovascular disease [325], [112].

AS is caused by recessive loss of function genetic variants in *ALMS1* [111], a 23-exon gene located on chromosome 2p13 [113]. Reported mutations in AS patients are prevalent in exons 8, 10 and 16 of the *ALMS1* gene [114]. The variants in *ALMS1* in AS patients leads to an absence of ALMS1 protein function [110], presumably through a lack of ALMS1 protein translation due to the presence of premature stop codons, resulting in protein truncation [114], [115].

ALMS1 is a cilia and centrosome protein, which is widely expressed in the body, particularly in glial cells, neuronal cells and cardiomyocytes [326]. A proposed role of ALMS1 involves cilia maintenance and cell cycle regulation [116]. However, the biological roles of ALMS1 are largely unknown.

Infantile cardiomyopathy is the earliest manifestation of cardiovascular dysfunction in AS, affecting approximately one third of individuals and associated with significant premature mortality [327]. Infantile cardiomyopathy presents as acute heart failure, characterised by severe left ventricular systolic dysfunction and features of a dilated cardiomyopathy, with onset between birth and 10 months [110].

Those who survive infantile cardiomyopathy often recover with no discernible long-term consequences, detectable on biomarker assessment, electrocardiography and multimodality cardiovascular imaging [327], [112].

Historically, most infants were not identified as having AS at the time of presenting with infantile cardiomyopathy, with diagnosis being made following the development of extracardiac features, such as nystagmus and photosensitivity [328]. Hence, there is limited characterisation of the infantile cardiomyopathy phenotype in AS. Infantile cardiomyopathy in AS does not predict onset of cardiovascular disease in adulthood [112], which argues that infantile cardiomyopathy is a distinct disease entity to adult-onset cardiomyopathy. The role of *ALMS1* in the heart is poorly understood. A gene trap mouse model with a KO of *Alms1* showed higher proliferation rates of cardiomyocytes in early postnatal hearts and impaired cell cycle arrest, resulting in cardiac hypertrophy at two weeks of age [329]. However, a more recent *Alms1* mouse model failed to recapitulate these findings and young postnatal hearts were found to be structurally and functionally normal at the same age [330].

Understanding the role of *ALMS1* in cardiomyocytes will enhance our knowledge of the pathophysiological mechanisms driving infantile cardiomyopathy in AS. Our aim was therefore to develop a 'disease in a dish model' of AS using *ALMS1* KO induced pluripotent stem cells (iPSC) and differentiating them into cardiomyocytes (iPSC-CMs). The immature nature of iPSC-CMs [149] makes them a suitable model to study the infantile heart. We subsequently characterised these cardiomyocytes lacking *ALMS1* compared to WT counterparts in

terms of their contractile behaviour, Ca^{2+} handling, metabolic capacity and cell senescence, at various stages of cardiac maturation.

In this study, we have validated the successful generation of a cellular model system for AS. Our experiments indicate striking differences in the AS cellular model, potentially providing insights into the pathogenesis of infantile cardiomyopathy in AS.

7.5 Materials and Methods

7.5.1 Generation of *ALMS1* knockout iPSC cells

iPSCs were generated with the support from the Genome Engineering Core Facility at the Wellcome Trust Centre for Human Genetics at the University of Oxford. Human induced pluripotent stem cell line KOLF2-C1 (HipSci, `https://www.hipsci.org/#/lines/HPSI0114i-kolf_2`) was used for genetic engineering. CRISPR/Cas9-mediated genome engineering was used to delete approximately 60kb of the *ALMS1* gene, spanning exons 10-13 (Figure Supplementary 7.11), referred to as *ALMS1* KO subsequently. Pluripotency was confirmed by fluorescence-activated cell sorting analysis for expression of stem cell markers OCT4, SOX2, NANOG and SSEA4 and karyotyping carried out by Chromosome Dynamics Core Facility at the Wellcome Centre for Human Genetics, UK. Clones of homozygous KO cells with confirmed deletion of the gene were selected and used for differentiation. The parental KOLF2 line served as WT control.

7.5.2 Differentiation of ventricular induced pluripotent stem cell-derived cardiomyocytes

iPSC cells, WT and *ALMS1* KO were differentiated into ventricular cardiomyocytes using an established and published protocol [179]. Briefly, iPSCs were plated and cultured in 6-well dishes, with initiation of differentiation at 70-80% confluency. The details can be found in the Supplementary Method section. Beating CMs were established on days 8-10. WT and *ALMS1* KO iPSC-CMs were differentiated in parallel. iPSC-CMs were differentiated for 20, 25, or 30 days. Using three different lengths of differentiation, we mimicked various stages of cardiac maturation.

7.5.3 Immunofluorescence

WT and *ALMS1* KO iPSC were immunostained for ALMS1 protein. iPSCs were plated at 1,000 cells per mm^2 onto coverslips and fixed with 4% paraformaldehyde in PBS for 15 minutes at room temperature, followed by PBS washes. Cells were permeabilised with blocking buffer consisting of 0.5% Triton-X-100 in PBS, 5% Fetal Bovine Serum and 1% Bovine Serum Albumin for 1 hour at room temperature. Primary antibodies, (Supplementary Table 7.1) were added in blocking buffer overnight at 4℃. Secondary antibodies (Supplementary Table 7.1) were diluted in blocking buffer and incubated at room temperature for 1 hour in the dark, followed by PBS washes and imaged using the EVOS M500 system.

At day 30, iPSC-CMs on coverslips were fixed and stained for p16 and p21 as above. They were imaged on a Zeiss LSM 880 using a C-Apochromat 63x/1.2

W Korr M27. Four images were taken per coverslip, with two to three coverslips imaged per condition, across three batches of iPSC-CM differentiations. Analysis of cytoplasmic and nuclear p16 and p21 staining were quantified using an Image J custom script. Briefly, DAPI and α-actinin images were thresholded and used to generate binary masks. The DAPI mask was used for quantifying nuclear expression of p16 and p21, whereas for cytoplasmic expression, a new mask was generated from the α-actinin mask by taking away the nuclear mask. The mean fluorescence intensity was then taken from within the masked areas in the original p16 and p21 fluorescence images.

7.5.4 Optical mapping

Day 15 iPSC-CMs were split into 35mm dishes at approximately 57,000 cells per mm^2 forming a beating confluent monolayer of iPSC-CMs. Between days 22-25, optical mapping was conducted using a fluorescent Ca^{2+} dye. Medium was removed from the dishes, and iPSC-CMs were incubated at 37℃ with 5μM Fura-2 AM Ca^{2+} dye in 1ml RPMI B27 + Insulin media for 20 minutes, followed by incubation with 2ml Tyrode's solution (129mM NaCl, 5.4mM KCl, 10mM HEPES, 48mM MgCl2, 1.8mM CaCl2, and 9.99mM Glucose) pH 7.44-7.48 for a further 20 minutes. The monolayer was excited at wavelength 380nm, with emission captured at 510/40nm. Ca^{2+} signals were recorded from dishes on a heating plate set to maintain the temperature at 37℃ under a 10x objective with the following settings: exposure interval 1.7ms, pixel size 8μm, 51x51 pixel resolution and 40% gain using Winfluor software. Files were converted to .MAT files and analysed

using optical mapping software Electromap [181]. Outputs such as Ca^{2+} transient durations (CTD) at 30%, 50% and 80% reuptake, time to peak, Ca^{2+} amplitude, and beat rate were produced. Files were analysed at peak-transient, focusing on Ca^{2+} extrusion.

7.5.5 MuscleMotion contraction analysis

Contraction of WT and *ALMS1* KO iPSC-CMs was assessed between days 20-30 of differentiation. WT and *ALMS1* KO iPSC-CM monolayers were recorded using a GoPro H6 camera attached to a microscope using a 10X objective for a duration of 20-25 seconds. Three videos per well were taken, with two to six wells per condition, across three batches of WT and *ALMS1* KO iPSC-CM differentiations. The videos were converted to TIF sequence files at a 59.94 frames per second using Davinci Resolve software (v18.0.3). TIF files were converted into a stacked TIF file, which was processed using a MuscleMotion macro in FIJI/ImageJ software (v2.9.0) [182]. MuscleMotion outputs included contraction amplitude, time to peak, relaxation time and peak-to-peak time. Each parameter from MuscleMotion was normalised to WT day 30 iPSC-CMs and portrayed as a percentage difference to *ALMS1* KO iPSC-CMs. To mitigate external factors such as room temperature, cells were only taken out of the incubator for up to 2 minutes at a time for recordings and returned to temperature-controlled incubators to maintain contractility.

7.5.6 Senescence associated β-galactosidase staining

Day 15 iPSC-CMs were plated at 1,000 cells per mm^2 onto coverslips and cultured to day 30 of differentiation. Senescence β-galactosidase Cell Staining kit (Cell Signalling Technology, cat no. 9860) was used for these experiments. Cell media was removed from coverslips and washed twice with 1X PBS. Cells were then fixed with 1X fixative solution for 15 minutes at room temperature. Cells were washed twice with PBS before addition of β-galactosidase staining solution and incubated overnight at 37℃. Following nuclear counterstaining, coverslips with incubated with DAPI (1:400) in PBS for 15 minutes and imaged using an EVOS M500 Imaging system at 20x magnification using the Cy5 channel for the β-galactosidase signal. The percentage of β-Galactosidase positive cells were quantified from each image, using two to four coverslips per condition across two to three differentiation batches.

7.5.7 Real-time quantitative polymerase chain reaction (RT-qPCR) transcription levels

RT-qPCR was conducted to assess transcriptional levels of Ca^{2+} channels in WT and *ALMS1* KO iPSC-CMs involved in contractility. KiCqStart™ SYBR primers were used (Supplementary Table 7.2) in combination with PowerUP SYBR Green Master Mix (Applied Biosystems, cat no. A25742). TaqMan probes were used with TaqMan Fast Advanced MasterMix 2X (Applied Biosystems, cat no.4444557). qPCR assays were conducted on the QuantStudio™ 5 Real-Time PCR System (Applied Biosystems). The following genes were investigated; *SLC8A1* (NCX1,

sodium-calcium exchanger), *SLC8A2* (NCX2, sodium-calcium exchanger) and *SLC8A3* (NCX3, sodium-calcium exchanger) responsible for exit of Ca^{2+} from the cell. *ATP2A2* encoding for SERCA, acting as a pump to transport Ca^{2+} from the cytosol back to the sarcoplasmic reticulum and *RYR2*, encoding for ryanodine receptor 2, acting as a Ca^{2+} activated channel releasing Ca^{2+} from the sarcoplasmic reticulum into the cytosol. *PLN*, coding for phospholamban was also studied, as depending on the state of phosphorylation, PLN can impact SERCA activity. L-type voltage gated calcium channels, Cav1.2, encoded by *CACNA1C* is the most predominant in the heart, Cav2.1, encoded by *CACNA1A*, Cav1.3, encoded by *CACNA1D* and Cav1.4 encoded by *CACNA1F* mediate the entry of Ca^{2+} into the cell. Fold changes in gene transcript expression were calculated using the $\triangle\triangle$Ct method, with 2-$\triangle(\triangle$Ct) using GAPDH as the housekeeping gene. Data was made relative to WT D30 expression levels. *CDKN1A* and *CDKN2A* transcript expression, encoding for p16 and p21 respectively, were also investigated and normalised to GAPDH expression.

7.5.8 Cellular Bioenergetics

At day 15, WT and *ALMS1* KO iPSC-CMs were passaged and cultured into Seahorse Extracellular Flux (XF) 96-well microplates (Agilent Technologies), coated with Geltrex at a density of 20,000 cells per well. Wells A1, H1, A12 and H12 were kept empty and used for background correction. On day 25, cells were washed into XF DMEM containing HEPES (pH 7.4) (Agilent Technologies) supplemented with 10mM glucose, 2mM glutamine and 1mM pyruvate. After calibration of the

XF sensor cartridge, the microwell plate containing cells was placed into the XF analyser and assessed using a metabolic profiling assay. In brief, following 3 baseline measurement cycles consisting of a 3-minute wait and 3-minute measure period, oligomycin (2μg/ml), BAM15 (3μM), rotenone plus antimycin A (2μM) and monensin (20μM) were added sequentially to probe ATP-coupled respiration, maximum respiratory capacity, non-mitochondrial oxygen consumption and maximal glycolysis, respectively.

After the assay, cell plates were centrifuged at 1000rpm for 5 minutes to pellet iPSC-CMs. Spent assay media was removed from each well and cell pellets were lysed in RIPA buffer (10μl) and protein concentrations determined using a Pierce Rapid Gold BCA Protein Assay Kit (ThermoFisher Scientific, A53225). Protein concentrations were measured using a SpectraMAX ABS plate reader (Molecular Devices, cat no. 736-0916) on Softmax Pro software (v 7.1.2). Data was normalised to protein concentrations. Following baseline correction and normalisation, multiple parameters were calculated from the data, including oxygen consumption rate (OCR), proton efflux rate (PER) and ATP synthesis rates. PER was corrected for mitochondrial contributions using pre-determined values of 0.38 for H^+:O_2 [19]. ATP synthesis rates were determined from OCR and corrected PERs using P/O2 ratios 5.45 (oxidative ATP), 1.53 (glycolytic ATP) and 0.334 (glycolytic ATP when glucose is completely oxidised), we therefore assume glucose is the only substrate being oxidised for these experiments [19].

7.5.9 Statistical Analysis

When comparing two groups, data was assessed for normality using the Shapiro-Wilk Test. Data that was not normally distributed underwent Mann Whitney statistical tests, whereas data normally distributed underwent an unpaired t-test. For more than 2 variables, data not normally distributed underwent a Kruskal-Wallis test with Dunn's multiple comparisons test. When comparing across multiple groups, data normally distributed underwent one-way ANOVA with šidák post hoc test. Significance was determined as $p < 0.05$ (*), < 0.01 (**), < 0.001 (***), < 0.0001 (****). Data was analysed and presented in GraphPad Prism version (v9.5.1).

7.6 Results

7.6.1 Validation of *ALMS1* KO in the cellular model

To confirm absence of the ALMS1 protein, immunostaining was conducted. A reduction of ALMS1 protein in *ALMS1* KO iPSCs compared to WT iPSCs was documented using microscopy (Figure 7.1). In WT cells, ALMS1 was found as one or two puncta per cell, in proximity to the nucleus. This agrees with its centrosomal localisation [113].

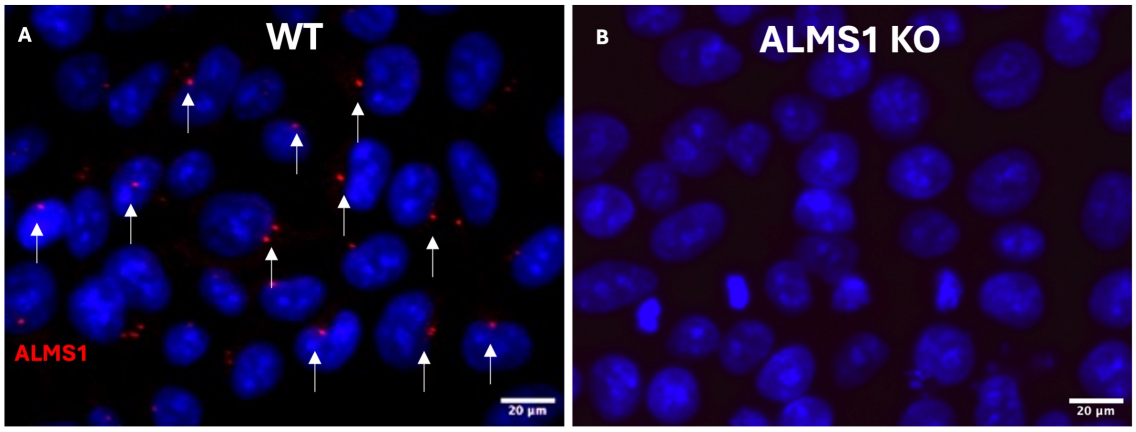

Figure 7.1: **ALMS1 Immunostaining images of WT and *ALMS1* KO iPSC**
(A) Representative immunostaining of ALMS1 protein (red) highlighted by arrows and DAPI nucleus stain (blue) in WT iPSCs (B) Immunostaining of ALMS1 in *ALMS1* KO iPSC cells (red) and DAPI nucleus stain (blue).

ALMS1 KO and WT iPSCs were successfully differentiated into iPSC-CMs with similar efficiency and producing comparable numbers. Onset of beating was similar for both genotypes (starting between day 8 and 10). Compared to WT, *ALMS1* KO iPSC-CMs showed increased expression of TNNT2 at day 20 ($p < 0.0001$), with similar trends also at day 25 and day 30 (Figure 7.2 C). However, they had a reduced ratio of myosin light chain 2 (ventricular) to myosin light chain 7 (atrial) at day 30 (*MYH2:MYH7*) ($p < 0.01$), with a similar trend at day 25 (Figure 7.2 B). In contrast, the myosin heavy chain 7 to 6 ratio (*MYH7:MYH6*) was similar between both genotypes (Figure 7.2 A). Taken together, this suggests there is no delay of *ALMS1* KO iPSC to differentiate into iPSC-CMs.

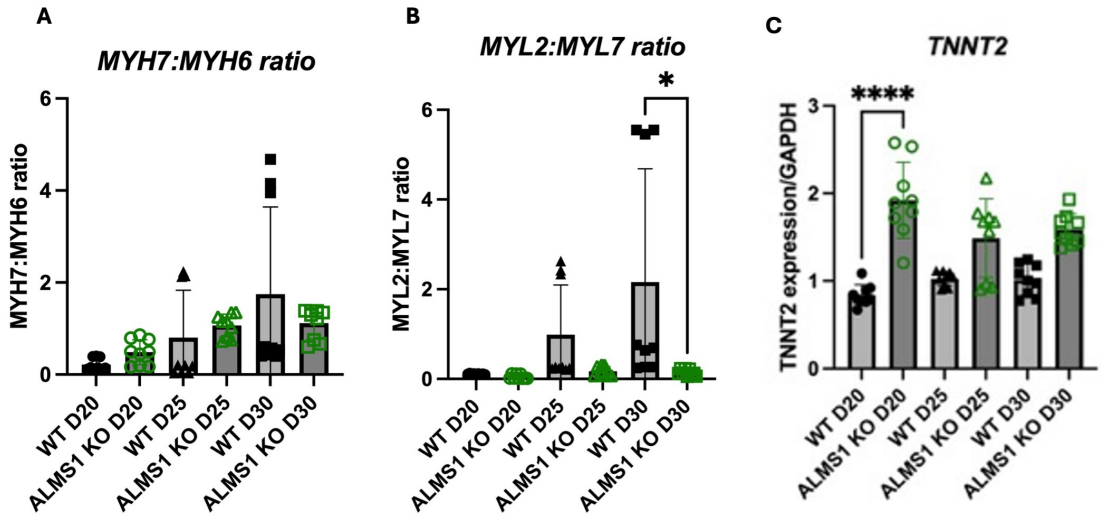

Figure 7.2: **qPCR of cardiac markers in WT and *ALMS1* KO iPSC-CMs between Days 20-30 of differentiation**
(A) *MYH7:MYH6* ratios indicating maturity (B) *MYL2:MYL7* ratio (C) *TNNT2* relative expression. Data normalised to *GAPDH* and made relative to WT day 30 conditions. Values are presented as mean $\pm$ SD. Each data point refers to 1 well of cells, plated as 3 technical replicates per condition. A total of n=3 batches of iPSC-CM differentiations were used. Statistical significance was assessed with a Kruskal-Wallis test as data was not normally distributed, with p values determined as <0.05 (*), < 0.0001 (****).

7.6.2 Contraction analysis

MuscleMotion analysis of videos of spontaneously beating iPSC-CMs was employed to investigate potential contractile changes in *ALMS1* KO cardiomyocytes. No significant differences were observed in contraction duration, referring to the time taken for contraction to occur (Figure 7.3 A). Contraction amplitude refers to the peak contraction force. Contraction amplitude was significantly higher in day 20 *ALMS1* KO iPSC-CMs compared to WT ($p<=0.05$) and showed an increased trend of amplitude at later time points, although not significant (Figure 7.3B). Similarly, peak amplitude portrayed an increased trend *ALMS1* KO iPSC-CMs compared to WT (Figure 7.3C).

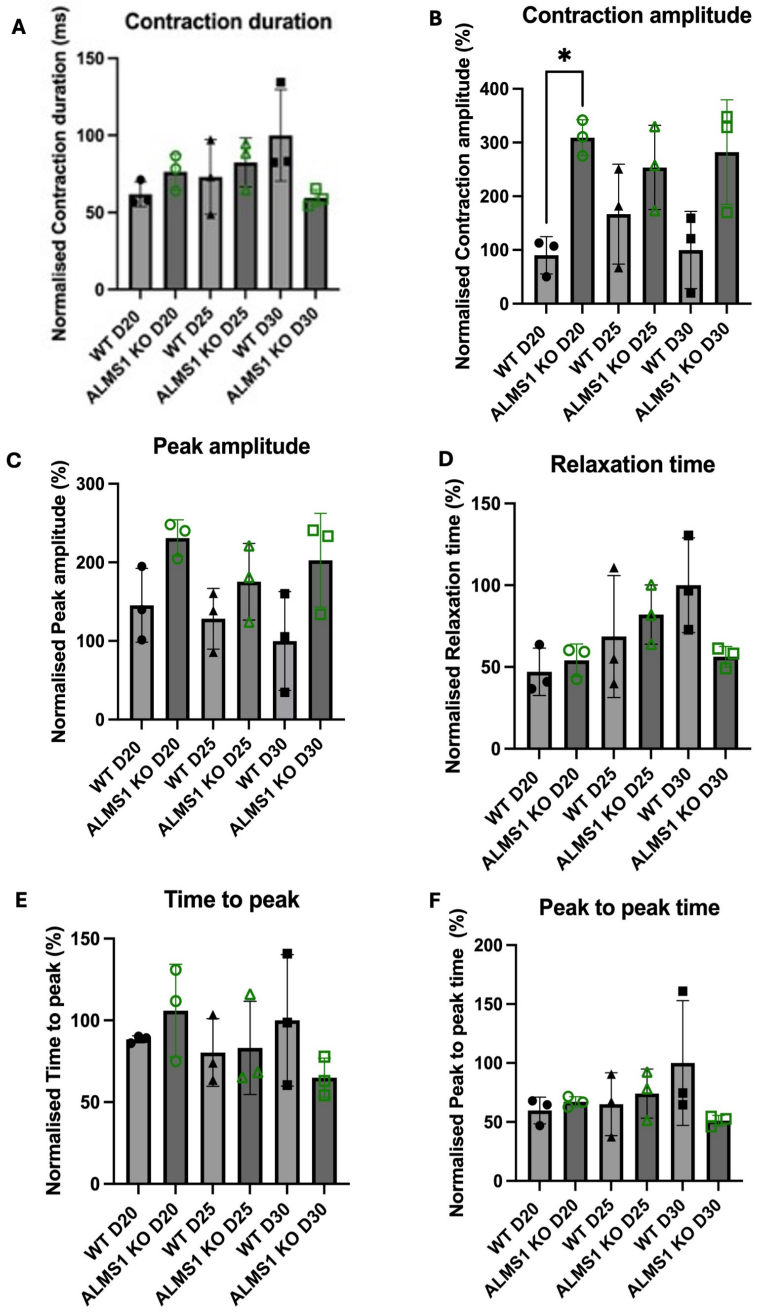

Figure 7.3: **Contractile parameters of WT and *ALMS1* KO iPSC-CMs assessed by MuscleMotion software**
Contractility parameters analysed from GoPro videos of WT and *ALMS1* KO iPSC-CMs over days 20-30 of differentiation, analysed using MuscleMotion. (A) Contraction duration, (B) Contraction amplitude, (C) Peak amplitude, (D) Relaxation time, (E) Time to peak and (F) Peak to peak time. Data presented as mean $\pm$ SD. Each data point refers to an average value per batch of cells, calculated from 3 areas per well across 2-3 wells of cells per condition. This was conducted with a total of n=3 batches of iPSC-CM differentiations. Statistical significance was assessed with a Kruskal-Wallis test as data was not normally distributed, with p values determined as < 0.05 (*)

7.6.3 Altered Ca^{2+} handling in *ALMS1* KO cardiomyocytes

Optical mapping of cells was conducted between days 22 and 25 of differentiation. *ALMS1* KO iPSC-CMs demonstrated shorter calcium transient durations (CTD)(at CTD30%, CTD50% and CTD80%) compared to control WT iPSC-CMs; CTD30 ($p<=0.05$), CTD50 ($p<= 0.01$), CTD80 ($p<=0.01$) (Figure 7.4 A-F). Furthermore, a significant decrease in the peak CTD30:80 ratio (Figure 7.4 J) was observed in *ALMS1* KO iPSC-CMs compared to WT iPSC-CMs ($p<=0.01$). No significant differences were observed in beat rate (frequency of contractions), calcium amplitude, time to peak or cycle length (Figure 7.4 G,H,I & K).

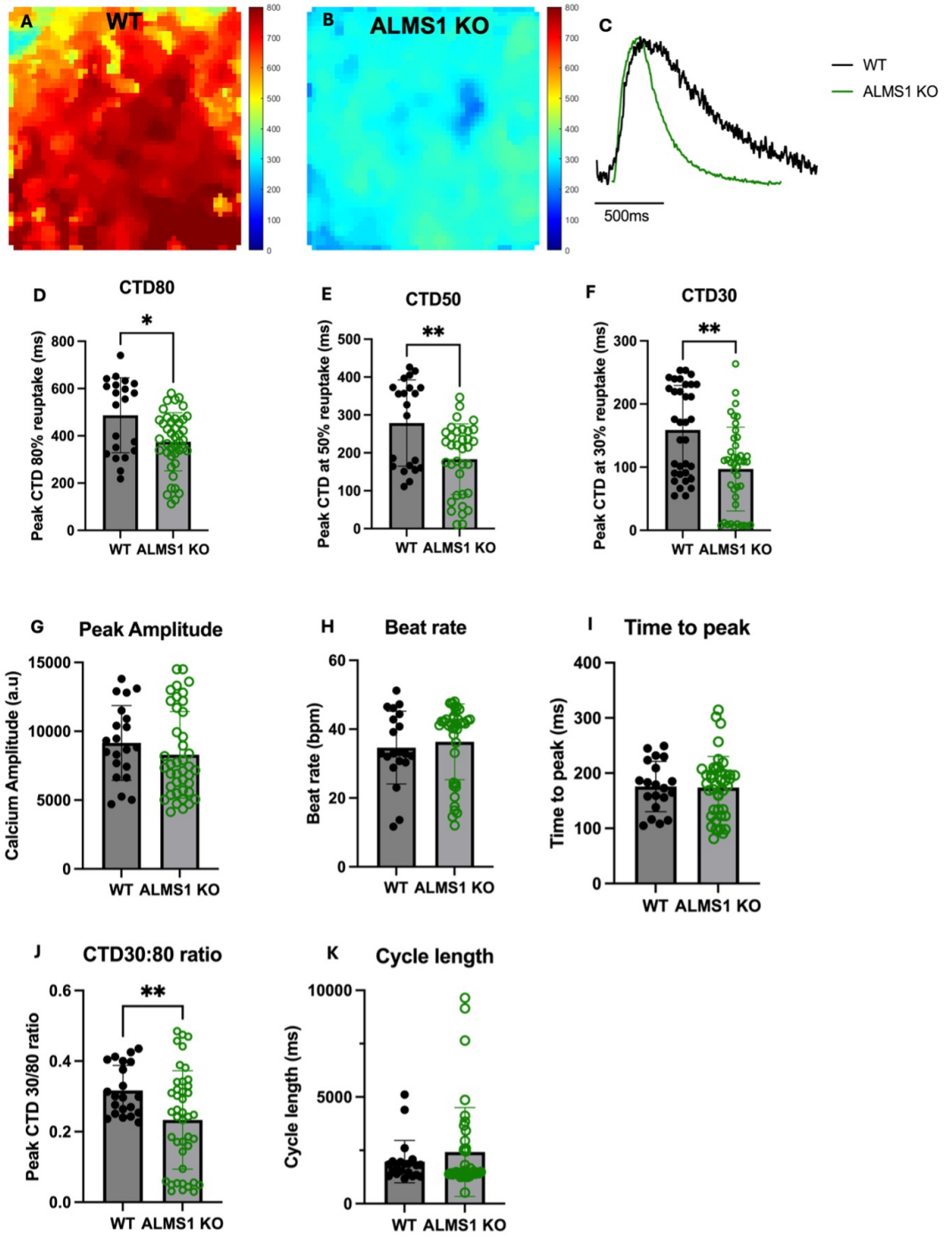

Figure 7.4: **Calcium optical mapping of WT and *ALMS1* KO iPSC-CMs using ElectroMap software**
Ca^{2+} optical mapping on days 22-25 iPSC-CMs analysed using ElectroMap software. (A) Ca^{2+} fluorescence heatmap of WT iPSC-CM monolayer (B) Ca^{2+} fluorescence heatmap of *ALMS1* KO iPSC-CM monolayer (C) Ca^{2+} transient schematics of WT and *ALMS1* KO iPSC-CMs (D) Ca^{2+} transient durations at 80% reuptake, (E) 50% reuptake and (F) 30% reuptake. (G) Ca^{2+} peak amplitude, (H) Beat rate calculated using cycle lengths, (I) Time taken to reach peak of Ca^{2+} transient, (J) CTD30:80 ratio and (K) Cycle lengths. Data presented as mean $\pm$ SD. Each data point refers to an area recorded per dish of cells, with 1-3 dishes recorded per condition. This was conducted across a total of n=6 batches of iPSC-CM differentiations, to account for batch to batch variability of cells. A Mann-Whitney test of significance was conducted on all parameters as data was not normally distributed. Significance was determined as $p < 0.05$ (*), < 0.01 (**), < 0.001 (***).

7.6.4 Changes in calcium handling genes in *ALMS1* KO cardiomyocytes

As changes in Ca^{2+} transients were observed, the expression of Ca^{2+} ion channels was investigated (Figure 7.5). Expression of L-type calcium channels were assessed, as they play a key role in the entry of Ca^{2+} into the CM. No significant changes were found in *CACNA1A* or *CACNA1C* (Figure 7.5 A & B). A significant reduction in *CACNA1D* expression was identified at day 30 in *ALMS1* KO cells compared to WT ($p<=0.0005$) (Figure 7.5 C). A significant reduction in *CACNA1F* was observed at an early timepoint ($p < 0.01$), with no significant differences between *ALMS1* KO and WT CMs at later points (Figure 7.5 D).

SLC8A1, encoding for the sodium-calcium exchanger, NCX1 plays a crucial role in Ca^{2+} homeostasis. Expression of *SLC8A1* was significantly reduced at day 25 in KO CMs compared to WT (Figure 7.5 G). *SLC8A2* showed significantly increased expression in *ALMS1* KO cells compared to WT at days 20 and 25 ($p<=0.05$) (Figure 7.5 H). Similar trends of increased expression of *SLC8A3* were seen in *ALMS1* KO iPSC-CMs compared to WT between days 20-30, although not significant (Figure 7.5 I).

No significant changes were seen in *RYR2* expression between WT and *ALMS1* KO iPSC-CMs (Figure 7.5 F). Expression levels of *ATP2A2* were significantly decreased in *ALMS1* KO iPSC-CMs compared to WT ($p<= 0.01$) at day 25, but showed no significant differences after this timepoint (Figure 7.5 E). Significant decreases in *PLN* expression were identified at days 25 and 30 in *ALMS1* KO cells compared to WT ($p <= 0.01$).

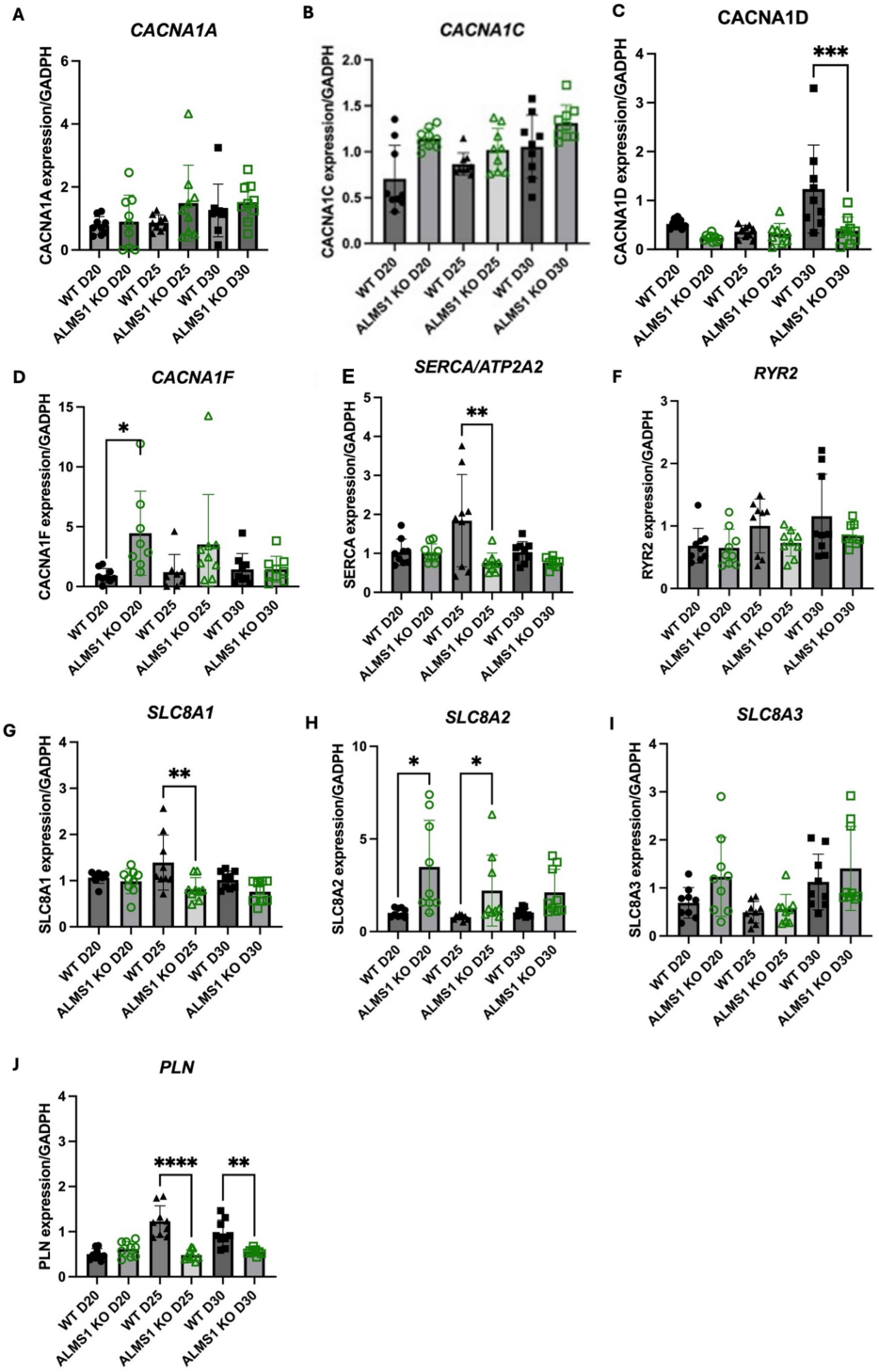

Figure 7.5: **qPCR of Ion channels involved in Ca^{2+} handling in WT and *ALMS1* KO iPSC-CMs**

WT and *ALMS1* KO iPSC-CMs between days 20-30 of differentiation. Ion channel gene expression of (A) *CACNA1A* (B) *CACNA1C* (C) *CACNA1D* (D) *CACNA1F* (E) *ATP2A2/SERCA* (F) *RYR2* (G) *SLC8A1* (H) *SLC8A2* (I) *SLC8A3* (J) *PLN*. Data were normalised to GAPDH and made relative to WT D30. Data plotted as mean $\pm$ SD. Each data point refers to 1 well of cells plated as 3 technical replicates per condition, across a total of n=3 batches of iPSC-CM differentiations. Statistical significance was assessed with a Kruskal-Wallis test for data not normally distributed, excluding SERCA, PLN and CACNA1D, which were normally distributed and thus underwent a one-way ANOVA. Significance determined as $p < 0.05$ (*), < 0.01(**).

7.6.5 Real-time metabolic profiling of *ALMS1* KO cardiomyocytes

To assess metabolic characteristics of *ALMS1* KO iPSC-CMs, metabolic profiles were determined from real-time cellular bioenergetics measurements using Seahorse XF analysis. These data show that *ALMS1* KO iPSC-CMs had significantly higher oxidative and glycolytic flux compared to WT iPSC-CMs ($p <= 0.0001$) (Figure 7.6 A-D). Specifically, *ALMS1* KO iPSC-CMs had significantly higher levels of basal mitochondrial respiration, mitochondrial ATP-coupled respiration and maximal mitochondrial respiration than WT ($p <= 0.0001$) (Figure 7.6 E-H). Similarly, basal glycolytic rates and maximal glycolytic rates were significantly increased in *ALMS1* KO iPSC-CMs compared to WT ($p <= 0.0001$) (Figure 7.6 D and 7.6 F). Consistently, total ATP synthesis rates were significantly higher in *ALMS1* KO iPSC-CMs compared to WT ($p <= 0.0001$) (Figure 7.6 H).

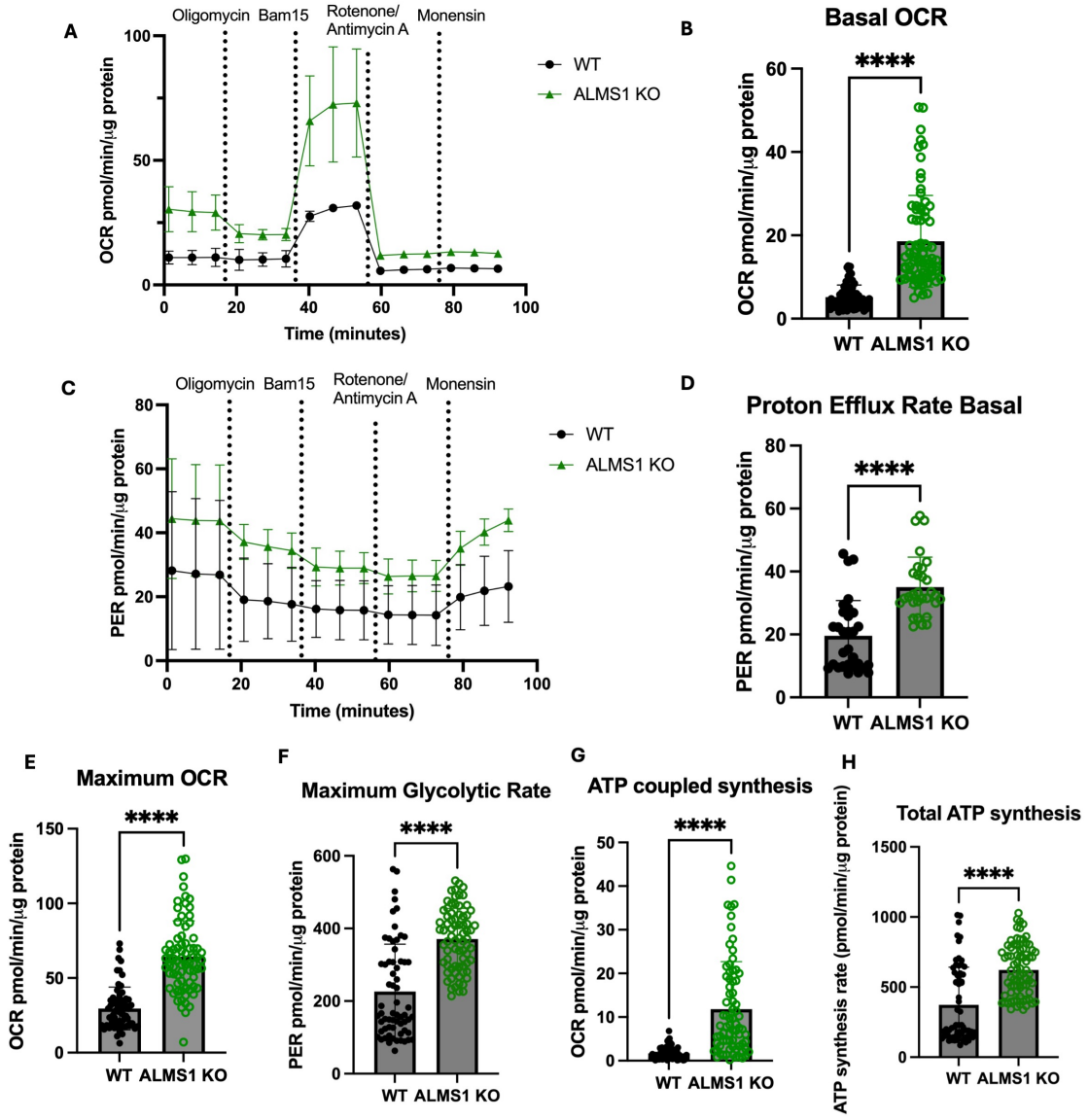

Figure 7.6: **OCR and ECAR assessed by Cell Mito-Stress Test Seahorse assay of WT and ALMS1 KO iPSC-CMs on day 25 iPSC-CMs**
(A) Oxygen consumption rate (OCR) of WT and *ALMS1* KO iPSC-CMs using Seahorse assay. (B) Quantification of Basal OCR (C) Proton efflux rate (PER) of WT and *ALMS1* KO iPSC-CMs (D) Quantification of PER Glycolytic Basal ECAR. (E) Maximal OCR. (F) Maximum Glycolytic rates (G) ATP coupled synthesis. (H) Total ATP synthesis. Data normalised to protein levels of cells. Values are presented as mean $\pm$ SD. Each data point refers to an average of 24 wells of cells per condition, across a total of n=2 batches of iPSC-CM differentiations. Statistical significance was assessed with a Mann-Whitney test as data was not normally distributed, with p values determined as < 0.0001 (****).

7.6.6 Cell Senescence

ALMS1 KO cells showed increased SA-β gal activity compared to WT iPSC-CM cells, ($p <= 0.0001$), suggesting *ALMS1* KO cells were more senescent (Figure 7.7). This is further reflected by a trend of increased p16 expression, a marker for cell senescence, using immunofluorescence in the cytoplasm of *ALMS1* KO cells (Figure 7.8). A trend towards increased transcript expression of *CDKN2A*, the gene coding for p16, was identified in *ALMS1* KO iPSC-CMs compared to WT iPSC-CMs at all time points (Figure 7.10 B), although not significantly different due to variability. Unlike p16, senescence marker p21 encoded by *CDKN1A* portrayed no trends or significant differences between WT and *ALMS1* KO iPSC-CMs (Figure 7.9). Taken together, these data suggest increased cell senescence in *ALMS1* KO cardiomyocytes.

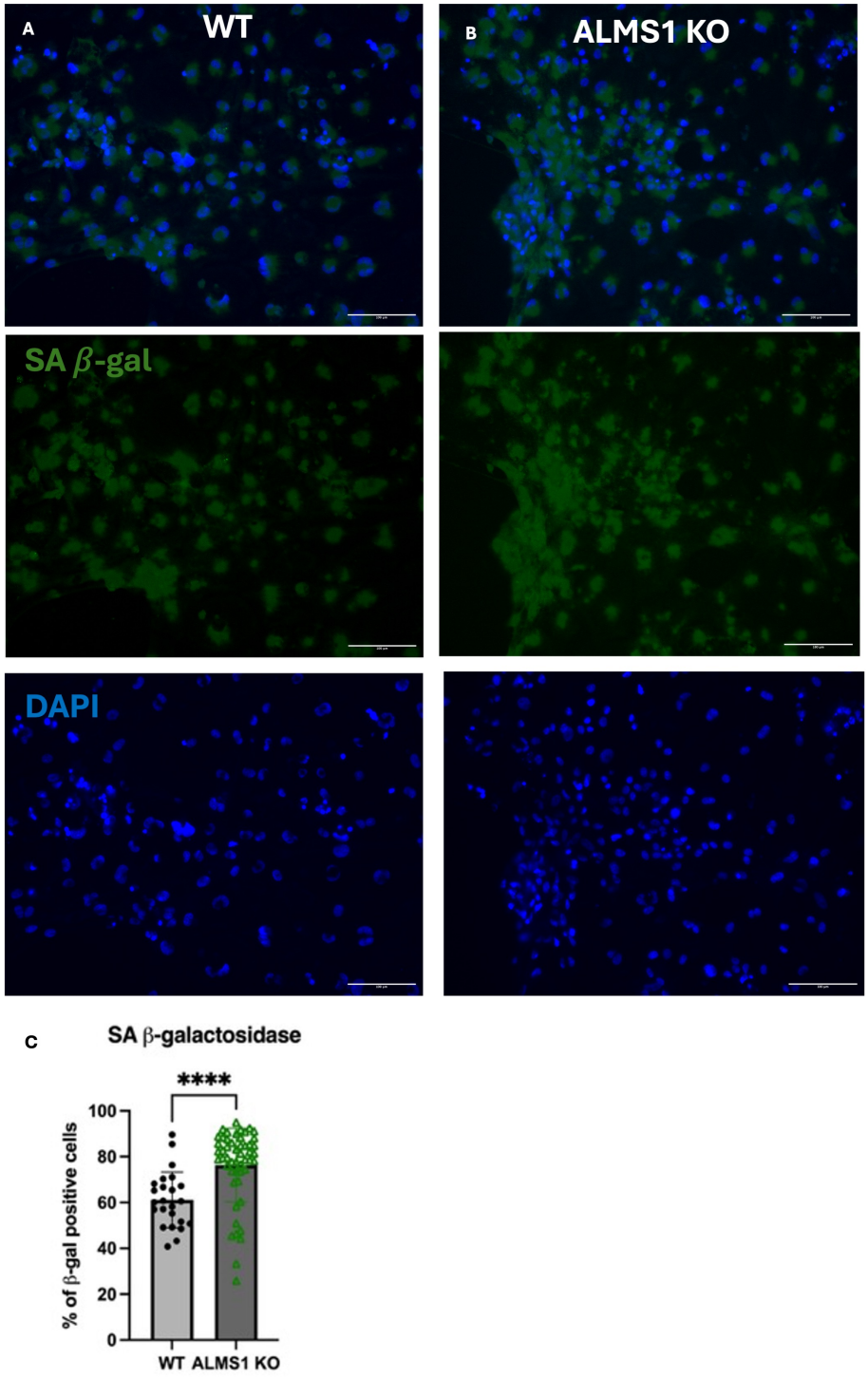

Figure 7.7: **Senescence associated-β-galactosidase staining in WT and *ALMS1* KO iPSC-CMs**
Microscopy images of β-galactosidase (green) and nuclei (blue) on day 30 iPSC-CMs. (A) WT iPSC-CMs (B) *ALMS1* KO iPSC-CMs. (C) Quantification of β-galactosidase positive cells across conditions. Each data point refers to an average of 3 different images per coverslip of iPSC-CMs, with data obtained from 4-6 coverslips per condition to capture well to well variability. This was conducted across a total of n=3 batches of iPSC-CM differentiations. Data normalised to cell number. Scale bars representative of 100μm. Statistical significance was assessed with a Mann Whitney test as data was not normally distributed, with p values determined as $p < 0.0001$ (****).

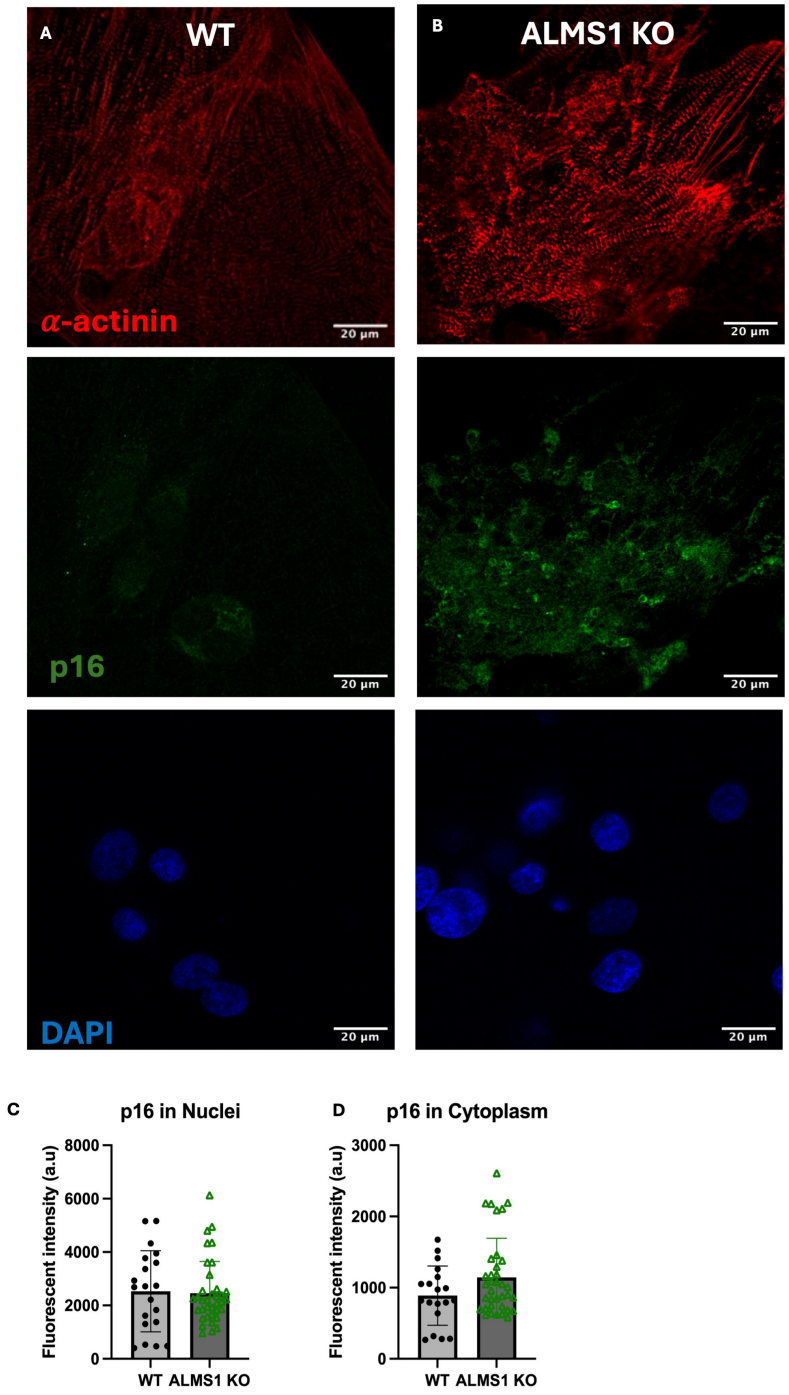

Figure 7.8: **Immunostaining of p16 in WT and ALMS1 KO iPSC-CMs**
Confocal microscopy images of p16 (green), sarcomeric α-actinin stain (red) and DAPI nucleus stain (blue) in (A) WT iPSC-CMs (B) *ALMS1* KO iPSC-CMs (C) Quantification of p16 in nucleus of cells across conditions (D) Quantification of p16 in cytoplasm of cells across conditions. Each data point refers to an area of a coverslip, with 4 different areas captured per well, 2-3 wells per condition captured. A total of n=3 batches of iPSC-CM differentiations were used. Scale bar representative of 20μm. Statistical significance was assessed with a Mann Whitney test as data was not normally distributed.

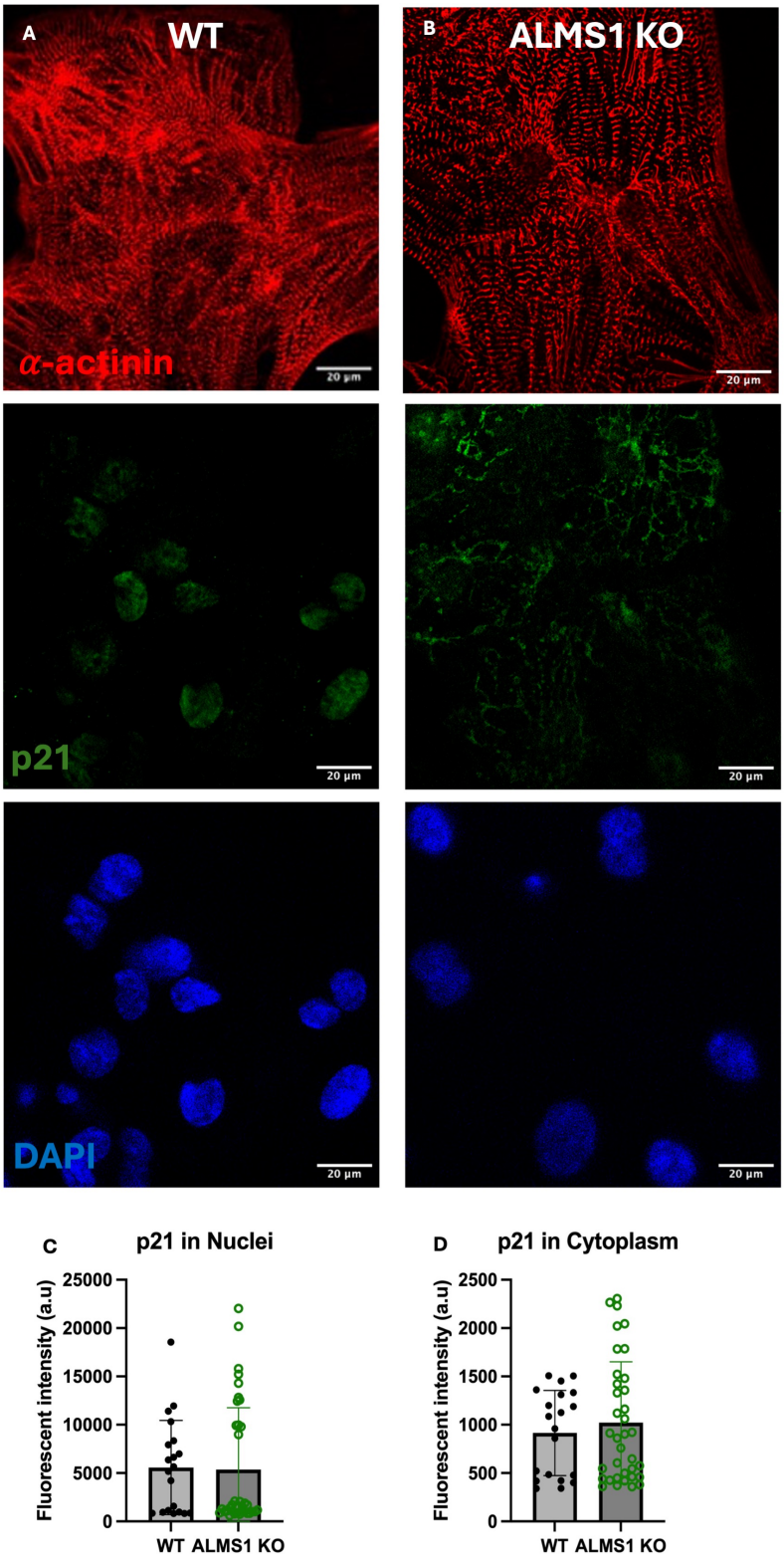

Figure 7.9: **Immunostaining of p21 in WT and *ALMS1* KO iPSC-CMs**
Confocal microscopy images of p21 (green), sarcomeric α-actinin stain (red) and DAPI nucleus stain (blue) in (A) WT iPSC-CMs (B) *ALMS1* KO iPSC-CMs (C) Quantification of p21 in nucleus of cells across conditions (D) Quantification of p21 in cytoplasm of cells across conditions. Each data point refers to an area of a coverslip, with 4 different areas captured per well, 2-3 wells per condition captured. A total of n=3 batches of iPSC-CM differentiations were used. Scale bar representative of 20μm. Statistical significance was assessed with a Mann Whitney test as data was not normally distributed.

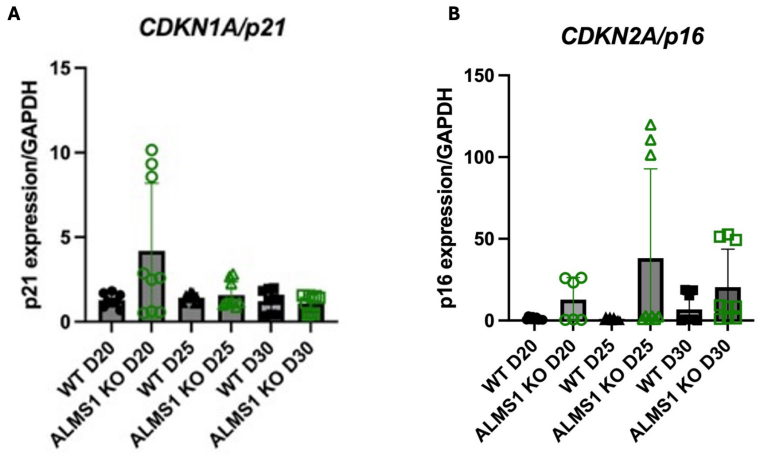

Figure 7.10: **qPCR of *CDKN1A* and *CDKN2A* in WT and *ALMS1* KO iPSC-CMs between Days 20-30 of differentiation**
(A) *CDKN1A*, encoding for p21 transcript expression (B) *CDKN2A*, encoding for p16 transcript expression. Data normalised to *GAPDH* and made relative to day 30 WT iPSC-CMs. Values are presented as mean ± SD. Each data point refers to 1 well of cells, plated as 3 technical replicates per condition. This was conducted using a total of n=3 batches of iPSC-CM differentiations. A Kruskal-Wallis statistical test was conducted as data was not normally distributed.

7.7 Discussion

The model of *ALMS1* KO iPSC-CMs enabled molecular characterisation of the lack of functional ALMS1 protein, mirroring the situation in AS patients. In cardiomyocytes, changes in calcium dynamics, contractility, senescence and metabolism were observed, reflecting the multi-faceted nature of AS.

7.7.1 Altered calcium dynamics and contractility in *ALMS1* KO iPSC-CMs

Optical mapping identified shorter CTDs in *ALMS1* KO iPSC-CMs, independent of calcium amplitude or cycle length (Figure 7.4), indicating alterations in calcium removal from the cytosol. The mechanisms driving these are unclear but are likely to have a role in the underlying pathogenesis of infantile cardiomyopathy in AS.

Our data are suggestive of downregulation of *NCX1* expression and increase

in *NCX2*, the effects of which on calcium transient are difficult to predict. Significant downregulation of *PLN* expression in *ALMS1* KO iPSC-CMs on days 25 and 30 may also affect the calcium transients, as PLN alters the calcium affinity of SERCA dependent on its phosphorylation state [23]. Indeed, *PLN* KO iPSC-CMs displayed increased SR calcium uptake and increased contractility [331], which is consistent with the *ALMS1* KO iPSC-CMs phenotype. The decreased *PLN* expression in *ALMS1* KO iPSC-CMs compared to WT may therefore alter calcium dynamics and contractility. However, it is important to note that PLN regulation occurs also at posttranslational level and that the phosphorylation status of PLN and its equilibrium between monomer and pentamere are crucial for its inhibitory action on SERCA [332]. These levels of regulation have not been assessed in the current study.

Calcium flux changes, directly affect calcium contractility, though our contractility data do not display significantly shorter relaxation times in *ALMS1* KO iPSC-CMs (Figure 7.3 D). We did however observe a clear increase in contraction amplitude in *ALMS1* KO iPSC-CMs. Mechanisms driving these may relate to faster calcium reuptake into the SR, though we have not quantified SR calcium content. Whilst no significant changes were detected in calcium amplitude, the use of non-ratiometric dyes does not allow direct comparisons in systolic and diastolic calcium concentrations in our experiments. Furthermore, post-translational modifications of myofilament proteins, which can modulate calcium sensitivity, are known to influence the force of contraction and could be responsible for the differences observed between *ALMS1* KO and WT iPSC-CMs [333].

The observed reduction in SERCA transcript expression is consistent with literature, suggesting age-related impairment of the SR to sequester calcium ions could be linked to a reduction in SERCA levels or alterations in SERCA: PLN ratios [86]. Studies have also demonstrated a reduction in transcript and protein levels of SERCA in aged CMs [20], which could be reflected by the accelerated ageing phenotype observed in AS. Furthermore, decreased SERCA levels with ageing have also been associated with decreased CTD's in myocytes [99], consistent with the significantly shorter CTD's identified in *ALMS1* KO CMs. Ageing has also been proposed to affect action potentials and diastole thus implicating changes in NCX activity. NCX channel expression has been proposed to decrease in the hearts of aged rats and mice [20], with other literature also suggesting a reduction of mRNA levels, protein expression and activity of NCX channels in male hearts [222], which are consistent with the observed reduction in NCX1 and NCX2 in KO CMs. The lack of changes in RYR2 transcript levels is also reflected in literature, with a number of studies suggesting that ageing does not alter the expression of RYR2 protein [222], [101].

7.7.2 Increased metabolic capacity of *ALMS1* KO iPSC-CMs

The transition from foetal to early postnatal heart is associated with wide-ranging changes in metabolism, to adjust from a hypoxic to normoxic environment and to meet the increasing energy demands of cardiac contractility and growth [334]. Cardiomyocytes have remarkable metabolic flexibility, allowing them to utilise a range of substrates such as glucose and fatty acids [335]. Foetal CMs display

a preference for glucose utilisation, associated with increased glycolytic activity and a lower capacity for oxidative phosphorylation [263].

In keeping with published literature, the increased glycolytic rates in *ALMS1* KO iPSC-CMs compared to WT counterparts, highlight their infantile metabolic nature and indicating higher glycolytic activity [336], [123]. The increased glycolysis in *ALMS1* KO iPSC-CMs correlates with the metabolic patterns seen in neonatal and foetal hearts [337].

In addition, oxidative phosphorylation is also significantly upregulated in *ALMS1* KO cells, alongside total ATP synthesis, portraying higher mitochondrial activity compared to WT cells. The increased metabolic rates coupled with an increased contraction amplitude and shorter calcium transients indicates *ALMS1* KO iPSC-CMs have a higher energetic demand, thus require an upregulation in both energy producing pathways to meet cellular demand. Furthermore, independent of cellular demand and total ATP synthesis, the maximum metabolic capacity of *ALMS1* KO cells was also shown to be significantly higher than WT cells.

Furthermore, the ATP index also portrayed *ALMS1* KO iPSC-CMs as predominantly glycolytic, with a higher baseline of glycolytic ATP synthesis compared to WT iPSC-CMs. The glycolytic behaviour of *ALMS1* KO iPSC-CMs could reflect a lack of ability to effectively switch substrates for energy utilisation, thus indicating issues with early myocardial metabolism issues in AS.

Additionally to the increased energy demand of *ALMS1* KO iPSC-CMs, they also displayed an increased ATP capacity, with increased total ATP production. The ability to distinguish different metabolic capacities of iPSC-CMs further high-

lights the benefit of this model for capturing changes in metabolism, and representing the metabolic dysregulation in AS.

7.7.3 Increased senescence in *ALMS1* KO iPSC-CMs

Previous published literature demonstrates that premature senescence of cardiomyocytes drives cardiomyopathy phenotypes by releasing senescence associated secretory phenotypes, contributing to myocardial remodelling [89], which led to the investigation of whether *ALMS1* KO iPSC-CMs portrayed features of cell senescence. A significant increase in the percentage of SA β-gal positive cells (Figure 7.7) in *ALMS1* KO iPSC-CMs compared to WT suggested an increased senescent state. Senescence of cardiomyocytes have been shown to be key players in myocardial remodelling, contributing to the progression of myocardial infarction and heart failure [338], [339]. This highlights another aspect of disease state of *ALMS1* KO iPSC-CMs.

Cell senescence is a programme whereby cells exit the cell cycle. It involves the activation of p16 as an inhibitor of CDK4/CDK6, thus leading to an upregulation of p21 and preventing progression through the cell cycle [340]. An increased trend of p16 and p21 expression in the cytoplasm of *ALMS1* KO CMs compared to WT cells was identified (Figure Supplementary 7.9, Figure 7.10), consistent with literature portraying activation of p16 in senescent cells [338], [341]. The trend of increased p16 transcript expression in *ALMS1* KO cells (Supplementary Figure 7.10) further supports findings, indicating senescence states of *ALMS1* KO iPSC-CMs.

7.7.4 Limitations

There are several limitations which need to be considered when interpreting this data. A limitation of iPSC-CMs as a cell model is the variation in data due to batch variability [342]. Due to the differentiation process for ventricular iPSC-CMs featuring several steps, this may alter the quality of differentiation and introduce variability, potentially affecting the reliability of the data. In order to overcome this, high quality control thresholds were put into place, with multiple biological and technical replicates conducted for each experiment. Ca^{2+} dynamics of iPSC-CMs may also differ from cardiomyocytes *in vivo*. This is because iPSC-CMs lack t-tubule structures [343], which play a key role in the excitation-contraction coupling process and Ca^{2+} release. This may affect the accuracy of Ca^{2+} handling experiments conducted in this study. Furthermore, limitations with optical mapping techniques, such as Ca^{2+} dye loading and heterogenous illumination may not accurately reflect changes in Ca^{2+} amplitude.

7.8 Conclusions

This novel cardiac characterisation of *ALMS1* KO iPSC-CMs in a cellular model reflecting the lack of functional cardiac ALMS1 protein in AS patients has identified several disturbances of normal cardiomyocyte function. These disturbances include altered Ca^{2+} extrusion in cells and increased contractility in *ALMS1* KO iPSC-CMs. These may be relevant in the context of driving infantile cardiomyopathy in AS. Furthermore, a switch towards glycolytic metabolism with increased respiratory capacity was observed. Finally, *ALMS1* KO iPSC-CMs portrayed

signs of increased senescence. The molecular alterations identified in *ALMS1* KO iPSC-CMs provide insights into cardiovascular changes in AS patients, by identifying changes that occur with ALMS1 depletion. Utilisation of iPSC-CMs served as a beneficial model for understanding the mechanisms underpinning infantile cardiomyopathy in AS, by allowing investigation into molecular changes at early time points, which can reflect early cardiac changes in AS. Further research is required to understand the molecular mechanisms of altered Ca^{2+} handling, changes in senescence and metabolism in *ALMS1* KO iPSC-CMs, identifying specific pathways or genes for developing targeted therapeutic approaches.

7.9 Supplementary material

7.9.1 Generation of *ALMS1* KO iPSC cells

The aim was to delete approximately 60kb of genomic sequence of *ALMS1* using single guide RNAs (sgRNA), which created double stranded breaks in the target region, exon 10 and exon 13, which could be repaired using nonhomologous end joining, thus deleting the intervening sequence. CRISPR/Cas9 site specific sgRNAs were designed with the following sequences; ALMS1-Cr1 (5'-GGCTTGCATCCCATTCCCCGTGG-3') and ALMS1-Cr2 (5'- TTGTGCCTAGCACCTGAGCTGGG -3').

Site-specific CRISPR/Cas9 nuclease as a riboprotein complex with Cr1 and Cr2 sgRNAs were electroporated into early passage KOLFC-C1 cells using the Neon Electroporation System (Thermo Fisher Scientific, 1200V, 30ms,2 pulses). Monoclonal expansion and PCR based genotyping of individual clones lead to the identification of putative knock-out clones. Sanger sequencing of the clones confirmed homozygous deletion in 3 independent clones (Clone-23, 26 and 40). These clones were validated as pluripotent by FACS analysis for expression of stem cell markers OCT4, SOX2, NANOG and SSEA4 (Human Pluripotent Stem Cell transcription factor Analysis kit (BD Biosciences 560589). A normal karyotype was confirmed and perfomed by Chromosome Dynamics Core Facility at the Wellcome Centre for Human Genetics, UK. Clone 23 with confirmed deletion of the gene was selected and used for differentiation. The parental KOLF2 line served as WT control.

7.9.2 Human iPSC-CM differentiation protocol

iPSC-CMs were seeded onto six-well plates coated with Geltrex, cultured in mTESR Plus media (StemCell Technologies). Media was changed every 48 hours until cells had reached 70-80% confluency. Media was then changed to StemPro-34 SFM (1X) supplemented with 2mM L-Glutamine, 1ng/mL Recombinant Human BMP4 and 1:100 Geltrex. After 24 hours, cells were changed to day 0 media, consisting of StemPro media supplemented with 10 ng/mL Recombinant Human BMP4, 8 ng/mL Activin A and 2mM L-Glutamine and incubated for 48 hours. On day 2, cells were changed to RPMI 1640 media with B27 supplement minus Insulin (50X), 10μM XAV939 and 10μM KY02111 and incubated for 48 hours. On day 4, cells were changed to RPMI 1640 media with B27 supplement (50X), 10μM XAV939 and 10μM KY02111 for 48 hours. The media on the cells were changed with RPMI 1640 media with B27 supplement (50X) every other day. After the initiation of differentiation on day 10, glucose starvation was conducted, with cells changed to RPMI 1640 media supplemented with no glucose B27 supplement (50X) for 24 hours. Cells were dissociated at day 15 into appropriate formats for experiments. iPSC-CMs were incubated with 1mL per well of TryplE Express (Gibco) for 8 minutes, followed by addition of plating media, consisting of RPMI 1640 media supplemented with B27, 10% Knockout Serum replacement (Gibco) and 2μM Thiazovivin to wash off cells. iPSC-CMs were centrifuged for 4 minutes at 215G at room temperature. iPSC-CM pellets were resuspended in plating media and seeded onto Geltrex-coated plates. After incubation for 24 hours, iPSC-CMs were changed back to RPMI 1640 media supplemented with

B27 every other day until experiment was conducted.

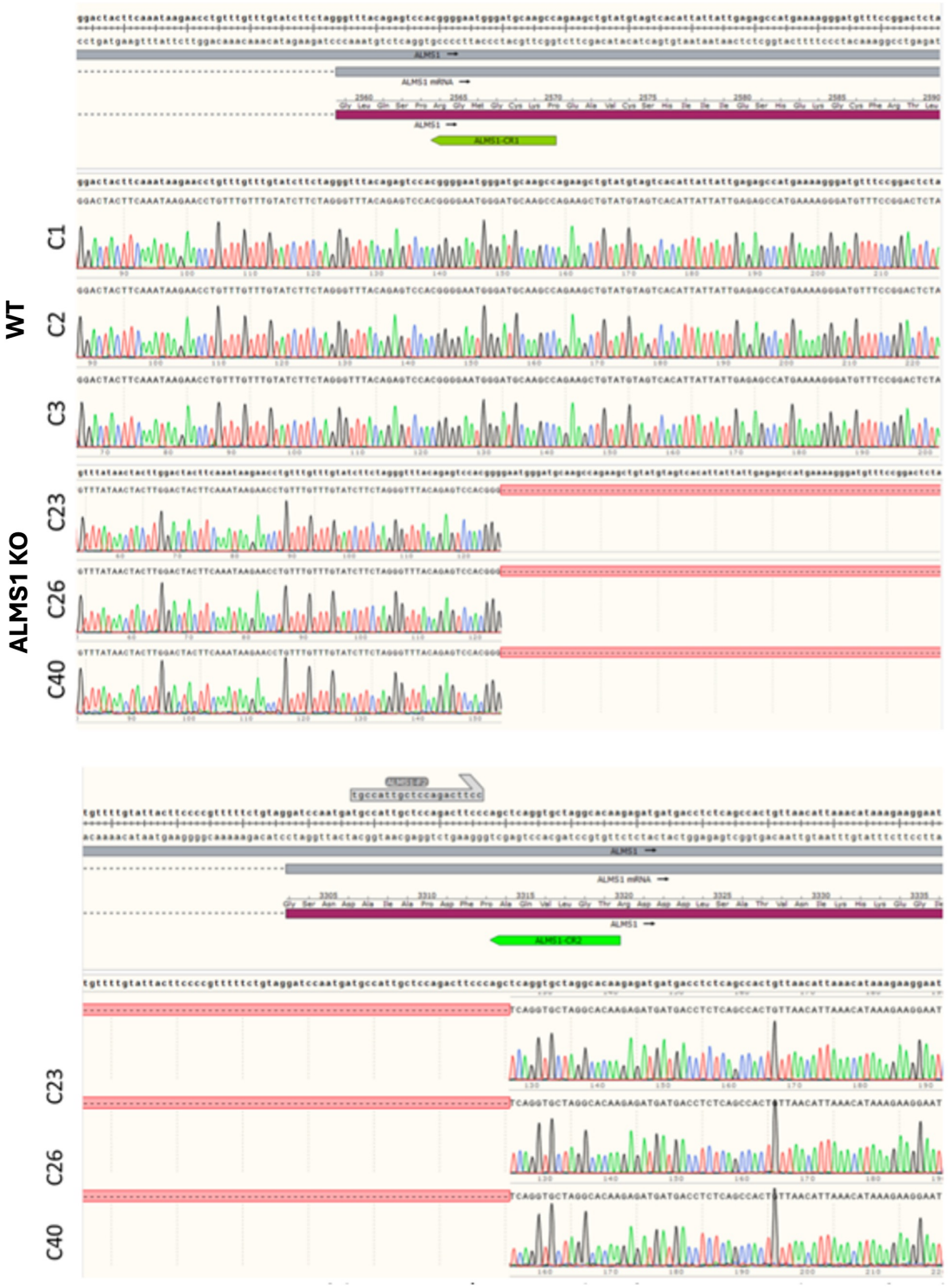

Figure 7.11: **Sanger sequencing of ALMS1 F1/R2 PCR products from C23, C26 and C40 confirmed site specific deletion at the CRISPR target site**
Control clones (C1, C2 and C3) showed wild type sequence at the target site.

Table 7.1: **Primary and secondary antibodies used for immunostaining**

Antigen	Host	Company	Concentration
ALMS1	Rabbit	Protein tech 27231-1-AP	1:1000
α-actinin	Mouse	Sigma-Aldrich A7811	1:500
p16-INK4A	Rabbit	Protein tech 10883-1-AP	1:200
p21	Rabbit	Protein tech 10355-1-AP	1:200
Alexa-Fluor 488 conjugated anti-Rabbit IgG	Goat	Thermo Fisher Scientific A-11034	1:200
Alexa-Fluor 568 conjugated anti-Mouse IgG	Goat	Thermo Fisher Scientific A-11019	1:200
DAPI (4', 6-Diaminido-2-Phenylindole, Dihydrochloride) Conjugated	N/A	Thermo Fisher Scientific D1306	1:400

Table 7.2: **TaqMan and SYBR primers used for qPCR**

Target gene	SYBR/TaqMan	Company
ATP2A2	SYBR F - AGA GTG GAA GGT GAT ACT TG R – GCA GAG TCA TTA CAA AGA GC	Merck
CACNA1C	SYBR F – GGA GAG TTT TCC AAA GAG AG R – TTT GAG ATC CTC TTC TAG CTG	Merck
CACNA1D	SYBR F - AAA ATG GGC ATC ATT CTT CC R - AGT TTC ATA ATA GCG GGT TC	Merck
CACNA1F	SYBR F - CAT TTT CAC CAT CCC AGA AG R - CTC ATC TAG GTA GGA AAG CC	Merck
GAPDH	SYBR F - GAT TCC ACC CAT GGC AAA TTC R – GTC ATG AGT CCT TCC ACG ATA C	Merck
SLC8A1	SYBR F- CAAGAGTACTGTGGACAAAC R-GCTTCAATGAACTGTTCTCTC	Merck
SLC8A2	SYBR F - TAA GAA CAC GGT GGA TAA AC R - ATT GCC TCT AAA AAC TGC TC	Merck
SLC8A3	SYBR F - ATA GTA GAT GAG GAG GAA TAC G R- GTC ACA TCT GAT ATT CCA CG	Merck
RYR2	F - CGT TGC GTA TCT TAG CTA TTC R - GGA CTT TCA AAG CAG TAG TAT C	Merck
ACTN2	TaqMan Hs05032285_s1	Thermo Fisher Scientific
CDKN1A (FAM-MGB)	TaqMan Hs00355782_m1	Thermo Fisher Scientific
CDKN2A (FAM-MGB)	TaqMan Hs00923894_m1	Thermo Fisher Scientific
TNNT2 (VIC-MGB)	TaqMan Hs00943911_m1	Thermo Fisher Scientific
MYH6	TaqMan Hs01101425_m1	Thermo Fisher Scientific
MYH7	TaqMan Hs01110632_m1	Thermo Fisher Scientific
MYL2	TaqMan Hs00166405_m1	Thermo Fisher Scientific
MYL7	TaqMan Hs01085598_g1	Thermo Fisher Scientific

Chapter 8

Final Discussion

8.1 Summary of results

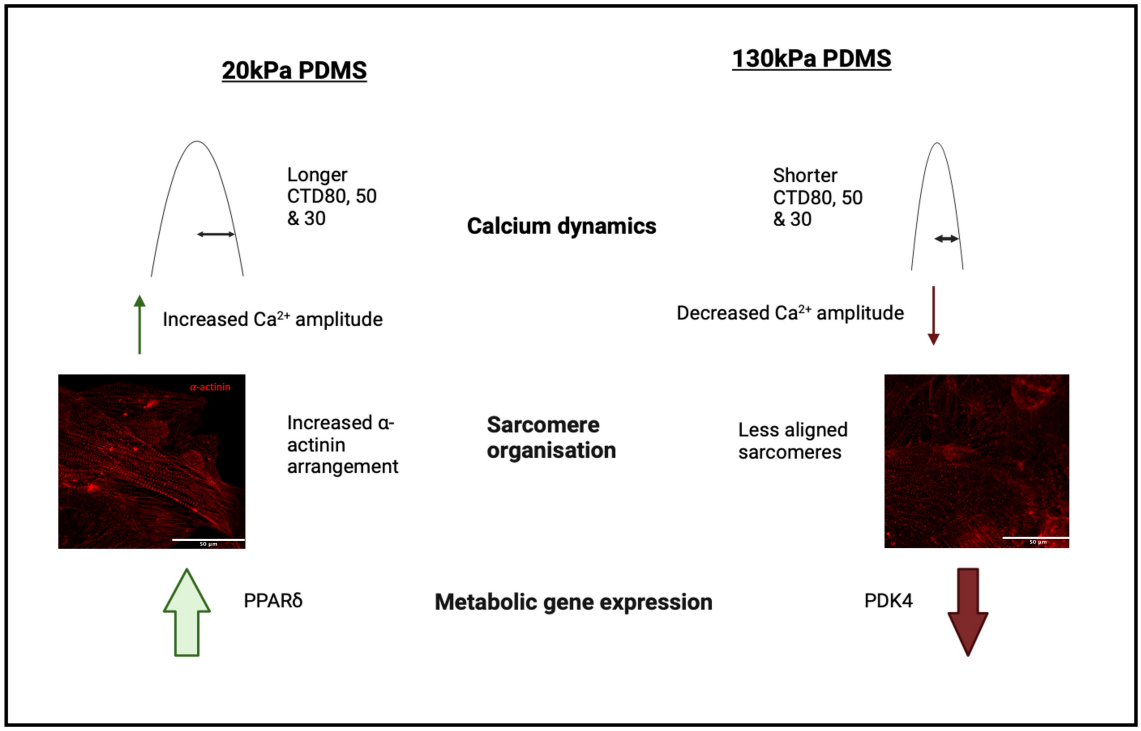

Figure 8.1: **Summary of differences between 20kPa and 130kPa PDMS substrates** Key differences of iPSC-CMs cultured on 20kPa PDMS compared to 130kPa PDMS substrates. Differences in calcium handling dynamics, cardiomyocyte structure and metabolic gene and protein expression were identified between soft and stiff substrates

The overall aim of this research was to investigate the effect of cardiovascular ageing on iPSC-CM morphology, function and metabolism by developing a physiological model reflecting the ageing ECM by manipulating stiffness. Ageing is

associated with a decline in physiological function and is the dominant risk factor for cardiac disease, with increased risk of hypertension, atherosclerosis and myocardial infarction [77]. Despite exercise being shown as a method to decrease age-related cardiac stiffness [344], molecular gene targets are being explored as therapeutic strategies to prevent ageing of the heart [345]. In order to understand how to reverse the effects of cardiac ageing, our understanding of how age-related cardiovascular changes affect heart function, particularly cardiac cell behaviour is essential for progression in the field.

The stiffening of the ECM and altered architecture are well established as features of cardiac ageing and can lead to alterations in the cellular composition of the heart [84], highlighting the importance of investigating changes in CMs. Current cardiac cell models utilise plastics for experiments, which do not recapitulate physiological stiffnesses of the heart [187]. Developing physiological models of the ageing cardiac environment can provide insight into how stiffening of the myocardium can impact CM structure, function and metabolism, which are key for maintaining cardiac homeostasis. Furthermore, exploring the cardiovascular phenotypes and changes occurring in age-related cardiac diseases such as AS can enhance our understanding of dysregulated mechanisms and pathways, providing novel future therapeutic targets.

The aims of the thesis were as follows:

1. Develop a representative model of the stiffness of a healthy and aged myocardium using biomaterial hydrogels (Chapter 3)

2. Molecular and cellular characterisation of the effect of stiffness of ECM mod-

els on iPSC-CM morphology, gene expression and contractility (Chapter 4)

3. Investigating the effect of ECM stiffness on iPSC-CM metabolism (Chapter 5)

4. Assessing Alström Syndrome as a model of accelerated ageing using Phenoage (Chapter 6)

5. Characterising the cardiovascular role of ALMS1 in Alström Syndrome using iPSC-CMs models (Chapter 7)

8.2 Chapter 3: Developing a hydrogel model of ECM stiffnesses

Chapter 3 explored the use of PEG and PDMS for hydrogel synthesis, with the aim of developing hydrogels with stiffnesses of 20kPa (healthy myocardium) and 130kPa (fibrotic myocardium). PEG was initially used for synthesis, due to its modifiable nature and previous use with cardiac cells [176]. Chemical synthesis of PEG precursors demonstrated successful synthesis and functionalisation, as shown with NMR. Mechanical characterisation of hydrogels showed specific combinations of PEG precursors produced hydrogels with Young's moduli of approximately 20kPa, thus effectively recapitulating the stiffness of the healthy myocardium. However, when culturing iPSC-CMs onto the PEG hydrogels, all iPSC-CMs died, indicating toxicity of the gels. Troubleshooting steps to remove toxicity from precursors, such as remaking PEG precursors with extra wash steps and removal of excess acids with acid-base extraction were unsuccessful, which therefore led to the use of PDMS as the preferred biomaterial for hydrogels. PDMS

had been used in the lab group before, with extensive literature also indicating compatibility with iPSC-CMs [202]. PDMS hydrogels were able to mimic physiological ECM stiffnesses, by creating hydrogels of 20kPa and 130kPa. They also displayed biocompatibility with iPSC-CMs and showed no issues with toxicity or attachment to PDMS hydrogels when coated with Geltrex.

8.2.1 Limitations of Chapter 3

A key limitation of this chapter was the inability to resolve the acid toxicity in PEG hydrogels. Alternative methods to resolve toxicity of PEG hydrogels could have been explored. The use of eluents such as hydrochloric acid, sodium hydroxide, sodium chloride, ascorbic acid and ethylenediaminetetraacetic acid could be used to desorb and facilitate the removal or elution of excess acids [346]. Despite the successful attachment of iPSC-CMs to PDMS hydrogels, a significant limitation of PDMS was the peeling of cell monolayers from the surface with extended cell culture periods, due to friction between the surfaces caused by contractility of iPSC-CMs. This prevented the use of PDMS hydrogels with iPSC-CM cultures beyond day 30, which further added to the major concern of immaturity of iPSC-CMs.

8.2.2 Chapter 3 Future work

The successful development of PDMS hydrogels and attachment of iPSC-CMs led to the implementation of this model to mimic the young and aged ECM for experiments in other chapters. Stiffnesses of PDMS hydrogels can be modified

by changing the ratio of components used, thus could be utilised for other models of stiffness with various cell types. Furthermore, 3D models of PDMS could also be used with iPSC-CMs to further mimic environmental conditions and improve maturation.

8.3 Chapter 4: Molecular and cellular characterisation of the effect of ECM stiffness on iPSC-CM morphology and contractility

Chapter 4 aimed to investigate how ECM stiffness altered iPSC-CM structure, contractility and Ca^{2+} handling dynamics. iPSC-CMs between days 20-30 of differentiation showed increased expression of cardiac maturity markers; increased expression of *MYH7/MHY6* ratio and *MYL2/MYL7* ratios from day 25 onwards at transcript level, which validated the use of this timepoint for future experiments. iPSC-CMs cultured on softer 20kPa PDMS gels exhibited cardiac maturity, with significantly increased expression of *MYH7* and *MYL2* compared to stiffer 130kPa PDMS gels. Improved sarcomeric alignment and significantly greater α-actinin organisation was observed in iPSC-CMs cultured on 20kPa PDMS gels compared to stiffer substrates. Contractility of iPSC-CMs did not significantly alter with substrate stiffness, although a slightly increased trend of contraction on softer substrates may be indicative of maturity [246]. Ca^{2+} handling dynamics of iPSC-CMs were significantly altered with stiffness, with iPSC-CMs cultured on healthy myocardial stiffness inducing longer CTD's and higher Ca^{2+} amplitude compared to those on 130kPa, indicative of a mature iPSC-CM phenotype [245]. However no significant changes were identified in Ca^{2+} channel gene expression with stiff-

nesses, which may be largely due to batch variability in iPSC-CMs contributing to the unexpected results.

8.3.1 Limitations of Chapter 4

There are several limitations within the work conducted in this chapter. The data in this chapter highlights the potential limitation of using 130kPa as the stiffness representative of a fibrotic ECM state, as the data does not show iPSC-CMs on 130kPa with a fibrotic phenotype in some cases, thus lacking the phenotype as expected between 20kPa and GPa stiffnesses of plastic/glass. Using a stiffer substrate to reflect a fibrotic state may demonstrate a greater disease phenotype and potentially heighten differences between the conditions. In addition, other factors may also be influencing contractility data, as literature has shown cell size can alter contractility of iPSC-CMs, with shorter cells having less force of contraction [240].

8.3.2 Chapter 4 Future work

The work in this chapter was sufficient to show structural and molecular changes in iPSC-CMs with ECM stiffnesses. Cell size and cell area could be assessed to further determine whether stiffness of the ECM impacts iPSC-CM morphology from other aspects and could correlate with observed changes in sarcomeric organisation. Optical mapping on iPSC-CM monolayers on stiffnesses with a voltage sensitive dye could also be conducted, to assess stiffness related changes in action potential durations, providing greater detail into contractility of iPSC-CMs.

Furthermore, transcript expression of genes involved with integrin signalling could also be explored to determine pathways specifically altered with ECM stiffnesses in iPSC-CMs.

8.4 Chapter 5: Investigating the effect of ECM stiffness on iPSC-CM metabolism

This chapter aimed to assess whether the switch in metabolic substrate utilised by the heart and CMs with ageing and CVD is linked to the increased stiffness of the ECM. Metabolic function of iPSC-CMs on PDMS stiffnesses was assessed using cellular bioenergetics assays, proteomics, gene expression experiments and isotope labelled mass spectrometry. At the time of writing, no previously published studies had assessed changes in central carbon metabolism in iPSC-CMs cultured on PDMS substrates representative of physiological stiffnesses. iPSC-CMs on plastic substrates demonstrated a significantly higher percentage of [U-^{13}C]-glucose in pyruvate and lactate compared to iPSC-CMs cultured on healthy myocardium stiffnesses, suggesting greater levels of glycolysis with stiffness. Consistent with the mass spectrometry data, Seahorse cellular bioenergetics also showed iPSC-CMs cultured on plastics had a significantly higher level of lactic acid production compared to iPSC-CMs cultured on both softer PDMS substrates, indicating a preference for glycolytic metabolism on stiffer substrates. Proteomics data also revealed iPSC-CMs cultured on plastic display a profile consistent with ageing and disease, with an upregulation of proteins linked to stress, such as Fis1 and aspartate aminotransferase, and a downregulation of HADH, a protein linked to fatty acid β-oxidation, reinforcing the glycolytic phenotype. Inter-

estingly, no significant changes were observed in transcript expression of genes related to fatty acid oxidation in iPSC-CMs on substrates, which again may be due to batch variability of iPSC-CMs. Contrary to previously published studies [312], [313], no changes in PPARα were found in iPSC-CMs on softer substrates. However, a significant increase in PPARδ in iPSC-CMs on 20kPa PDMS compared to plastic indicated potential upregulation of fatty acid oxidation and CM maturity [321].

8.4.1 Limitations of Chapter 5

Several limitations can be identified in this chapter. The Seahorse cellular bioenergetics data should be considered with caution, as the choice of PDMS as a biomaterial used for iPSC-CM culture can influence the level of respiration of cells. Previous studies have shown rat CMs cultured on PDMS substrates displayed decreased levels of basal respiration, ATP production and maximal respiration compared to gelatin-based substrates, independent of substrate rigidity [347]. The variation in substrate material and potential impact in metabolic function thus needs to be considered. In addition, the assay itself displayed huge variability between replicates, with some wells displaying expected metabolic profiles whereas others showing different profiles. This may be due to the hydrogels not consistently being the same thickness in each well, therefore disrupting the working distance between the injector wells and the sensor plate, thus not effectively injecting across the plate. To overcome this issue, wells that were clearly observed as not effectively injected with inhibitors were excluded from analysis.

Limitations can also be found in the proteomics experiments. Few genes were identified as significantly differentially up or downregulated, which may indicate substrate stiffnesses only subtly alter iPSC-CMs rather than large fold changes, highlighting the importance of utilising other methods to confirm metabolic changes. Data quality from proteomics can also vary largely due to variation in sample preparation [348], pH conditions and labelling efficiency [349]. Data analysis and thresholds such as FDR, fold change and p-value significance ($p <= 0.05$) can vary with experiments and are typically set to reduce false positives [350]. A fold change threshold of 1.5 was set for this experiment, as seen in previous studies conducting proteomics using iPSC-CMs [351]. It can be argued that fold changes of greater than 2 may further refine proteins of interest that could impact biological function, thus data could be further analysed using more stringent thresholds. Furthermore, to reduce variability of iPSC-CMs within samples, and across batches, running multiple samples per condition per batch of iPSC-CMs would improve the strength of the results. This may provide greater insight into potential outliers or false positives.

8.4.2 Chapter 5 Future work

Further elucidating the role of PPARδ in ECM stiffness and ageing would be of interest. PPARδ agonists and antagonists could be used with iPSC-CMs to characterise molecular and metabolic changes and help identify pathways and mechanisms through which PPARδ may be having an effect. Repeating the current set of metabolic experiments with iPSC-CMs in low glucose media levels supple-

mented with fatty acids may also provide data of greater physiological relevance. Investigating the phosphorylation state of PDC with western blotting would also allow insight into the effect of stiffness on PDK and PDC function.

8.5 Chapter 6: Assessing Alström Syndrome as a model of accelerated ageing and longitudinal cardiovascular changes

Chapter 6 aimed to investigate whether patients with AS displayed an accelerated ageing phenotype using a biological measure known as Phenoage. Phenoage is a predictor of biological age calculated using chronological age and nine blood test parameters representative of the functional state of organs [352]. In addition, retrospective analysis of echocardiography was performed to assess cardiovascular changes in AS patients over time. A key finding of this research was 85% of AS patients in the cohort displayed a higher Phenoage compared to chronological age, indicating multi-organ dysfunction at an earlier age than expected, thus exhibiting accelerated biological ageing. Elevated serum creatinine levels, increased alkaline phosphatase levels and reduced serum albumin levels were identified in AS patients, consistent with renal injury, kidney disease and inflammatory states seen in ageing populations [353], [354], [355]. A reduction in left ventricular size was observed in AS patients, consistent with studies showing a reduction in left ventricular size with ageing [356]. Furthermore, increased left ventricular wall thickness was also identified, which has also been associated with CM hypertrophy, typically observed in ageing hearts [357].

8.5.1 Limitations of Chapter 6

Limitations of this study need to be considered when analysing the findings. Phenoage was calculated for the patients' final follow-up assessment, as CRP values were not consistently tested for during the entire study period, thus excluding some patients from the cohort for Phenoage analysis. The number of scans per patient also varied due to the COVID-19 pandemic, with a loss of follow-up for some patients after this period. The small number of patients can also be considered a limitation, however this is due to the ultra-rare nature of AS; a way to overcome this issue involves a multi-centre international study, thus increasing the number of patients.

8.5.2 Chapter 6 Future work

The chapter succeeded in identifying AS a disease model of accelerated ageing, with patients displaying a higher Phenoage compared to chronological age. Further research could investigate whether similar trends in Phenoage are observed in other cohorts of AS patients outside of the UK, to determine whether location has any impact on the accelerated ageing phenotype.

8.6 Chapter 7: Understanding the cardiovascular role of ALMS1 in Alström Syndrome using iPSC-CMs

Chapter 7 aimed to understand the cardiovascular role of *ALMS1* in AS, often characterised by infantile cardiomyopathy. This chapter utilised a 'disease in a dish' model by differentiating *ALMS1* KO iPSC-CMs and characterising their con-

tractility, Ca^{2+} handling dynamics, ion channel transcript expression, senescence state and cellular bioenergetics. KO iPSC-CMs models were used to reflect the lack of functional ALMS1 protein seen in AS patients. At the time of writing, no previously published studies had assessed the cardiac role of *ALMS1* in iPSC-CMs. *ALMS1* KO iPSC-CMs exhibited shorter CTD's with potential alterations in Ca^{2+} extrusion from the cytosol. A downregulation of *NCX1* transcript expression and significant decrease in *PLN* expression in *ALMS1* KO iPSC-CMs at days 25 and 30 may also contribute to the altered Ca^{2+} handling dynamics observed. Despite changes in Ca^{2+} handling, no significant changes were detected in contractility parameters in KO iPSC-CMs, although a clear increase in contraction amplitude was identified. KO iPSC-CMs also displayed altered bioenergetics, with increased glycolytic activity and higher mitochondrial activity as well as increased oxidative phosphorylation and total ATP production. Furthermore, *ALMS1* KO iPSC-CMs demonstrated an increased senescent state with a higher percentage of SA-β-gal positive cells compared to WT.

8.6.1 Limitations of Chapter 7

Batch to batch variability of iPSC-CMs can be observed in contractility data and ion channel transcript expression results, which may be due to the complex steps of the differentiation process, creating differences in the quality of cells, thus contributing to variability. In order to reduce variability, high quality cells and multiple biological and technical replicates were used for experiments. Ca^{2+} handling data also needs to be considered with caution, as iPSC-CMs do not have t-tubules,

which play a key role in Ca^{2+} release and excitation-contraction coupling.

8.6.2 Chapter 7 Future work

Chapter 7 succeeded in unveiling the potential cardiac roles *ALMS1* may play in the development of infantile cardiomyopathy in AS but did not determine molecular mechanisms that are responsible. Future work could include identifying the phosphorylation state of PLN in KO iPSC-CMs, to determine how this could impact SERCA activity and consequently Ca^{2+} uptake. Expression of key metabolic genes could be conducted using qPCR to investigate specific changes linked to the increased metabolic activity observed in KO iPSC-CMs. In addition, *ALMS1* KO iPSC-CMs could be cultured on stiffnesses of PDMS, to explore how the fibrotic phenotype in AS can impact CM function further.

8.7 General Limitations

A key limitation reflected across experiments in all chapters is the batch-to-batch variation of iPSC-CMs, which causes the large spread of datapoints, contributing to the lack of significant differences across conditions. The variability of batches was typically overcome with increased number of iPSC-CM differentiations for experiments. Another key limitation which can influence results obtained is the lack of t-tubules in iPSC-CMs, which are typically present in adult CMs, but are not present in the iPSC-CM model. Gap junctions and t-tubules are important for cell excitability and coupling of electrical activity in the myocardium and have been shown to mediate electrical communication between cells [9]. The limitations of

iPSC-CM models are therefore highlighted, with iPSC-CMs exhibiting structural immaturity [343].

8.8 Concluding remarks

Ageing continues to be a major risk factor for CVD, with an increase in the proportion of the population consisting of aged or elderly individuals. As the prevalence of age-related CVD increases, the significance of understanding age-related disease mechanisms and pathways could provide the field with novel therapeutic targets. Current cardiac research using plastic or glass for cell experiments are not reflective of physiological conditions, as they are far stiffer than the healthy myocardium. The thesis developed a representative model of the ageing myocardium by mimicking ECM stiffnesses using PDMS hydrogels and investigating changes in iPSC-CM structure and metabolism with varying stiffnesses. The thesis revealed iPSC-CMs cultured on aged or diseased stiffnesses demonstrated decreased cardiac maturity, disrupted sarcomeric organisation, altered Ca^{2+} handling dynamics and a switch back to glycolytic metabolism compared to traditional plastics for cardiac investigations. The work presented therefore highlights the benefits of using models with physiological stiffnesses, as iPSC-CMs show different phenotypes with age-related stiffness, displaying the significance of the environment cardiac cells are in.

The thesis also explored ageing and CVD in a clinical context, by assessing cardiovascular changes over time in AS, and characterised AS as a model of accelerating ageing using Phenoage. The use of genetically edited iPSC-CMs to

characterise the cardiac role of *ALMS1* in AS demonstrated altered Ca^{2+} handling dynamics, cellular bioenergetics and increased senescence. Although this work identified several areas in which *ALMS1* may impact the development of AS and infantile cardiomyopathy, further research is required to determine the exact disease mechanisms responsible.

The progression of stem cell based technology for modelling cardiovascular pathologies has enabled researchers to investigate disease mechanisms in detail, particularly with advancements such as genetically edited iPSC-CMs. The immaturity of iPSC-CMs remains a prominent issue in the field, but is being resolved with the use of maturation techniques such as soft substrates, fatty acid enriched media and co-culture models. The development of 3D self-assembling organoid models further improves the field of cardiac physiological models.

In conclusion, the work presented highlights the benefits of using iPSC technology to investigate cardiovascular diseases and emphasises the importance of physiological model development for the cardiac field. Understanding the molecular mechanisms of ageing and CVD can help enable the development of novel therapeutic strategies.

Bibliography

[1] Litviňuková M, Talavera-López C, Maatz H, Reichart D, Worth CL, Lindberg EL, et al. Cells of the adult human heart. Nature. 2020;588(7838):466-72. Available from: https://www.ncbi.nlm.nih.gov/pubmed/32971526.

[2] Doll S, Dreßen M, Geyer PE, Itzhak DN, Braun C, Doppler SA, et al. Region and cell-type resolved quantitative proteomic map of the human heart. Nat Commun. 2017;8(1):1469. Available from: https://www.ncbi.nlm.nih.gov/pubmed/29133944.

[3] Xiao S, Shaw RM. Cardiomyocyte protein trafficking: Relevance to heart disease and opportunities for therapeutic intervention. Trends Cardiovasc Med. 2015;25(5):379-89. Available from: https://www.ncbi.nlm.nih.gov/pubmed/25649302.

[4] Woodcock EA, Matkovich SJ. Cardiomyocytes structure, function and associated pathologies. Int J Biochem Cell Biol. 2005;37(9):1746-51. Available from: https://www.ncbi.nlm.nih.gov/pubmed/15950518.

[5] Walker CA, Spinale FG. The structure and function of the cardiac myocyte: a review of fundamental concepts. J Thorac Cardiovasc Surg. 1999;118(2):375-82. Available from: https://www.ncbi.nlm.nih.gov/pubmed/10425017.

[6] Barrick SK, Greenberg MJ. Cardiac myosin contraction and mechanotransduction in health and disease. J Biol Chem. 2021;297(5):101297. Available from: https://www.ncbi.nlm.nih.gov/pubmed/34634306.

[7] Wang Z, Grange M, Wagner T, Kho AL, Gautel M, Raunser S. The molecular basis for sarcomere organization in vertebrate skeletal muscle. Cell. 2021;184. Available from: https://www.cell.com/cell/fulltext/S0092-8674(21)00236-1?_returnURL=https%3A%2F%2Flinkinghub.elsevier.com%2Fretrieve%2Fpii%2FS0092867421002361%3Fshowall%3Dtrue#figures.

[8] Nikolaidou T, Aslanidi OV, Zhang H, Efimov IR. Structure-function relationship in the sinus and atrioventricular nodes. Pediatr Cardiol. 2012;33(6):890-9. Available from: https://www.ncbi.nlm.nih.gov/pubmed/22391764.

[9] Rohr S. Role of gap junctions in the propagation of the cardiac action potential. Cardiovasc Res. 2004;62(2):309-22. Available from: https://www.ncbi.nlm.nih.gov/pubmed/15094351.

[10] Bers DM. Cardiac excitation-contraction coupling. Nature. 2002;415(6868):198-205. Available from: https://www.ncbi.nlm.nih.gov/pubmed/11805843.

[11] Fearnley CJ, Roderick HL, Bootman MD. Calcium signaling in cardiac myocytes. Cold Spring Harb Perspect Biol. 2011;3(11):a004242. Available from: https://www.ncbi.nlm.nih.gov/pubmed/21875987.

[12] Fabiato A, Fabiato F. Calcium release from the sarcoplasmic reticulum [Journal Article]. Circ Res. 1977;40(2):119-29. Available from: https://www.ncbi.nlm.nih.gov/pubmed/403028.

[13] Berridge MJ, Bootman MD, Roderick HL. Calcium signalling: dynamics, homeostasis and remodelling [Journal Article]. Nat Rev Mol Cell Biol. 2003;4(7):517-29. Available from: https://www.ncbi.nlm.nih.gov/pubmed/12838335.

[14] Bers DM. Calcium fluxes involved in control of cardiac myocyte contraction [Journal Article]. Circ Res. 2000;87(4):275-81. Available from: https://www.ncbi.nlm.nih.gov/pubmed/10948060.

[15] Ernst P, Bidwell PA, Dora M, Thomas DD, Kamdar F. Cardiac calcium regulation in human induced pluripotent stem cell cardiomyocytes: Implications for disease modeling and maturation. Front Cell Dev Bio. 2023;10(986107):936-53. Available from: https://www.frontiersin.org/journals/cell-and-developmental-biology/articles/10.3389/fcell.2022.986107/full.

[16] Striessnig J, Pinggera A, Kaur G, Bock G, Tuluc P. L-type Ca. Wiley Interdiscip Rev Membr Transp Signal. 2014;3(2):15-38. Available from: https://www.ncbi.nlm.nih.gov/pubmed/24683526.

[17] Shah K, Seeley S, Schulz C, Fisher J, Gururaja Rao S. Calcium Channels in the Heart: Disease States and Drugs. Cells. 2022;11(6). Available from: https://www.ncbi.nlm.nih.gov/pubmed/35326393.

[18] Lanner JT, Georgiou DK, Joshi AD, Hamilton SL. Ryanodine receptors: structure, expression, molecular details, and function in calcium release. Cold Spring Harb Perspect Biol. 2010;2(11):a003996. Available from: https://www.ncbi.nlm.nih.gov/pubmed/20961976.

[19] Guo Y, Cao Y, Jardin BD, Zhang X, Zhou P, Guatimosim S, et al. Ryanodine receptor 2 (RYR2) dysfunction activates the unfolded protein response and perturbs cardiomyocyte maturation. Cardiovasc Res. 2023;119(1):221-35. Available from: https://www.ncbi.nlm.nih.gov/pubmed/35576474.

[20] Hamilton S, Terentyev D. Altered Intracellular Calcium Homeostasis and Arrhythmogenesis in the Aged Heart. Int J Mol Sci. 2019;20(10). Available from: https://www.ncbi.nlm.nih.gov/pubmed/31091723.

[21] Dobrev D, Wehrens XH. Role of RyR2 phosphorylation in heart failure and arrhythmias: Controversies around ryanodine receptor phosphorylation in cardiac disease. Circ Res. 2014;114(8):1311-9; discussion 1319. Available from: https://www.ncbi.nlm.nih.gov/pubmed/24723656.

[22] Zhihao L, Jingyu N, Lan L, Michael S, Rui G, Xiyun B, et al. SERCA2a: a key protein in the Ca. Heart Fail Rev. 2020;25(3):523-35. Available from: https://www.ncbi.nlm.nih.gov/pubmed/31701344.

[23] van Opbergen CJ, Delmar M, van Veen TA. Potential new mechanisms of pro-arrhythmia in arrhythmogenic cardiomyopathy: focus on calcium sensitive pathways. Neth Heart J. 2017;25(3):157-69. Available from: https://www.ncbi.nlm.nih.gov/pubmed/28102477.

[24] Simmerman HK, Jones LR. Phospholamban: protein structure, mechanism of action, and role in cardiac function. Physiol Rev. 1998;78(4):921-47. Available from: https://www.ncbi.nlm.nih.gov/pubmed/9790566.

[25] Funk F, Kronenbitter A, Hackert K, Oebbeke M, Klebe G, Barth M, et al. Phospholamban pentamerization increases sensitivity and dynamic range of cardiac relaxation. Cardiovasc Res. 2023;119(7):1568-82. Available from: https://www.ncbi.nlm.nih.gov/pubmed/36869774.

[26] Wittmann T, Lohse MJ, Schmitt JP. Phospholamban pentamers attenuate PKA-dependent phosphorylation of monomers. J Mol Cell Cardiol.

2015;80:90-7. Available from: https://www.ncbi.nlm.nih.gov/pubmed/25562800.

[27] Scranton K, John S, Angelini M, Steccanella F, Umar S, Zhang R, et al. Cardiac function is regulated by the sodium-dependent inhibition of the sodium-calcium exchanger NCX1. Nat Commun. 2024;15(1):3831. Available from: https://www.ncbi.nlm.nih.gov/pubmed/38714663.

[28] Ottolia M, Torres N, Bridge JH, Philipson KD, Goldhaber JI. Na/Ca exchange and contraction of the heart. J Mol Cell Cardiol. 2013;61:28-33. Available from: https://www.ncbi.nlm.nih.gov/pubmed/23770352.

[29] Song R, Zhang L. Cardiac ECM: Its Epigenetic Regulation and Role in Heart Development and Repair. Int J Mol Sci. 2020;21(22). Available from: https://www.ncbi.nlm.nih.gov/pubmed/33203135.

[30] Aujla PK, Kassiri Z. Diverse origins and activation of fibroblasts in cardiac fibrosis. Cell Signal. 2021;78:109869. Available from: https://www.ncbi.nlm.nih.gov/pubmed/33278559.

[31] Gaetani R, Zizzi EA, Deriu MA, Morbiducci U, Pesce M, Messina E. When Stiffness Matters: Mechanosensing in Heart Development and Disease [Journal Article]. Front Cell Dev Biol. 2020;8:334. Available from: https://www.ncbi.nlm.nih.gov/pubmed/32671058.

[32] Israeli-Rosenberg S, Manso AM, Okada H, Ross RS. Integrins and integrin-associated proteins in the cardiac myocyte. Circ Res. 2014;114(3):572-86. Available from: https://www.ncbi.nlm.nih.gov/pubmed/24481847.

[33] Wu X, Sun Z, Foskett A, Trzeciakowski JP, Meininger GA, Muthuchamy M. Cardiomyocyte contractile status is associated with differences in fibronectin and integrin interactions. Am J Physiol Heart Circ Physiol. 2010;298(6):H2071-81. Available from: https://www.ncbi.nlm.nih.gov/pubmed/20382852.

[34] Münch J, Abdelilah-Seyfried S. Sensing and Responding of Cardiomyocytes to Changes of Tissue Stiffness in the Diseased Heart. Front Cell Dev Biol. 2021;9:642840. Available from: https://www.ncbi.nlm.nih.gov/pubmed/33718383.

[35] Ross RS, Borg TK. Integrins and the myocardium. Circ Res. 2001;88(11):1112-9. Available from: https://www.ncbi.nlm.nih.gov/pubmed/11397776.

[36] Cai X, Wang KC, Meng Z. Mechanoregulation of YAP and TAZ in Cellular Homeostasis and Disease Progression. Front Cell Dev Biol. 2021;9:673599. Available from: https://www.ncbi.nlm.nih.gov/pubmed/34109179.

[37] Park HJ, De Jesus Morales KJ, Bheri S, Kassouf BP, Davis ME. Bidirectional relationship between cardiac extracellular matrix and cardiac cells in ischemic heart disease. Stem Cells. 2021;39(12):1650-9. Available from: https://www.ncbi.nlm.nih.gov/pubmed/34480804.

[38] Kolwicz SC, Purohit S, Tian R. Cardiac metabolism and its interactions with contraction, growth, and survival of cardiomyocytes. Circ Res. 2013;113(5):603-16. Available from: https://www.ncbi.nlm.nih.gov/pubmed/23948585.

[39] Stanley WC, Recchia FA, Lopaschuk GD. Myocardial substrate metabolism in the normal and failing heart. Physiol Rev. 2005;85(3):1093-129. Available from: https://www.ncbi.nlm.nih.gov/pubmed/15987803.

[40] Lopaschuk GD, Ussher JR, Folmes CD, Jaswal JS, Stanley WC. Myocardial fatty acid metabolism in health and disease. Physiol Rev. 2010;90(1):207-58. Available from: https://www.ncbi.nlm.nih.gov/pubmed/20086077.

[41] BING RJ, SIEGEL A, UNGAR I, GILBERT M. Metabolism of the human heart. II. Studies on fat, ketone and amino acid metabolism. Am J Med;16(4):504-15. Available from: https://www.ncbi.nlm.nih.gov/pubmed/13148192.

[42] Doenst T, Nguyen TD, Abel ED. Cardiac metabolism in heart failure: implications beyond ATP production. Circ Res. 2013;113(6):709-24. Available from: https://www.ncbi.nlm.nih.gov/pubmed/23989714.

[43] Ng SM, Neubauer S, Rider OJ. Myocardial Metabolism in Heart Failure. Curr Heart Fail Rep. 2023;20:63-75. Available from: https://link.springer.com/article/10.1007/s11897-023-00589-y#citeas.

[44] Schulze PC, Drosatos K, Goldberg IJ. Lipid Use and Misuse by the Heart. Circ Res. 2016;118(11):1736-51. Available from: https://www.ncbi.nlm.nih.gov/pubmed/27230639.

[45] Abel ED. Glucose transport in the heart. Front Biosci. 2004;9:201-15. Available from: https://www.ncbi.nlm.nih.gov/pubmed/14766360.

[46] Tian R, Abel ED. Responses of GLUT4-deficient hearts to ischemia underscore the importance of glycolysis. Circulation. 2001;103(24):2961-6. Available from: https://www.ncbi.nlm.nih.gov/pubmed/11413087.

[47] Chandel NS. Glycolysis. Cold Spring Harb Perspect Biol. 2021;13(5). Available from: https://www.ncbi.nlm.nih.gov/pubmed/33941515.

[48] Tran DH, Wang ZV. Glucose Metabolism in Cardiac Hypertrophy and Heart Failure. J Am Heart Assoc. 2019;8(12):e012673. Available from: https://www.ncbi.nlm.nih.gov/pubmed/31185774.

[49] Chen S, Zou Y, Song C, Cao K, Cai K, Wu Y, et al. The role of glycolytic metabolic pathways in cardiovascular disease and potential therapeutic approaches. Basic Res Cardiol. 2023;118(1):48. Available from: https://www.ncbi.nlm.nih.gov/pubmed/37938421.

[50] Printz RL, Koch S, Potter LR, O'Doherty RM, Tiesinga JJ, Moritz S, et al. Hexokinase II mRNA and gene structure, regulation by insulin, and evolution. J Biol Chem. 1993;268(7):5209-19. Available from: https://www.ncbi.nlm.nih.gov/pubmed/8444897.

[51] Buchanan JL, Taylor EB. Mitochondrial Pyruvate Carrier Function in Health and Disease across the Lifespan. Biomolecules. 2020;10(8). Available from: https://www.ncbi.nlm.nih.gov/pubmed/32784379.

[52] Patel MS, Nemeria NS, Furey W, Jordan F. The pyruvate dehydrogenase complexes: structure-based function and regulation. J Biol Chem. 2014;289(24):16615-23. Available from: https://www.ncbi.nlm.nih.gov/pubmed/24798336.

[53] Kato M, Li J, Chuang JL, Chuang DT. Distinct Structural Mechanisms for Inhibition of Pyruvate Dehydrogenase Kinase Isoforms by AZD7545, Dichloroacetate, and Radicicol. Structure. 2007;15:992-1004. Available from: https://www.ncbi.nlm.nih.gov/pmc/articles/pmid/17683942/.

[54] Arnold PK, Finley LWS. Regulation and function of the mammalian tricarboxylic acid cycle. J Biol Chem. 2023;299(2):102838. Available from: https://www.ncbi.nlm.nih.gov/pubmed/36581208.

[55] Martínez-Reyes I, Chandel NS. Mitochondrial TCA cycle metabolites control physiology and disease. Nat Commun. 2020;11(1):102. Available from: https://www.ncbi.nlm.nih.gov/pubmed/31900386.

[56] Bhullar SK, Dhalla NS. Status of Mitochondrial Oxidative Phosphorylation during the Development of Heart Failure. Antioxidants (Basel). 2023;12(11). Available from: https://www.ncbi.nlm.nih.gov/pubmed/38001794.

[57] Uno S, Kimura H, Murai M, Miyoshi H. Exploring the quinone/inhibitor-binding pocket in mitochondrial respiratory complex I by chemical biology approaches. J Biol Chem. 2019;294(2):679-96. Available from: https://www.ncbi.nlm.nih.gov/pubmed/30425100.

[58] Sun F, Huo X, Zhai Y, Wang A, Xu J, Su D, et al. Crystal structure of mitochondrial respiratory membrane protein complex II. Cell. 2005;121(7):1043-57. Available from: https://www.ncbi.nlm.nih.gov/pubmed/15989954.

[59] Zhao RZ, Jiang S, Zhang L, Yu ZB. Mitochondrial electron transport chain, ROS generation and uncoupling (Review). Int J Mol Med. 2019;44(1):3-15. Available from: https://www.ncbi.nlm.nih.gov/pubmed/31115493.

[60] Logan A, Pell VR, Shaffer KJ, Evans C, Stanley NJ, Robb EL, et al. Assessing the Mitochondrial Membrane Potential in Cells and In Vivo using Targeted Click Chemistry and Mass Spectrometry. Cell Metab. 2016;23(2):379-85. Available from: https://www.ncbi.nlm.nih.gov/pubmed/26712463.

[61] Nolfi-Donegan D, Braganza A, Shiva S. Mitochondrial electron transport chain: Oxidative phosphorylation, oxidant production, and methods of measurement. Redox Biol. 2020;37:101674. Available from: https://www.ncbi.nlm.nih.gov/pubmed/32811789.

[62] Phypers B, Pierce T. Lactate physiology in health and disease. Continuing Education in Anaesthesia Critical Care Pain. 2006;6(3):128-32. Available from: https://doi.org/10.1093/bjaceaccp/mkl018.

[63] Harmer AR, Chisholm DJ, McKenna MJ, Hunter SK, Ruell PA, Naylor JM, et al. Sprint training increases muscle oxidative metabolism during high-intensity exercise in patients with type 1 diabetes. Diabetes Care. 2008;31(11):2097-102. Available from: https://www.ncbi.nlm.nih.gov/pubmed/18716051.

[64] Ouyang J, Wang H, Huang J. The role of lactate in cardiovascular diseases. Cell Commun Signal. 2023;21(1):317. Available from: https://www.ncbi.nlm.nih.gov/pubmed/37924124.

[65] Stanley WC. Myocardial lactate metabolism during exercise. Med Sci Sports Exerc. 1991;23(8):920-4. Available from: https://www.ncbi.nlm.nih.gov/pubmed/1956265.

[66] Wu P, Zhu T, Huang Y, Fang Z, Luo F. Current understanding of the contribution of lactate to the cardiovascular system and its therapeutic relevance. Front Endocrinol (Lausanne). 2023;14:1205442. Available from: https://www.ncbi.nlm.nih.gov/pubmed/37396168.

[67] Li X, Yang Y, Zhang B, Lin X, Fu X, An Y, et al. Lactate metabolism in human health and disease. Signal Transduct Target Ther. 2022;7(1):305. Available from: https://www.ncbi.nlm.nih.gov/pubmed/36050306.

[68] van Hall G. Lactate kinetics in human tissues at rest and during exercise. Acta Physiol (Oxf). 2010;199(4):499-508. Available from: https://www.ncbi.nlm.nih.gov/pubmed/20345411.

[69] Li X, Bi X. Integrated Control of Fatty Acid Metabolism in Heart Failure. Metabolites. 2023;13(5). Available from: https://www.ncbi.nlm.nih.gov/pubmed/37233656.

[70] Schulze PC, Drosatos K, Goldberg IJ. Lipid Use and Misuse by the Heart. Circ Res. 2016;118(11):1736-51. Available from: https://www.ncbi.nlm.nih.gov/pubmed/27230639.

[71] Longo N, Frigeni M, Pasquali M. Carnitine transport and fatty acid oxidation. Biochim Biophys Acta. 2016;1863(10):2422-35. Available from: https://www.ncbi.nlm.nih.gov/pubmed/26828774.

[72] He L, Kim T, Long Q, Liu J, Wang P, Zhou Y, et al. Carnitine palmitoyltransferase-1b deficiency aggravates pressure overload-induced cardiac hypertrophy caused by lipotoxicity. Circulation. 2012;126(14):1705-16. Available from: https://www.ncbi.nlm.nih.gov/pubmed/22932257.

[73] Foundation BH. BHF Statistics UK Factsheet January 2024; 2024. Available from: https://www.bhf.org.uk/-/media/files/for-professionals/research/heart-statistics/bhf-cvd-statistics-uk-factsheet.pdf.

[74] Rodgers JL, Jones J, Bolleddu SI, Vanthenapalli S, Rodgers LE, Shah K, et al. Cardiovascular Risks Associated with Gender and Aging. J Cardiovasc Dev Dis. 2019;6(2). Available from: https://www.ncbi.nlm.nih.gov/pubmed/31035613.

[75] Coats AJS. Ageing, demographics, and heart failure. Eur Heart J Suppl. 2019;21(Suppl L):L4-7. Available from: https://www.ncbi.nlm.nih.gov/pubmed/31885504.

[76] Yazdanyar A, Newman AB. The burden of cardiovascular disease in the elderly: morbidity, mortality, and costs. Clin Geriatr Med. 2009;25(4):563-77, vii. Available from: https://www.ncbi.nlm.nih.gov/pubmed/19944261.

[77] North BJ, Sinclair DA. The intersection between aging and cardiovascular disease. Circ Res. 2012;110(8):1097-108. Available from: https://www.ncbi.nlm.nih.gov/pubmed/22499900.

[78] Tracy E, Rowe G, LeBlanc AJ. Cardiac tissue remodeling in healthy aging: the road to pathology. Am J Physiol Cell Physiol. 2020;319(1):C166-82. Available from: https://www.ncbi.nlm.nih.gov/pubmed/32432929.

[79] Burchfield JS, Xie M, Hill JA. Pathological ventricular remodeling: mechanisms: part 1 of 2. Circulation. 2013;128(4):388-400. Available from: https://www.ncbi.nlm.nih.gov/pubmed/23877061.

[80] Paneni F, Diaz Cañestro C, Libby P, Lüscher TF, Camici GG. The Aging Cardiovascular System: Understanding It at the Cellular and Clinical Levels. J Am Coll Cardiol. 2017;69(15):1952-67. Available from: https://www.ncbi.nlm.nih.gov/pubmed/28408026.

[81] Burkauskiene A. Age-related changes in the structure of myocardial collagen network of auricle of the right atrium in healthy persons and ischemic heart disease patients. Medicina (Kaunas). 2005;41(2):145-54. Available from: https://www.ncbi.nlm.nih.gov/pubmed/15758582.

[82] Bradshaw AD, Baicu CF, Rentz TJ, Van Laer AO, Bonnema DD, Zile MR. Age-dependent alterations in fibrillar collagen content and myocardial diastolic function: role of SPARC in post-synthetic procollagen processing. Am J Physiol Heart Circ Physiol. 2010;298(2):H614-22. Available from: https://www.ncbi.nlm.nih.gov/pubmed/20008277.

[83] Annoni G, Luvarà G, Arosio B, Gagliano N, Fiordaliso F, Santambrogio D, et al. Age-dependent expression of fibrosis-related genes and collagen deposition in the rat myocardium. Mech Ageing Dev. 1998;101(1-2):57-72. Available from: https://www.ncbi.nlm.nih.gov/pubmed/9593313.

[84] Ribeiro ASF, Zerolo BE, López-Espuela F, Sánchez R, Fernandes VS. Cardiac System during the Aging Process. Aging Dis. 2023;14(4):1105-22. Available from: https://www.ncbi.nlm.nih.gov/pubmed/37163425.

[85] Lakatta EG, Levy D. Arterial and cardiac aging: major shareholders in cardiovascular disease enterprises: Part II: the aging heart in health: links to heart disease. Circulation. 2003;107(2):346-54. Available from: https://www.ncbi.nlm.nih.gov/pubmed/12538439.

[86] Babušíková E, Lehotský J, Dobrota D, Račay P, Kaplán P. Age-associated changes in Ca(2+)-ATPase and oxidative damage in sarcoplasmic reticulum of rat heart. Physiol Res. 2012;61(5):453-60. Available from: https://www.ncbi.nlm.nih.gov/pubmed/22881224.

[87] López-Otín C, Blasco MA, Partridge L, Serrano M, Kroemer G. Hallmarks of aging: An expanding universe. Cell. 2023;186. Available from: https://www.sciencedirect.com/science/article/pii/S0092867422013770.

[88] Tang X, Li PH, Chen HZ. Cardiomyocyte Senescence and Cellular Communications Within Myocardial Microenvironments [Journal Article]. Front Endocrinol (Lausanne). 2020;11:280. Tang, Xiaoqiang Li, Pei-Heng Chen, Hou-Zao 2020/6/9. Available from: https://www.ncbi.nlm.nih.gov/pubmed/32508749.

[89] Camacho-Encina M, Booth LK, Redgrave RE, Folaranmi O, Spyridopoulos I, Richardson GD. Cellular Senescence, Mitochondrial Dysfunction, and Their Link to Cardiovascular Disease. Cells. 2024;13(4). Available from: https://www.ncbi.nlm.nih.gov/pubmed/38391966.

[90] Burchfield JS, Xie M, Hill JA. Pathological ventricular remodeling: mechanisms: part 1 of 2. Circulation. 2013;128(4):388-400. Available from: https://www.ncbi.nlm.nih.gov/pubmed/23877061.

[91] Kendall RT, Feghali-Bostwick CA. Fibroblasts in fibrosis: novel roles and mediators. Front Pharmacol. 2014;5:123. Available from: https://www.ncbi.nlm.nih.gov/pubmed/24904424.

[92] Horn MA, Trafford AW. Aging and the cardiac collagen matrix: Novel mediators of fibrotic remodelling. J Mol Cell Cardiol. 2016;93:175-85. Available from: https://www.ncbi.nlm.nih.gov/pubmed/26578393.

[93] Bonnans C, Chou J, Werb Z. Remodelling the extracellular matrix in development and disease. Nat Rev Mol Cell Biol. 2014;15(12):786-801. Available from: https://www.ncbi.nlm.nih.gov/pubmed/25415508.

[94] Engler AJ, Carag-Krieger C, Johnson CP, Raab M, Tang HY, Speicher DW, et al. Embryonic cardiomyocytes beat best on a matrix with heart-like elasticity: scar-like rigidity inhibits beating. J Cell Sci. 2008;121(Pt 22):3794-802. Available from: https://www.ncbi.nlm.nih.gov/pubmed/18957515.

[95] Travers JG, Kamal FA, Robbins J, Yutzey KE, Blaxall BC. Cardiac Fibrosis: The Fibroblast Awakens. Circ Res. 2016;118(6):1021-40. Available from: https://www.ncbi.nlm.nih.gov/pubmed/26987915.

[96] Jiang W, Xiong Y, Li X, Yang Y. Cardiac Fibrosis: Cellular Effectors, Molecular Pathways, and Exosomal Roles. Front Cardiovasc Med. 2021;8:715258. Available from: https://www.ncbi.nlm.nih.gov/pubmed/34485413.

[97] Cho N, Razipour SE, McCain ML. Featured Article: TGF-1 dominates extracellular matrix rigidity for inducing differentiation of human cardiac fibroblasts to myofibroblasts. Exp Biol Med (Maywood). 2018;243(7):601-12. Available from: https://www.ncbi.nlm.nih.gov/pubmed/29504479.

[98] Chin IL, Hool L, Choi YS. Interrogating cardiac muscle cell mechanobiology on stiffness gradient hydrogels. Biomater Sci. 2021;9(20):6795-806. Available from: https://www.ncbi.nlm.nih.gov/pubmed/34542112.

[99] Herraiz-Martínez A, Álvarez García J, Llach A, Molina CE, Fernandes J, Ferrero-Gregori A, et al. Ageing is associated with deterioration of calcium homeostasis in isolated human right atrial myocytes. Cardiovasc Res. 2015;106(1):76-86. Available from: https://www.ncbi.nlm.nih.gov/pubmed/25712961.

[100] Harvey RD, Hell JW. CaV1.2 signaling complexes in the heart. J Mol Cell Cardiol. 2013;58:143-52. Available from: https://www.ncbi.nlm.nih.gov/pubmed/23266596.

[101] Zhu X, Altschafl BA, Hajjar RJ, Valdivia HH, Schmidt U. Altered Ca2+ sparks and gating properties of ryanodine receptors in aging cardiomyocytes. Cell Calcium. 2005;37(6):583-91. Available from: https://www.ncbi.nlm.nih.gov/pubmed/15862349.

[102] Xu A, Narayanan N. Effects of aging on sarcoplasmic reticulum Ca2+-cycling proteins and their phosphorylation in rat myocardium. Am J Physiol.

1998;275(6):H2087-94. Available from: https://www.ncbi.nlm.nih.gov/pubmed/9843808.

[103] Boyden PA, Smith GL. Ca2+ leak, what is it? Why should we care? Can it be managed? Heart Rhythm. 2018;15:607-14. Available from: https://www.ncbi.nlm.nih.gov/pmc/articles/pmid/29157722/.

[104] Park WJ, Oh JG. SERCA2a: a prime target for modulation of cardiac contractility during heart failure. BMB Rep. 2013;46(5):237-43. Available from: https://www.ncbi.nlm.nih.gov/pubmed/23710633.

[105] Despa S, Bers DM. Na transport in the normal and failing heart - remember the balance. J Mol Cell Cardiol. 2013;61:2-10. Available from: https://www.ncbi.nlm.nih.gov/pubmed/23608603.

[106] Janapati V, Wu A, Davis N, Derrico CA, Levengood J, Schummers J, et al. Post-transcriptional regulation of the Na+/Ca2+ exchanger in aging rat heart. Mech Ageing Dev. 1995;84(3):195-208. Available from: https://www.ncbi.nlm.nih.gov/pubmed/8788775.

[107] Ozturk N, Olgar Y, Er H, Kucuk M, Ozdemir S. Swimming exercise reverses aging-related contractile abnormalities of female heart by improving structural alterations. Cardiol J. 2017;24(1):85-93. Available from: https://www.ncbi.nlm.nih.gov/pubmed/27665854.

[108] ALSTROM CH, HALLGREN B, NILSSON LB, ASANDER H. Retinal degeneration combined with obesity, diabetes mellitus and neurogenous deafness: a specific syndrome (not hitherto described) distinct from the Laurence-Moon-Bardet-Biedl syndrome: a clinical, endocrinological and genetic examination based on a large pedigree. Acta Psychiatr Neurol Scand Suppl. 1959;129:1-35. Available from: https://www.ncbi.nlm.nih.gov/pubmed/13649370.

[109] Patel L, Roy A, Alvior AMB, Yuan M, Baig S, Bunting KV, et al. Phenoage and longitudinal changes on transthoracic echocardiography in Alström syndrome: a disease of accelerated ageing? Geroscience. 2024;46:1989-99. Available from: https://link.springer.com/article/10.1007/s11357-023-00959-3#citeas.

[110] Brofferio A, Sachdev V, Hannoush H, Marshall JD, Naggert JK, Sidenko S, et al. Characteristics of cardiomyopathy in Alström syndrome: Prospective single-center data on 38 patients. Mol Genet Metab. 2017;121(4):336-43. Available from: https://www.ncbi.nlm.nih.gov/pubmed/28610912.

[111] Marshall JD, Bronson RT, Collin GB, Nordstrom AD, Maffei P, Paisey RB, et al. New Alström syndrome phenotypes based on the evaluation of 182 cases. Arch Intern Med. 2005;165(6):675-83. Available from: https://www.ncbi.nlm.nih.gov/pubmed/15795345.

[112] Roy A, Patel L, Yuan M, O'Shea C, Alvior AMB, Charalambides M, et al. Defining the cardiovascular phenotype of adults with Alström syndrome. Int J Cardiol. 2024;409:132212. Available from: https://www.ncbi.nlm.nih.gov/pubmed/38806112.

[113] Hearn T. ALMS1 and Alström syndrome: a recessive form of metabolic, neurosensory and cardiac deficits. J Mol Med (Berl). 2019;97(1):1-17. Available from: https://www.ncbi.nlm.nih.gov/pubmed/30421101.

[114] Marshall JD, Muller J, Collin GB, Milan G, Kingsmore SF, Dinwiddie D, et al. Alström Syndrome: Mutation Spectrum of ALMS1. Hum Mutat. 2015;36(7):660-8. Available from: https://www.ncbi.nlm.nih.gov/pubmed/25846608.

[115] Tsai MC, Yu HW, Liu T, Chou YY, Chiou YY, Chen PC. Rare Compound Heterozygous Frameshift Mutations in. Front Genet. 2018;9:110. Available from: https://www.ncbi.nlm.nih.gov/pubmed/29720996.

[116] Álvarez Satta M, Castro-Sánchez S, Valverde D. Alström syndrome: current perspectives. Appl Clin Genet. 2015;8:171-9. Available from: https://www.ncbi.nlm.nih.gov/pubmed/26229500.

[117] Sithara T, Drosatos K. Metabolic Complications in Cardiac Aging. Front Physiol. 2021;12:669497. Available from: https://www.ncbi.nlm.nih.gov/pubmed/33995129.

[118] Xie S, Xu SC, Deng W, Tang Q. Metabolic landscape in cardiac aging: insights into molecular biology and therapeutic implications. Signal Transduct Target Ther. 2023;8(1):114. Available from: https://www.ncbi.nlm.nih.gov/pubmed/36918543.

[119] Karwi QG, Uddin GM, Ho KL, Lopaschuk GD. Loss of Metabolic Flexibility in the Failing Heart. Front Cardiovasc Med. 2018;5:68. Available from: https://www.ncbi.nlm.nih.gov/pubmed/29928647.

[120] De Jong KA, Lopaschuk GD. Complex Energy Metabolic Changes in Heart Failure With Preserved Ejection Fraction and Heart Failure With Re-

duced Ejection Fraction. Can J Cardiol. 2017;33(7):860-71. Available from: https://www.ncbi.nlm.nih.gov/pubmed/28579160.

[121] Tatarková Z, Kuka S, Račay P, Lehotský J, Dobrota D, Mištuna D, et al. Effects of aging on activities of mitochondrial electron transport chain complexes and oxidative damage in rat heart. Physiol Res. 2011;60(2):281-9. Available from: https://www.ncbi.nlm.nih.gov/pubmed/21114360.

[122] Tocchi A, Quarles E, Basisty N, Gitari L, Rabinovitch P. Mitochondrial Dysfunction in Cardiac Ageing. Biochim Biophys Acta. 2015;1847:1424-33.

[123] Morciano G, Vitto VAM, Bouhamida E, Giorgi C, Pinton P. Mitochondrial Bioenergetics and Dynamism in the Failing Heart. Life (Basel). 2021;11(5). Available from: https://www.ncbi.nlm.nih.gov/pubmed/34066065.

[124] Tran DH, Wang ZV. Glucose Metabolism in Cardiac Hypertrophy and Heart Failure. J Am Heart Assoc. 2019;8(12):e012673. Available from: https://www.ncbi.nlm.nih.gov/pubmed/31185774.

[125] Dai DF, Chen T, Johnson SC, Szeto H, Rabinovitch PS. Cardiac aging: from molecular mechanisms to significance in human health and disease. Antioxid Redox Signal. 2012;16(12):1492-526. Available from: https://www.ncbi.nlm.nih.gov/pubmed/22229339.

[126] Dai DF, Rabinovitch PS. Cardiac aging in mice and humans: the role of mitochondrial oxidative stress. Trends Cardiovasc Med. 2009;19(7):213-20. Available from: https://www.ncbi.nlm.nih.gov/pubmed/20382344.

[127] Milani-Nejad N, Janssen PM. Small and large animal models in cardiac contraction research: advantages and disadvantages. Pharmacol Ther. 2014;141(3):235-49. Available from: https://www.ncbi.nlm.nih.gov/pubmed/24140081.

[128] Pitrez PR, Monteiro LM, Borgogno O, Nissan X, Mertens J, Ferreira L. Cellular reprogramming as a tool to model human aging in a dish. Nat Commun. 2024;15(1):1816. Available from: https://www.ncbi.nlm.nih.gov/pubmed/38418829.

[129] Takahashi K, Yamanaka S. Induction of pluripotent stem cells from mouse embryonic and adult fibroblast cultures by defined factors. Cell. 2006;126(4):663-76. Available from: https://www.ncbi.nlm.nih.gov/pubmed/16904174.

[130] Takahashi K, Tanabe K, Ohnuki M, Narita M, Ichisaka T, Tomoda K, et al. Induction of pluripotent stem cells from adult human fibroblasts by defined factors. Cell. 2007;131(5):861-72. Available from: https://www.ncbi.nlm.nih.gov/pubmed/18035408.

[131] Lian X, Hsiao C, Wilson G, Zhu K, Hazeltine LB, Azarin SM, et al. Robust cardiomyocyte differentiation from human pluripotent stem cells via temporal modulation of canonical Wnt signaling. Proc Natl Acad Sci U S A. 2012;109(27):E1848-57. Available from: https://www.ncbi.nlm.nih.gov/pubmed/22645348.

[132] Funakoshi S, Yoshida Y. Recent progress of iPSC technology in cardiac diseases. Arch Toxicol. 2021;95(12):3633-50. Available from: https://www.ncbi.nlm.nih.gov/pubmed/34657219.

[133] Sinnecker D, Goedel A, Laugwitz KL, Moretti A. Induced pluripotent stem cell-derived cardiomyocytes: a versatile tool for arrhythmia research. Circ Res. 2013;112(6):961-8. Available from: https://www.ncbi.nlm.nih.gov/pubmed/23569105.

[134] Parrotta EI, Lucchino V, Scaramuzzino L, Scalise S, Cuda G. Modeling Cardiac Disease Mechanisms Using Induced Pluripotent Stem Cell-Derived Cardiomyocytes: Progress, Promises and Challenges. Int J Mol Sci. 2020;21(12). Available from: https://www.ncbi.nlm.nih.gov/pubmed/32575374.

[135] Almeida HV, Tenreiro MF, Louro AF, Abecasis B, Santinha D, Calmeiro T, et al. Human Extracellular-Matrix Functionalization of 3D hiPSC-Based Cardiac Tissues Improves Cardiomyocyte Maturation. ACS Appl Bio Mater. 2021;4(2):1888-99. Available from: https://www.ncbi.nlm.nih.gov/pubmed/35014458.

[136] Zhu R, Blazeski A, Poon E, Costa KD, Tung L, Boheler KR. Physical developmental cues for the maturation of human pluripotent stem cell-derived cardiomyocytes. Stem Cell Res Ther. 2014;5(5):117. Available from: https://www.ncbi.nlm.nih.gov/pubmed/25688759.

[137] Li S, Chen G, Li RA. Calcium signalling of human pluripotent stem cell-derived cardiomyocytes. J Physiol. 2013;591(21):5279-90. Available from: https://www.ncbi.nlm.nih.gov/pubmed/24018947.

[138] Robertson C, Tran DD, George SC. Concise review: maturation phases of human pluripotent stem cell-derived cardiomyocytes. Stem Cells.

2013;31(5):829-37. Available from: https://www.ncbi.nlm.nih.gov/pubmed/23355363.

[139] Tohyama S, Hattori F, Sano M, Hishiki T, Nagahata Y, Matsuura T, et al. Distinct metabolic flow enables large-scale purification of mouse and human pluripotent stem cell-derived cardiomyocytes. Cell Stem Cell. 2013;12(1):127-37. Available from: https://www.ncbi.nlm.nih.gov/pubmed/23168164.

[140] Tu C, Chao BS, Wu JC. Strategies for Improving the Maturity of Human Induced Pluripotent Stem Cell-Derived Cardiomyocytes. Circ Res. 2018;123(5):512-4. Available from: https://www.ncbi.nlm.nih.gov/pubmed/30355143.

[141] Wu P, Deng G, Sai X, Guo H, Huang H, Zhu P. Maturation strategies and limitations of induced pluripotent stem cell-derived cardiomyocytes. Biosci Rep. 2021;41(6). Available from: https://www.ncbi.nlm.nih.gov/pubmed/33057659.

[142] Zimmermann WH, Schneiderbanger K, Schubert P, Didié M, Münzel F, Heubach JF, et al. Tissue engineering of a differentiated cardiac muscle construct. Circ Res. 2002;90(2):223-30. Available from: https://www.ncbi.nlm.nih.gov/pubmed/11834716.

[143] Hirt MN, Boeddinghaus J, Mitchell A, Schaaf S, Börnchen C, Müller C, et al. Functional improvement and maturation of rat and human engineered heart tissue by chronic electrical stimulation. J Mol Cell Cardiol. 2014;74:151-61. Available from: https://www.ncbi.nlm.nih.gov/pubmed/24852842.

[144] Lundy SD, Zhu WZ, Regnier M, Laflamme MA. Structural and functional maturation of cardiomyocytes derived from human pluripotent stem cells. Stem Cells Dev. 2013;22(14):1991-2002. Available from: https://www.ncbi.nlm.nih.gov/pubmed/23461462.

[145] Ufford K, Friedline S, Tong Z, Tang VT, Dobbs AS, Tsan YC, et al. Myofibrillar Structural Variability Underlies Contractile Function in Stem Cell-Derived Cardiomyocytes. Stem Cell Reports. 2021;16(3):470-7. Available from: https://www.ncbi.nlm.nih.gov/pubmed/33577793.

[146] Napiwocki BN, Stempien A, Lang D, Kruepke RA, Kim G, Zhang J, et al. Micropattern platform promotes extracellular matrix remodeling by human PSC-derived cardiac fibroblasts and enhances contractility of co-cultured

cardiomyocytes. Physiol Rep. 2021;9(19):e15045. Available from: https://www.ncbi.nlm.nih.gov/pubmed/34617673.

[147] Yang X, Rodriguez ML, Leonard A, Sun L, Fischer KA, Wang Y, et al. Fatty Acids Enhance the Maturation of Cardiomyocytes Derived from Human Pluripotent Stem Cells. Stem Cell Reports. 2019;13(4):657-68. Available from: https://www.ncbi.nlm.nih.gov/pubmed/31564645.

[148] Yoshida S, Sumomozawa K, Nagamine K, Nishizawa M. Hydrogel Microchambers Integrated with Organic Electrodes for Efficient Electrical Stimulation of Human iPSC-Derived Cardiomyocytes. Macromol Biosci. 2019;19(6):e1900060. Available from: https://www.ncbi.nlm.nih.gov/pubmed/31038841.

[149] Wu P, Deng G, Sai X, Guo H, Huang H, Zhu P. Maturation strategies and limitations of induced pluripotent stem cell-derived cardiomyocytes. Biosci Rep. 2021;41(6). Available from: https://www.ncbi.nlm.nih.gov/pubmed/33057659.

[150] Feaster TK, Cadar AG, Wang L, Williams CH, Chun YW, Hempel JE, et al. Matrigel Mattress: A Method for the Generation of Single Contracting Human-Induced Pluripotent Stem Cell-Derived Cardiomyocytes. Circ Res. 2015;117(12):995-1000. Available from: https://www.ncbi.nlm.nih.gov/pubmed/26429802.

[151] Ahmed RE, Anzai T, Chanthra N, Uosaki H. A Brief Review of Current Maturation Methods for Human Induced Pluripotent Stem Cells-Derived Cardiomyocytes. Front Cell Dev Biol. 2020;8:178. Available from: https://www.ncbi.nlm.nih.gov/pubmed/32266260.

[152] Felisbino MB, Rubino M, Travers JG, Schuetze KB, Lemieux ME, Anseth KS, et al. Substrate stiffness modulates cardiac fibroblast activation, senescence, and proinflammatory secretory phenotype. Am J Physiol Heart Circ Physiol. 2024;326(1):H61-73. Available from: https://www.ncbi.nlm.nih.gov/pubmed/37889253.

[153] Yahalom-Ronen Y, Rajchman D, Sarig R, Geiger B, Tzahor E. Reduced matrix rigidity promotes neonatal cardiomyocyte dedifferentiation, proliferation and clonal expansion. Elife. 2015;4. Available from: https://www.ncbi.nlm.nih.gov/pubmed/26267307.

[154] Vu TVA, Lorizio D, Vuerich R, Lippi M, Nascimento DS, Zacchigna S. Extracellular Matrix-Based Approaches in Cardiac Regeneration: Challenges and Opportunities. Int J Mol Sci. 2022;23(24). Available from: https://www.ncbi.nlm.nih.gov/pubmed/36555424.

[155] Aisenbrey EA, Murphy WL. Synthetic alternatives to Matrigel. Nat Rev Mater. 2020;5(7):539-51. Available from: https://www.ncbi.nlm.nih.gov/pubmed/32953138.

[156] Bejleri D, Streeter BW, Nachlas ALY, Brown ME, Gaetani R, Christman KL, et al. A Bioprinted Cardiac Patch Composed of Cardiac-Specific Extracellular Matrix and Progenitor Cells for Heart Repair. Adv Healthc Mater. 2018;7(23):e1800672. Available from: https://www.ncbi.nlm.nih.gov/pubmed/30379414.

[157] Rector RS, Payne RM, Ibdah JA. Mitochondrial trifunctional protein defects: clinical implications and therapeutic approaches. Adv Drug Deliv Rev. 2008;60(13-14):1488-96. Available from: https://www.ncbi.nlm.nih.gov/pubmed/18652860.

[158] Majid QA, Fricker ATR, Gregory DA, Davidenko N, Hernandez Cruz O, Jabbour RJ, et al. Natural Biomaterials for Cardiac Tissue Engineering: A Highly Biocompatible Solution. Front Cardiovasc Med. 2020;7:554597. Available from: https://www.ncbi.nlm.nih.gov/pubmed/33195451.

[159] Dimatteo R, Darling NJ, Segura T. In situ forming injectable hydrogels for drug delivery and wound repair. Adv Drug Deliv Rev. 2018;127:167-84. Available from: https://www.ncbi.nlm.nih.gov/pubmed/29567395.

[160] Chow A, Stuckey DJ, Kidher E, Rocco M, Jabbour RJ, Mansfield CA, et al. Human Induced Pluripotent Stem Cell-Derived Cardiomyocyte Encapsulating Bioactive Hydrogels Improve Rat Heart Function Post Myocardial Infarction. Stem Cell Reports. 2017;9(5):1415-22. Available from: https://www.ncbi.nlm.nih.gov/pubmed/28988988.

[161] Catoira MC, Fusaro L, Di Francesco D, Ramella M, Boccafoschi F. Overview of natural hydrogels for regenerative medicine applications. J Mater Sci Mater Med. 2019;30(10):115. Available from: https://www.ncbi.nlm.nih.gov/pubmed/31599365.

[162] Drury JL, Mooney DJ. Hydrogels for tissue engineering: scaffold design variables and applications. Biomaterials. 2003;24(24):4337-51. Available from: https://www.ncbi.nlm.nih.gov/pubmed/12922147.

[163] Peters JT, Wechsler ME, Peppas NA. Advanced biomedical hydrogels: molecular architecture and its impact on medical applications. Regen Biomater. 2021;8(6):rbab060. Available from: https://www.ncbi.nlm.nih.gov/pubmed/34925879.

[164] Mano JF, Silva GA, Azevedo HS, Malafaya PB, Sousa RA, Silva SS, et al. Natural origin biodegradable systems in tissue engineering and regenerative medicine: present status and some moving trends. J R Soc Interface. 2007;4(17):999-1030. Available from: https://www.ncbi.nlm.nih.gov/pubmed/17412675.

[165] Liu X, Ma PX. Phase separation, pore structure, and properties of nanofibrous gelatin scaffolds. Biomaterials. 2009;30(25):4094-103. Available from: https://www.ncbi.nlm.nih.gov/pubmed/19481080.

[166] McCain ML, Agarwal A, Nesmith HW, Nesmith AP, Parker KK. Micromolded gelatin hydrogels for extended culture of engineered cardiac tissues. Biomaterials. 2014;35(21):5462-71. Available from: https://www.ncbi.nlm.nih.gov/pubmed/24731714.

[167] Oyama TG, Oyama K, Kimura A, Yoshida F, Ishida R, Yamazaki M, et al. Collagen hydrogels with controllable combined cues of elasticity and topography to regulate cellular processes. Biomed Mater. 2021;16(4). Available from: https://www.ncbi.nlm.nih.gov/pubmed/34030146.

[168] Burdick JA, Prestwich GD. Hyaluronic acid hydrogels for biomedical applications. Adv Mater. 2011;23(12):H41-56. Available from: https://www.ncbi.nlm.nih.gov/pubmed/21394792.

[169] Kaiser NJ, Kant RJ, Minor AJ, Coulombe KLK. Optimizing Blended Collagen-Fibrin Hydrogels for Cardiac Tissue Engineering with Human iPSC-derived Cardiomyocytes. ACS Biomater Sci Eng. 2019;5(2):887-99. Available from: https://www.ncbi.nlm.nih.gov/pubmed/30775432.

[170] Bhana B, Iyer RK, Chen WL, Zhao R, Sider KL, Likhitpanichkul M, et al. Influence of substrate stiffness on the phenotype of heart cells. Biotechnol Bioeng. 2010;105(6):1148-60. Available from: https://www.ncbi.nlm.nih.gov/pubmed/20014437.

[171] Hall ML, Ogle BM. Cardiac Extracellular Matrix Modification as a Therapeutic Approach. Adv Exp Med Biol. 2018;1098:131-50. Available from: https://www.ncbi.nlm.nih.gov/pubmed/30238369.

[172] Lin CC, Anseth KS. PEG hydrogels for the controlled release of biomolecules in regenerative medicine. Pharm Res. 2009;26(3):631-43. Available from: https://www.ncbi.nlm.nih.gov/pubmed/19089601.

[173] Martin S, Bhushan B. Transparent, wear-resistant, superhydrophobic and superoleophobic poly(dimethylsiloxane) (PDMS) surfaces. Journal of Colloid and Interface Science. 2017;488:118-26. Available from: https://www.sciencedirect.com/science/article/pii/S002197971630861X.

[174] Gray DS, Tien J, Chen CS. Repositioning of cells by mechanotaxis on surfaces with micropatterned Young's modulus. J Biomed Mater Res A. 2003;66(3):605-14. Available from: https://www.ncbi.nlm.nih.gov/pubmed/12918044.

[175] Yeh YC, Corbin EA, Caliari SR, Ouyang L, Vega SL, Truitt R, et al. Mechanically dynamic PDMS substrates to investigate changing cell environments. Biomaterials. 2017;145:23-32. Available from: https://www.ncbi.nlm.nih.gov/pubmed/28843064.

[176] Crocini C, Walker CJ, Anseth KS, Leinwand LA. Three-dimensional encapsulation of adult mouse cardiomyocytes in hydrogels with tunable stiffness. Prog Biophys Mol Biol. 2020;154:71-9. Available from: https://www.ncbi.nlm.nih.gov/pubmed/31122749.

[177] Vlachopoulou ME, Petrou PS, Kakabakos SE, Tserepi A, Beltsios K, Gogolides E. Effect of surface nanostructuring of PDMS on wetting properties, hydrophobic recovery and protein adsorption. Microelectronic Engineering. 2009;86(4):1321-4. Available from: https://www.sciencedirect.com/science/article/pii/S0167931708005388.

[178] Neves MI, Moroni L, Barrias CC. Modulating Alginate Hydrogels for Improved Biological Performance as Cellular 3D Microenvironments. Front Bioeng Biotechnol. 2020;8:665. Available from: https://www.ncbi.nlm.nih.gov/pubmed/32695759.

[179] Cumberland MJ, Euchner J, Azad AJ, T N Vo N, Kirchhof P, Holmes AP, et al. Generation of a human iPSC-derived cardiomyocyte/fibroblast engineered heart tissue model. F1000Res. 2024;12:1224. Available from: https://www.ncbi.nlm.nih.gov/pubmed/38298530.

[180] Morris TA, Naik J, Fibben KS, Kong X, Kiyono T, Yokomori K, et al. Striated myocyte structural integrity: Automated analysis of sarcomeric z-

discs. PLoS Comput Biol. 2020;16(3):e1007676. Available from: https://www.ncbi.nlm.nih.gov/pubmed/32130207.

[181] O'Shea C, Holmes AP, Yu TY, Winter J, Wells SP, Correia J, et al. ElectroMap: High-throughput open-source software for analysis and mapping of cardiac electrophysiology. Sci Rep. 2019;9(1):1389. Available from: https://www.ncbi.nlm.nih.gov/pubmed/30718782.

[182] Sala L, van Meer BJ, Tertoolen LGJ, Bakkers J, Bellin M, Davis RP, et al. MUSCLEMOTION: A Versatile Open Software Tool to Quantify Cardiomyocyte and Cardiac Muscle Contraction In Vitro and In Vivo. Circ Res. 2018;122(3):e5-e16. Available from: https://www.ncbi.nlm.nih.gov/pubmed/29282212.

[183] Karlstaedt A. Stable Isotopes for Tracing Cardiac Metabolism in Diseases. Front. 2021;8. Available from: https://www.frontiersin.org/journals/cardiovascular-medicine/articles/10.3389/fcvm.2021.734364/full.

[184] Gu X, Yuan M, Yi L, Qiang W. Measurement of mitochondrial respiration in adherent cells by Seahorse XF96 Cell Mito Stress Test. STAR Protocols. 2021;2(1):100245. Available from: https://www.sciencedirect.com/science/article/pii/S266616720302032X.

[185] Frangogiannis NG. The extracellular matrix in myocardial injury, repair, and remodeling. J Clin Invest. 2017;127(5):1600-12. Available from: https://www.ncbi.nlm.nih.gov/pubmed/28459429.

[186] Rienks M, Papageorgiou AP, Frangogiannis NG, Heymans S. Myocardial extracellular matrix: an ever-changing and diverse entity. Circ Res. 2014;114(5):872-88. Available from: https://www.ncbi.nlm.nih.gov/pubmed/24577967.

[187] Ahmed RE, Anzai T, Chanthra N, Uosaki H. A Brief Review of Current Maturation Methods for Human Induced Pluripotent Stem Cells-Derived Cardiomyocytes. Front Cell Dev Biol. 2020;8:178. Available from: https://www.ncbi.nlm.nih.gov/pubmed/32266260.

[188] Hinz B. Matrix mechanics and regulation of the fibroblast phenotype. Periodontol 2000. 2013;63(1):14-28. Available from: https://www.ncbi.nlm.nih.gov/pubmed/23931051.

[189] Felisbino MB, Rubino M, Travers JG, Schuetze KB, Lemieux ME, Anseth KS, et al. Substrate stiffness modulates cardiac fibroblast activation,

senescence, and proinflammatory secretory phenotype [Journal Article]. Am J Physiol Heart Circ Physiol. 2024;326(1):H61-73. Felisbino, Marina B Rubino, Marcello Travers, Joshua G Schuetze, Katherine B Lemieux, Madeleine E Anseth, Kristi S Aguado, Brian A McKinsey, Timothy A 2023/10/27. Available from: https://www.ncbi.nlm.nih.gov/pubmed/37889253.

[190] Seal A, Daliu AK, Banerjee M, Mukhopadhyay AK, Phani KK. Mechanical properties of very thin cover slip glass disk. Bull Mater Sci. 2001;24:151-5. Available from: https://link.springer.com/article/10.1007/BF02710092#citeas.

[191] Kim TT, Dyck JR. The role of CD36 in the regulation of myocardial lipid metabolism. Biochim Biophys Acta. 2016;1861(10):1450-60. Available from: https://www.ncbi.nlm.nih.gov/pubmed/26995462.

[192] Chen TA, Zhao BB, Balbin RA, Sharma S, Ha D, Kamp TJ, et al. Engineering a robust and anisotropic cardiac-specific extracellular matrix scaffold for cardiac patch tissue engineering. Matrix Biol Plus. 2024;23:100151. Available from: https://www.ncbi.nlm.nih.gov/pubmed/38882397.

[193] Barbulescu GI, Bojin FM, Ordodi VL, Goje ID, Barbulescu AS, Paunescu V. Decellularized Extracellular Matrix Scaffolds for Cardiovascular Tissue Engineering: Current Techniques and Challenges. Int J Mol Sci. 2022;23(21). Available from: https://www.ncbi.nlm.nih.gov/pubmed/36361824.

[194] Jang Y, Park Y, Kim J. Engineering Biomaterials to Guide Heart Cells for Matured Cardiac Tissue. Coatings. 2020;10(10):925. Available from: https://www.mdpi.com/2079-6412/10/10/925.

[195] Geckil H, Xu F, Zhang X, Moon S, Demirci U. Engineering hydrogels as extracellular matrix mimics. Nanomedicine (Lond). 2010;5(3):469-84. Available from: https://www.ncbi.nlm.nih.gov/pubmed/20394538.

[196] Vasile C, Pamfil D, Stoleru E, Baican M. New Developments in Medical Applications of Hybrid Hydrogels Containing Natural Polymers. Molecules. 2020;25(7). Available from: https://www.ncbi.nlm.nih.gov/pubmed/32230990.

[197] Chow A, Stuckey DJ, Kidher E, Rocco M, Jabbour RJ, Mansfield CA, et al. Human Induced Pluripotent Stem Cell-Derived Cardiomyocyte Encapsulating Bioactive Hydrogels Improve Rat Heart Function Post Myocar-

dial Infarction. Stem Cell Reports. 2017;9(5):1415-22. Available from: https://www.ncbi.nlm.nih.gov/pubmed/28988988.

[198] Zhu J. Bioactive modification of poly(ethylene glycol) hydrogels for tissue engineering. Biomaterials. 2010;31(17):4639-56. Available from: https://www.ncbi.nlm.nih.gov/pubmed/20303169.

[199] Lee S, Tong X, Yang F. The effects of varying poly(ethylene glycol) hydrogel crosslinking density and the crosslinking mechanism on protein accumulation in three-dimensional hydrogels. Acta Biomater. 2014;10(10):4167-74. Available from: https://www.ncbi.nlm.nih.gov/pubmed/24887284.

[200] Galie PA, Khalid N, Carnahan KE, Westfall MV, Stegemann JP. Substrate stiffness affects sarcomere and costamere structure and electrophysiological function of isolated adult cardiomyocytes. Cardiovasc Pathol. 2013;22(3):219-27. Available from: https://www.ncbi.nlm.nih.gov/pubmed/23266222.

[201] Victor A, Ribeiro J, F Araújo F. Study of PDMS characterization and its applications in biomedicine: A review. Journal of Mechanical Engineering and Biomechanics. 2019;4(1):1-9.

[202] Petersen AP, Lyra-Leite DM, Ariyasinghe NR, Cho N, Goodwin CM, Kim JY, et al. Microenvironmental Modulation of Calcium Wave Propagation Velocity in Engineered Cardiac Tissues. Cell Mol Bioeng. 2018;11(5):337-52. Available from: https://www.ncbi.nlm.nih.gov/pubmed/31719889.

[203] Macdougall LJ, Wiley KL, Kloxin AM, Dove AP. Design of synthetic extracellular matrices for probing breast cancer cell growth using robust cyctocompatible nucleophilic thiol-yne addition chemistry. Biomaterials. 2018;178:435-47. Available from: https://www.ncbi.nlm.nih.gov/pubmed/29773227.

[204] Patel L, Worch JC, Dove AP, Gehmlich K. The Utilisation of Hydrogels for iPSC-Cardiomyocyte Research. Int J Mol Sci. 2023;24. Available from: https://www.mdpi.com/1422-0067/24/12/9995.

[205] Hall C, Gehmlich K, Denning C, Pavlovic D. Complex Relationship Between Cardiac Fibroblasts and Cardiomyocytes in Health and Disease. J Am Heart Assoc. 2021;10(5):e019338. Available from: https://www.ncbi.nlm.nih.gov/pubmed/33586463.

[206] Subramani R, Izquierdo-Alvarez A, Bhattacharya P, Meerts M, Moldenaers P, Ramon H, et al. The Influence of Swelling on Elastic Properties of Polyacrylamide Hydrogels. Front Mater. 2020;7. Available from: https://www.frontiersin.org/journals/materials/articles/10.3389/fmats.2020.00212/full.

[207] Della Sala F, Biondi M, Guarnieri D, Borzacchiello A, Ambrosio L, Mayol L. Mechanical behavior of bioactive poly(ethylene glycol) diacrylate matrices for biomedical application. J Mech Behav Biomed Mater. 2020;110:103885. Available from: https://www.ncbi.nlm.nih.gov/pubmed/32957192.

[208] Harnett EM, Alderman J, Wood T. The surface energy of various biomaterials coated with adhesion molecules used in cell culture. Colloids Surf B Biointerfaces. 2007;55(1):90-7. Available from: https://www.ncbi.nlm.nih.gov/pubmed/17207976.

[209] Park KH, Na K, Chung HM. Enhancement of the adhesion of fibroblasts by peptide containing an Arg-Gly-Asp sequence with poly(ethylene glycol) into a thermo-reversible hydrogel as a synthetic extracellular matrix. Biotechnol Lett. 2005;27(4):227-31. Available from: https://www.ncbi.nlm.nih.gov/pubmed/15742141.

[210] Bellis SL. Advantages of RGD peptides for directing cell association with biomaterials. Biomaterials. 2011;32(18):4205-10. Available from: https://www.ncbi.nlm.nih.gov/pubmed/21515168.

[211] Ruoslahti E. RGD and other recognition sequences for integrins. Annu Rev Cell Dev Biol. 1996;12:697-715. Available from: https://www.ncbi.nlm.nih.gov/pubmed/8970741.

[212] Camci-Unal G, Annabi N, Dokmeci MR, Liao R, Khademhosseini A. Hydrogels for cardiac tissue engineering. NPG Asia Mater. 2014;6. Available from: https://www.nature.com/articles/am201419#citeas.

[213] Poole LB. The basics of thiols and cysteines in redox biology and chemistry. Free Radic Biol Med. 2015;80:148-57. Available from: https://www.ncbi.nlm.nih.gov/pubmed/25433365.

[214] Ajsuvakova OP, Tinkov AA, Aschner M, Rocha JBT, Michalke B, Skalnaya MG, et al. Sulfhydryl groups as targets of mercury toxicity. Coord Chem Rev. 2020;417. Available from: https://www.ncbi.nlm.nih.gov/pubmed/32905350.

[215] Ahmed EM. Hydrogel: Preparation, characterization, and applications: A review. J Adv Res. 2015;6(2):105-21. Available from: https://www.sciencedirect.com/science/article/pii/S2090123213000969?via%3Dihub.

[216] Cui J, Lackey MA, Tew GN, Crosby AJ. Mechanical Properties of End-Linked PEG/PDMS Hydrogels. Macromolecules. 2012;45(15):6104-10. Available from: https://doi.org/10.1021/ma300593g.

[217] Rao C, Prodromakis T, Kolker L, Chaudhry UA, Trantidou T, Sridhar A, et al. The effect of microgrooved culture substrates on calcium cycling of cardiac myocytes derived from human induced pluripotent stem cells. Biomaterials. 2013;34(10):2399-411. Available from: https://www.ncbi.nlm.nih.gov/pubmed/23261219.

[218] Sacchetto C, Vitiello L, de Windt LJ, Rampazzo A, Calore M. Modeling Cardiovascular Diseases with hiPSC-Derived Cardiomyocytes in 2D and 3D Cultures. Int J Mol Sci. 2020;21(9). Available from: https://www.ncbi.nlm.nih.gov/pubmed/32403456.

[219] Chin IL, Hool L, Choi YS. A Review of in vitro Platforms for Understanding Cardiomyocyte Biology. Front Bioeng Biotechnol. 2019;7:133. Available from: https://www.ncbi.nlm.nih.gov/pubmed/31231644.

[220] Yi B, Xu Q, Liu W. An overview of substrate stiffness guided cellular response and its applications in tissue regeneration. Bioact Mater. 2022;15:82-102. Available from: https://www.ncbi.nlm.nih.gov/pubmed/35386347.

[221] Ozcebe SG, Bahcecioglu G, Yue XS, Zorlutuna P. Effect of cellular and ECM aging on human iPSC-derived cardiomyocyte performance, maturity and senescence. Biomaterials. 2021;268:120554. Available from: https://www.ncbi.nlm.nih.gov/pubmed/33296796.

[222] Feridooni HA, Dibb KM, Howlett SE. How cardiomyocyte excitation, calcium release and contraction become altered with age. J Mol Cell Cardiol. 2015;83:62-72. Available from: https://www.ncbi.nlm.nih.gov/pubmed/25498213.

[223] Cesarovic N, Lipiski M, Falk V, Emmert MY. Animals in cardiovascular research. Eur Heart J. 2020;41(2):200-3. Available from: https://www.ncbi.nlm.nih.gov/pubmed/31909425.

[224] Oikonomopoulos A, Kitani T, Wu JC. Pluripotent Stem Cell-Derived Cardiomyocytes as a Platform for Cell Therapy Applications: Progress and Hurdles for Clinical Translation. Mol Ther. 2018;26(7):1624-34. Available from: https://www.ncbi.nlm.nih.gov/pubmed/29699941.

[225] Reilly L, Munawar S, Zhang J, Crone WC, Eckhardt LL. Challenges and innovation: Disease modeling using human-induced pluripotent stem cell-derived cardiomyocytes. Front Cardiovasc Med. 2022;9:966094. Available from: https://www.ncbi.nlm.nih.gov/pubmed/36035948.

[226] Majid QA, Fricker ATR, Gregory DA, Davidenko N, Hernandez Cruz O, Jabbour RJ, et al. Natural Biomaterials for Cardiac Tissue Engineering: A Highly Biocompatible Solution. Front Cardiovasc Med. 2020;7:554597. Available from: https://www.ncbi.nlm.nih.gov/pubmed/33195451.

[227] Sacchetto C, Vitiello L, de Windt LJ, Rampazzo A, Calore M. Modeling Cardiovascular Diseases with hiPSC-Derived Cardiomyocytes in 2D and 3D Cultures. Int J Mol Sci. 2020;21(9). Available from: https://www.ncbi.nlm.nih.gov/pubmed/32403456.

[228] Galie PA, Khalid N, Carnahan KE, Westfall MV, Stegemann JP. Substrate stiffness affects sarcomere and costamere structure and electrophysiological function of isolated adult cardiomyocytes. Cardiovasc Pathol. 2013;22(3):219-27. Available from: https://www.ncbi.nlm.nih.gov/pubmed/23266222.

[229] Guo Y, Pu WT. Cardiomyocyte Maturation: New Phase in Development. Circ Res. 2020;126(8):1086-106. Available from: https://www.ncbi.nlm.nih.gov/pubmed/32271675.

[230] Murphy JF, Mayourian J, Stillitano F, Munawar S, Broughton KM, Agullo-Pascual E, et al. Adult human cardiac stem cell supplementation effectively increases contractile function and maturation in human engineered cardiac tissues. Stem Cell Res Therapy. 2019;10(373). Available from: https://stemcellres.biomedcentral.com/articles/10.1186/s13287-019-1486-4#citeas.

[231] Dhahri W, Sadikov Valdman T, Wilkinson D, Pereira E, Ceylan E, Andharia N, et al. In Vitro Matured Human Pluripotent Stem Cell-Derived Cardiomyocytes Form Grafts With Enhanced Structure and Function in Injured Hearts. Circulation. 2022;145(18):1412-26. Available from: https://www.ncbi.nlm.nih.gov/pubmed/35089805.

[232] Hailstones D, Barton P, Chan-Thomas P, Sasse S, Sutherland C, Hardeman E, et al. Differential regulation of the atrial isoforms of the myosin light chains during striated muscle development. J Biol Chem. 1992;267(32):23295-300. Available from: https://www.ncbi.nlm.nih.gov/pubmed/1429676.

[233] Hersch N, Wolters B, Dreissen G, Springer R, Kirchgeßner N, Merkel R, et al. The constant beat: cardiomyocytes adapt their forces by equal contraction upon environmental stiffening. Biol Open. 2013;2(3):351-61. Available from: https://www.ncbi.nlm.nih.gov/pubmed/23519595.

[234] Jimenez-Vazquez EN, Jain A, Jones DK. Enhancing iPSC-CM Maturation Using a Matrigel-Coated Micropatterned PDMS Substrate. Curr Protoc. 2022;2(11):e601. Available from: https://www.ncbi.nlm.nih.gov/pubmed/36383047.

[235] Rao C, Prodromakis T, Kolker L, Chaudhry UA, Trantidou T, Sridhar A, et al. The effect of microgrooved culture substrates on calcium cycling of cardiac myocytes derived from human induced pluripotent stem cells. Biomaterials. 2013;34(10):2399-411. Available from: https://www.ncbi.nlm.nih.gov/pubmed/23261219.

[236] Skorska A, Johann L, Chabanovska O, Vasudevan P, Kussauer S, Hillemanns M, et al. Monitoring the maturation of the sarcomere network: a super-resolution microscopy-based approach. Cell Mol Life Sci. 2022;79(3):149. Available from: https://www.ncbi.nlm.nih.gov/pubmed/35199227.

[237] Ribeiro AJ, Ang YS, Fu JD, Rivas RN, Mohamed TM, Higgs GC, et al. Contractility of single cardiomyocytes differentiated from pluripotent stem cells depends on physiological shape and substrate stiffness. Proc Natl Acad Sci U S A. 2015;112(41):12705-10. Available from: https://www.ncbi.nlm.nih.gov/pubmed/26417073.

[238] Körner A, Mosqueira M, Hecker M, Ullrich ND. Substrate Stiffness Influences Structural and Functional Remodeling in Induced Pluripotent Stem Cell-Derived Cardiomyocytes [Journal Article]. Front Physiol. 2021;12:710619. Körner, Arlene Mosqueira, Matias Hecker, Markus Ullrich, Nina D 2021/9/8. Available from: https://www.ncbi.nlm.nih.gov/pubmed/34489730.

[239] Sewanan LR, Schwan J, Kluger J, Park J, Jacoby DL, Qyang Y, et al. Extracellular Matrix From Hypertrophic Myocardium Provokes Impaired Twitch Dynamics in Healthy Cardiomyocytes. JACC Basic Transl Sci. 2019;4(4):495-505. Available from: https://www.ncbi.nlm.nih.gov/pubmed/31468004.

[240] Wheelwright M, Win Z, Mikkila JL, Amen KY, Alford PW, Metzger JM. Investigation of human iPSC-derived cardiac myocyte functional maturation by single cell traction force microscopy. PLoS One. 2018;13(4):e0194909. Available from: https://www.ncbi.nlm.nih.gov/pubmed/29617427.

[241] Nishimura S, Nagai S, Katoh M, Yamashita H, Saeki Y, Okada J, et al. Microtubules modulate the stiffness of cardiomyocytes against shear stress. Circ Res. 2006;98(1):81-7. Available from: https://www.ncbi.nlm.nih.gov/pubmed/16306445.

[242] Gorski PA, Ceholski DK, Hajjar RJ. Altered myocardial calcium cycling and energetics in heart failure–a rational approach for disease treatment. Cell Metab. 2015;21(2):183-94. Available from: https://www.ncbi.nlm.nih.gov/pubmed/25651173.

[243] Pioner JM, Santini L, Palandri C, Martella D, Lupi F, Langione M, et al. Optical Investigation of Action Potential and Calcium Handling Maturation of hiPSC-Cardiomyocytes on Biomimetic Substrates. Int J Mol Sci. 2019;20(15). Available from: https://www.ncbi.nlm.nih.gov/pubmed/31382622.

[244] Herron TJ, Rocha AM, Campbell KF, Ponce-Balbuena D, Willis BC, Guerrero-Serna G, et al. Extracellular Matrix-Mediated Maturation of Human Pluripotent Stem Cell-Derived Cardiac Monolayer Structure and Electrophysiological Function. Circ Arrhythm Electrophysiol. 2016;9(4):e003638. Available from: https://www.ncbi.nlm.nih.gov/pubmed/27069088.

[245] Boothe SD, Myers JD, Pok S, Sun J, Xi Y, Nieto RM, et al. The Effect of Substrate Stiffness on Cardiomyocyte Action Potentials. Cell Biochem Biophys. 2016;74(4):527-35. Available from: https://www.ncbi.nlm.nih.gov/pubmed/27722948.

[246] Körner A, Mosqueira M, Hecker M, Ullrich ND. Substrate Stiffness Influences Structural and Functional Remodeling in Induced Pluripotent Stem

Cell-Derived Cardiomyocytes. Front Physiol. 2021;12:710619. Available from: https://www.ncbi.nlm.nih.gov/pubmed/34489730.

[247] Tallawi M, Rai R, Boccaccini AR, Aifantis KE. Effect of substrate mechanics on cardiomyocyte maturation and growth. Tissue Eng Part B Rev. 2015;21(1):157-65. Available from: https://www.ncbi.nlm.nih.gov/pubmed/25148904.

[248] Martewicz S, Serena E, Zatti S, Keller G, Elvassore N. Substrate and mechanotransduction influence SERCA2a localization in human pluripotent stem cell-derived cardiomyocytes affecting functional performance. Stem Cell Res. 2017;25:107-14. Available from: https://www.ncbi.nlm.nih.gov/pubmed/29125993.

[249] Itzhaki I, Rapoport S, Huber I, Mizrahi I, Zwi-Dantsis L, Arbel G, et al. Calcium handling in human induced pluripotent stem cell derived cardiomyocytes. PLoS One. 2011;6(4):e18037. Available from: https://www.ncbi.nlm.nih.gov/pubmed/21483779.

[250] Aschar-Sobbi R, Emmett TL, Kargacin GJ, Kargacin ME. Phospholamban phosphorylation increases the passive calcium leak from cardiac sarcoplasmic reticulum. Pflugers Arch. 2012;464(3):295-305. Available from: https://www.ncbi.nlm.nih.gov/pubmed/22772476.

[251] Traister A, Li M, Aafaqi S, Lu M, Arab S, Radisic M, et al. Integrin-linked kinase mediates force transduction in cardiomyocytes by modulating SERCA2a/PLN function. Nat Commun. 2014;5:4533. Available from: https://www.ncbi.nlm.nih.gov/pubmed/25208486.

[252] Kolanowski TJ, Antos CL, Guan K. Making human cardiomyocytes up to date: Derivation, maturation state and perspectives. Int J Cardiol. 2017;241:379-86. Available from: https://www.ncbi.nlm.nih.gov/pubmed/28377185.

[253] Yang X, Pabon L, Murry CE. Engineering adolescence: maturation of human pluripotent stem cell-derived cardiomyocytes. Circ Res. 2014;114(3):511-23. Available from: https://www.ncbi.nlm.nih.gov/pubmed/24481842.

[254] Han JF, Wu Q, Xia Y, Wagner MB, Xu C. Cell alignment induced by anisotropic electrospun fibrous scaffolds alone has limited effect on cardiomyocyte maturation. Stem Cell Research. 2016;16(373):740-50.

Available from: https://www.sciencedirect.com/science/article/pii/S187350611630023X.

[255] Allen ACB, Barone E, Momtahan N, Crosby CO, Tu C, Deng W, et al. Temporal Impact of Substrate Anisotropy on Differentiating Cardiomyocyte Alignment and Functionality. Tissue Eng Part A. 2019;25:1426-37. Available from: https://www.ncbi.nlm.nih.gov/pmc/articles/pmid/30727863/.

[256] Wanjare M, Hou L, Nakayama KH, Kim JJ, Mezak NP, Abilez OJ, et al. Anisotropic microfibrous scaffolds enhance the organization and function of cardiomyocytes derived from induced pluripotent stem cells. Biomater Sci. 2017;5:1567-78. Available from: https://pubs.rsc.org/en/content/articlelanding/2017/bm/c7bm00323d.

[257] Garbern JC, Lee RT. Mitochondria and metabolic transitions in cardiomyocytes: lessons from development for stem cell-derived cardiomyocytes. Stem Cell Res Ther. 2021;12(1):177. Available from: https://www.ncbi.nlm.nih.gov/pubmed/33712058.

[258] Ventura-Clapier R, Garnier A, Veksler V, Joubert F. Bioenergetics of the failing heart. Biochim Biophys Acta. 2011;1813(7):1360-72. Available from: https://www.ncbi.nlm.nih.gov/pubmed/20869993.

[259] Ramachandra CJA, Chua J, Cong S, Kp MMJ, Shim W, Wu JC, et al. Human-induced pluripotent stem cells for modelling metabolic perturbations and impaired bioenergetics underlying cardiomyopathies. Cardiovasc Res. 2021;117(3):694-711. Available from: https://www.ncbi.nlm.nih.gov/pubmed/32365198.

[260] RANDLE PJ, GARLAND PB, HALES CN, NEWSHOLME EA. The glucose fatty-acid cycle. Its role in insulin sensitivity and the metabolic disturbances of diabetes mellitus. Lancet. 1963;1(7285):785-9. Available from: https://www.ncbi.nlm.nih.gov/pubmed/13990765.

[261] Martínez MS, García A, Luzardo E, Chávez-Castillo M, Olivar LC, Salazar J, et al. Energetic metabolism in cardiomyocytes: molecular basis of heart ischemia and arrhythmogenesis. Vessel Plus. 2017;1(12).

[262] Sithara T, Drosatos K. Metabolic Complications in Cardiac Aging. Front Physiol. 2021;12:669497. Available from: https://www.ncbi.nlm.nih.gov/pubmed/33995129.

[263] Ramachandra CJA, Chua J, Cong S, Kp MMJ, Shim W, Wu JC, et al. Human-induced pluripotent stem cells for modelling metabolic perturbations and impaired bioenergetics underlying cardiomyopathies. Cardiovasc Res. 2021;117(3):694-711. Available from: https://www.ncbi.nlm.nih.gov/pubmed/32365198.

[264] WARBURG O. On the origin of cancer cells. Science. 1956;123(3191):309-14. Available from: https://www.ncbi.nlm.nih.gov/pubmed/13298683.

[265] Park JS, Burckhardt CJ, Lazcano R, Solis LM, Isogai T, Li L, et al. Mechanical regulation of glycolysis via cytoskeleton architecture. Nature. 2020;578(7796):621-6. Available from: https://www.ncbi.nlm.nih.gov/pubmed/32051585.

[266] Correia C, Koshkin A, Duarte P, Hu D, Teixeira A, Domian I, et al. Distinct carbon sources affect structural and functional maturation of cardiomyocytes derived from human pluripotent stem cells. Sci Rep. 2017;7(1):8590. Available from: https://www.ncbi.nlm.nih.gov/pubmed/28819274.

[267] Vučković S, Dinani R, Nollet EE, Kuster DWD, Buikema JW, Houtkooper RH, et al. Characterization of cardiac metabolism in iPSC-derived cardiomyocytes: lessons from maturation and disease modeling. Stem Cell Res Ther. 2022;13(1):332. Available from: https://www.ncbi.nlm.nih.gov/pubmed/35870954.

[268] Depre C, Vanoverschelde JLJ, Taegtmeyer H. Glucose for the Heart. Circulation. 1999;99. Available from: https://www.ahajournals.org/doi/10.1161/01.cir.99.4.578.

[269] Dong S, Qian L, Cheng Z, Chen C, Wang K, Hu S, et al. Lactate and Myocardiac Energy Metabolism. Front Physiol. 2021;12:715081. Available from: https://www.ncbi.nlm.nih.gov/pubmed/34483967.

[270] Nyberg M, Jones AM. Matching of O. Front Physiol. 2022;13:898395. Available from: https://www.ncbi.nlm.nih.gov/pubmed/35774284.

[271] Emanuelli G, Zoccarato A, Reumiller CM, Papadopoulos A, Chong M, Rebs S, et al. A roadmap for the characterization of energy metabolism in human cardiomyocytes derived from induced pluripotent stem cells. J Mol Cell Cardiol. 2022;164:136-47. Available from: https://www.ncbi.nlm.nih.gov/pubmed/34923199.

[272] Ge H, Tian M, Pei Q, Tan F, Pei H. Extracellular Matrix Stiffness: New Areas Affecting Cell Metabolism. Front Oncol. 2021;11:631991. Available from: https://www.ncbi.nlm.nih.gov/pubmed/33718214.

[273] Kashihara T, Sadoshima J. Regulation of myocardial glucose metabolism by YAP/TAZ signaling. J Cardiol. 2024;83(5):323-9. Available from: https://www.ncbi.nlm.nih.gov/pubmed/38266816.

[274] Desler C, Durhuus JA, Hansen TL, Anugula S, Zelander NT, Bøggild S, et al. Partial inhibition of mitochondrial-linked pyrimidine synthesis increases tumorigenic potential and lysosome accumulation. Mitochondrion. 2022;64:73-81. Available from: https://www.ncbi.nlm.nih.gov/pubmed/35346867.

[275] Lesnefsky EJ, Chen Q, Hoppel CL. Mitochondrial Metabolism in Aging Heart. Circ Res. 2016;118(10):1593-611. Available from: https://www.ncbi.nlm.nih.gov/pubmed/27174952.

[276] Jastroch M, Divakaruni AS, Mookerjee S, Treberg JR, Brand MD. Mitochondrial proton and electron leaks. Essays Biochem. 2010;47:53-67. Available from: https://www.ncbi.nlm.nih.gov/pubmed/20533900.

[277] Zhang H, Alder NN, Wang W, Szeto H, Marcinek DJ, Rabinovitch PS. Reduction of elevated proton leak rejuvenates mitochondria in the aged cardiomyocyte. Elife. 2020;9. Available from: https://www.ncbi.nlm.nih.gov/pubmed/33319746.

[278] Murphy E, Steenbergen C. Mechanisms underlying acute protection from cardiac ischemia-reperfusion injury. Physiol Rev. 2008;88(2):581-609. Available from: https://www.ncbi.nlm.nih.gov/pubmed/18391174.

[279] Quarrie R, Cramer BM, Lee DS, Steinbaugh GE, Erdahl W, Pfeiffer DR, et al. Ischemic preconditioning decreases mitochondrial proton leak and reactive oxygen species production in the postischemic heart. J Surg Res. 2011;165(1):5-14. Available from: https://www.ncbi.nlm.nih.gov/pubmed/21035133.

[280] Amjad S, Nisar S, Bhat AA, Shah AR, Frenneaux MP, Fakhro K, et al. Role of NAD+ in regulating cellular and metabolic signaling pathways. Molecular Metabolism. 2021;49. Available from: https://www.sciencedirect.com/science/article/pii/S2212877821000351.

[281] Ihenacho UK, Meacham KA, Harwig MC, Widlansky ME, Hill RB. Mitochondrial Fission Protein 1: Emerging Roles in Organellar Form and Function in Health and Disease. Front Endocrinol (Lausanne). 2021;12:660095. Available from: https://www.ncbi.nlm.nih.gov/pubmed/33841340.

[282] Li A, Gao M, Jiang W, Qin Y, Gong G. Mitochondrial Dynamics in Adult Cardiomyocytes and Heart Diseases. Front Cell Dev Biol. 2020;8:584800. Available from: https://www.ncbi.nlm.nih.gov/pubmed/33392184.

[283] Wang X, Song H, Liang J, Jia Y, Zhang Y. Abnormal expression of HADH, an enzyme of fatty acid oxidation, affects tumor development and prognosis (Review). Mol Med Rep. 2022;26(6). Available from: https://www.ncbi.nlm.nih.gov/pubmed/36239258.

[284] Zangari J, Petrelli F, Maillot B, Martinou JC. The Multifaceted Pyruvate Metabolism: Role of the Mitochondrial Pyruvate Carrier. Biomolecules. 2020;10(7). Available from: https://www.ncbi.nlm.nih.gov/pubmed/32708919.

[285] Gray LR, Tompkins SC, Taylor EB. Regulation of pyruvate metabolism and human disease. Cell Mol Life Sci. 2014;71(14):2577-604. Available from: https://www.ncbi.nlm.nih.gov/pubmed/24363178.

[286] Shi H, Yuan M, Cai J, Lan L, Wang Y, Wang W, et al. HTRA1-driven detachment of type I collagen from endoplasmic reticulum contributes to myocardial fibrosis in dilated cardiomyopathy. J Transl Med. 2024;22(1):297. Available from: https://www.ncbi.nlm.nih.gov/pubmed/38515161.

[287] Fredriksson-Lidman K, Van Itallie CM, Tietgens AJ, Anderson JM. Sorbin and SH3 domain-containing protein 2 (SORBS2) is a component of the acto-myosin ring at the apical junctional complex in epithelial cells. PLoS One. 2017;12(9):e0185448. Available from: https://www.ncbi.nlm.nih.gov/pubmed/28961272.

[288] McLendon JM, Zhang X, Matasic DS, Kumar M, Koval OM, Grumbach IM, et al. Knockout of Sorbin And SH3 Domain Containing 2 (Sorbs2) in Cardiomyocytes Leads to Dilated Cardiomyopathy in Mice. J Am Heart Assoc. 2022;11(13):e025687. Available from: https://www.ncbi.nlm.nih.gov/pubmed/35730644.

[289] Doenst T, Nguyen TD, Abel ED. Cardiac metabolism in heart failure: implications beyond ATP production. Circ Res. 2013;113(6):709-24. Available from: https://www.ncbi.nlm.nih.gov/pubmed/23989714.

[290] Xie S, Xu SC, Deng W, Tang Q. Metabolic landscape in cardiac aging: insights into molecular biology and therapeutic implications. Signal Transduct Target Ther. 2023;8(1):114. Available from: https://www.ncbi.nlm.nih.gov/pubmed/36918543.

[291] Declercq PE, Falck JR, Kuwajima M, Tyminski H, Foster DW, McGarry JD. Characterization of the mitochondrial carnitine palmitoyltransferase enzyme system. I. Use of inhibitors. J Biol Chem. 1987;262(20):9812-21. Available from: https://www.ncbi.nlm.nih.gov/pubmed/3597441.

[292] van der Leij FR, Cox KB, Jackson VN, Huijkman NC, Bartelds B, Kuipers JR, et al. Structural and functional genomics of the CPT1B gene for muscle-type carnitine palmitoyltransferase I in mammals. J Biol Chem. 2002;277(30):26994-7005. Available from: https://www.ncbi.nlm.nih.gov/pubmed/12015320.

[293] Angelini A, Saha PK, Jain A, Jung SY, Mynatt RL, Pi X, et al. PHDs/CPT1B/VDAC1 axis regulates long-chain fatty acid oxidation in cardiomyocytes. Cell Rep. 2021;37(1):109767. Available from: https://www.ncbi.nlm.nih.gov/pubmed/34610308.

[294] Flam E, Jang C, Murashige D, Yang Y, Morley MP, Jung S, et al. Integrated landscape of cardiac metabolism in end-stage human nonischemic dilated cardiomyopathy. Nat Cardiovasc Res. 2022;1(9):817-29. Available from: https://www.ncbi.nlm.nih.gov/pubmed/36776621.

[295] Zhao L, Zou X, Feng Z, Luo C, Liu J, Li H, et al. Evidence for association of mitochondrial metabolism alteration with lipid accumulation in aging rats. Exp Gerontol. 2014;56:3-12. Available from: https://www.ncbi.nlm.nih.gov/pubmed/24518876.

[296] Pagan LU, Gomes MJ, Gatto M, Mota GAF, Okoshi K, Okoshi MP. The Role of Oxidative Stress in the Aging Heart. Antioxidants (Basel). 2022;11(2). Available from: https://www.ncbi.nlm.nih.gov/pubmed/35204217.

[297] Koonen DP, Febbraio M, Bonnet S, Nagendran J, Young ME, Michelakis ED, et al. CD36 expression contributes to age-induced cardiomyopathy in mice. Circulation. 2007;116(19):2139-47. Available from: https://www.ncbi.nlm.nih.gov/pubmed/17967771.

[298] Shu H, Peng Y, Hang W, Nie J, Zhou N, Wang DW. The role of CD36 in cardiovascular disease. Cardiovasc Res. 2022;118(1):115-29. Available from: https://www.ncbi.nlm.nih.gov/pubmed/33210138.

[299] Calmettes G, Ribalet B, John S, Korge P, Ping P, Weiss JN. Hexokinases and cardioprotection. J Mol Cell Cardiol. 2015;78:107-15. Available from: https://www.ncbi.nlm.nih.gov/pubmed/25264175.

[300] Wu R, Wyatt E, Chawla K, Tran M, Ghanefar M, Laakso M, et al. Hexokinase II knockdown results in exaggerated cardiac hypertrophy via increased ROS production. EMBO Mol Med. 2012;4(7):633-46. Available from: https://www.ncbi.nlm.nih.gov/pubmed/22517678.

[301] Vallerie SN, Bornfeldt KE. Metabolic Flexibility and Dysfunction in Cardiovascular Cells. Arterioscler Thromb Vasc Biol. 2015;35(9):e37-42. Available from: https://www.ncbi.nlm.nih.gov/pubmed/26310811.

[302] García M, Pujol A, Ruzo A, Riu E, Ruberte J, Arbós A, et al. Phosphofructo-1-kinase deficiency leads to a severe cardiac and hematological disorder in addition to skeletal muscle glycogenosis. PLoS Genet. 2009;5(8):e1000615. Available from: https://www.ncbi.nlm.nih.gov/pubmed/19696889.

[303] Zhou M, Sun X, Wang C, Wang F, Fang C, Hu Z. PFKM inhibits doxorubicin-induced cardiotoxicity by enhancing oxidative phosphorylation and glycolysis. Sci Rep. 2022;12(1):11684. Available from: https://www.ncbi.nlm.nih.gov/pubmed/35804014.

[304] Pettersen IKN, Tusubira D, Ashrafi H, Dyrstad SE, Hansen L, Liu XZ, et al. Upregulated PDK4 expression is a sensitive marker of increased fatty acid oxidation. Mitochondrion. 2019;49:97-110. Available from: https://www.ncbi.nlm.nih.gov/pubmed/31351920.

[305] Fatmi MK, Ren D, Fedorova J, Zoungrana LI, Wang H, Davitt K, et al. Cardiomyocyte Pdk4 response is associated with metabolic maladaptation in aging. Aging Cell. 2023;22(4):e13800. Available from: https://www.ncbi.nlm.nih.gov/pubmed/36797808.

[306] Lopez CA, Al-Siddiqi HHAA, Purnama U, Iftekhar S, Bruyneel AAN, Kerr M, et al. Physiological and pharmacological stimulation for in vitro maturation of substrate metabolism in human induced pluripotent stem cell-derived cardiomyocytes. Sci Rep. 2021;11(1):7802. Available from: https://www.ncbi.nlm.nih.gov/pubmed/33833285.

[307] Elnwasany A, Ewida HA, Szweda PA, Szweda LI. Inhibition of Pyruvate Dehydrogenase in the Heart as an Initiating Event in the Development of

Diabetic Cardiomyopathy. Antioxidants (Basel). 2023;12(3). Available from: https://www.ncbi.nlm.nih.gov/pubmed/36979003.

[308] Sheeran FL, Angerosa J, Liaw NY, Cheung MM, Pepe S. Adaptations in Protein Expression and Regulated Activity of Pyruvate Dehydrogenase Multienzyme Complex in Human Systolic Heart Failure. Oxid Med Cell Longev. 2019;2019:4532592. Available from: https://www.ncbi.nlm.nih.gov/pubmed/30881593.

[309] Moreau R, Heath SH, Doneanu CE, Harris RA, Hagen TM. Age-related compensatory activation of pyruvate dehydrogenase complex in rat heart. Biochem Biophys Res Commun. 2004;325(1):48-58. Available from: https://www.ncbi.nlm.nih.gov/pubmed/15522199.

[310] Škerlová J, Berndtsson J, Nolte H, Ott M, Stenmark P. Structure of the native pyruvate dehydrogenase complex reveals the mechanism of substrate insertion. Nat Commun. 2021;12(1):5277. Available from: https://www.ncbi.nlm.nih.gov/pubmed/34489474.

[311] Lee TW, Bai KJ, Lee TI, Chao TF, Kao YH, Chen YJ. PPARs modulate cardiac metabolism and mitochondrial function in diabetes. J Biomed Sci. 2017;24(1):5. Available from: https://www.ncbi.nlm.nih.gov/pubmed/28069019.

[312] Kelly DP. PPARs of the heart: three is a crowd. Circ Res. 2003;92(5):482-4. Available from: https://www.ncbi.nlm.nih.gov/pubmed/12649261.

[313] Barger PM, Brandt JM, Leone TC, Weinheimer CJ, Kelly DP. Deactivation of peroxisome proliferator-activated receptor-alpha during cardiac hypertrophic growth. J Clin Invest. 2000;105(12):1723-30. Available from: https://www.ncbi.nlm.nih.gov/pubmed/10862787.

[314] Hamblin M, Chang L, Fan Y, Zhang J, Chen YE. PPARs and the cardiovascular system. Antioxid Redox Signal. 2009;11(6):1415-52. Available from: https://www.ncbi.nlm.nih.gov/pubmed/19061437.

[315] Hondares E, Pineda-Torra I, Iglesias R, Staels B, Villarroya F, Giralt M. PPARdelta, but not PPARalpha, activates PGC-1alpha gene transcription in muscle. Biochem Biophys Res Commun. 2007;354(4):1021-7. Available from: https://www.ncbi.nlm.nih.gov/pubmed/17275789.

[316] Erol A. The Functions of PPARs in Aging and Longevity. PPAR Res. 2007;2007:39654. Available from: https://www.ncbi.nlm.nih.gov/pubmed/18317516.

[317] Son NH, Park TS, Yamashita H, Yokoyama M, Huggins LA, Okajima K, et al. Cardiomyocyte expression of PPARgamma leads to cardiac dysfunction in mice. J Clin Invest. 2007;117(10):2791-801. Available from: https://www.ncbi.nlm.nih.gov/pubmed/17823655.

[318] Chen L, Qin Y, Liu B, Gao M, Li A, Li X, et al. PGC-1a-Mediated Mitochondrial Quality Control: Molecular Mechanisms and Implications for Heart Failure. Front Cell Dev Biol. 2022;10:871357. Available from: https://www.ncbi.nlm.nih.gov/pubmed/35721484.

[319] Liu Y, Colby JK, Zuo X, Jaoude J, Wei D, Shureiqi I. The Role of PPAR-in Metabolism, Inflammation, and Cancer: Many Characters of a Critical Transcription Factor. Int J Mol Sci. 2018;19(11). Available from: https://www.ncbi.nlm.nih.gov/pubmed/30373124.

[320] Feyen DAM, McKeithan WL, Bruyneel AAN, Spiering S, Hörmann L, Ulmer B, et al. Metabolic Maturation Media Improve Physiological Function of Human iPSC-Derived Cardiomyocytes. Cell Rep. 2020;32(3):107925. Available from: https://www.ncbi.nlm.nih.gov/pubmed/32697997.

[321] Wickramasinghe NM, Sachs D, Shewale B, Gonzalez DM, Dhanan-Krishnan P, Torre D, et al. PPARdelta activation induces metabolic and contractile maturation of human pluripotent stem cell-derived cardiomyocytes. Cell Stem Cell. 2022;29(4):559-76.e7. Available from: https://www.ncbi.nlm.nih.gov/pubmed/35325615.

[322] Cheng L, Ding G, Qin Q, Huang Y, Lewis W, He N, et al. Cardiomyocyte-restricted peroxisome proliferator-activated receptor-delta deletion perturbs myocardial fatty acid oxidation and leads to cardiomyopathy. Nat Med. 2004;10(11):1245-50. Available from: https://www.ncbi.nlm.nih.gov/pubmed/15475963.

[323] Wang P, Liu J, Li Y, Wu S, Luo J, Yang H, et al. Peroxisome proliferator-activated receptor delta is an essential transcriptional regulator for mitochondrial protection and biogenesis in adult heart. Circ Res. 2010;106(5):911-9. Available from: https://www.ncbi.nlm.nih.gov/pubmed/20075336.

[324] Chistiakov DA, Sobenin IA, Revin VV, Orekhov AN, Bobryshev YV. Mitochondrial aging and age-related dysfunction of mitochondria. Biomed Res Int. 2014;2014:238463. Available from: https://www.ncbi.nlm.nih.gov/pubmed/24818134.

[325] Marshall JD, Beck S, Maffei P, Naggert JK. Alström syndrome. Eur J Hum Genet. 2007;15(12):1193-202. Available from: https://www.ncbi.nlm.nih.gov/pubmed/17940554.

[326] Karlsson M, Zhang C, Méar L, Zhong W, Digre A, Katona B, et al. A single-cell type transcriptomics map of human tissues. Sci Adv. 2021;7(31). Available from: https://www.ncbi.nlm.nih.gov/pubmed/34321199.

[327] Bond J, Flintoff K, Higgins J, Scott S, Bennet C, Parsons J, et al. The importance of seeking ALMS1 mutations in infants with dilated cardiomyopathy. J Med Genet. 2005;42(2):e10. Available from: https://www.ncbi.nlm.nih.gov/pubmed/15689433.

[328] Loughery E. ASUK Early Years Questionnaire; 2019.

[329] Shenje LT, Andersen P, Halushka MK, Lui C, Fernandez L, Collin GB, et al. Mutations in Alström protein impair terminal differentiation of cardiomyocytes. Nat Commun. 2014;5:3416. Available from: https://www.ncbi.nlm.nih.gov/pubmed/24595103.

[330] McKay EJ, Luijten I, Broadway-Stringer S, Thomson A, Weng X, Gehmlich K, et al. Female Alms1-deficient mice develop echocardiographic features of adult but not infantile Alström Syndrome cardiomyopathy. Dis Model Mech. 2024. Available from: https://www.ncbi.nlm.nih.gov/pubmed/38756069.

[331] Jiang Y, Li X, Guo T, Lu WJ, Ma S, Chang Y, et al. Ranolazine rescues the heart failure phenotype of PLN-deficient human pluripotent stem cell-derived cardiomyocytes. Stem Cell Reports. 2022;17(4):804-19. Available from: https://www.ncbi.nlm.nih.gov/pubmed/35334215.

[332] Kimura Y, Kurzydlowski K, Tada M, MacLennan DH. Phospholamban inhibitory function is activated by depolymerization. J Biol Chem. 1997;272(24):15061-4. Available from: https://www.ncbi.nlm.nih.gov/pubmed/9182523.

[333] Dowrick JM, Taberner AJ, Han JC, Tran K. Methods for assessing cardiac myofilament calcium sensitivity. Front Physiol. 2023;14:1323768. Available from: https://www.ncbi.nlm.nih.gov/pubmed/38116581.

[334] Piquereau J, Ventura-Clapier R. Maturation of Cardiac Energy Metabolism During Perinatal Development. Front Physiol. 2018;9:959. Available from: https://www.ncbi.nlm.nih.gov/pubmed/30072919.

[335] Vallerie SN, Bornfeldt KE. Metabolic Flexibility and Dysfunction in Cardiovascular Cells. Arterioscler Thromb Vasc Biol. 2015;35(9):e37-42. Available from: https://www.ncbi.nlm.nih.gov/pubmed/26310811.

[336] Dassie F, Favaretto F, Bettini S, Parolin M, Valenti M, Reschke F, et al. Alström syndrome: an ultra-rare monogenic disorder as a model for insulin resistance, type 2 diabetes mellitus and obesity. Endocrine. 2021;71(3):618-25. Available from: https://www.ncbi.nlm.nih.gov/pubmed/33566311.

[337] Razeghi P, Young ME, Alcorn JL, Moravec CS, Frazier OH, Taegtmeyer H. Metabolic gene expression in fetal and failing human heart. Circulation. 2001;104(24):2923-31. Available from: https://www.ncbi.nlm.nih.gov/pubmed/11739307.

[338] Redgrave RE, Dookun E, Booth LK, Camacho Encina M, Folaranmi O, Tual-Chalot S, et al. Senescent cardiomyocytes contribute to cardiac dysfunction following myocardial infarction. NPJ Aging. 2023;9(1):15. Available from: https://www.ncbi.nlm.nih.gov/pubmed/37316516.

[339] Hu C, Zhang X, Teng T, Ma ZG, Tang QZ. Cellular Senescence in Cardiovascular Diseases: A Systematic Review. Aging Dis. 2022;13(1):103-28. Available from: https://www.ncbi.nlm.nih.gov/pubmed/35111365.

[340] Häseli S, Deubel S, Jung T, Grune T, Ott C. Cardiomyocyte Contractility and Autophagy in a Premature Senescence Model of Cardiac Aging. Oxid Med Cell Longev. 2020;2020:8141307. Available from: https://www.ncbi.nlm.nih.gov/pubmed/32377307.

[341] Liu JY, Souroullas GP, Diekman BO, Krishnamurthy J, Hall BM, Sorrentino JA, et al. Cells exhibiting strong P16 INK4A promoter activation in vivo display features of senescence. Proc Natl Acad Sci U S A. 2019;116(7):2603-11. Available from: https://www.ncbi.nlm.nih.gov/pubmed/30683717.

[342] Carvalho AB, Coutinho KCDS, Barbosa RAQ, de Campos DBP, Leitão IC, Pinto RS, et al. Action potential variability in human pluripotent stem

cell-derived cardiomyocytes obtained from healthy donors. Front Physiol. 2022;13:1077069. Available from: https://www.ncbi.nlm.nih.gov/pubmed/36589430.

[343] Kiss E, Fischer C, Sauter JM, Sun J, Ullrich ND. The Structural and the Functional Aspects of Intercellular Communication in iPSC-Cardiomyocytes. Int J Mol Sci. 2022;23(8). Available from: https://www.ncbi.nlm.nih.gov/pubmed/35457277.

[344] Howden EJ, Sarma S, Lawley JS, Opondo M, Cornwell W, Stoller D, et al. Reversing the Cardiac Effects of Sedentary Aging in Middle Age-A Randomized Controlled Trial: Implications For Heart Failure Prevention. Circulation. 2018;137(15):1549-60. Available from: https://www.ncbi.nlm.nih.gov/pubmed/29311053.

[345] Cattaneo M, Beltrami AP, Thomas AC, Spinetti G, Alvino VV, Avolio E, et al. The longevity-associated BPIFB4 gene supports cardiac function and vascularization in ageing cardiomyopathy. Cardiovasc Res. 2023;119(7):1583-95. Available from: https://www.ncbi.nlm.nih.gov/pubmed/36635236.

[346] Darban Z, Shahabuddin S, Gaur R, Ahmad I, Sridewi N. Hydrogel-Based Adsorbent Material for the Effective Removal of Heavy Metals from Wastewater: A Comprehensive Review. Gels. 2022;8. Available from: https://www.ncbi.nlm.nih.gov/pmc/articles/PMC9140941/.

[347] Lyra-Leite DM, Andres AM, Cho N, Petersen AP, Ariyasinghe NR, Kim SS, et al. Matrix-guided control of mitochondrial function in cardiac myocytes. Acta Biomater. 2019;97:281-95. Available from: https://www.ncbi.nlm.nih.gov/pubmed/31401347.

[348] Garbis S, Lubec G, Fountoulakis M. Limitations of current proteomics technologies. J Chromatogr A. 2005;1077(1):1-18. Available from: https://www.ncbi.nlm.nih.gov/pubmed/15988981.

[349] Hutchinson-Bunch C, Sanford JA, Hansen JR, Gritsenko MA, Rodland KD, Piehowski PD, et al. Assessment of TMT Labeling Efficiency in Large-Scale Quantitative Proteomics: The Critical Effect of Sample pH. ACS Omega. 2021;6(19):12660-6. Available from: https://www.ncbi.nlm.nih.gov/pubmed/34056417.

[350] The M, Tasnim A, Käll L. How to talk about protein-level false discovery rates in shotgun proteomics. Proteomics. 2016;16(18):2461-9. Available from: https://www.ncbi.nlm.nih.gov/pubmed/27503675.

[351] Cai W, Zhang J, de Lange WJ, Gregorich ZR, Karp H, Farrell ET, et al. An Unbiased Proteomics Method to Assess the Maturation of Human Pluripotent Stem Cell-Derived Cardiomyocytes. Circ Res. 2019;125(11):936-53. Available from: https://www.ncbi.nlm.nih.gov/pubmed/31573406.

[352] Levine ME, Lu AT, Quach A, Chen BH, Assimes TL, Bandinelli S, et al. An epigenetic biomarker of aging for lifespan and healthspan. Aging (Albany NY). 2018;10(4):573-91. Available from: https://www.ncbi.nlm.nih.gov/pubmed/29676998.

[353] Kanasaki K, Kitada M, Koya D. Pathophysiology of the aging kidney and therapeutic interventions. Hypertens Res. 2012;35(12):1121-8. Available from: https://www.ncbi.nlm.nih.gov/pubmed/23076406.

[354] Baig S, Dowd R, Edwards NC, Hodson J, Fabritz L, Vijapurapu R, et al. Prospective cardiovascular magnetic resonance imaging in adults with Alström syndrome: silent progression of diffuse interstitial fibrosis [Journal Article]. Orphanet J Rare Dis. 2020;15(1):139. Baig, Shanat Dowd, Rory Edwards, Nicola C Hodson, James Fabritz, Larissa Vijapurapu, Ravi Liu, Boyang Geberhiwot, Tarekegn Steeds, Richard P 2020/6/7. Available from: https://www.ncbi.nlm.nih.gov/pubmed/32503575.

[355] Lai KY, Wu TH, Liu CS, Lin CH, Lin CC, Lai MM, et al. Body mass index and albumin levels are prognostic factors for long-term survival in elders with limited performance status. Aging (Albany NY). 2020;12(2):1104-13. Available from: https://www.ncbi.nlm.nih.gov/pubmed/31945744.

[356] Peverill RE. Changes in left ventricular size, geometry, pump function and left heart pressures during healthy aging. Rev Cardiovasc Med. 2021;22(3):717-29. Available from: https://www.ncbi.nlm.nih.gov/pubmed/34565071.

[357] Singam NSV, Fine C, Fleg JL. Cardiac changes associated with vascular aging. Clin Cardiol. 2020;43(2):92-8. Available from: https://www.ncbi.nlm.nih.gov/pubmed/31845364.